

**Process-Property-Fabric Architecture Relationships  
in Fibre-Reinforced Composites**

by

Neil Robert Lewarne Pearce

A thesis submitted to the University of Plymouth

in partial fulfilment for the degree of

Doctor of Philosophy

Department of Mechanical and Marine Engineering

Faculty of Technology

In collaboration with the University of Bristol and Carr Reinforcements Limited

November 2001

90 0499132 0



UNIVERSITY OF PLYMOUTH	
Item No.	9004991320
Date	- 5 DEC 2001 T
Class No.	T620.118 PEA
Cont. No.	X 704344563
PLYMOUTH LIBR 3Y	

**REFERENCE ONLY**

**LIBRARY STORE**

*brdsc - thesis unsuitable for microfilming - too many published papers.*

*This copy of the thesis has been supplied on condition that anyone who consults it is understood to recognise that its copyright rests with its author and that no quotation from the thesis and no information derived from it may be published without the author's prior written consent.*

## **Process-Property-Fabric Architecture Relationships in Fibre-Reinforced Composites**

### **Abstract**

The use of fibre-reinforced polymer matrix composite materials is growing at a faster rate than GDP in many countries. An improved understanding of their processing and mechanical behaviour would extend the potential applications of these materials. For unidirectional composites, it is predicted that localised absence of fibres is related to longitudinal compression failure. The use of woven reinforcements permits more effective manufacture than for unidirectional fibres. It has been demonstrated experimentally that compression strengths of woven composites are reduced when fibres are clustered. Summerscales predicted that clustering of fibres would increase the permeability of the reinforcement and hence expedite the processing of these materials. Commercial fabrics are available which employ this concept using flow-enhancing bound tows. The net effect of clustering fibres is to enhance processability whilst reducing the mechanical properties. The effects reported above were qualitative correlations. Gross differences in the appearance of laminate sections are apparent for different weave styles. For the quantification of subtle changes in fabric architecture, the use of automated image analysis is essential. Griffin used Voronoi tessellation to measure the microstructures of composites made using flow-enhancing tows. The data was presented as histograms with no single parameter to quantify microstructure. This thesis describes the use of automated image analysis for the measurement of the microstructures of woven fibre-reinforced composites, and pioneers the use of fractal dimensions as a single parameter for their quantification. It further considers the process-property-structure relationships for commercial and experimental fabric reinforcements in an attempt to resolve the processing *versus* properties dilemma. A new flow-enhancement concept has been developed which has a reduced impact on laminate mechanical properties.

## List of Contents

Title page	i
Copyright notice	ii
Abstract	iii
Contents	iv
List of Appendices	v
List of Figures	vi
List of Tables	ix
Acknowledgements	xi
Author declaration	xii
External Training attended	xiii
Internal Training attended	xiii
Journal papers	xiii
Conference papers	xiv
Introduction	1
Experimental	8
Materials	8
Brochier fabrics	8
New concept Carr fabrics	9
Measurement of permeability/fabrication of test plates	10
Microscopical analysis	11
Preparation	11
Image analysis	11
Fabric architecture and void distribution	11
Fractal characterisation	11
Mechanical Testing	15
Results	16
Brochier fabrics	16
New concept Carr fabrics	17
Comparison of different fabric sets	19
Fractal dimension and permeability	19
Fractal dimension and mechanical properties	20
Conclusions	22
Brochier fabrics	23
New concept Carr fabrics	24
Convergent flow	25
Recommendations for further work	27
Summary	28
Acknowledgement	29
References	29

## **List of Appendices**

### **Appendix A Journal papers published during and since the research programme**

- A1** Composites Manufacturing, March 1995, 6(1), 15-21.
- A2** Composites Part A: Applied Science and Manufacturing, 1998, 29A(1/2), 19-27.  
Publishers erratum, 1998, 29A(5/6), 707.
- A3** Composites Part A: Applied Science and Manufacturing, 1998, 29A(1/2), 141-152.
- A4** Composites Part A: Applied Science and Manufacturing, 1998, 29A(7), 829-837.
- A5** Composites Part A: Applied Science and Manufacturing, 2000, 31A(12), 1433-1441.
- A6** Journal of Microscopy, February 2001, 201(2), 153-162.

### **Appendix B Experimental procedures and software**

- B1** Reinforcement fabrics tested for permeability in University of Plymouth programmes
- B2** Procedure for the conduct of a permeability experiment.
- B3** Mathematics for calculation of anisotropic permeability from a radial flow experiment
- B4** Software for interrogation of flow front images and calculation of permeability.
- B5** Procedure for preparation of polished sections.
- B6** Software for quantification of microstructural features (Quantimet 570)
- B7** Selective images taken during the production and testing of mechanical test specimens

### **Appendix C Text and data-files on CD-ROM**

<b>List of Figures</b>	<b>Page</b>
Figure 1: Schematics of Carr fabrics (weft direction shown as vertical)	3
Figure 2: Voronoi tessellation of a section of glass fibre composite.	4
Figure 3a: Histogram of pore space areas for Carr fabric 126.	6
Figure 3b: Cumulative curve of pore space zones less than a given value for Carr fabrics.	6
Figure 4: Flow area and permeability plotted against percentage FET for Carr bound tow FET.	7
Figure 5: Strengths of Carr fabrics plotted against proportion of flow-enhancing tows in the weft.	7
Figure 6: Schematics and transverse micrographs of Brochier weaves.	8
Figure 7: Transverse micrographs of new concept Carr fabrics.	9
Figure 8: Frame-grabbed images of a typical radial flow permeability experiment at 36, 201 and 653 seconds.	10
Figure 9: Sections of Brochier weaves with sample frames from the determination of fractal dimensions.	12
Figure 10: Sections of new concept Carr weaves with sample frames from the determination of fractal dimensions.	13
Figure 11: Principal in-plane permeabilities in x (K1) and y (K2) of the Brochier fabrics	16
Figure 12: Permeability plotted against fractal dimension for weft (left) and warp (right) new concept Carr fabrics.	17
Figure 13: Weft tensile strength plotted against fractal dimension for new concept Carr fabrics.	19
Figure 14: Permeability plotted against fractal dimension for Brochier and new concept Carr fabrics.	20
Figure 15: Modulus plotted against fractal dimension for Brochier and new concept Carr fabrics	21
Figure 16: Strength plotted against fractal dimension for Brochier and new concept Carr fabrics	21
Figure A1-1: The load/time response of a single isolated layer (upper plot) and of a stack of five fabric layers (lower plot) under similar conditions	A1-7
Figure A1-2: Time taken to achieve the target pressure against number of layers	A1-7
Figure A1-3: Pressure plotted against fibre volume fraction during the initial loading cycle to 300 kPa, (A) 50 mm square samples, (B) 71 mm square samples, (C) 100 mm square samples.	A1-8
Figure A1-4: The data from Figure 3 plotted on log-log axes	A1-9
Figure A1-5: The apparent mean layer thickness of the fabric samples	A1-10
Figure A1-6: Residual load plotted against apparent fibre volume fraction for small samples	A1-11
Figure A1-7: Residual load plotted against apparent fibre volume fraction for medium samples	A1-12
Figure A1-8: Residual load plotted against apparent fibre volume fraction for large samples	A1-13
Figure A2-1: Schematic of 2x2 twill weave	A2-3
Figure A2-2: Schematic of 5-harness satin weave	A2-3
Figure A2-3: Schematic of 5-harness satin Injectex weave	A2-3
Figure A2-4: Multi-port injection strategy	A2-4
Figure A2-5: Principal permeabilities of the twill, satin and Injectex fabrics	A2-7
Figure A2-6: ILSS of the twill, satin and Injectex fabrics	A2-8
Figure A2-7: Measured void volume fractions	A2-9

Figure A2-8: Micrograph of twill fabric	A2-9
Figure A2-9: Micrograph of satin fabric	A2-9
Figure A2-10: Micrograph of injectex fabric	A2-9
Figure A2-11: Normalised plot of cumulative porespace area feature frequencies	A2-11
Figure A2-12: Porespace area feature frequencies	A2-11
Figure A2-13: Normalised permeabilities, ILSS and porespace feature count for twill, satin and Injectex	A2-12
Figure A3-1: Schematic of 2x2 twill weave	A3-5
Figure A3-2: Schematic of 5-harness satin weave	A3-5
Figure A3-3: Schematic of 5-harness satin Injectex weave	A3-5
Figure A3-4: Injection at mid-side ports on two adjacent edges	A3-6
Figure A3-5: Injection at three points along one edge	A3-6
Figure A3-6: Injection via a gallery along one edge and one mid-side port	A3-6
Figure A3-7: Injection from two mid-side ports	A3-11
Figure A3-8: Injection from three ports on one edge	A3-11
Figure A3-9: Injection from a mid-side port and gallery	A3-11
Figure A3-10: Flow convergence from two mid-side ports	A3-11
Figure A3-11: Flow convergence from three ports on one edge	A3-11
Figure A3-12: Flow convergence from mid-side port/gallery	A3-11
Figure A3-13: Ultrasound C-scan of two mid-side ports experiment	A3-12
Figure A3-14: Ultrasound C-scan of three ports on one edge experiment	A3-12
Figure A3-15: Ultrasound C-scan of mid-side port/gallery experiment	A3-12
Figure A3-16: Averaged values of ILSS for specimens from convergent and direct flow areas	A3-13
Figure A3-17: Micrograph of 2x2 twill weave	A3-14
Figure A3-18: Micrograph of 5-harness satin weave	A3-14
Figure A3-19: Micrograph of 5-harness satin Injectex weave	A3-14
Figure A3-20: Averaged void volume fractions for specimens from convergent and direct flow areas	A3-15
Figure A3-21: Measured voidage / Normalised ILSS: Line and edge port injection. 5-Harness satin 65°C	A3-16
Figure A4-1: Schematic of 2x2 twill weave	A4-3
Figure A4-2: Schematic of 5-harness satin weave	A4-3
Figure A4-3: Schematic of 5-harness satin Injectex weave	A4-3
Figure A4-4: Principal permeabilities of the twill, satin and Injectex fabrics	A4-5
Figure A4-5: ILSS of the twill, satin and Injectex fabrics	A4-8
Figure A4-6: Tensile secant moduli of the twill, satin and Injectex fabrics	A4-8
Figure A4-7: Compressive secant moduli of the twill, satin and Injectex fabrics	A4-9
Figure A4-8: Tensile failure stress	A4-9
Figure A4-9: Compressive failure stress	A4-10
Figure A4-10: Representative images showing selective stages of fractal data generation	A4-11
Figure A4-11: Richardson plot showing fabric fractal dimensions	A4-12
Figure A5-1: Micrographs of sections from 'normal' (left) and flow-enhanced (right) satin fabrics at the same fibre volume fraction	A5-2
Figure A5-2: Flow front images at 36, 201 and 653 seconds (first to third box from the left respectively) and a composite of the detected flow front for 45 frames (right).	A5-4
Figure A5-3: Representative images showing the stages of fractal data generation for a Brochier twill fabric	A5-5
Figure A5-4: Fabric permeabilities (left: directional values,	



right: effective isotropic in-plane value).	A5-5
Figure A5-5: Averaged Tensile and Compressive Moduli in Warp and Weft	A5-6
Figure A5-6: Averaged Tensile and Compressive Strengths in Warp and Weft	A5-6
Figure A5-7: Richardson plot showing fabric fractal dimensions measured in the weft direction	A5-7
Figure A5-8: Richardson plot showing fabric fractal dimensions measured in the warp direction	A5-7
Figure A5-9: Fractal dimensions plotted against permeability (both measured in the weft direction)	A5-8
Figure A5-10: Fractal dimensions plotted against permeability (both measured in the warp direction), plotted on the same scale as Figure 9.	A5-8
Figure A6-1: Schematics of Carr fabrics	A6-2
Figure A6-2: Schematics and transverse micrographs of Brochier weaves. Image frame is 3.6 x 3.0 mm.	A6-3
Figure A6-3: Frame-grabbed images of a typical radial flow permeability experiment at 36, 201 and 653 seconds. The square mould has an edge length of 440 mm.	A6-3
Figure A6-4: Voronoi tessellation of a section of glass fibre composite (fibre diameters ~10-30 $\mu\text{m}$ )	A6-4
Figure A6-5: Sections of Brochier weaves with sample frames from the determination of fractal dimensions. Top row: twill, middle row: satin, bottom row: Injectex. Image frame is 3.6 x 3.0 mm.	A6-5
Figure A6-6a: Histogram of pore space areas for Carr fabric 126	A6-6
Figure A6-6b: Cumulative curve of pore space zones less than a given value for Carr fabrics.	A6-6
Figure A6-7: Flow area and permeability plotted against percentage FET for Carr bound tow FET	A6-6
Figure A6-8: Strengths of Carr fabrics plotted against proportion of flow-enhancing tows in the weft.	A6-7
Figure A6-9: Principal in-plane permeabilities in x ( $K_1$ ) and y ( $K_2$ ) of the Brochier fabrics (units of permeability are $\times 10^{-12} \text{ m}^2$ )	A6-7
Figure A6-10: Permeability plotted against fractal dimension for weft (left) and warp (right) new concept Carr fabrics.	A6-8
Figure A6-11: Weft tensile strength plotted against fractal dimension for new concept Carr fabrics.	A6-9
Figure A6-12: Permeability plotted against fractal dimension for Brochier and new concept Carr fabrics.	A6-9
Figure B2.1: Schematic diagram of the permeability apparatus.	B2-2
Figure B2.2: DATA shuttle worksheet for permeability testing.	B2-3
Figure B2.3: DATA shuttle display during permeability testing	B2-3
Figure B3-1: Frame-grabbed images of a typical radial flow permeability experiment at 36, 201 and 653 seconds. The square mould has an edge length of 440 mm.	B3-1
Figure B3-2: Flow through an elemental volume.	B3-7
Figure B7-1: Demoulded plate following permeability experiment	B7-1
Figure B7-2: Universal milling machining used to cut plates	B7-1
Figure B7-3: End tabs and pre-preg film adhesive positioned on trimmed plate	B7-2
Figure B7-4: Stack of trimmed plates with end tabs applied prior to vacuum consolidation	B7-2

Figure B7-5: Vacuum consolidation of trimmed plates and end tabs	B7-2
Figure B7-6: End tabs adhered to oven cured / vacuum consolidated plates	B7-3
Figure B7-7: Check for trueness of adhered end tabs on plate	B7-3
Figure B7-8: Stack of mechanical test plates for new concept Carr fabrics	B7-3
Figure B7-9: Cutting of tension / compression mechanical test coupons with Universal milling machine	B7-4
Figure B7-10: Cutting of tension / compression mechanical test coupons with Universal milling machine	B7-4
Figure B7-11: Cutting of tension / compression mechanical test coupons with Universal milling machine	B7-5
Figure B7-12: Front view of compression test coupon	B7-5
Figure B7-13: Side view of compression test coupon	B7-5
Figure B7-14: Close of the end of a compression test coupon	B7-6
Figure B7-15: Tensile test coupons with strain gauges applied	B7-6
Figure B7-16: Close up of strain gauges on tensile test coupon	B7-6
Figure B7-17: Compression test coupon in anti-buckling guide prior to align with spacers (front face shown)	B7-7
Figure B7-18: Compression test coupon in anti-buckling guide prior to align with spacers (rear face shown)	B7-7
Figure B7-19: Side view of compression test coupon in anti-buckling guides	B7-7
Figure B7-20: Close up of the end of the anti-buckling guide	B7-8
Figure B7-21: Compression test coupon in anti-buckling guide	B7-8
Figure B7-22: Equipment used to test, control and record tension and compression testing	B7-8
Figure B7-23: Compression test specimen (with anti-buckling guide fitted) during testing	B7-9
Figure B7-24: Failed tensile test coupon (intact coupon shown to indicate failure location)	B7-9

## List of Tables

	Page
Table 1: Details of image analysis for determination of fractal dimensions.	14
Table 2: Mechanical properties of Brochier fabrics normal to the FET.	17
Table 3: Ranking of measured properties and quantified microstructures normal to the FET.	17
Table 4: Mechanical properties of new concept Carr fabrics.	18
Table 5: Fractal dimensions and permeabilities for two sets of fabric.	20
Table A1-1: Characteristic equations for compliance of typical reinforcing materials (from Quinn and Randall, 1990 [16])	A1-5
Table A1-2: The load applied to each sample to achieve the required pressure	A1-5
Table A1-3: The power law variables for the initial loading to 300 kPa	A1-5
Table A1-4: The apparent mean fabric layer thicknesses (micrometres) at the end of the initial loading cycle	A1-5
Table A1-5: The gradients of the successive residual load values versus volume fraction graphs	A1-6
Table A1-6: The variables in the exponential decay equation	A1-6
Table A2-1: Fabrics studied	A2-2
Table A2-2: Unit cell sizes for the fabrics	A2-5
Table A2-3: Microscopical specimen preparation	A2-5
Table A2-4: Range of measured permeabilities for quasi-isotropic lay-ups	A2-7
Table A2-5: Porespace area measurements (mm <sup>2</sup> )	A2-10

Table A3-1: Experimental parameters	A3-7
Table A3-2: Parameters used for ultrasound C-scanning	A3-8
Table A3-3: Unit cell sizes for the fabrics	A3-8
Table A3-4: Microscopical specimen preparation	A3-9
Table A3-5: Summary of Interlaminar Shear Strength (ILSS) results	A3-13
Table A3-6: Comparison of ILSS mean values reported by UoP and KTH	A3-14
Table A3-7: Summary of results for void volume fraction (%)	A3-15
Table A3-8: Magnitude (%), fabric and specimen location of the highest void volume fractions measured	A3-16
Table A3-9: Generalised comparison of ILSS and Permeability results for the three fabrics	A3-17
Table A4-1: Fabrics studied	A4-2
Table A4-2: Approximate unit cell sizes for the fabrics	A4-4
Table A4-3: Microscopical specimen preparation	A4-4
Table A4-4: Details of detection boxes used for fractal analysis	A4-5
Table A4-5: Range of measured permeabilities for quasi-isotropic lay-ups	A4-6
Table A4-6: Summary of results for all tests showing ranking of fabrics	A4-7
Table A5-1: Fabrics studied	A5-3
Table A5-2: Detection boxes used for fractal analysis	A5-5
Table A5-3: Fractal dimensions and linearity	A5-8
Table A5-4: Ranking of weft tensile strength and fractal dimension	A5-9
Table A6-1: Details of image analysis for determination of fractal dimensions	A6-4
Table A6-2: Mechanical properties of Brochier fabrics normal to the FET	A6-7
Table A6-3: Ranking of measured properties and quantified microstructures normal to the FET	A6-8
Table A6-4: Mechanical properties of new concept Carr fabrics	A6-8
Table A6-5: Fractal dimensions and permeabilities for two sets of fabric	A6-9
Table B1-1: Carr Reinforcements twisted tow flow-enhancing 2x2 twill fabrics	B1-1
Table B1-2: Fabrics supplied for BRITE EurAM II programme BE5477	B1-1
Table B1-3: New concept Carr Reinforcements flow-enhancing fabrics	B1-1
Table B5-1: Microscopical specimen preparation	B5-1

## **Acknowledgements**

The author is grateful to the University of Plymouth for the post of Research Assistant during the conduct of this research and to the Engineering and Physical Sciences Research Council who funded the programme under grant GR/K04699. A complementary grant GR/J77405 was awarded to Dr Felicity Guild for travel to permit the collaboration with the University of Bristol.

The author would like to thank Eric Taylor at Carr Reinforcements Limited for the weaving of fabrics especially for this research programme and for helpful technical discussions and advice.

Grateful thanks are due to Dr John Summerscales and Dr Felicity Guild (Department of Mechanical Engineering – University of Bristol) for supervision of this research degree and to Dr John Lockett and Dr Bob Pittilo (both of Polymer Engineering Group) as EPSRC monitors on the programme. Further, I am grateful for the comments of David Short and the late Derek Sargeant on the MPhil-to-PhD transfer document.

The author is also grateful for assistance with experiments and/or for helpful discussions. The following people should be acknowledged: Professor Eirian Jones, Dr Eddie Carter, Dr Mansell Davies, Dr Patrick Griffin, Dr Stephen Grove, Dr Rana Moyeed, Dr Tim Searle, Jim Craen, Andy Lewis, Brian Lord, Terry Richards, Paul Russell and Christopher Williams. The omission of any appropriate name here does not constitute a deliberate rebuff. I am also grateful to anonymous referees for their respective comments on the manuscripts of journal papers.

Last but certainly not least, I would like to thank my parents for their support throughout my early life and for their encouragement during the production of this thesis.

## Author's Declaration

At no time during the registration for the degree of Doctor of Philosophy has the author been registered for any other University award.

This study has been part financed by EPSRC and Carr Reinforcements Limited in collaboration with the Department of Mechanical and Marine Engineering.

Relevant scientific seminars and conferences were attended. Papers were presented at some of these meetings and subsequently published in refereed journals. The details are on the following pages.

Signed. *N R Pearce* .....

Date. *13/11/01* .....

### ***External training attended:***

SAMPE UK Seminar: Resin Transfer Moulding  
Yeovil, 3 May 1995.

3rd International Conference on Microscopy of Composite Materials, Royal Microscopical Society,  
Oxford, 1-3 April 1996

17th International Conference and Student Seminar of the SAMPE European Chapter,  
Society for the Advancement of Materials and Process Engineering,  
Basel - Switzerland, 28-30 May 1996.

4th International Conference on Flow Processes in Composite Materials,  
Aberystwyth, 9-11 September 1996.

SAMPE UK Seminar: Textile based Composites for Structural Applications  
Cranfield, 19 September 1996.

Symposium: Liquid Moulding Technologies,  
Nottingham, 16 April 1997.

9th International Conference on Composite Structures,  
Paisley - Scotland, 1-3 September 1997.

5th International Conference on Automated Composites,  
Glasgow - Scotland, 4-5 September 1997.

### ***Internal training attended:***

Writing and Publishing for PhD students, 24 May 1995

Presentation skills, 6-7 July 1995

Use of the Internet, 23 November 1995

### ***Journal papers:***

NRL Pearce and J Summerscales

*The compressibility of a reinforcement fabric*

Composites Manufacturing, March 1995, 6(1), 15-21.

NRL Pearce, FJ Guild and J Summerscales (Aberystwyth conference, September 1996)

*An investigation into the effects of fabric architecture on the processing and properties of fibre reinforced composites produced by resin transfer moulding*

Composites Part A: Applied Science and Manufacturing, 1998, 29A(1/2), 19-27.

Publishers erratum (viscosities should be *mPa.s* not *MPa.s*), 1998, 29A(5/6), 707.

NRL Pearce, FJ Guild and J Summerscales (Aberystwyth conference, September 1996)

*A study of the effects of convergent flow fronts on the properties of fibre reinforced composites produced by resin transfer moulding*

Composites Part A: Applied Science and Manufacturing, 1998, 29A(1/2), 141-152.

NRL Pearce, J Summerscales and FJ Guild (Glasgow conference, September 1997)

*The use of automated image analysis for the investigation of fabric architecture on the processing and properties of fibre reinforced composites produced by RTM*

Composites Part A: Applied Science and Manufacturing, 1998, 29A(7), 829-837.

NRL Pearce, J Summerscales and FJ Guild (Plymouth conference, July 1999)

*Improving the resin transfer moulding process for fabric-reinforced composites by modification of the fibre architecture*

Composites Part A: Applied Science and Manufacturing, 2000, 31A(12), 1433-1441.

J Summerscales, NRL Pearce, P Russell and FJ Guild

*Voronoi cells, fractal dimensions and fibre composites*

Journal of Microscopy, February 2001, 201(2), 153-162.

## **Conference papers:**

NRL Pearce, FJ Guild and J Summerscales

*The relationship between microstructure, process and mechanical performance for carbon-fibre reinforced composites produced by resin transfer moulding*

3rd International Conference on Microscopy of Composite Materials, Royal Microscopical Society, OXFORD, 1-3 April 1996. Proceedings Royal Microscopical Society, March 1996, 31(1), 46. Abstract only.

FJ Guild, NRL Pearce, PR Griffin and J Summerscales

*Optimisation of reinforcement fabrics for resin transfer moulding of high fibre volume fraction composites*

7th European Conf on Composite Materials (ECCM-7), LONDON, 14-16 May 1996, volume 1, pp 273-278.

NRL Pearce, PR Griffin, J Summerscales and FJ Guild

*Optimisation of reinforcement fabrics for resin transfer moulding of high fibre volume fraction composites*

17th International Conference, SAMPE European Chapter, BASEL, 28-30 May 1996, pp 225-236.

NRL Pearce, FJ Guild and J Summerscales (refereed in Composites A, 1998)

*An investigation into the effects of fabric architecture on the processing and properties of fibre reinforced composites produced by resin transfer moulding*

4th International Conf on Flow Processes in Composite Materials, ABERYSTWYTH, 9-11 September 1996.

NRL Pearce, FJ Guild and J Summerscales (refereed in Composites A, 1998)

*A study of the effects of convergent flow fronts on the properties of fibre reinforced composites produced by resin transfer moulding*

4th International Conf on Flow Processes in Composite Materials, ABERYSTWYTH, 9-11 September 1996.

NRL Pearce, J Summerscales and FJ Guild (refereed in Composites A, 1998)

*The influence of fabric architecture on the processing and properties of fibre reinforced composites produced by RTM*

5th International Conference on Automated Composites, GLASGOW, 4-5 September 1997, pp 319-326. ISBN 1-86125-003-7.

NRL Pearce, FJ Guild and J Summerscales

*The use of fractal dimensions to analyse fabric architecture for fibre reinforced composites produced by RTM*

4th International Conf on Microscopy of Composite Materials, CIRENCESTER, 6-8 April 1998, abstract p.195.

NRL Pearce, J Summerscales and FJ Guild

*The modification of fabric architecture to improve the processing of continuous fibre reinforced composites manufactured by RTM*

7th International Conference on Fibre-Reinforced Composites, NEWCASTLE-UPON-TYNE, 15-17 April 1998.

NRL Pearce, J Summerscales and FJ Guild

*The effect of flow-enhancement tows on the mechanical properties of composites produced by the resin transfer moulding process*

5th International Conference on Deformation and Fracture of Composites, IOM Communications, LONDON, 18-19 March 1999, 101-110. ISBN 1-86125-096-7.

NRL Pearce, J Summerscales and FJ Guild

*Improving the resin transfer moulding process for fabric-reinforced composites by modification of the fibre architecture*

5th International Conference: Flow Process in Composite Materials (FPCM-5), PLYMOUTH, 12-14 July 1999. Advanced Composites Manufacturing Centre, Plymouth, 1999, pp 303-310. ISBN 1-870918-01-0.

J Summerscales, NRL Pearce, P Russell and FJ Guild

*Voronoi cells, fractal dimensions and fibre composites*

5th International Conference on Microscopy of Composite Materials, Royal Microscopical Society, OXFORD, 2-4 April 2000.

John Summerscales, Felicity Guild, Neil Pearce and Paul Russell

*Process-property-structure relationships for woven fibre composites*

8th International Conference on Fibre-Reinforced Composites, NEWCASTLE-UPON-TYNE, 13-15 September 2000, pp 121-130. ISBN 1-85573-550-4.

## Introduction

The manufacture of fibre reinforced composites has been reviewed by Åström [1], Gutowski [2] and Davé and Loos [3]. Resin Transfer Moulding (RTM) [4-8] is emerging as the most probable route to mass production for composite components of complex shape. In RTM a mould is loaded with dry fibres, resin then flows into the dry fabric stack and the resin cures to produce a solid component. The success of the process is critically dependent on the rate at which the resin percolates through the fibres. The Darcy equation [9] is commonly used for simulation of the process. For a fixed geometry, the flow rate is proportional to the pressure gradient and inversely proportional to the resin viscosity. The constant of proportionality is known as the permeability of the porous medium. Summerscales [10] predicted that clustering of fibres would increase the resin flow rate in the reinforcement and hence expedite the processing of these materials. Thirion *et al.* [11] have reported commercial fabrics which employ this concept using flow-enhancing bound tows.

Unidirectional (UD) fibres offer the highest mechanical performance when stresses are primarily in either tension or compression along the fibre axis. For more uniformly distributed stresses, it is common to use cross/angle-ply UD fibre composites. However, the absence of transverse reinforcement within each layer makes these materials liable to splitting parallel to the fibres. For applications where high stiffness and high strength are required together with toughness, woven composites can provide a reasonable balance of stiffness, strength and toughness whilst offering improved processability.



For unidirectional composites, the finite element method (FEM) has been used to predict that the type of packing [12] or the degree of randomness [13] affects the transverse modulus. Further, FEM has indicated that localised absence of fibres is related to longitudinal compression failure [14]. Basford *et al.* [15] have demonstrated experimentally that compression strengths of woven composites were reduced when fibres were more clustered. The net effect of clustering fibres is generally to enhance processability whilst reducing the mechanical properties.

The effects reported above were qualitative correlations. To improve the design tools for reinforcement fabrics, a method for quantification of the variations in the micro-/meso-structure of woven reinforcement fabrics was sought. Gross differences in the appearance of microscopy sections are apparent for different weave styles. For subtle variations within a single weave style, the eye cannot easily discern changes. The use of automated image analysis [16, 17] is essential for the quantification of subtle changes in fabric architecture.

The microstructure of fibre reinforced composites is normally defined by specifying the form of the reinforcement and quantified by measuring the fibre volume fraction and the fibre length/orientation distributions. This data may be insufficient where clustering of fibres occurs. The classification of structured populations can be achieved by a variety of parameters. Early techniques included nearest-neighbour analysis [18], chi-squared analysis for point patterns [19], quadrat analysis [20], mean free path and mean random spacing [21], space auto-correlograms [22], area fraction variance analysis and mean intercept

length analysis [23] and (for hybrid composites) contiguity index [24]. More recently the classification of the structures within composite materials has used either tessellation techniques [25-29] or fractal dimensions [30-32].

This thesis describes the use of automated image analysis for the measurement of areas of contiguous porespace, and pioneers the use of fractal dimensions for quantification of the microstructures of woven fibre-reinforced composites. The process-property-structure relationships for commercial and experimental fabric reinforcement materials have been studied experimentally in an attempt to resolve the processing *versus* properties dilemma.

Previous work [Griffin, PhD, University of Plymouth, 1995] used Voronoi tessellation to seek relationships between microstructural features and measured permeabilities. A series of Carr Reinforcements twill fabrics incorporating bound Flow-Enhancing Tows (FET) were assessed. The fabrics were based on a 380 g/m<sup>2</sup> 6K carbon 2x2 twill fabric (Figure 1). The flow enhancement was achieved by binding regularly spaced weft tows to constrain them to remain approximately elliptical under compression, thereby creating large porespaces adjacent to the bound tow.

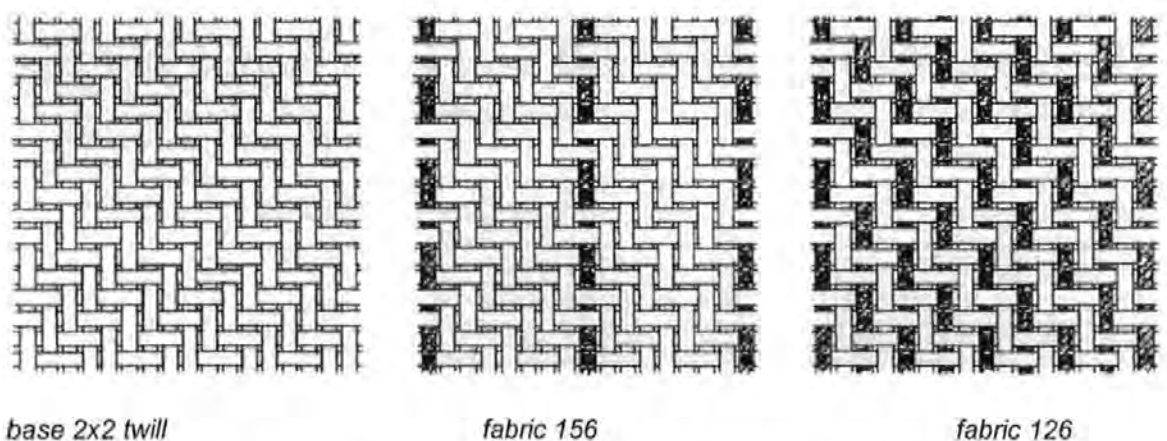


**Figure 1: Schematics of Carr fabrics (weft direction shown as vertical)**

There were four variants plus the reference base fabric:

- fabric twill = normal
- fabric 156 = 12½% FET (1 in 8)
- fabric 150 = 17% FET (1 in 6)
- fabric 148 = 25% FET (1 in 4)
- fabric 126 = 50% FET (1 in 2)

The permeating fluids were Scott Bader Resin E (initial ambient viscosity (IAV): 4600 mPa.s [1 mPa.s = 1 centipoise]) and Jotun 4210 (IAV = 2600 mPa.s) unsaturated polyester resins. The results have been reported more fully elsewhere [33-36] and are summarised below.

Image analysis was undertaken using a Quantimet 570 image analysis system. Dirichlet tessellations were constructed such that any point within a cell was closer to the centre of gravity of the feature within that cell than the centre of gravity of any other cell. The boundaries between Dirichlet cells are straight lines that are in effect the perpendicular bisectors between the centres of gravity of features. Dirichlet tessellation characterises clustering from the positions of the features.

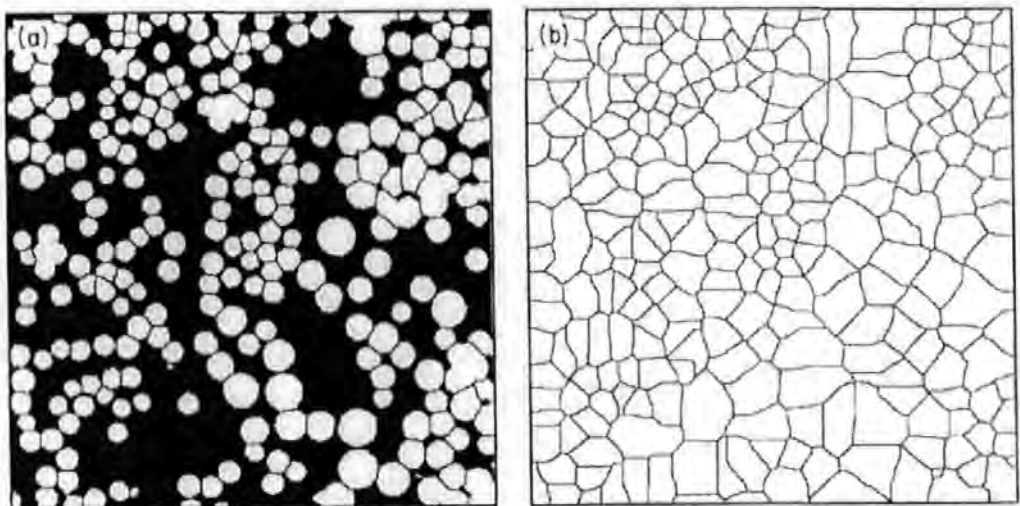


**Figure 2: Voronoi tessellation of a section of glass fibre composite (fibre diameters ~10-30  $\mu\text{m}$ )**

A specific form of tessellation known as the Voronoi cell was used. The features were "grown" until the surfaces met and filled the whole space. This normally results in non-linear boundaries between cells. Such characterisation of clustering by growing techniques is strongly influenced by the size and shape of the features as well as their positions. A rigorous treatment of the spatial statistics was given by Cressie [37]. Figure 2a illustrates how, for individual filaments within a bundle, each point in space is assigned to the nearest particle and Figure 2b shows the boundaries constructed from this information. The cells of the tessellation are then analysed to characterise the regions influenced by the non-overlapping particles. The parameters recorded were area, maximum width (horizontal feret), maximum height (vertical feret), perimeter and  $x$ - and  $y$ - centres of gravity.

The areas of pore space were collected and histograms were drawn: for example, fabric 126 data is shown in figure 3a. Comparing the histograms, it was apparent that different shapes of histograms were associated with the different fabrics. The differences in the data were clearest when the cumulative curves were plotted as the number of zones/less than a given size. These cumulative curves, for all 5 fabrics, are shown in figure 3b. The cumulative number has been 'normalised' to account for the small differences in total area measured for the different fabrics. This plot is truncated at small porespace areas corresponding to  $\sim 2\%$  of the area of a typical tow. The relative separation of the plots at around  $0.05 \text{ mm}^2$  was judged to correlate

with the relative values of permeability (Figure 4), albeit that the range of flow areas chosen was somewhat arbitrary.

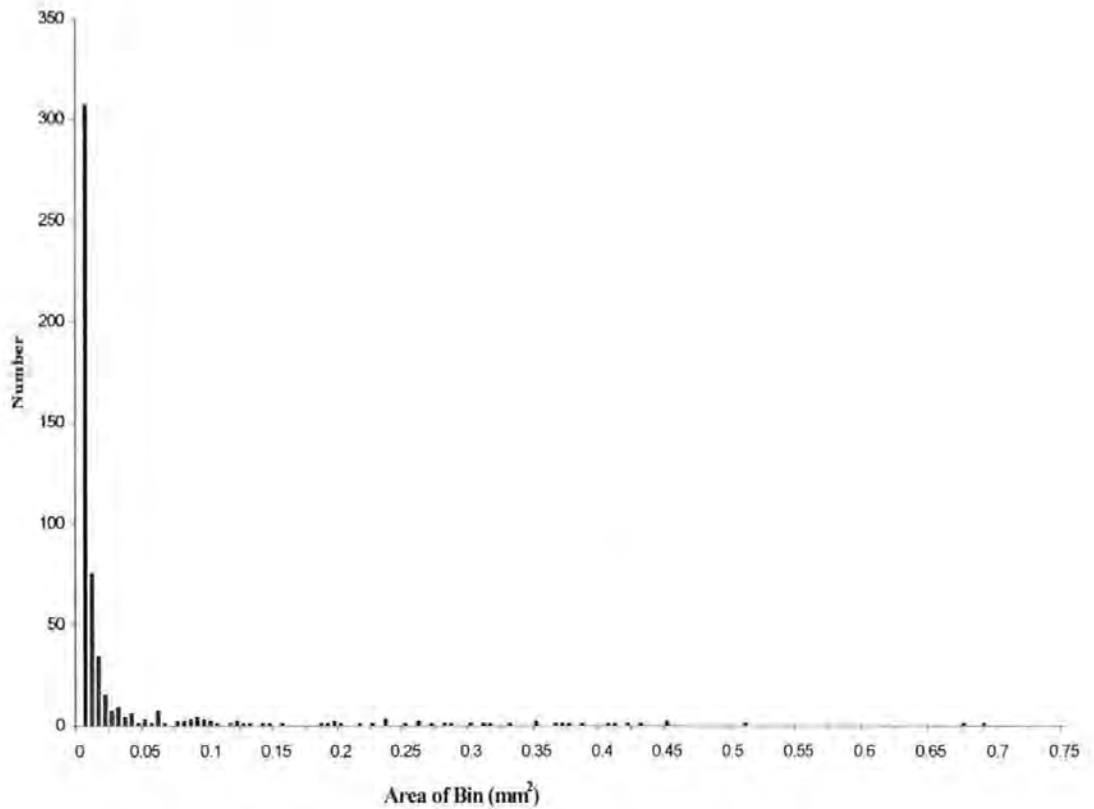


**Figure 3a: Histogram of pore space areas for Carr fabric 126**

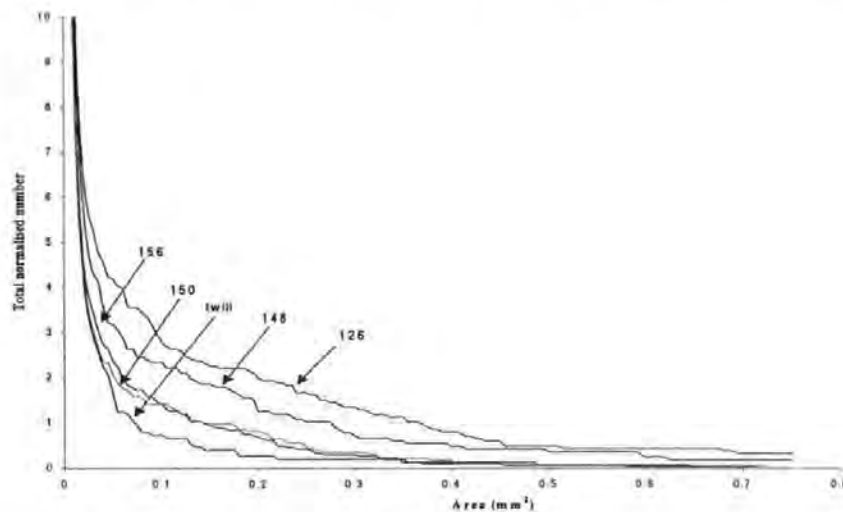


**Figure 3b:  
Cumulative curve of pore space zones less than a given value for Carr fabrics**

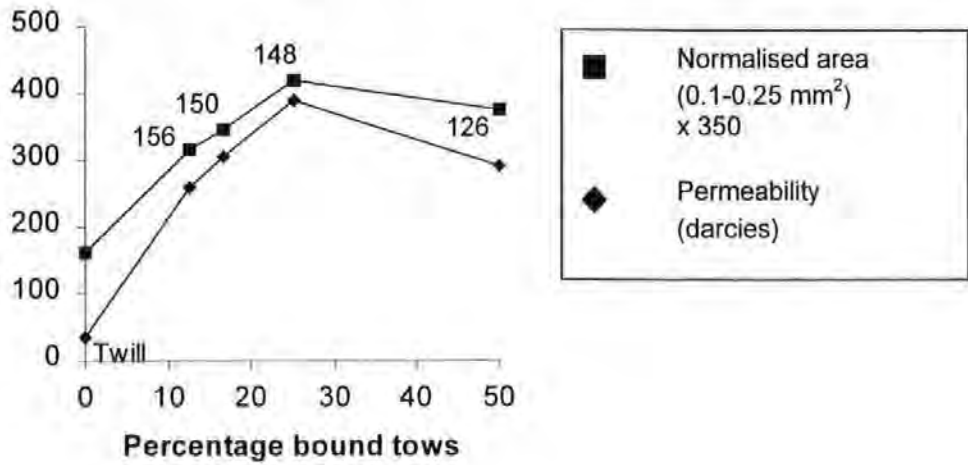


**Figure 4:**

Flow area and permeability plotted against percentage FET for Carr bound tow FET Basford *et al.* [15] measured mechanical properties for these composites at constant fibre volume fraction in an Instron 1175 screw-driven test machine. Both the compression strengths (CRAG method 401 at 2 mm/min) and the apparent interlaminar shear strengths (CRAG method 100 at 1 mm/min) decreased with increasing proportion of flow-enhancing tows at constant fibre volume fraction (~43%). The mean values for six specimens of each type are shown in Figure 5. The maximum standard deviation was 26 MPa for compression strengths and 5.2 MPa for ILSS.

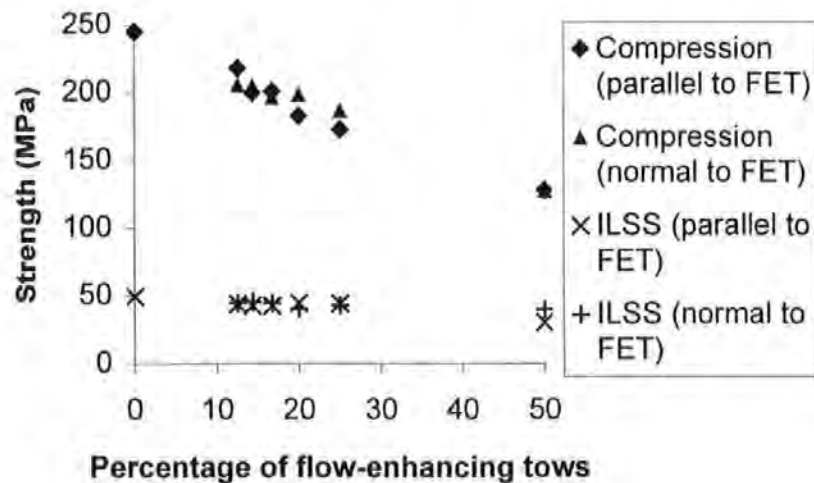


**Figure 5: Strengths of Carr fabrics plotted against proportion of flow-enhancing tows in the weft.**

## EXPERIMENTAL

### Materials

Two sets of woven carbon fibre reinforcement fabrics were studied (Appendix B1) in the following sequence:

- Brochier twill, satin and Injectex FET satin
- Carr Reinforcements twill fabric with new concept FET

### Brochier fabrics

Schematics and transverse micrographs of the fabrics are shown in Figure 6:

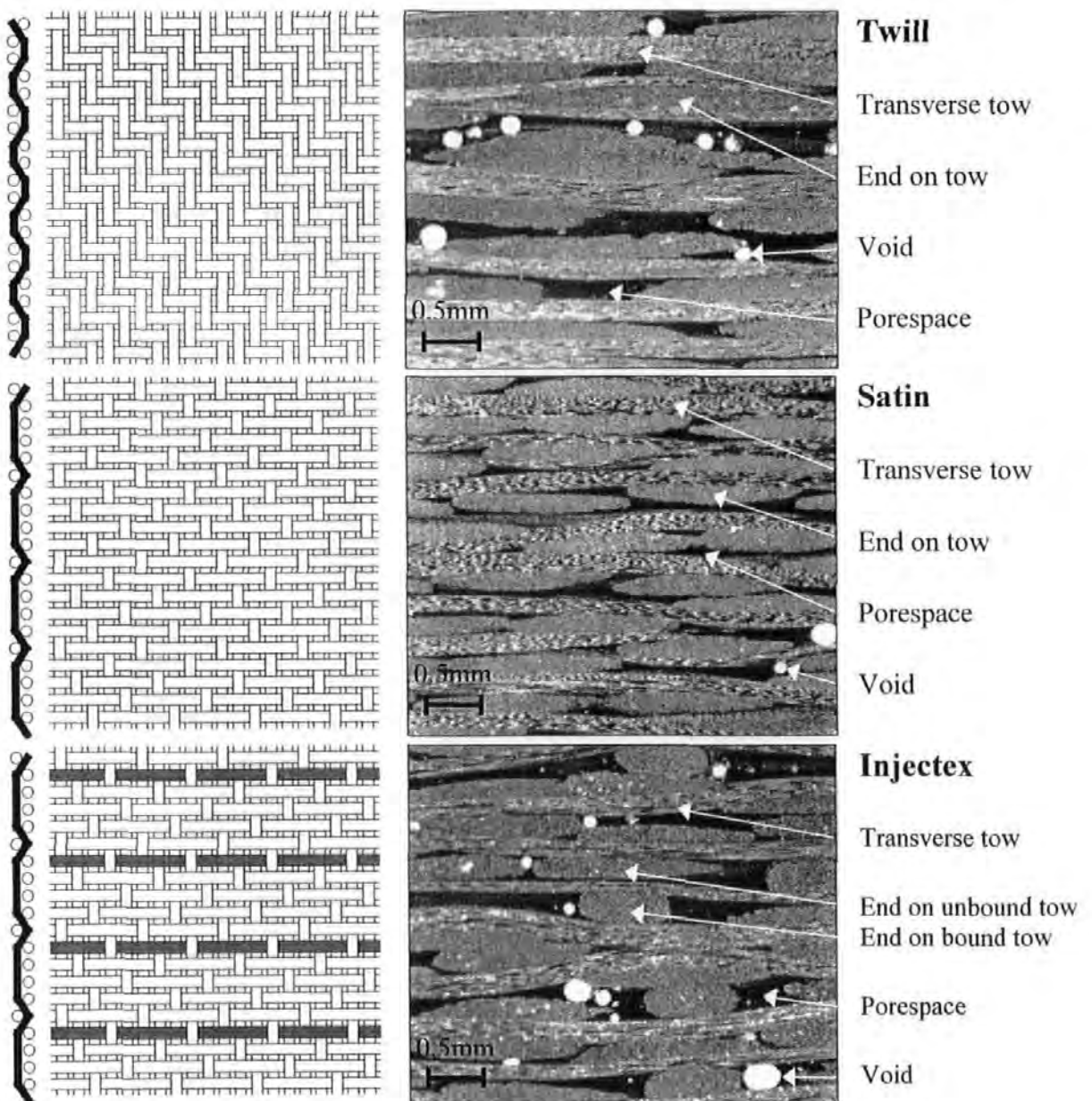


**Figure 6: Schematics and transverse micrographs of Brochier weaves.  
Image frame is 3.6 x 3.0 mm.**

The Brochier fabrics were all 290 g/m<sup>2</sup> 6K carbon fibre fabrics:

- 2x2 twill (designated E3853/G986)
- normal 5-harness satin (designated E3833/G963)
- flow-enhanced Injectex 5-harness satin (every fifth tow bound in one direction, designated E3795)

The permeating fluid was Ciba-Geigy LY564-1/HY2954 epoxy resin (IAV~600 mPa.s). The results have been reported more fully elsewhere (Appendix A2. Appendix A4. Pearce *et al.*, 1998a/b) [38, 39].

### *New concept Carr fabrics*

The new concept Carr fabrics are based on a 372 g/m<sup>2</sup> 6K carbon 2x2 twill fabric. Transverse micrographs of the fabrics are shown in Figure 7:

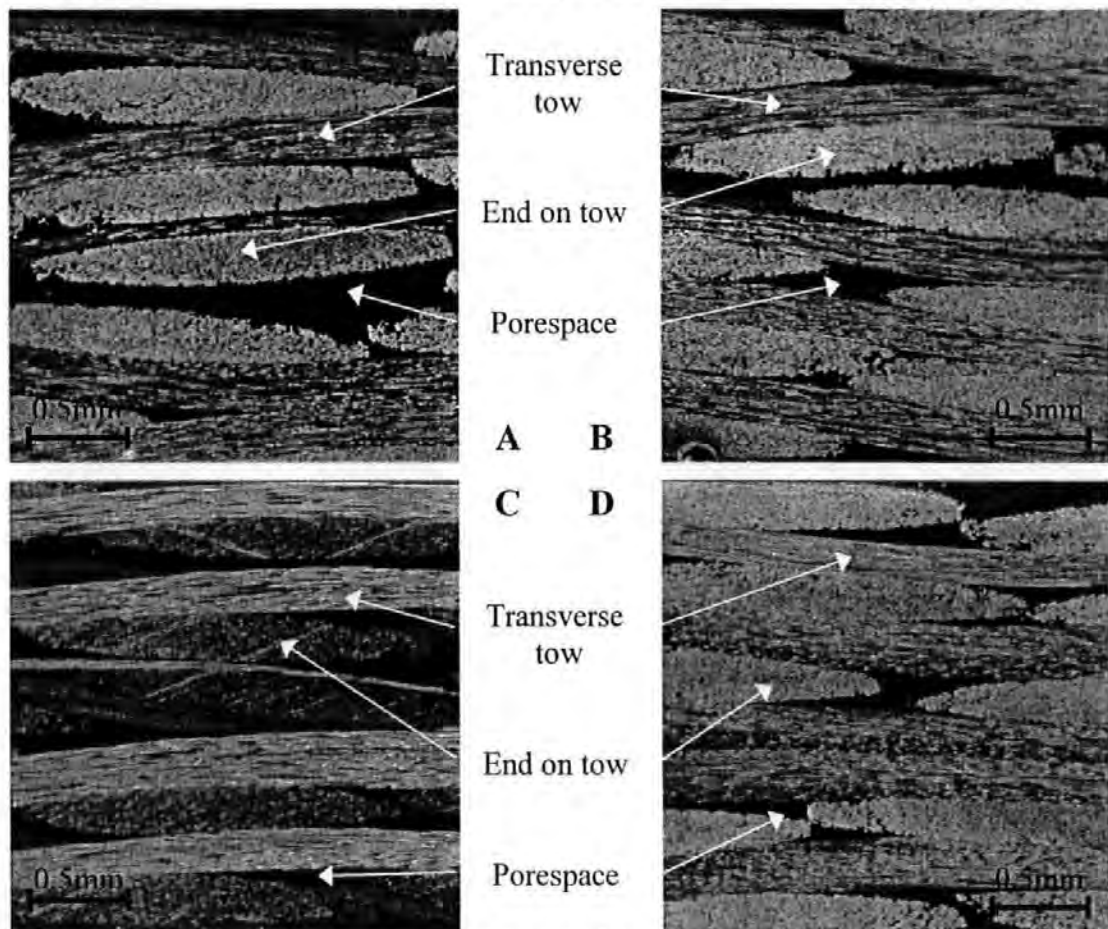


**Figure 7: Transverse micrographs of new concept Carr fabrics.**

Flow enhancement is achieved by substitution of some 6K weft tows by 3K tows with a consequent reduction in fabric areal weight:



	<b>Fabric</b>	<b>Description</b>	<b>Areal weight</b>
•	D	normal twill	372 g/m <sup>2</sup>
•	C	14% FET (1 in 6)	358 g/m <sup>2</sup>
•	B	20% FET (1 in 4)	353 g/m <sup>2</sup>
•	A	33% FET (1 in 2)	340 g/m <sup>2</sup>

The permeating fluid was SP Ampreg 26 epoxy resin with slow hardener (IAV = 310 mPa.s). The results have been reported more fully elsewhere (Appendix A5. Pearce *et al.*, 2000) [40]. It is not possible to discern differences between these fabrics with the unaided eye for either dry fabric or sectioned composites.

### *Measurement of permeability/fabrication of test plates*

The composite plates were manufactured during radial flow permeability experiments conducted in a glass topped aluminium mould with controlled cavity depth. The apparatus and technique, as used for the Brochier fabrics, has been described elsewhere [41] and is subject to progressive refinement (Appendix B2). Figure 7 shows frame grabbed images of the advancing flow front during a typical flow experiment prior to the determination of permeability. The images were taken at 36, 201 and 653 seconds into mould fill. The theory used for calculation of the permeability has been published (Appendix B3) [42] and the software is included at Appendix B4.



**Figure 8: Frame-grabbed images of a typical radial flow permeability experiment at 36, 201 and 653 seconds. The square mould has an edge length of 440 mm.**

## **Microscopical analysis**

### *Preparation (Appendix B5)*

The woven fabric composites were sampled in both warp and weft directions. Individual pieces of full specimen thickness by up to 25 mm length were mounted by casting in cylindrical pots. Each block was polished in six stages to 1  $\mu\text{m}$  and finished with  $\text{AlSiO}_2$  for 2 min [38-40].

### *Image analysis (Appendix B6)*

Image analysis was undertaken using a Quantimet 570 image analysis system.

#### *Fabric architecture and void distributions*

Flow front experiments were conducted with multiple resin feed ports. To characterise the fabric architecture, measurements of contiguous porespace were made (Appendix A2) [38]. To study the effect of convergent flow fronts (Appendix A3) [43], local void volume fractions and interlaminar shear strengths were correlated. The Quantimet 570 was used to measure the following features: individual void areas, numbers of voids, total void area, counts and areas of porespace. It was assumed that voids were randomly distributed within the resin. Therefore, the area fraction of voidage should give a good indication of void volume fraction provided the sample size is adequate. The above Appendices provide a self-contained description of this work.

#### *Fractal characterisation*

Figures 8 and 9 show representative images from the image analysis used to create the data for the fractal characterisation of the Brochier and new concept

Carr fabrics respectively. To determine the fractal dimension, the microscope image was recorded with 256 grey levels. In the case of the Brochier fabrics, surface-breaking voids were filled with magnesium silicate (talc), appearing white to permit them to be easily detected. These voids were then converted to black along with all other (darker) intertow porespace. This process was not necessary for the new concept Carr fabrics as no voids were detected. The tows were then represented by white. The whole image was then sequentially mapped with a grid of boxes of increasing size, and those boxes containing porespace were flagged:

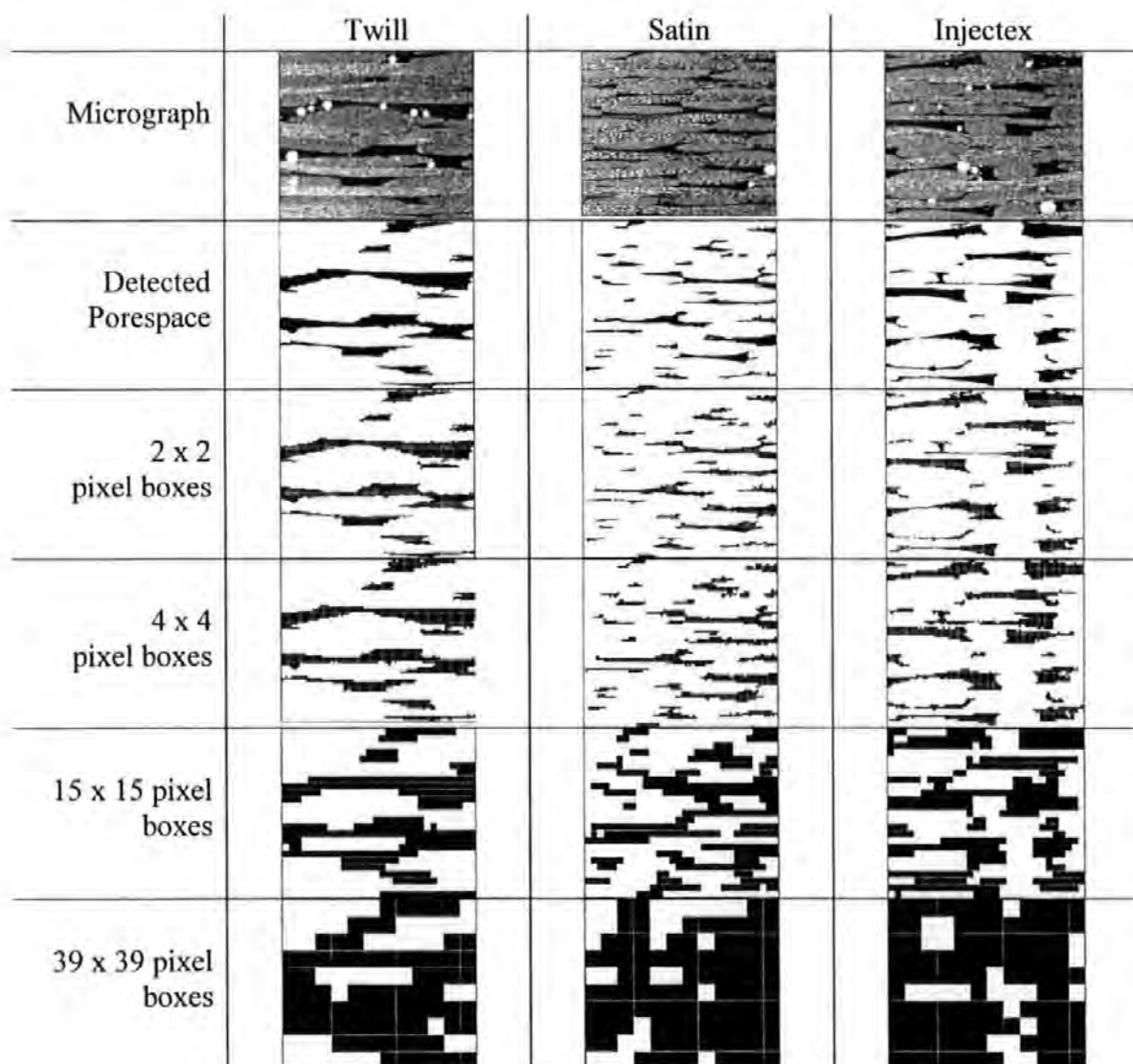


Figure 9:

Sections of Brochier weaves with sample frames for the determination of fractal dimensions. Image frame is 3.6 x 3.0 mm.

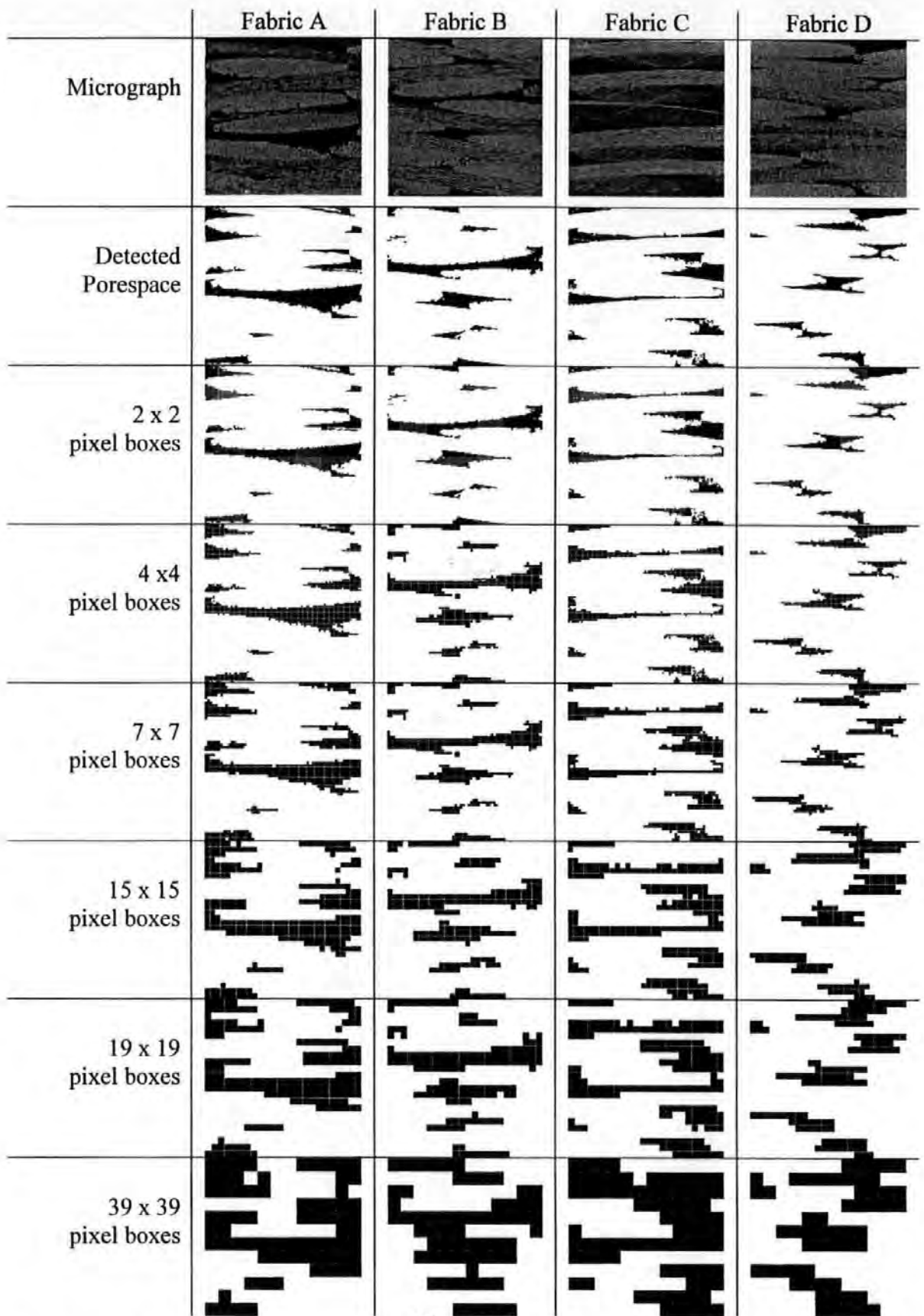


Figure 10:

Sections of new concept Carr weaves with sample frames from the determination of fractal dimensions. Image frame is 2.2 x 2.2 mm.

Note that the micrographs of Figure 9 were taken manually following the analyses in order to depict the process. Whilst care was taken to replicate the

image size and content there are discernable differences between the micrographs and the porespace / boxed images that were created originally as part of the image analysis.

For both the Brochier and new concept Carr fabrics a range of square box sizes was used. In each case, the porespace area was measured as the total 'flagged' area. The log (area of filled boxes) was plotted against log (box size). This is known as a Richardson plot. The slope of the graph is the fractal dimension ( $\delta$ ) and gives a unique measurement of the porespace size and distribution. The measurement details are summarised in Table 1.

**Table 1: Details of image analysis for determination of porespace or fractal dimensions**

	<b>Brochier [38] Appendix A2</b>	<b>Brochier [39] Appendix A4</b>	<b>New concept Carr [40] Appendix A5</b>
Published reference	Pearce <i>et al.</i> , 1998a	Pearce <i>et al.</i> , 1998b	Pearce <i>et al.</i> , 2000
Pixel frame	512 x 400	480 x 400	480 x 480
Analysis frame area (mm)	4 x 3.125	3.6 x 3.0	2.2 x 2.2
Linear resolution (nm/pixel)	7812	7500	4583
Contiguous frames per sample	six	three	four
Measured area (mm)	24 x 3.125	10.8 x 3	8.8 x 2.2
Specimens per fabric	one	ten	three

In the form that fractal dimensions are derived, a value of 0 corresponds to a line and a value of 1 to an area (note that conventional notation for dimensions has line = 1, area = 2, volume = 3). At a small box size, the measure of porespace will be a fairly accurate measurement of porespace area. By increasing the size of the boxes a relatively small area of porespace will be represented by significantly larger boxes thereby exaggerating the porespace measured. For porespace that is evenly dispersed the measured area will be exaggerated more than for porespace that is clustered. Exaggerating the measure of porespace results in a Richardson plot with a

steeper slope and hence a higher fractal dimension, hence the fractal dimension indicates the degree of clustering.

### **Mechanical testing**

The preparation of test coupons is illustrated in Appendix B7.

Mechanical testing was conducted using CRAG test methods [44]:

- Interlaminar shear properties were measured using CRAG method 100 in an Instron 1175 screw-driven universal testing machine with a 10 kN load cell.
- Tensile properties were measured using CRAG method 302 at 5 mm/min crosshead displacement in an Instron 1175 screw-driven universal testing machine with a 100 kN load cell.
- Compression properties were measured using CRAG method 401 at an actuator displacement speed of 2.4 mm/min in an Instron 8500 servo-hydraulic universal testing machine with a 200 kN load cell.
- All mechanical test data was recorded using a Strawberry Tree data logger recording at 10 Hz. All tension and compression specimens were monitored with TMG 350  $\Omega$  12.5 mm strain gauges to permit secant moduli to be calculated at 2500  $\mu\epsilon$ .

## RESULTS

### *Brochier fabrics*

Appendix A2 provides a self-contained report of the measurement of porespace areas. This was achieved by direct measurement of the porespace rather than by use of Voronoi tessellation.

The use of fractal dimensions to analyse the porespace features normal to the flow enhancing tows clearly differentiates between the structures of the Brochier fabrics: Injectex FET ( $\delta = 0.356$ ), twill ( $\delta = 0.364$ ) and satin without FET ( $\delta = 0.424$ ). The weave style influences porespace distribution (and hence permeability) and fibre crimp (and hence mechanical properties). The relative permeabilities of the fabrics are shown in Figure 9 and the mechanical properties are presented in Table 2. The ranked experimental results (Table 3) for the Brochier fabrics clearly show that a conflict exists between processing (satin is the worst fabric) and mechanical properties (satin is the best fabric).

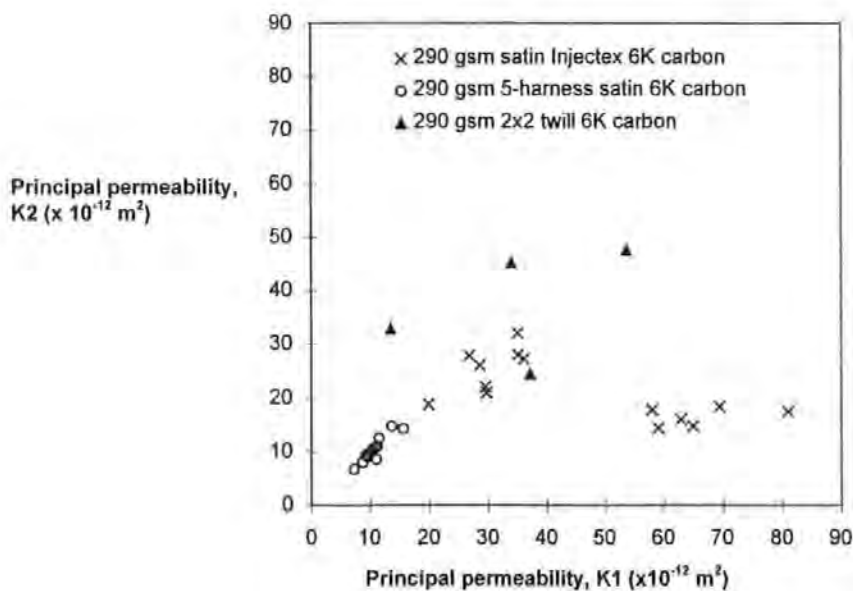


**Figure 11: Principal in-plane permeabilities in x (K1) and y (K2) of the Brochier fabrics (units of permeability are  $\times 10^{-12} \text{ m}^2$ )**

**Left-hand Injectex data points are for cross-plyed fabrics.**  
**Right-hand Injectex data points are for fabrics with all flow-enhancing tows parallel.**

**Table 2: Mechanical properties of Brochier fabrics normal to the FET**

	<i>Compression</i>	<i>Tension</i>
	<b>Young's moduli (GPa)</b>	
Injectex	50 ± 1.0	52 ± 2.4
Satin	54 ± 1.1	57 ± 1.3
Twill	51 ± 1.3	54 ± 1.3
	<b>Strengths (MPa)</b>	
Injectex	339 ± 37.2	767 ± 42.7
Satin	458 ± 66.2	906 ± 34.3
Twill	360 ± 56.5	781 ± 46.2

**Table 3: Ranking of measured properties and quantified microstructures normal to the FET**

	Lowest	Middle	Highest
<i>Processing</i>			
Permeability	satin	Injectex	twill
<i>Mechanical properties</i>			
Tensile strengths & moduli	Injectex	twill	satin
Compressive strengths & moduli	Injectex	twill	satin
<i>Microscopical analysis</i>			
Inter-tow porespace area	satin	twill	Injectex
Fractal dimension ( $\delta$ )	Injectex	twill	satin

### *New concept Carr fabrics*

For the new concept Carr fabrics, the permeabilities and fractal dimensions are both ranked in the sequence ACBD (Figure 10). The fractal dimension ( $\delta$ ) of the base fabric (D) is essentially the same in warp and weft. The value of  $\delta$  is similar for the warp direction for all fabrics.

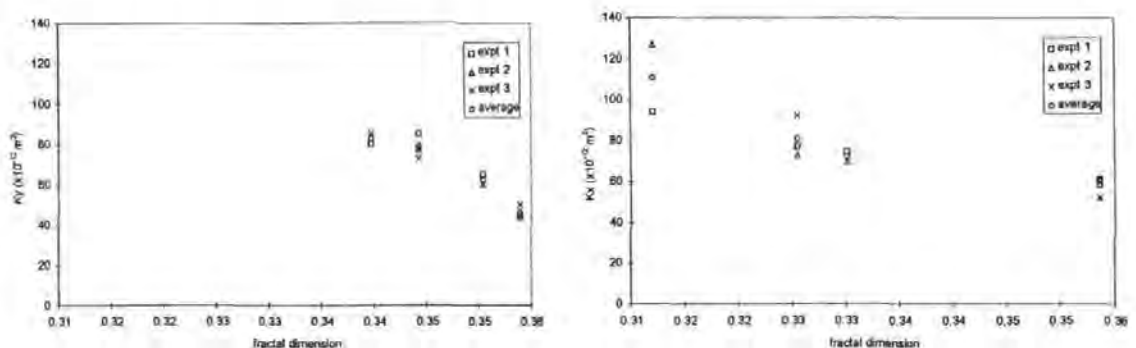


**Figure 12: Permeability plotted against fractal dimension for warp (left) and weft (right) new concept Carr fabrics**



The mechanical properties of the new concept Carr fabrics are very similar and show very low scatter for all directions without FET: both warp and weft in the base fabric and the warp direction in FET fabrics (Table 4). The higher scatter in the tensile strength is attributed to the alignment of the mechanical grips in the screw-driven machine being less accurate than that of the hydraulic grips in the servo-hydraulic machine.

**Table 4: Mechanical properties of new concept Carr fabrics**

Secant moduli (GPa)				
	<i>Compression</i>		<i>Tension</i>	
	Warp	Weft	Warp	Weft
A	47 ± 1.10%	40 ± 0.75%	49 ± 0.89%	42 ± 0.37%
B	48 ± 1.02%	43 ± 0.58%	49 ± 1.34%	45 ± 0.82%
C	47 ± 1.24%	44 ± 0.38%	49 ± 0.70%	45 ± 1.25%
D	48 ± 0.51%	47 ± 0.44%	50 ± 0.38%	49 ± 0.84%
%SD	0.58%	5.28%	0.58%	5.70%
Strengths (MPa)				
	<i>Compression</i>		<i>Tension</i>	
	Warp	Weft	Warp	Weft
A	315 ± 1.01%	317 ± 0.25%	706 ± 4.49%	542 ± 3.41%
B	317 ± 0.14%	316 ± 0.86%	704 ± 2.88%	595 ± 3.51%
C	317 ± 0.23%	314 ± 1.55%	718 ± 4.08%	556 ± 4.97%
D	317 ± 0.22%	317 ± 0.18%	720 ± 4.93%	602 ± 3.44%
%SD	0.24%	0.33%	1.01%	4.43%

The weft compression and weft tension moduli decrease broadly in line with the expectations from rule-of-mixtures. The weft tensile strengths decrease in the same sequence as the fractal dimension (Figure 11). The compression and warp tension strengths are barely affected by the presence of the FET.

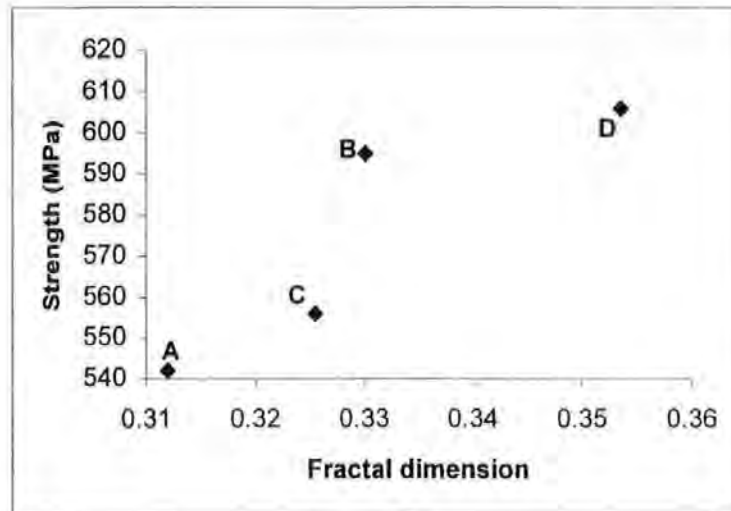


**Figure 13:**

**Weft tensile strength plotted against fractal dimension for new concept Carr fabrics**

### *Comparison of different fabric sets*

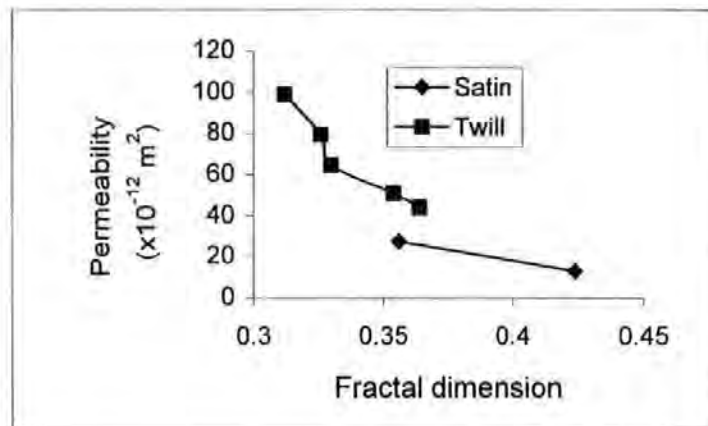
#### *Fractal dimension and permeability*

Table 5 and Figure 12 present the fractal dimensions and measured permeabilities of the Brochier and new concept Carr FET fabrics. The point at the right-hand end of the twill fabric line is for Brochier material of a lower areal weight, whilst the other points are for new concept Carr fabrics. Note that both the Brochier satin and the new concept Carr fabrics may have permeability doubled by the insertion of flow-enhancement tows.

With both fabric sets, the permeability is dependent on the degree to which the porespace is clustered as indicated by a lower fractal dimension. Clustered porespace will increase the volume for channel flow with a relative reduction in the volume for capillary flow. As resin flows more easily via channel flow the permeability of fabrics with clustered porespace is higher.

**Table 5: Fractal dimensions and permeabilities for two sets of fabric**

Fabric	Fractal dimensions (standard deviation)	Permeability ( $10^{-12} \text{ m}^2$ )
<i>Brochier fabrics: 290 gsm</i>		
Satin (no FET)	0.424 (0.0251)	8-18
Twill	0.364 (0.0218)	34-54
Injectex FET	0.356 (0.0160)	19-36
<i>Carr fabrics: 340-372 gsm</i>		
D (base twill)	0.354 (0.0142)	41-61
B (20% FET)	0.330 (0.0106)	54-75
C (14% FET)	0.326 (0.0216)	67-92
A (33% FET)	0.312 (0.0243)	72-126

**Figure 14: Permeability plotted against fractal dimension for Brochier and new concept Carr fabrics**

### *Fractal dimension and mechanical properties*

The moduli of the Brochier and new concept Carr fabrics are plotted in Figure 15. The strengths of the Brochier and new concept Carr fabrics are plotted in Figure 16. There is an upward trend running through the data from the two different sets of fabrics. However, as the surface treatment and fabric areal weights differ it would be unwise to draw conclusions from this apparent trend.

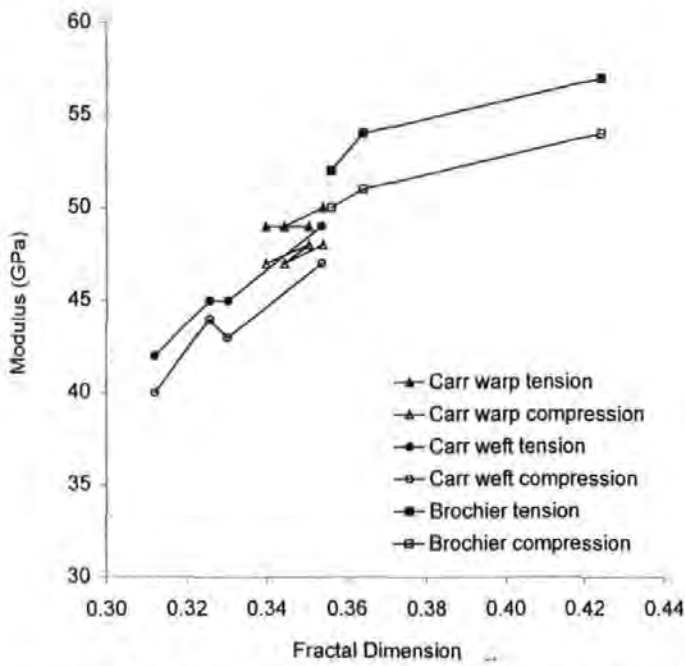


**Figure 15: Modulus plotted against fractal dimension for Brochier and new concept Carr fabrics**

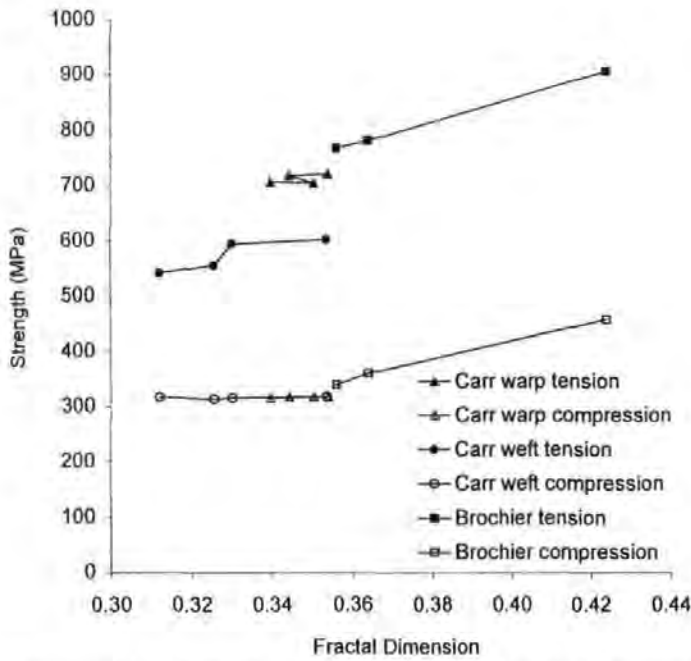


**Figure 16: Strength plotted against fractal dimension for Brochier and new concept Carr fabrics**

## **Conclusions**

- An understanding of the architecture of woven reinforcement fabrics has permitted the design of reinforcements in which there is a significant increase in processability (higher permeability) without the unpredictable deterioration in mechanical properties associated with bound tows in comparisons of fabrics at constant fibre volume fraction.
- The University of Plymouth permeability apparatus has been enhanced by the use of a thicker glass plate giving minimal mould thickness changes during an experiment.
- The University of Plymouth permeability apparatus has been enhanced by the implementation of a pressure control system giving 2000 mbar (+12/-0 mbar).
- The enhanced permeability apparatus produces results with low statistical variation. The quality of the data (standard deviation <7%) is comparable with the best permeability measurements around the world.
- The project used direct measurement of areas instead of Voronoi tessellation to quantify complex microstructures.
- This project was the first ever to make use of fractal dimensions for the quantification of sections of continuous fibre woven reinforcement fabric laminates.
- High-quality laminates were produced during this research which had very low statistical variation, most notably on compression properties.

- Processing and mechanical properties can be correlated to quantified microstructures as detailed below.

### ***Brochier fabrics***

- Permeability experiments have been conducted on three Brochier fabrics: twill, satin and satin Injectex. The architecture of the fabrics differed, but fibre type, surface treatment and fibre volume fractions were all equivalent. The measured permeabilities fall in a definite order: twill > Injectex > satin.
- ILSS testing has also shown a definite ranking, but in reverse to that of the permeability: satin > Injectex > twill.
- The satin fabric had the highest number, and highest proportion of small flow areas ( $<0.06 \text{ mm}^2$ ), and very few areas of porespace  $>0.25 \text{ mm}^2$ . This is believed to explain the lower permeability and higher ILSS measured.
- Twill had the smallest number of flow areas but a significant number of large porespaces. The large porespaces were thought to result in the high permeability but low ILSS observed.
- Unlike the satin and twill fabrics, the Injectex (flow enhanced satin) had a significant number of porespace areas in the range  $0.08 \text{ mm}^2 - 0.3 \text{ mm}^2$ . The porespaces in this range were thought to explain the increase in permeability and decrease in ILSS compared to the satin. (Griffin [36] attributed the increase in permeability to the introduction of flow areas in the range  $0.10 \text{ mm}^2 - 0.25 \text{ mm}^2$ ).

- The permeabilities for the three fabrics were ranked in the same sequence as the proportion of larger porespace and in reverse sequence to fractal dimensions, and ranked in the same order as descending ILSS.
- Of the Brochier fabric laminates tested, the satin weave provided the best mechanical properties, but the lowest permeability.
- Cross-plyed Brochier Injectex (flow-enhanced satin) fabric laminates exhibited a higher permeability than the satin fabric laminates, but at the expense of mechanical properties.
- The Brochier twill fabric had permeability significantly higher than both the satin and cross-plyed Injectex fabrics whilst, with the exception of interlaminar shear strength (this parameter is rarely used for mechanical design) possessing slightly better mechanical properties than Injectex.
- The slopes of the Richardson plots for the Brochier laminates are ranked in the reverse sequence to the tensile and compressive moduli and strengths.

#### *New concept Carr fabrics*

- In collaboration with Carr Reinforcements Limited, novel fabrics have been designed, woven and tested. The fabrics offer increased permeability. These are the first flow-enhanced fabrics to give predictable mechanical properties, albeit that the flow enhancement concept causes a reduction in fabric areal weight. Previous flow-enhanced fabrics suffered deterioration in mechanical properties at constant fibre volume fraction.

- For the new concept Carr fabrics, the increase in permeability is not consistent with the proportion of flow enhancing tows, but is ranked in the same sequence as the fractal dimension determined from polished sections.
- The rate at which the elastic modulus of the new concept Carr fabric laminates decreases is consistent with the reduction in the fibre volume fraction in the two in-plane test directions.
- The weft tensile strength of the new concept Carr fabric laminates is ranked in the same sequence as the fractal dimension.
- The compression strength of the new concept Carr fabric laminates is unaffected by the substitution of smaller flow enhancing tows. It is assumed that the smaller tows have lower crimp angle and thus the larger tows of the base fabric are the first to fail.

### *Convergent flow*

- Experiments were conducted which considered the effects of convergent flows in RTM (Appendix A3).
- Prior to convergence, flow fronts act independently and in a manner which can be predicted, based on previously conducted permeability experiments.
- The angle and location at which flow fronts meet relative to mould edges affects the way in which they interact:
  - When flow fronts meet at a mould edge they merge and act as a single front.
  - When flow fronts meet head-on there will be increased voidage along the knit line and at any adjacent corners. Voids formed in this manner may



retain their position during subsequent flow due to the cancelling of driving pressures.

- C-scan results can provide a useful indication of void distribution. However, in the absence of reference materials, they can only show relative material quality, not known levels of voidage.
- Void volume fractions were higher from areas of convergent flow and ILSS results consistently lower, indicating the adverse influence of flow convergence.
- The injection strategy with two ports on adjacent edges resulted in the highest detected void volume fractions.
- All of the experiments were conducted with vacuum drawn in the mould cavity. Vacuum reduces the quantity of gas which can be trapped. The void volume fractions would be expected to be higher where the process is driven by positive pressure alone.
- A good correlation can be found between ILSS and void volume fraction results taken from adjacent specimens, although this is highly dependent on void distribution.
- The three fabrics tested showed a clear ranking in terms of ILSS. This ranking is believed to be primarily due to the influence of fabric architecture on crimp, and porespace size and distribution.
- Measured values of ILSS and permeability are ranked in reverse sequence.
- It is worth noting that multiport injection strategies are possible in which flows do not converge [45]. Resin can be introduced sequentially into a

mould from injection ports which have been passed by the global flow front. This will maintain the pressure gradient between the active injection port and the flow front, and hence increase flow rate.

### **Recommendations for further work**

- Improve the resolution of the vision system of the permeability apparatus
- The permeability values were derived at nominally constant fibre volume fraction (subject to the variation inherent in the new concept Carr fabrics). Given the power law variation in the clamping pressure/fibre volume fraction response (Appendix A1) and the non-linear dependence of permeability on fibre volume fraction [46], it would be appropriate to establish the permeability vs fibre volume fraction response for the fabrics.
- Establish whether the dependence of permeability on the permeating fluid is a real issue or an imagined problem [47-49].
- Measure the crimp angles in the woven fabrics and then use the fibre orientation distribution factor ( $\cos^4\alpha$ ) to predict mechanical properties for the different fabrics
- Establish a set of data for comparable non-crimp fabrics as these are becoming the preferred materials in civil aircraft.
- The use of new concept Carr fabrics may permit a reduction in the consumables used in resin infusion under flexible tooling (RIFT) processes [50] for the manufacture of composites. In the proprietary SCRIMP<sup>TM</sup> process, resin is flowed over the laminate surface in a flow medium. It may be appropriate to use the new concept Carr fabrics within the laminate

in place of the flow medium and thus not need the flow medium or peel ply in the process.

## **Summary**

Routes by which the microstructural features of woven composites may be quantified have been considered. These techniques have been applied to real woven reinforcement materials. Permeability and mechanical properties can be correlated to quantified microstructures, even when no differences can be discerned by eye. New concept Carr fabrics have been developed which appear to achieve appropriate process-property-structure relationships for commercial application, *i.e.* flow enhancement with minimal reduction in mechanical properties.

## Acknowledgement

This section of the thesis is an extension of the paper presented at the Fifth International Conference on Microscopy of Composite Materials (Oxford, April 2000) and subsequently published in the Journal of Microscopy (Appendix A6).

## References

- 1 B T Åström, *Manufacturing of Polymer Composites*, Chapman & Hall, London, 1997. ISBN 0-412-81960-0.
- 2 T G Gutowski, *Advanced Composites Manufacturing* John Wiley, New York, 1997. ISBN 0-471-15301-x.
- 3 R S Davé and A C Loos, *Processing of Composites*, Hanser Publishers, Munich, 1999. ISBN 1-56990-226-7.
- 4 K van Harten, 'Production by resin transfer moulding', in R A Sheno and J F Wellicome (editors): *Composite Materials in Maritime Structures*, Cambridge University Press, Cambridge, 1993, Chapter 4, 86-126.
- 5 K Potter, *Resin Transfer Moulding*, Chapman & Hall, London, 1997, ISBN 0-412-72570-3.
- 6 C D Rudd, A C Long, K N Kendall and C G E Mangin, *Liquid Composite Moulding*, Woodhead Publishing, Cambridge, 1997, ISBN 1-85573-242-4.
- 7 T M Kruckenberg and R Paton (editors), *Resin Transfer Moulding for Aerospace Structures*, Kluwer Academic Publishers, Dordrecht NL, 1998, ISBN 0-412-73150-9.
- 8 W P Benjamin and S W Beckwith, *Resin Transfer Moulding*, SAMPE Monograph 3, Covina CA, 1999, ISBN 0-938-99483-2.
- 9 H P G Darcy, *Les Fontaines Publiques de la Ville de Dijon*, Dalmont, Paris, 1856.
- 10 J Summerscales, A model for the effect of fibre clustering on the flow rate in resin transfer moulding, *Composites Manufacturing*, 1993, 4(1), 27-31.

- 11 J M Thirion *et al*, New developments in resin transfer moulding of high-performance composite parts, *Composites (Paris)*, 1988, 28(3), 81-84. *Institute of Metals Materials Information Translation*.
- 12 M R Wisnom, Factors affecting the transverse tensile strength of unidirectional continuous silicon carbide fibre reinforced 6061 aluminium, *Journal of Composite Materials*, 1990, 24(7), 707-726.
- 13 F J Guild *et al*, A predictive model for the mechanical behaviour of transverse fibre composites, 4th Int Conf Fibre-Reinforced Composites, Liverpool, 1990, 89-99.
- 14 F J Guild *et al*, A model for unidirectional composites in longitudinal tension and compression, *Composites Science and Technology*, 1989, 36(1), 7-26.
- 15 D M Basford *et al*, The relationship between mechanical performance and microstructure in composites with flow-enhancing tows, *Composites*, 1995, 26(9), 675-679.
- 16 F J Guild and J Summerscales, Microstructural image analysis applied to fibre composite materials – a review, *Composites*, 1993, 24(5), 383-394.
- 17 J Summerscales (ed), *Microstructural Characterisation of Fibre-Reinforced Composites*, Woodhead, Cambridge, 1998. ISBN 1-85573-240-8.
- 18 P J Clark and F C Evans, Distance to the nearest neighbour as a measure of spatial relationships in population, *Ecology*, 1954, 35(4), 445-453.
- 19 P Davis, Data description and presentation, Chapter 3 in *Describing Point Patterns*, OUP, Oxford, 1974, 29-35.
- 20 P Greig-Smith, The use of random and contiguous quadrats in the study of plant communities, *Annals of Botany - London*, 1952, NS16, 293-316.
- 21 W R Cribb, Quantitative metallography of polyphase microstructures, *Scripta Metallurgica*, 1978, 12, 893-898.
- 22 K S M A Mirza, A statistical study of the structure of mixtures of particulate solids, PhD thesis, University of Exeter, 1970.
- 23 Q F Li, R Smith and D G McCartney, Quantitative evaluation of fiber distributions in a continuously reinforced aluminium alloy using automatic image analysis, *Materials Characterization*, 1992, 28(3), 189-203.
- 24 D Short & J Summerscales, The definition of microstructures in hybrid reinforced plastics, 5th European Conference, SAMPE, Montreux, June 1984.

- 25 J Summerscales, D Green and F J Guild, Effect of processing dwell time on the microstructure of a fibre reinforced composite, *Journal of Microscopy*, February 1993, 169(2), 173-182.
- 26 R Pyrz, Quantitative description of the microstructure of composites, Part 1: morphology of unidirectional composite systems, *Composites Science and Technology*, 1994, 50(2), 197-208.
- 27 S Ghosh, Z Nowak and K Lee, Tessellation-based computational methods for the characterization and analysis of heterogeneous microstructures, *Composites Science and Technology*, 1997, 57(9), 1187-1210.
- 28 R Pyrz, Morphological Characterization of Microstructures, *Comprehensive Composite Materials, vol. 1: Fiber Reinforcements and General Theory of Composites*, Elsevier, Oxford, 2000, Chapter 16, pp 465-478.
- 29 R Pyrz, The Application of Morphological Methods to Polymer Matrix Composites, *Comprehensive Composite Materials, vol. 2: Polymer Matrix Composites*, Elsevier, Oxford, 2000, Chapter 15, pp 553-576.
- 30 M Taya, K Muramatsu, D J Lloyd and R Watanabe, Determination of distribution patterns of fillers in composites by micromorphological parameters, *JSME International Journal Series I*, 1991, 34(2), 198-206.
- 31 S S Cross, The application of fractal geometric analysis to microscopic images, *Micron*, 1994, 25(1), 101-113.
- 32 C M Worrall and G M Wells, Fibre distribution in discontinuous fibre reinforced plastic: characterisation and effect on material performance, 7th European Conference on Composite Materials, London, May 1996, vol. 1, pp 247-252.
- 33 P R Griffin, S M Grove, P M Russell, D Short, J Summerscales and F J Guild, The effect of reinforcement architecture on the long-range flow in fibrous reinforcements, *Composites Manufacturing*, 1995, 6(3/4), 221-228.
- 34 P R Griffin, S M Grove, F J Guild, P M Russell and J Summerscales, The effect of microstructure on flow promotion in resin transfer moulding reinforcement fabrics, *Journal of Microscopy*, March 1995, 177(3), 207-217.
- 35 F J Guild, N R L Pearce, P R Griffin and J Summerscales, Optimisation of reinforcement fabrics for the resin transfer moulding of high fibre volume fraction composites, 7th European Conference on Composite Materials, London, May 1996, volume 1, pp 273-278.

- 36 J Summerscales, P R Griffin, S M Grove and F J Guild, Quantitative microstructural examination of RTM fabrics designed for enhanced flow, *Composite Structures*, 1995, 32(1-4), 519-529.
- 37 N A C Cressie, *Statistics for Spatial Data*, John Wiley, New York, 1993. ISBN 0-471-00255-0.
- 38 N R L Pearce, J Summerscales and F J Guild, An investigation into the effects of fibre architecture on the processing and properties of fibre reinforced composites produced by resin transfer moulding, *Composites*, 1998, 29A(1), 19-27 and 29A(5/6), 707.
- 39 N R L Pearce, J Summerscales and F J Guild, The use of automated image analysis for the investigation of fibre architecture on the processing and properties of fibre reinforced composites made by RTM, *Composites*, 1998, 29A(7), 829-837.
- 40 N R L Pearce, J Summerscales and F J Guild, Improving the resin transfer moulding process for fabric-reinforced composites by modification of the fibre architecture, Fifth International Conference on Flow Process in Composite Materials, Plymouth, 12-14 July 1999, pp 303-310. ISBN 1-870918-01-0. *Composites Part A*, 2000, 31A(12), 1433-1441.
- 41 E Carter, A W Fell, P R Griffin and J Summerscales, Data validation procedures for the automated determination of the two-dimensional permeability tensor of a fabric reinforcement, *Composites*, 1996, 27A(4), 255-261.
- 42 E Carter, A W Fell and J Summerscales, A simplified model for the derivation of the permeability tensor of an anisotropic fibre bed, *Composites Manufacturing*, 1995, 6(3/4), 228-235.
- 43 N R L Pearce, J Summerscales and F J Guild, A study of the effects of convergent flow fronts on the properties of fibre reinforced composites produced by RTM, *Composites*, 1998, 29A(1), 141-152.
- 44 P T Curtis, CRAG test methods for the measurement of the engineering properties of fibre reinforced plastics, Royal Aerospace Establishment Technical Report RAE TR 88 012, February 1988.
- 45 AW Chan and RJ Morgan, Sequential multiple port injection for resin transfer moulding of polymer composites, *SAMPE Quarterly*, 1992, 24(1), 45-49.
- 46 D Cripps, TJ Searle and J Summerscales, Chapter 21: *Open Mould Techniques for Thermoset Composites*, In R Talreja and J-A Manson (editors): "Comprehensive Composite Materials Encyclopædia, volume

- 2: Polymer Matrix Composites", Elsevier Science, Oxford, July 2000, pp 737-761. ISBN: 0-08-043720-6.
- 47 DA Steenkamer, DJ Wilkins and VM Karbhari, Influence of test fluid on fabric permeability measurements and implications for processing of liquid moulded composites *Journal of Materials Science Letters*, 1 July 1993, 12(13), 971-973.
- 48 DA Steenkamer, SH McKnight, DJ Wilkins and VM Karbhari, *Experimental characterization of permeability and fibre wetting for liquid moulding*, *Journal of Materials Science*, 15 June 1995, 30(12), 3207-3215.
- 49 PR Griffin, *The Flow of Liquid Polymers through Fibrous Reinforcements*, PhD thesis, University of Plymouth, September 1995.
- 50 CD Williams, J Summerscales and SM Grove, Resin infusion under flexible tooling (RIFT): a review, *Composites Part A: Applied Science and Manufacturing*, July 1996, 27A(7), 517-524.



# *The Compressibility of a Reinforcement Fabric*

Neil Pearce and John Summerscales  
Advanced Composites Manufacturing Centre  
School of Manufacturing, Materials and Mechanical Engineering  
University of Plymouth  
Plymouth PL4 8AA

## **Abstract**

The resin transfer moulding (RTM) process involves the loading of dry reinforcement into a mould. After the mould is closed, resin is flowed into the mould cavity and cured. The RTM process has traditionally been used to produce low volume fraction composites. There is now increasing interest in using the process to manufacture high fibre-volume-fraction composites for structural applications.

A series of experiments have been conducted to monitor the force required to compress a typical plain-woven glass fibre reinforcement. The load-displacement curves for monotonic loading, and for relaxation after repeated re-loading cycles to a maximum load are presented. The loading cycle responses for the fabric have been fitted to power law relationships, and the relaxation cycles have been fitted to exponential decay functions.

## **Introduction**

Resin transfer moulding (RTM) and the variants of the process are primarily used for low fibre volume fraction components. A limited number of well engineered components using higher fibre volume fraction have been produced, such as car bodies [1], marine propellers [2], radomes [3], and aircraft propeller blades [4]. There is increasing interest in utilising the RTM processes to produce components with high fibre volume fractions.

In a unidirectional array of fibres within a composite, the separation of the surfaces are on average given by  $s$ , which can be written in terms of fibre diameter,  $d$ , for a given fibre volume fraction,  $v_f$ ; as  $s = d[(\beta/v_f)^{1/2} - 1]$ , where  $\beta$  is a constant equal to 0.912 for a hexagonal array and to 0.785 for a square array [5]. The values of  $\beta$  correspond to the maximum packing fraction for each array.

Kanovich et al [6] have shown that where fibres of different diameters are used, even if the distance between the reinforcing elements increases, the reinforcement content remains high by filling the spaces between the main fibres with fibres of a smaller diameter, thus cutting down on 'ballast' matrix. A greater volume fraction of fibres can be incorporated into the matrix by mixing the fibre diameters.

In a plain-weave reinforcement fabric it is believed that the degree of nesting of adjacent fabric layers is dependent on the relative phase relationship between the tows of each layer, and that nesting will directly affect the volume fraction and hence the mechanical properties of the composite [7]. The approximation of the path of the tows by a sine wave is no longer considered appropriate because of fibre movement during processing [7].

The construction of commercial structural composite components aims to maximise the fibre content to achieve high-performance. However, in practice the processes are constrained by factors such as mould closing forces due to the compression resistance of the fabric and (for resin transfer moulding) the reduced permeability of the fabric bed due to the high packing density. In real structures the limiting fibre volume fractions are typically:

- 35% random fibres (eg: chopped strand mat)
- 55% bidirectional fibres (eg: woven fabrics)
- 75% unidirectional preimpregnated materials

It is therefore essential to the prediction of the facilities required for successful RTM that the compression response of the reinforcement fabric is known. Data has been reported for the compressibility of textile fabrics and fibrous reinforcements and empirical equations have been derived for individual data sets [8-17]. The stiffness of a fibre bed is related to the fibre volume fraction by a power law. Quinn and Randall [16] proposed that the volume fraction ( $V_f$ ) was related to the square root of the applied pressure ( $P$ ) by the equation below where  $K_1$  and  $K_2$  are constants (see Table 1 for typical values):

$$V_f = K_1 + K_2\sqrt{P}$$

Toll and Månson [18] have presented a micromechanical analysis which confirms the values of the exponent (3 for 3-D wads, 5 for the random planar case) and suggests that the power law may also be applied to aligned fibre bundles (exponent is 7-11 for weaves and 7-15.5 for rovings).

The work reported here confirms the exponent for a woven glass fibre cloth, and extends the response data to repeated compression cycles of the same fabric stack.

## **Experimental procedure**

### ***Materials***

The reinforcement fabric tested was a plain weave of E-glass yarns with an areal weight of 625 gm<sup>2</sup>, 310 warp tows per metre and high crimp. Tests were conducted on single layers and on stacks of two, three, four or five layers to establish the effect of fabric/platen and fabric/fabric interactions. Tests were conducted on 100 mm square, 71 mm square and 50 mm square samples (one-half and one-quarter of the largest area respectively) to consider the contribution of edge effects.

No attempt was made to align the fabric layers so that there was perfect nesting of the undulations in the fabric surfaces. This procedure would be excessively time-consuming and would not be representative of current commercial practice in RTM processing. However, in order to eliminate any effects from the natural curvature of the rolled (as supplied) fabric, the samples were aligned with (reasonable) care such that all warp and weft axes were parallel throughout.

### ***Testing machine and procedure***

The samples were placed horizontally between polished steel circular platens of 150 mm diameter in an Instron 1175 universal testing machine with an Instron 100 kN load cell set to 5 % full scale. The chart speed was 10 mm/min, and each time the digital displacement indicator changed (every 100  $\mu$ m) a mark was made on the chart. The cross-head speed was the slowest available on the machine (0.05 mm/min) to permit accurate control of the target peak load, to maximise the opportunity to interpolate the cross-head position from the chart and to minimise the chance of accidental damage to the machine. The interpolation of cross-head position from the chart could thus be determined to  $\pm 2.5$   $\mu$ m. The platens were driven to touch to set the zero thickness datum. Note that in set-up tests, not reported here, the fabric assembly offered greater resistance to compression at faster loading rates.

In a typical RTM process a one metre square moulding might be clamped by two pneumatic clamping units (eg Plasteck Hypalock) each exerting a force of around 5 tonnes (100 kPa). In order to conduct realistic compression tests representing commercial RTM practice each combination of number of layers of fabric, and of fabric size, was tested to 100 kPa, 200 kPa or 300 kPa (see Table 2 for the applied loads at which each test was conducted).

Once the target peak load had been reached, the cross-head displacement was stopped for five minutes. During this time the load on the fabric was continuously recorded. After five minutes the cross-head was restarted until the target peak load was again achieved. Five such fabric relaxation cycles were recorded for each of the tests. In all 45 different tests were conducted (one to five layers, three pressure levels and three sample sizes).

The overall size of the fabric samples for each test was measured prior to loading and on completion of the five relaxation cycles using a vernier caliper.

## Results and discussion

The load-time graphs for tests to 300 kPa on a single layer (solid line) and on five layers (dotted line) of 100 mm square fabric samples are shown in Figure 1. The time for a single layer to reach the target load is less in the single layer than for the full five layers. However, the time for five layers to compress to the same target load is only around three times that for a single layer.

The time to reach the (300 kPa) target load is plotted in Figure 2 for each sample size and each number of layers. The onset of load on the fabric is difficult to discern so the crossing of the 4 kPa load was taken as the start of the test in each case as this position could be clearly discerned. There is a linear increase in the time required to reach the target load for each additional layer. This increase in time is less than that required to reach target load in a single layer at the loading rate tested here.

The apparent volume fraction (fibres/fibres-plus-air) was calculated from the position of the platens. The total volume was taken as the compression plate spacing multiplied by the area of the test sample. The fibre volume ( $V_f$ ) was calculated from the number of layers ( $j$ ), the areal weight ( $W_f$ ), the separation of the plates ( $d$ ) and the fibre density ( $\rho_f$ ) as  $V_f = j.W_f/d.\rho_f$ . The pressure required to achieve each volume fraction is plotted in Figure 3 for the initial loading cycle of the 300 kPa tests at each sample area.

The same data is plotted on log-log axes in Figures 4a-c. The data has been fitted to a power-law equation of the form  $y = a.x^n$ . The variables determined for each curve fitting are given in Table 3, and the values of 'n' for fabric stacks are in the range 7-11 as reported elsewhere [14, 16, 17]. The single layer tests have values of 'n' in the range 4.8 to 5.8 and achieve higher fibre volume fractions than the fabric stacks.

The total fabric thickness for each fabric stack was calculated at the end of the initial loading cycle. The apparent layer thickness was calculated by dividing the total thickness by the number of layers. The results from all tests are given in Table 4 and plotted in Figure 5. The lowest layer thickness is that of the single layer in isolation. The two layer stack has an intermediate layer thickness, whilst the layer thickness becomes more constant (within experimental scatter) at three layers or greater.

The single layer is compressed with both fabric faces against the polished steel platens. In the fabric stacks each additional layer introduces fabric to fabric interactions. It is probable that the friction between fabric and steel is lower than that between two touching fabric layers where the two fabric surfaces may act to pin the fibres which they contact in the adjacent layer or be constrained by cohesive forces between the fibre surface coatings. The constraint imposed in this manner possibly combined with failure to nest all peaks and troughs of one fabric layer into the undulations of the adjacent fabric layer results in each additional layer contributing a greater thickness than the single layer in isolation.

For each test, the residual load and the apparent fibre volume fraction were calculated at the end of

each of the five relaxation cycles. The residual load (as a percentage of the target load) is plotted against fibre volume fraction in Figure 6 (small sample area), Figure 7 (medium sample area) and Figure 8 (large sample area). These figures exhibit a straight line relationship. The gradients of each of the lines are given in Table 5.

The dissipation of strain energy stored in a compressed fabric (stack) reduces the pressure on the plates. The rate of energy dissipation is dependent on the quantity of energy stored and therefore the rate of dissipation decays with time. The rate of decay was fitted to a single-exponential equation ( $y = a + b.exp(ct)$ ) and also to a double-exponential equation ( $y = a + b.exp(ct) + d.exp(et)$ ), where  $y$  is the proportion of maximum load on the platens,  $t$  is the relaxation time and  $a, b, c, d, e$  are variables obtained by curve fitting.

Note that this rearrangement takes place at constant fibre volume fraction (platens stationary) and the subsequent reloading to target load increases the fibre volume fraction and achieves the target load in a shorter time. Inevitably at the subsequent higher volume fraction there is a reduced possibility of fibre rearrangement and a lower fall in the load over the same time period.

The area of the fibre stack after completion of each of the tests was found not to have changed discernably from the initial value. This infers that all the movement which occurs during compression results in rearrangement by internal translation and rotation of the individual fibres and not by gross outward displacement. Energy may be stored in the system as strain. Yurgartis et al [7] have previously reported similar results: *"across-ply compaction during lamination of a plain-weave composite, while it does not significantly change the weaves wavelength (yarn spacings), can substantially affect crimp angles and distort waveforms"*. This result has important implications for RTM processes in that it implies that fabric may be cut accurately to size without a requirement to allow for an increase in area when compressed.

## Conclusions

The fabric tested acted as a well-behaved system, with good reproducibility between tests. The following points were observed:

- compression results in through-thickness compaction without measurable lateral spreading
- the initial loading cycle can be described by a power law expression
- the exponent of the power law equation is lower for a single layer in isolation than for a stack of fabric layers
- there is a linear increase in the time to reach a target pressure with each additional fabric layer
- the gradient of the time-to-target-pressure line is independent of the size of the sample tested and of the number of layers tested
- fabric-fabric interactions provide a greater constraint than fabric-platen interaction
- after loading, relaxation occurs even at the lowest available compression rate
- the stored energy is dissipated in a manner which can be represented by an exponential decay relationship
- a higher fibre volume fraction is achieved on each successive reloading to the initial target pressure
- the degree of relaxation is linearly proportional to the fibre volume fraction increase
- if time permits in the loading of fibres into the mould prior to mould closure, a higher volume fraction may be achieved by closing to a preset clamping position (and corresponding force), allowing relaxation to occur and repeatedly moving the mould faces together to re-establish the maximum closing force.

**Acknowledgements**

The authors acknowledge the assistance of Mr Terry Richards (UoP SMMME) with the mechanical testing, helpful discussions with Dr Stephen Grove, Mr Peter Gates and Mr Christopher Williams (UoP SMMME), and Gail Merrett and Peter Rimmer (UoP Library) for rapid checking of references.

**Table 1: Characteristic equations for compliance of typical reinforcing materials (from Quinn and Randall, 1990 [16])**

<i>Material</i>	<i>K1</i>	<i>K2</i>	<i>V<sub>f</sub> @ 157 kPa</i>
E-glass continuous strand mat	9.7	0.37	24 %
E-glass chopped strand mat	20	0.46	38 %
E-glass roving	32	0.75	62 %
E-glass woven fabric	40	0.45	58 %
E-glass woven roving	21	0.60	45 %
Kevlar fabric	47	0.51	67 %
Unidirectional carbon fibre cloth	34	0.80	66 %
±45° carbon fibre fabric	35	0.51	55 %

**Table 2: The load applied to each sample to achieve the required pressure**

<i>Pressure</i>	<i>Sample area: Applied Load.....</i>		
	<i>0.0025 m<sup>2</sup></i>	<i>0.0050 m<sup>2</sup></i>	<i>0.0100 m<sup>2</sup></i>
100 kPa	0.25 kN	0.5 kN	1 kN
200 kPa	0.50 kN	1.0 kN	2 kN
300 kPa	0.75 kN	1.5 kN	3 kN

**Table 3: The power law variables for the initial loading to 300 kPa**

<i>No.layers</i>	<i>Sample area:0.0025 m<sup>2</sup></i>		<i>0.0050 m<sup>2</sup></i>		<i>0.0100 m<sup>2</sup></i>	
	<i>a</i>	<i>n</i>	<i>a</i>	<i>n</i>	<i>a</i>	<i>n</i>
1	6.4	5.8	3.6	5.4	1.8	4.8
2	27	7.4	25.5	7.4	8.2	6.5
3	41.6	8.1	22.6	7.4	18.7	7.2
4	19.6	7.5	35.2	8.1	18.2	7.5
5	35.4	7.9	88.2	8.8	23	7.6

**Table 4: The apparent mean fabric layer thicknesses (micrometres) at the end of the initial loading cycle**

<i>No.layers</i>	<i>Sample area: 0.0025 m<sup>2</sup></i>			<i>0.0050 m<sup>2</sup></i>	<i>0.0100 m<sup>2</sup></i>
	<i>Pressure 100 kPa</i>				
1	494			396	435
2	512			450	479
3	523			474	—
4	523			481	498
5	537			500	486
	<i>Pressure 200 kPa</i>				
1	455			419	381
2	456			454	443
3	491			465	443
4	526			466	458
5	486			475	452
	<i>Pressure 300 kPa</i>				
1	413			375	353
2	448			448	406
3	449			437	435
4	427			440	422
5	447			464	433

**Table 5: The gradients of the residual load versus volume fraction graphs**

No.layers	Sample area:		
	0.0025 m <sup>2</sup>	0.0050 m <sup>2</sup>	0.0100 m <sup>2</sup>
	<b>Pressure 100 kPa</b>		
1	9.5	5.3	6.4
2	9.9	6.9	6.2
3	9.0	6.5	---
4	7.8	7.2	7.3
5	9.0	7.4	7.5
	<b>Pressure 200 kPa</b>		
1	7.6	5.9	6.2
2	7.7	7.0	8.4
3	8.1	7.8	7.0
4	9.8	7.2	7.3
5	7.5	7.7	7.0
	<b>Pressure 300 kPa</b>		
1	6.1	3.7	5.2
2	7.6	10.0	6.4
3	7.9	7.6	7.7
4	6.5	7.4	7.5
5	6.5	8.3	7.0

**Table 6:**

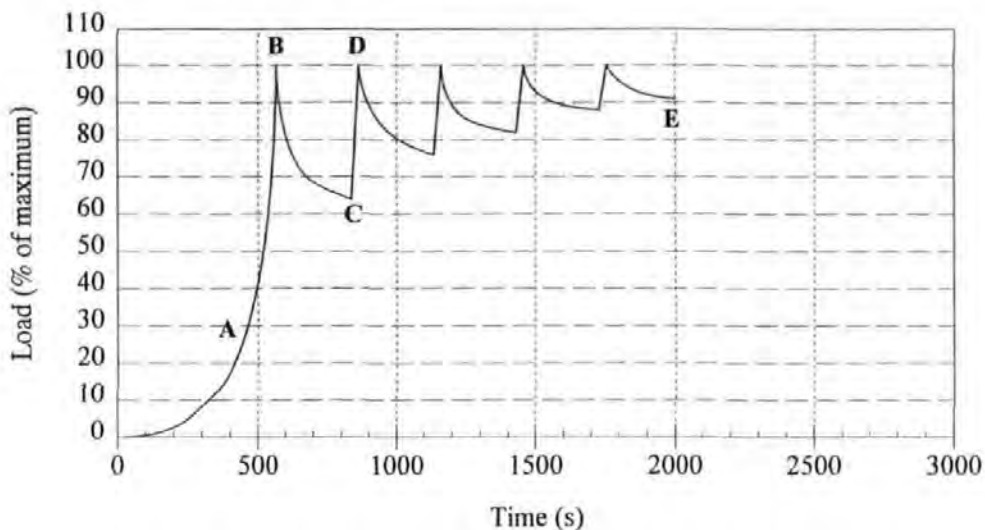
**The variables in the exponential decay equations for three layer experiments at 200kPa**

**Fitted to  $y = a + b.exp^{ct}$  from t=0 seconds**

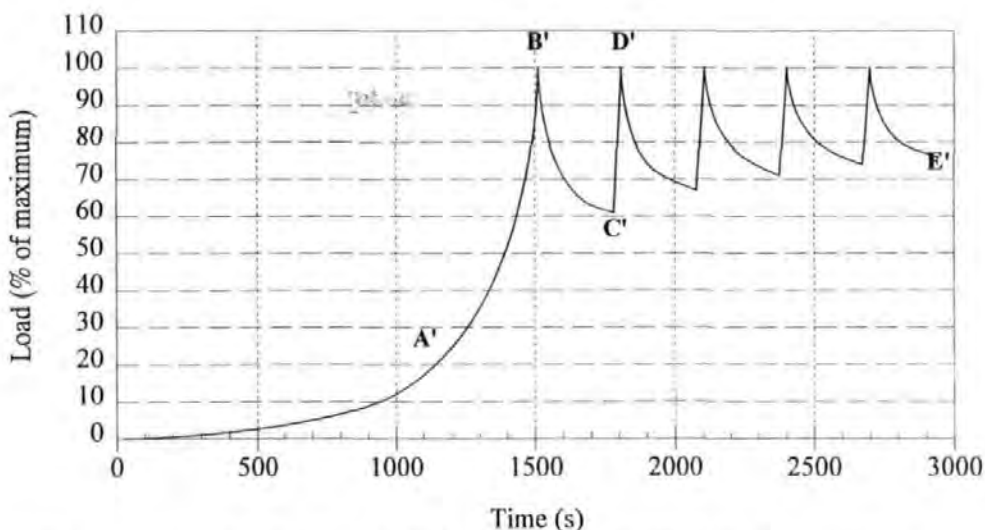
Sample size (mm)	Relaxation	a	b	c
50 x 50	1	65.8	35.5	-0.0122
	2	72.9	25.9	-0.0147
	3	83.2	16.8	-0.8199
	4	85.4	14.6	-0.7720
	5	87.6	12.4	-0.8290
100 x 100	1	60.6	39.4	-0.0189
	2	74.7	25.4	-0.6563
	3	78.4	21.6	-0.5780
	4	81.1	18.9	-0.6220
	5	85.2	14.8	-0.7910

**Fitted to  $y = a + b.exp^{ct} + d.exp^{et}$  from t=1 second**

Sample area (mm)	Relaxation	a	b	c	d	e
50 x 50	1	65.1	-7.33	-1.928	36.4	-0.013
	2	70.8	21.4	-1.190	22.9	-0.0086
	3	74.6	25.9	-1.570	20.1	-0.0071
	4	77.7	23.7	-1.601	17.7	-0.0060
	5	79.1	24.9	-1.840	17.0	-0.0051
100 x 100	1	60.4	21.0	-2.090	37.7	-0.0178
	2	63.9	30.2	-1.159	26.8	-0.0069
	3	68.6	34.3	-1.403	23.1	-0.0060
	4	72.1	28.9	-1.430	21.1	-0.0053
	5	72.2	28.3	-1.541	21.8	-0.0035



Plot representative of: 0.01 m<sup>2</sup> sample, X1 layer, max load = 0.2 MPa, X-Head speed = 0.05 mm/min.



Plot representative of: 0.01 m<sup>2</sup> sample, X5 layers, max load = 0.2 MPa, X-Head speed = 0.05 mm/min.

**Figure 1:** The load/time response of a single isolated layer (upper plot) and of a stack of five fabric layers (lower plot) under similar conditions

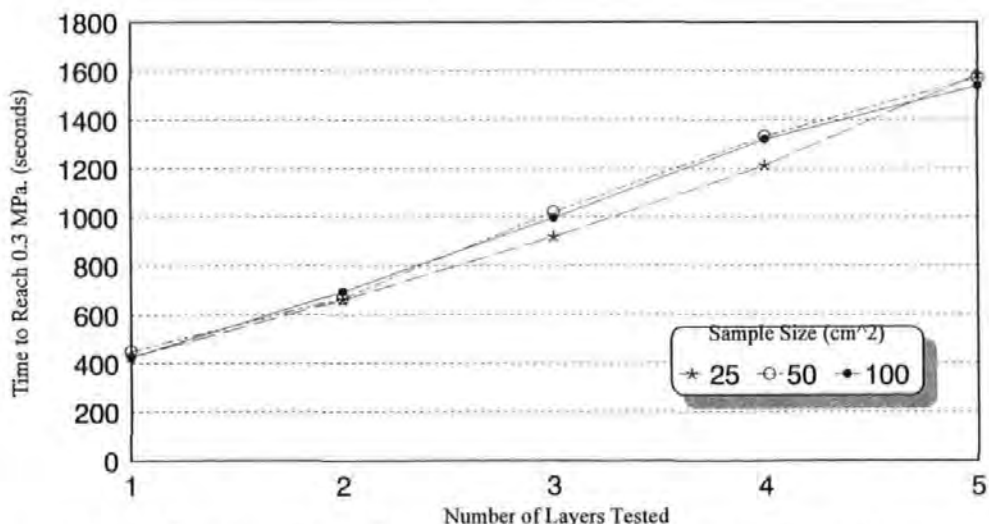
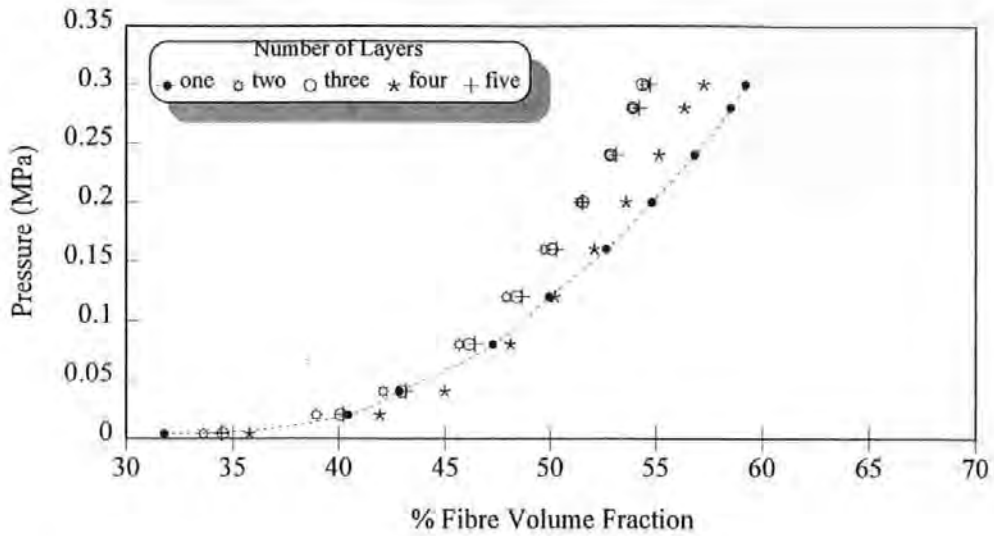
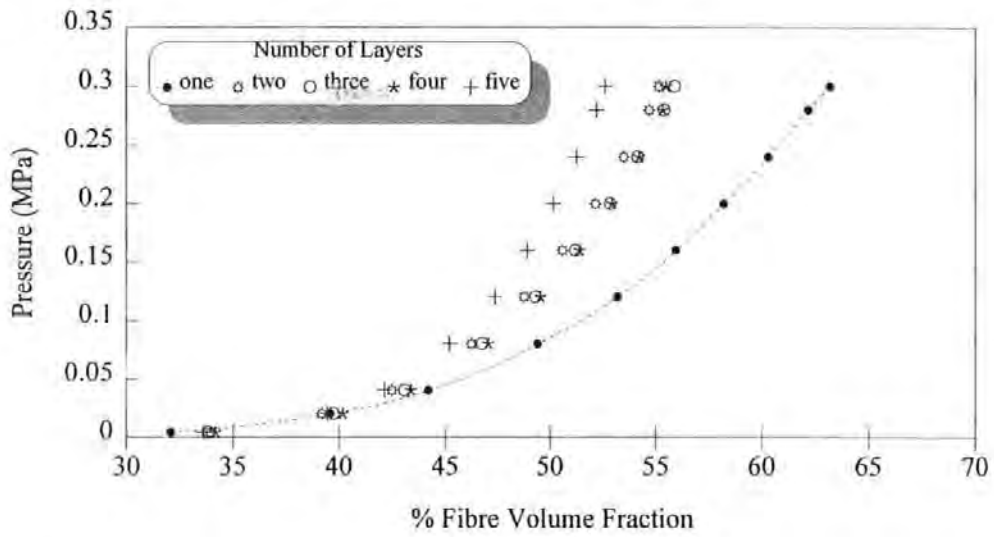


**Figure 2:** Time taken to achieve the target pressure against number of layers

(A)



(B)



(C)

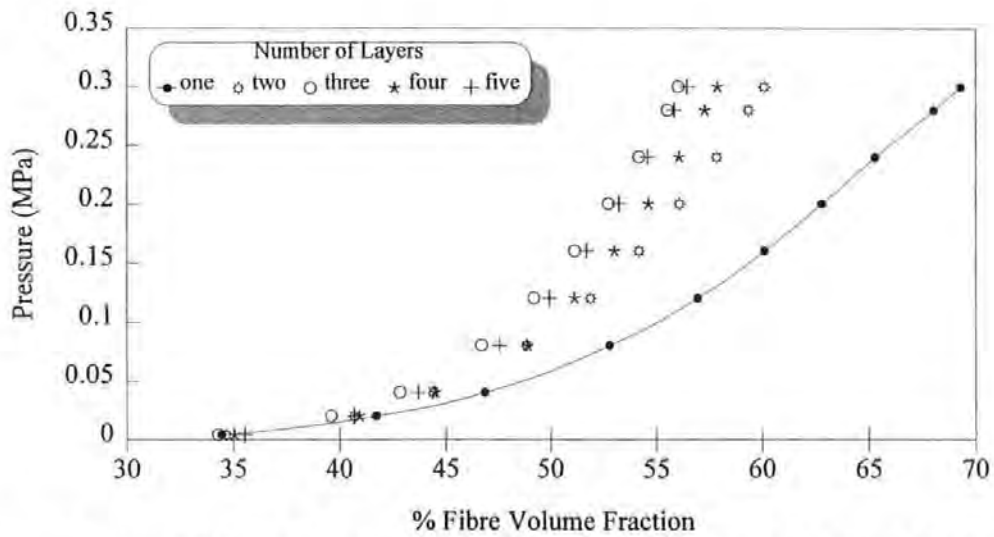


**Figure 3:** Pressure plotted against fibre volume fraction during the initial loading cycle to 300 kPa, (A) 50 mm square samples, (B) 71 mm square samples, (C) 100 mm square samples.



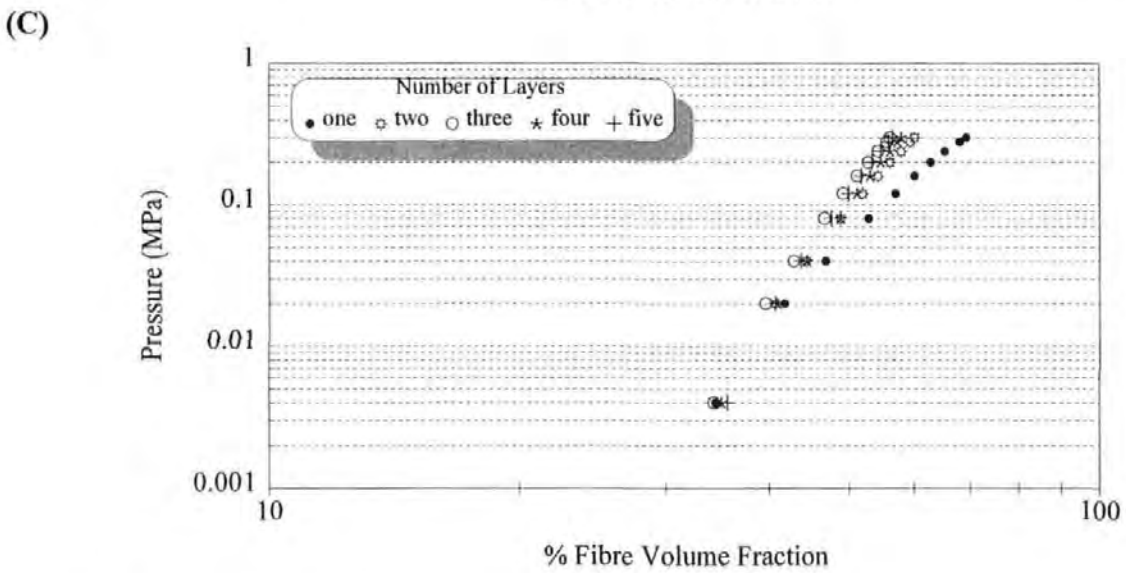
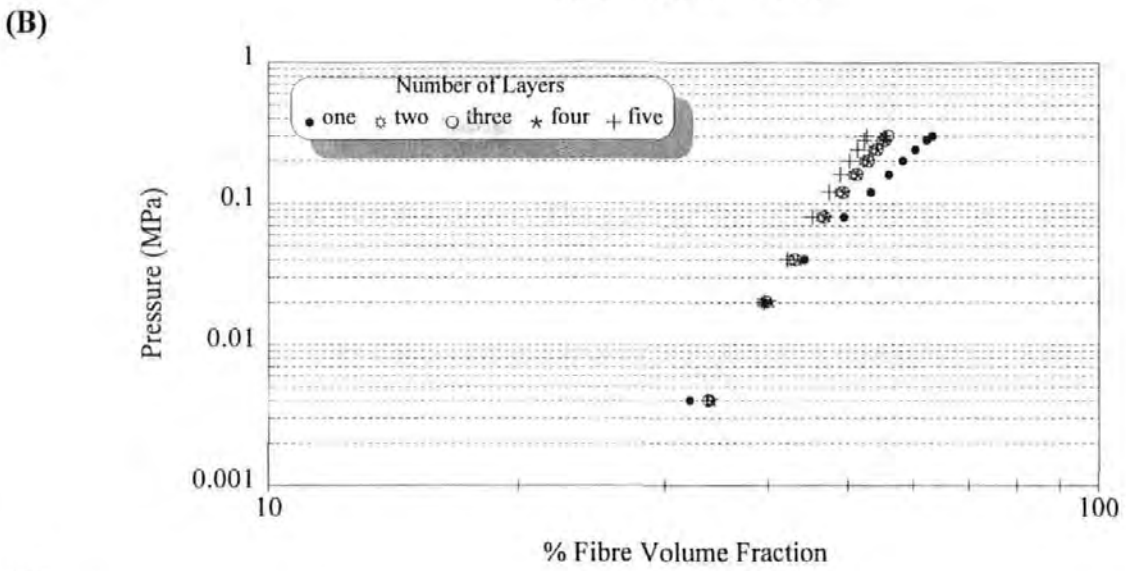
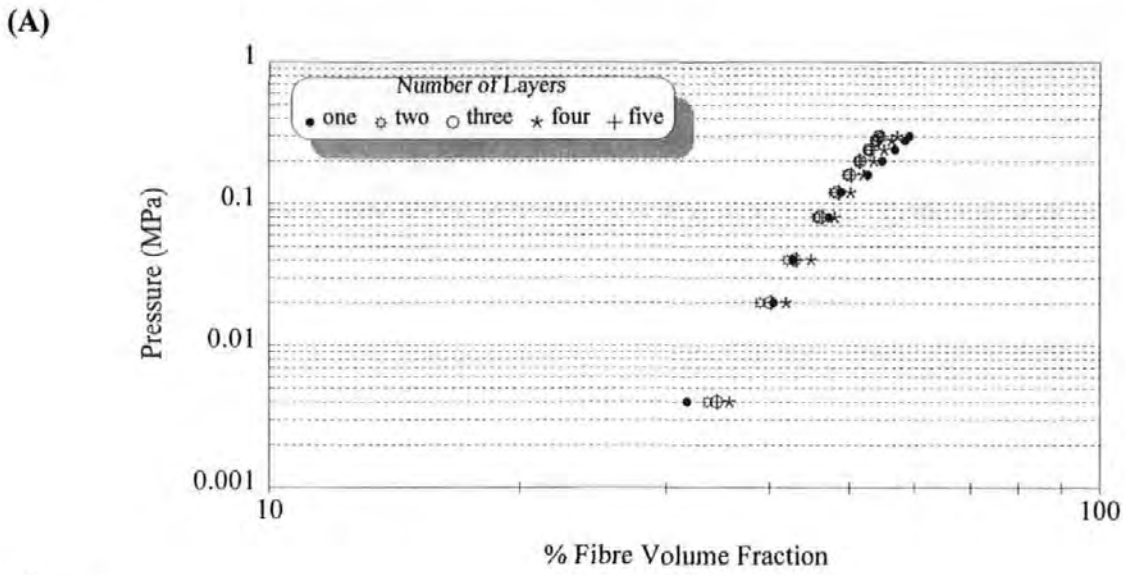
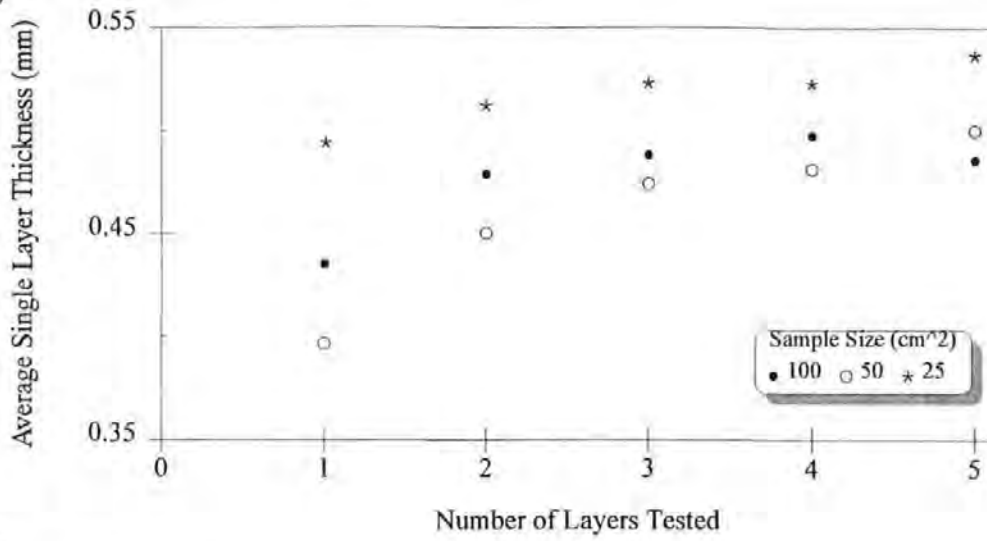
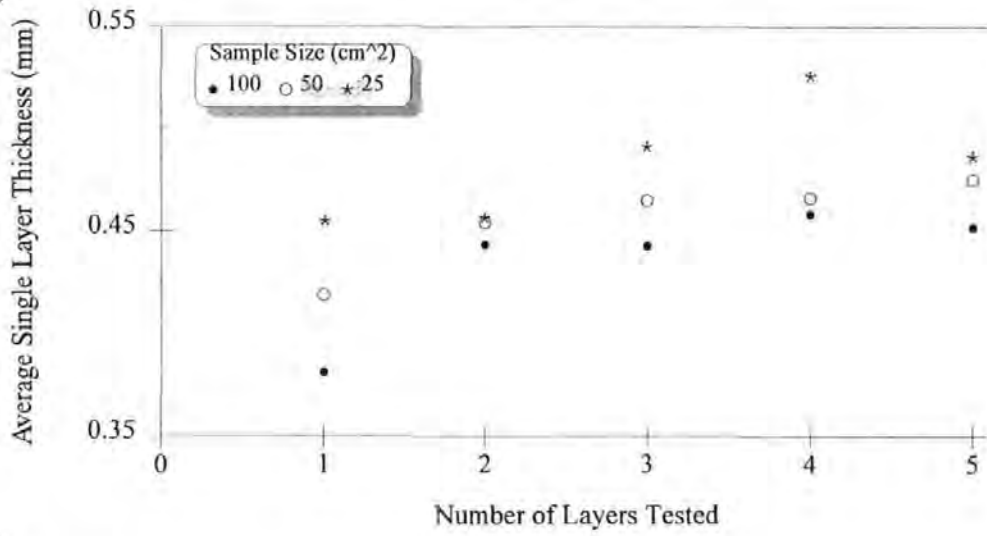


**Figure 4:** The data from Figure 3 plotted on log-log axes

(100 kPa)



(200 kPa)



(300 kPa)

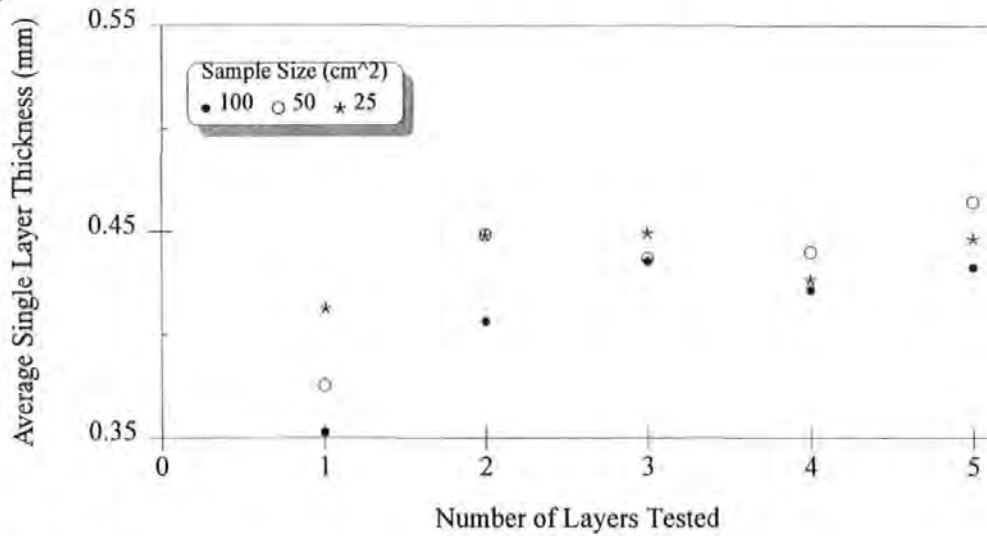
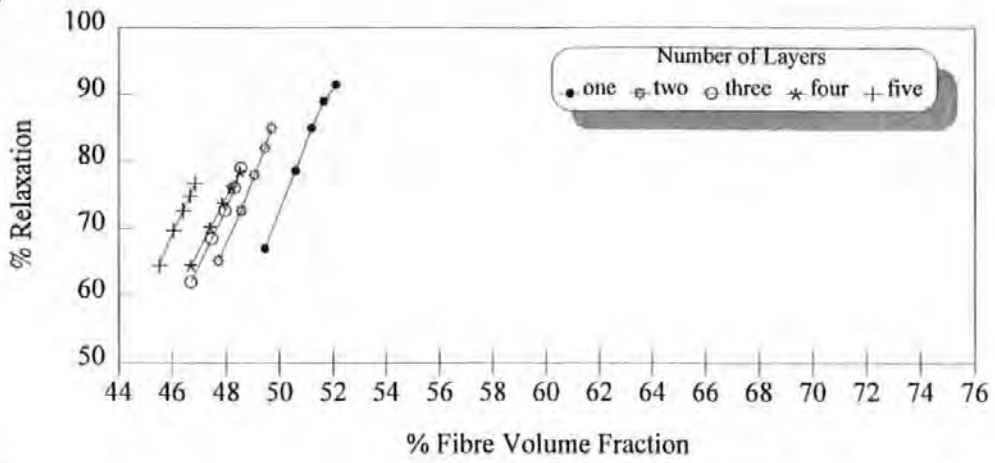
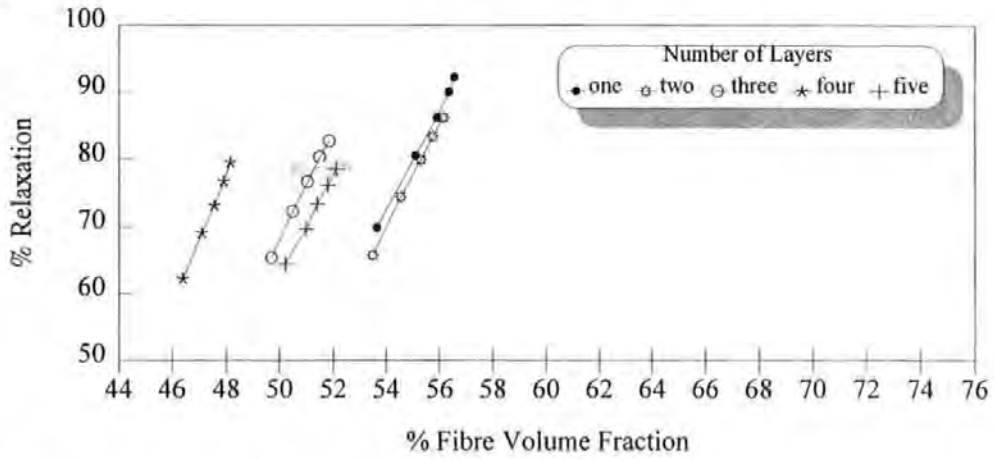


Figure 5: The apparent mean layer thickness of the fabric samples

(100 kPa)



(200 kPa)



(300 kPa)

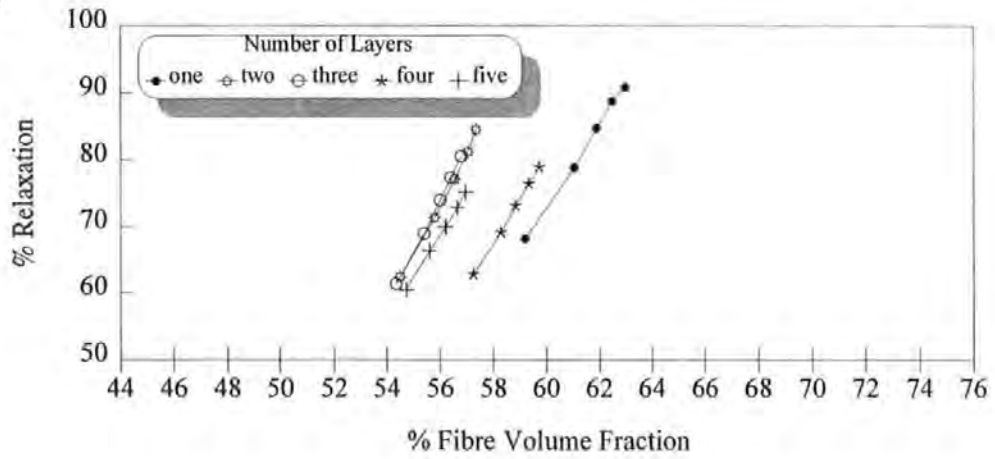
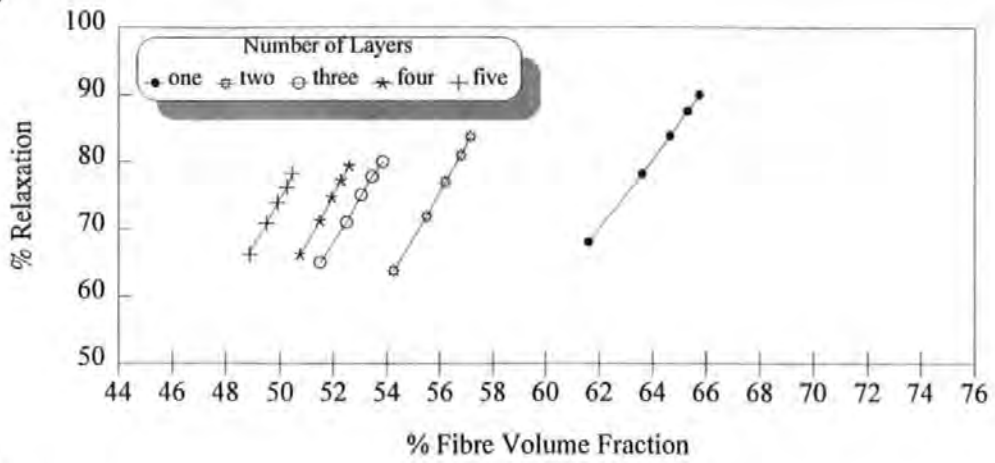
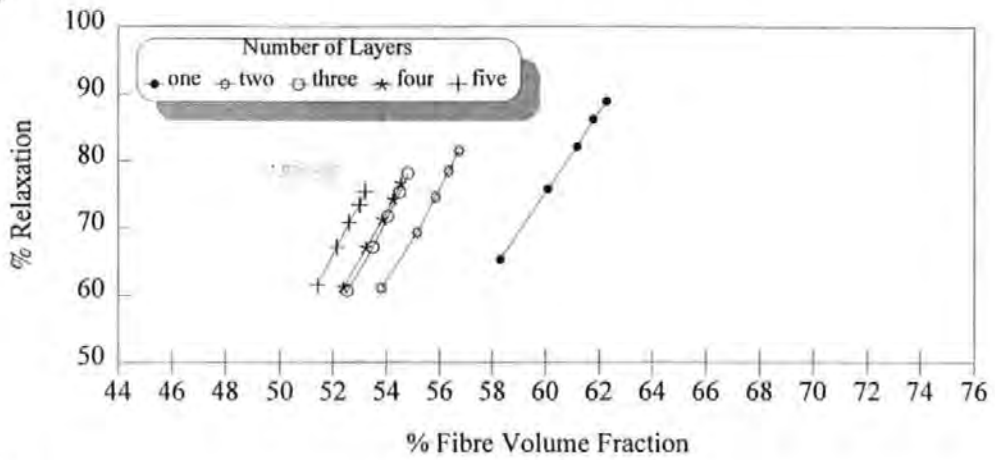


Figure 6: Residual load plotted against apparent fibre volume fraction for small samples

(100 kPa)



(200 kPa)



(300 kPa)

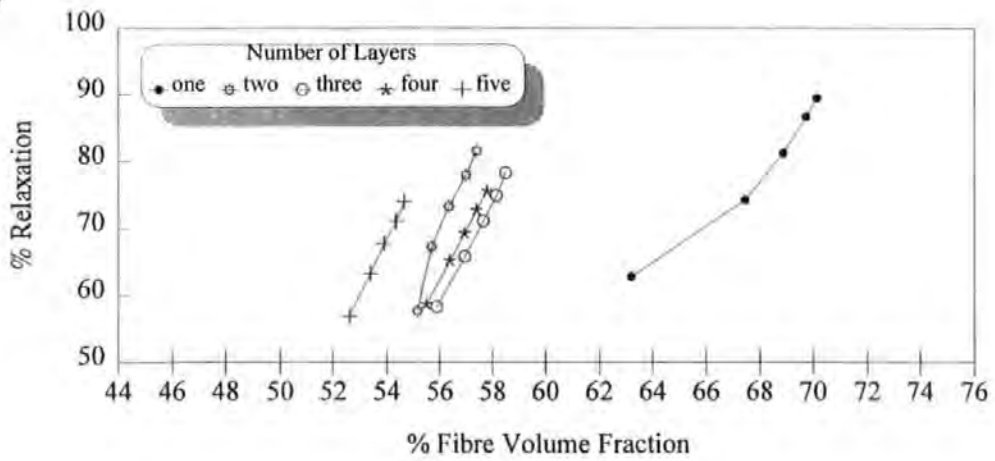
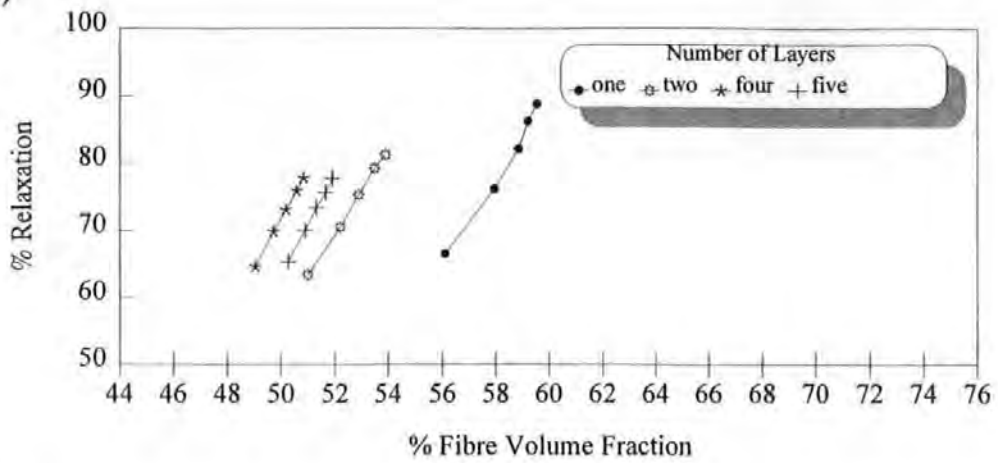
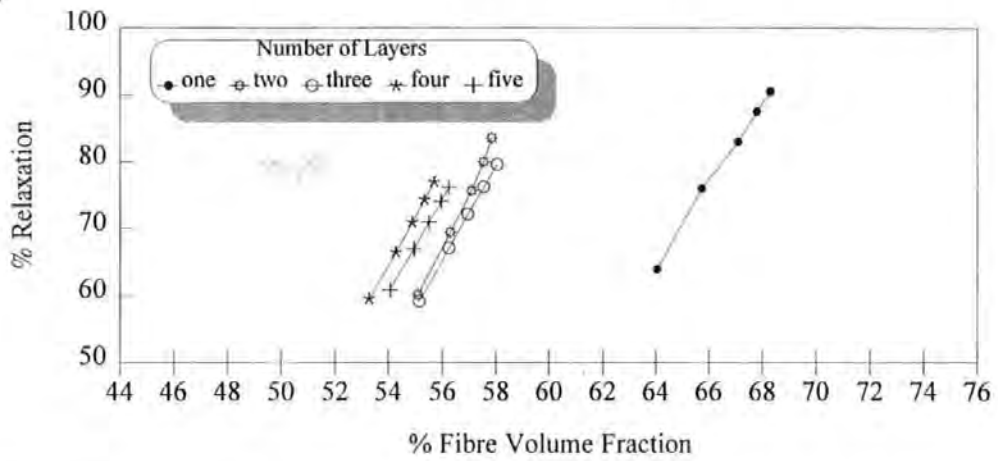


Figure 7: Residual load plotted against apparent fibre volume fraction for medium samples

(100 kPa)



(200 kPa)



(300 kPa)

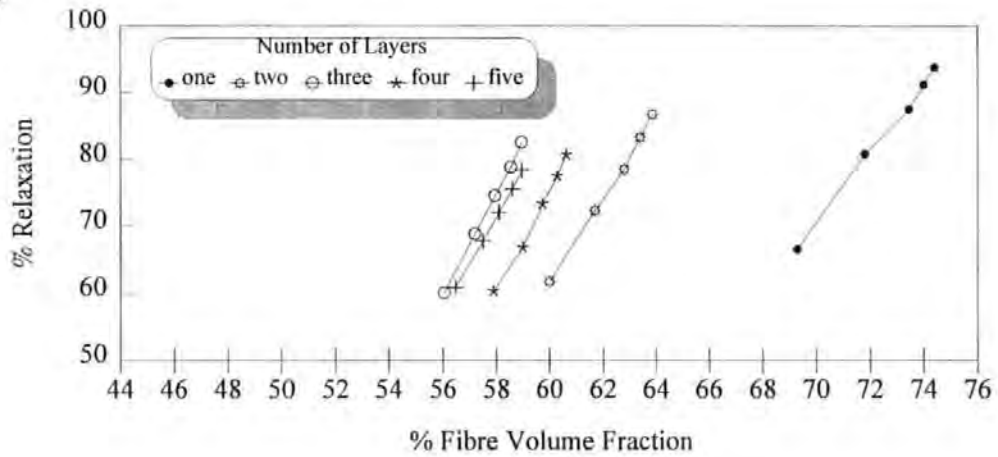


Figure 8: Residual load plotted against apparent fibre volume fraction for large samples

## References

- 1 AA Adams and JH Roberts "Vacuum impregnation"  
Conf.preprints 'Hands-Off GRP II', PRI, Coventry, May 1985, paper 5.
- 2 T Searle and D Short "Are composite propellers the way forward for small boats?"  
Materials World, February 1994, 2(2), 69-70.
- 3 T Cook and MC Cray "Supersonic radomes in composite materials"  
3rd Technology Conf, SAMPE Europe, London, March 1983, volume 1, paper 4.
- 4 RFJ McCarthy "Fifteen years experience with composite propeller blades"  
Preprints 1st Intl Conf, SAMPE Europe, Cannes, January 1981.
- 5 J Aveston and A Kelly "Tensile first cracking strain and strength of a hybrid composite"  
Proceedings of the Royal Society of London, 21 January 1980, A294(1411), 519-534.
- 6 MZ Kanovich, MA Koltunov and SL Roginskii  
"Investigation into the fibre packing density in a unidirectional composite"  
Polymer Mechanics, 1976, 12(3), 493-495.
- 7 SW Yurgartis, K Morey and J Jortner  
"Measurement of yarn shape and nesting in plain-weave composites"  
Composites Science and Technology, 1993, 46(1), 39-50.
- 8 FT Peirce  
"Geometrical principles applicable to the design of functional fabrics"  
Textile Research Journal, March 1947, 17(3), 123-134.
- 9 RM Hoffman and LF Beste  
"Some relations of fibre properties to fabric hand"  
Textile Research Journal, 1951, 21(2), 66-77.
- 10 H Bogaty, NRS Hollies, JC Hintermaier and M Harris  
"The nature of fabric surface: thickness pressure relationships"  
Textile Research Journal, 1953, 23(2), 108-114.
- 11 CJ Bartlett and DP Bloechle  
"The use of the parallel plate plastometer to characterize glass reinforced resins"  
Journal of Elastomers and Plastics, October 1978, 10(4), 369-385.
- 12 J Gutowski, J Kingery and D Boucher  
"Experiments in composites consolidation: fibre deformation"  
44th ANTEC Technical Papers, SPE, Boston MA, April/May 1986, 1316-1320.
- 13 TH Hou "Resin flow model for composite prepreg lamination process"  
44th ANTEC Technical Papers, SPE, Boston MA, April/May 1986, 1300-1305.
- 14 R Gauvin and M Chibani  
"Modelization of the clamping force and mould filling in RTM"  
Proc 43rd Annual Conf, SPI Composites Institute, Cincinnati OH, February 1988.
- 15 GL Batch and CW Macosko  
"A model for two-stage fibre deformation in composite processing"  
Proc 20th Int Tech Conf, SAMPE, Minneapolis MN, September 1988, 641-650.
- 16 JA Quinn and JE Randall  
"Compliance of composite reinforcement materials"  
Proc 4th Int Conf Fibre-Reinforced Composites, Institution of Mechanical Engineers, Liverpool, March 1990, paper C400/046, 105-112.
- 17 YR Kim, SP McCarthy and JP Fanucci  
"Compressibility and relaxation of fiber reinforcements during composite processing"  
Polymer Composites, 1991, 12(1), 13-19.
- 18 S Toll and J-AE Manson "An analysis of the compressibility of fibre assemblies"  
Proc 6th Int Conf Fibre-Reinforced Composites, Institute of Materials, Newcastle-upon-Tyne, 29-31 March 1994, paper 25.

## **List of Tables**

- Table 1: Characteristic equations for compliance of typical reinforcing materials (from Quinn and Randall, 1990 [16])
- Table 2: The load applied to each sample to achieve the required pressure
- Table 3: The power law variables for the initial loading to 300 kPa
- Table 4: The apparent mean fabric layer thicknesses (micrometres) at the end of the initial loading cycle
- Table 5: The gradients of the successive residual load values versus volume fraction graphs
- Table 6: The variables in the exponential decay equation

## **List of Figures**

- Figure 1: The load/time response of a single isolated layer (upper plot) and of a stack of five fabric layers (lower plot) under similar conditions
- Figure 2: Time taken to achieve the target pressure against number of layers
- Figure 3: Pressure plotted against fibre volume fraction during the initial loading cycle to 300 kPa, (A) 50 mm square samples, (B) 71 mm square samples, (C) 100 mm square samples.
- Figure 4: The data from Figure 3 plotted on log-log axes
- Figure 5: The apparent mean layer thickness of the fabric samples
- Figure 6: Residual load plotted against apparent fibre volume fraction for small samples
- Figure 7: Residual load plotted against apparent fibre volume fraction for medium samples
- Figure 8: Residual load plotted against apparent fibre volume fraction for large samples

# AN INVESTIGATION INTO THE EFFECTS OF FABRIC ARCHITECTURE ON THE PROCESSING AND PROPERTIES OF FIBRE REINFORCED COMPOSITES PRODUCED BY RESIN TRANSFER MOULDING

N R L PEARCE\*, F J GUILD<sup>+</sup> AND J SUMMERSCALES\*

\* School of Manufacturing, Materials and Mechanical Engineering,  
University of Plymouth, Plymouth, Devon PL4 8AA

+ Department of Materials Science and Engineering  
University of Surrey, Guildford, Surrey GU2 5XH

**Abstract:** The use of resin transfer moulding (RTM) as an economic and efficient means of producing high performance fibre-reinforced composites is critically limited by the permeability of the fabrics employed. Commercial fabrics are available where the architecture of their reinforcement is designed to cluster the fibres, giving higher permeabilities than conventional fabrics. This has been shown to improve processing times but there is evidence that such clustering is detrimental to the mechanical performance of the resulting composite materials.

The objective of this work was to relate variations in permeability and mechanical performance to differences in composite microstructure. This was achieved by producing carbon/epoxy plates of different weave styles by RTM in a transparent mould. The progress of the resin was recorded by a video camera during injection, and the images were processed by a frame-grabbing computer, permitting the permeabilities of the fabrics to be calculated.

Further plates were manufactured using the same fabrics, and sectioned for microstructural image analysis and interlaminar shear strength (ILSS) testing to CRAG standards. Relationships were sought between measured permeabilities and finished microstructures using a Quantimet 570 automatic image analyser. It has been shown that variations in permeabilities and mechanical properties can be related to observed differences in the microstructure.

## INTRODUCTION

Resin transfer moulding (RTM) is a process for producing polymer-matrix composites. A dry preform of reinforcement fibres is placed into a mould, which is closed before resin is injected. Once the resin has cured, the near net-shape component is removed from the mould. RTM differs from other composite manufacturing processes as it involves long-range flow of resin through the porespace between the reinforcement fibres. The process and the governing equations have been well described<sup>1-3</sup>.

Darcy<sup>4</sup> found that the flow rate of a fluid was proportional to the pressure drop and inversely proportional to the bed length. The coefficient of proportionality is known as the permeability. The equation now normally includes a dependence of the permeability on the fluid viscosity. The permeability must be either measured or predicted. Kozeny<sup>5</sup> and Carman<sup>6</sup> related the flow rate to the microstructure of the medium using the Blake concept<sup>7</sup> of the hydraulic radius of the bed. The equation<sup>8</sup> uses a *mean* hydraulic radius which may only apply if fibres have either uniform or truly random packing.



Summerscales<sup>9</sup> used a *specific* hydraulic radius to model the effect of variations in the reinforcement architecture on the flow rate. The flow rate in a clustered array of fibres was predicted to be significantly greater than for a uniform distribution of individual fibres at the same fibre volume fraction. Thirion et al<sup>10</sup> have shown that the linear flow rate through similar reinforcement fibres at the same fibre volume fraction was more rapid in commercial fabrics when clustered flow-enhancing tows were present.

The presence of uneven fibre distribution has been predicted to lead to degradation of the mechanical properties of continuous fibre reinforced laminates<sup>11</sup>. This prediction may be confirmed by recent measurements of the mechanical properties of such laminates. These show reductions in the longitudinal compressive strength and interlaminar shear strengths with increasing proportions of clustered tows<sup>12</sup>. The requirements for good mechanical performance appear to be in conflict with those of large pore space for rapid manufacturing using the RTM technique.

The evaluation of real materials requires automated microstructural image analysis. These techniques for fibre-reinforced composites has been reviewed by Guild and Summerscales<sup>13</sup>. Quantitative microscopy, using spatial statistics, is capable of revealing subtle relationships amongst the fibres in the composite. Summerscales et al<sup>14</sup> have used the Voronoi half-interparticle distance to study the microstructure of carbon fibre-reinforced plastics processed by the vacuum-bag technique using different process dwell times.

A series of papers<sup>15-17</sup> have reported the effect of substituting flow-enhancing tows into a 2x2 twill weave fabric on the long range flow rates. The effect of fabric architecture on compression and interlaminar shear strengths has been reported for the same fabrics<sup>12</sup>. The work has recently been published in summary form<sup>18-19</sup>. This paper reports similar results for a different set of fabrics: a twill, a 5 harness satin and a flow enhanced 5 harness satin Injectex.

## EXPERIMENTAL

### Materials

The conventional and flow-enhancing fabric (FEF) carbon-fibre reinforcements in this study were obtained from Brochier SA (now Hexcel Composites, Dagneux - France). All three fabrics had the same areal weight (290 gsm) and were woven from the same batch of fibre. As the fabrics were of equal areal weight, fibre volume fractions would be the same for a given number of laminae within a given mould cavity thickness. The fabrics are described in Table 1 and shown schematically in Figures 1, 2 and 3.

**Table 1 Fabrics studied**

<i>Designation</i>	<i>Description</i>
E3853 G986	2x2 twill weave 6K carbon fibre fabric
E3795	5-harness satin weave 6K carbon fibre fabric
E3833 G963	5-harness satin Injectex weave 6K carbon fibre fabric

Figures 1-3 show the differences between the weave styles and indicate the tortuosity of the path the tows take through the fabric (crimp). The Injectex fabric has the same weave style as the satin but a modified architecture to improve its permeability. One in five tows are bound, (as shaded) this maintains the size of porespace around these tows when stacked with other layers within a mould.

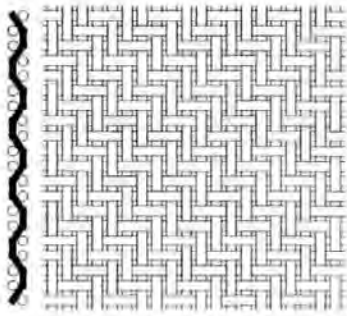


**Figure 1 Schematic of 2x2 twill weave**

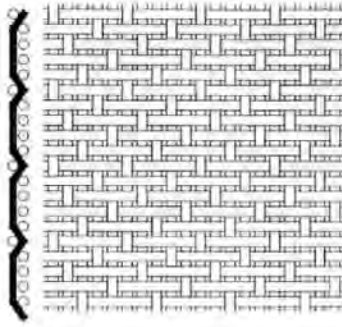


**Figure 2 Schematic of 5-harness satin weave**

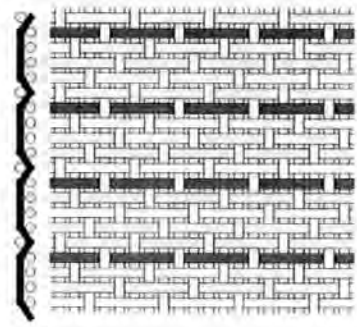


**Figure 3 Schematic of 5-harness satin Injectex weave**

The resin matrix system was Ciba-Geigy LY564-1/HY2954 epoxy. This has an initial viscosity of 500-700 mPas at 25°C and 80-125 mPas at 60°C (manufacturers data sheet K6B of April 1991). The NIP (non-injection point: time taken for the viscosity to rise to 1000 mPas) is 85 minutes at 25°C and 42 minutes at 65°C.

### **Permeability measurements**

Radial flow permeability experiments were conducted on each of the three fabrics at nominal fibre volume fractions of 49%, 54% and 60%. The varying volume fractions were achieved by using nine, ten or eleven layers of each fabric in a 400 mm square, 3.0 mm deep flat mould with a 20 mm thick glass top. The flow fluid was introduced through a central inlet port at a constant differential fluid pressure between  $1.53\text{--}2.21 \times 10^3$  Pa absolute.

During injection the flow front isochrones were monitored using a Minitron camera fitted with a Computar V1218 12.5 mm f1.8 C-mount lens (Optimum Vision Limited, Petersfield). The camera was mounted 1000 mm above the centre of the glass plate on a welded steel support frame. Illumination was provided by three 500W floodlights mounted to either side and behind the apparatus. The light was diffused by white fluted plastic sheets attached to the support frame.

The video signal was recorded as a series of grey-scale digital images using a Synapse video frame grabber and C\_Images software (Foster Findlay Associates, Newcastle-upon-Tyne). The frame grabber has a resolution of 768 x 512 pixels and thus can resolve lengths to less than 1 mm when focused on the full square flow region of 400 mm edge length (i.e. the error is of the order of  $\pm 1$  pixel or  $\pm 1$  mm). This is better than the resolution achievable when tracing the flow front isochrone onto an acetate sheet given the thickness of the drawn line, the time taken to trace the full flow front and the potential for parallax errors when working from an edge of the apparatus.

The flow front isochrones were recorded at equal intervals. The permeability values were calculated using the radial form of Darcy's equation. This approach is similar to that of Adams et al<sup>20</sup> and Chan and Hwang<sup>21</sup>. The experimental apparatus and data validation routines have been described in the literature<sup>22</sup> and the theory is published<sup>23</sup>.

### Sectioning of plates for interlaminar shear strength (ILSS) and microscopical testing

The three fabrics characterised by the permeability experiments had also been used during a series of multi-port experiments investigating the effect of convergent flow on mechanical properties of composites produced by RTM<sup>24</sup>. As part of the study, composite plates had been manufactured to the same specification as those of the permeability tests, i.e., 10 layers of each fabric in a 3 mm thick mould giving a 54% fibre volume fraction. One of the injection styles used for the multi-port experiments had been sectioned in such a manner that it provided 49 pairs of ILSS and microscopy specimens (see Figure 4) for each of the fabrics.

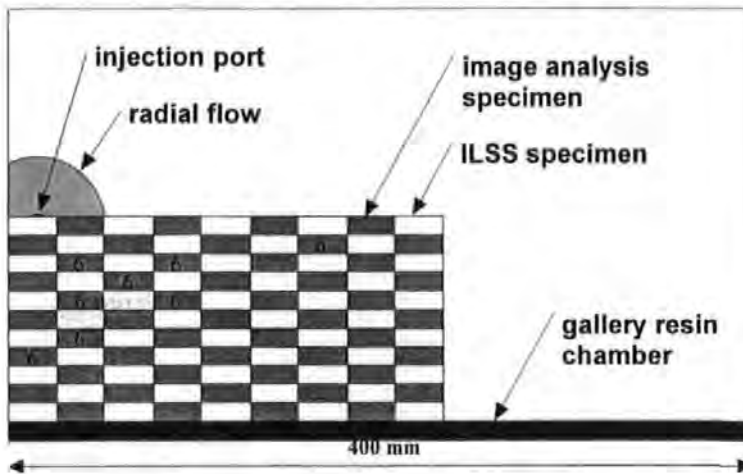


**Figure 4 Multi-port injection strategy**

Only 16 pairs of specimens had been examined per plate. It was decided to use 10 of the remaining 33 pairs to characterise the microstructure, and measure the ILSS for the fabrics.

The injection style had been designed to cause flow fronts to converge, with the expectancy of increased void volume fraction localised to the area where the flows met. Although the level of void content would have no effect on the measurement of porespace, it would adversely effect the ILSS measurements<sup>25</sup>. For this reason, the 10 pairs of specimens were taken from the lower edge of each plate (next to the resin gallery) away from the area of convergence.

For the multiport experiments, CRAG Specification 100<sup>26</sup> had been used to determine the ILSS. The size of ILSS specimens being dependent on plate thickness: for the 3 mm thick plates, the specimens were 25 mm x 15 mm.

The specimens had been cut using a Tyslide diamond slitting saw (serial number MB1116) fitted with a specially constructed attachment designed to ensure repeatability of specimen dimensions. The edges of the specimens were found to be flat and smooth and required no further machining, therefore the specimens had been cut to net size.

The minimum size of the microscopy specimens was constrained by the repeat cell size of the fabrics: that of the spacing between tows with identical positioning within the fabric architecture. The repeat sizes for the fabrics were measured and are reported in Table 2.

**Table 2 Unit cell sizes for the fabrics**

<i>Fabric</i>	<i>Repeat size (mm)</i>
Twill	12
Satin	7
Injectex	7

The maximum repeat distance was 12 mm, measured from the twill fabric. The dimensions of the microscopy specimens were equal to those of the ILSS specimens (i.e. 25 mm x 15 mm). Therefore, there were at least two repeat cells for each of the ten fabric layers per specimen. It was therefore believed that each microscopy specimen would be truly representative of the plate from which it was removed.

The ILSS and microscopy specimens had been marked out adjacent to one another to facilitate comparison. The edge of the microscopy specimen lying next to the ILSS specimen was identified so that this edge could be polished. It was assumed that the voidage would be similar in adjacent microscopical and ILSS samples for the purpose of the subsequent analysis.

### ILSS testing

The thickness and width of each specimen was measured using a Mitutoyo digital micrometer (serial number 293-766) with a resolution of 0.001 mm. The measurements were stored in a Microsoft Excel 5.0 spreadsheet.

ILSS testing was performed to CRAG specification 100 using an Instron 1175 Universal Testing Machine (serial number HO525) fitted with a 10 KN load cell (serial number UK833). Control of the Instron and data acquisition were achieved using a Strawberry Tree parallel port data acquisition system and 486DX100 PC. Load cell output voltage was automatically converted to force in Newtons and logged against time at a rate of 10 Hz. The data acquired from each specimen test was saved to disk for subsequent processing in the Excel spreadsheet.

### Preparation of specimens for optical microscopy

Specimens were individually potted in an epoxy casting resin. They were then prepared using a Buehler 2000 Metpol grinder/polisher with Metlap fluid dispenser. All specimens were prepared following the procedure shown in Table 3.

**Table 3 Microscopical specimen preparation**

<i>step</i>	<i>Platen</i>				<i>Head</i>		<i>time</i>
	<i>surface</i>	<i>abrasive</i>	<i>speed (rpm)</i>	<i>direction</i>	<i>speed (rpm)</i>	<i>force (lbs)</i>	
1	SiC paper	240 grit	150	complementary	120	15	until plane
2	"	400 grit	"	"	"	20	2 min
3	"	600 grit	"	"	"	"	"
4	"	800 grit	"	"	"	"	"
5	nylon cloth	6 $\mu$ m diamond	50	contra	"	30	5 min
6	texmet cloth	1 $\mu$ m diamond	100	complementary	60	"	"
7	mastertex cloth	Al SiO <sub>2</sub>	50	contra	"	5	2 min

As voidage adversely affects ILSS it was decided to measure the void volume fraction of the microscopy specimens for comparison with the ILSS results. To facilitate this a magnesium silicate (talc) powder was used to fill the surface breaking voids. This has been found to enhance the detection of voids in the plane of the specimens, allowing greyscale thresholding to be adjusted such that voids which lie beneath the surface are not measured.

### Microstructural image analysis

The microstructural analysis was achieved using a Quantimet 570 image analysis system. Images were acquired using a Kyowa STZ tri-nocular stereo zoom microscope (serial number 850101) and Fujitsu TCZ-230EA low light level black and white video camera (serial number 20006728). The process was performed in a darkened room using incident illumination from a Flexilux 150 HL Universal ring illuminator.

The Quantimet 570 has an adjustable image frame of 512 x 512 pixels maximum, with 256 grey levels (black = 0 and white = 255). The magnification of the microscope was adjusted to give an on-screen field of view of 4 mm x 4 mm by using a calibrated reference.

The image frame was set to 512 x 400 pixels, giving a linear resolution of 7812 nm/pixel, and a detection size of 4 mm width x 3.125 mm depth. Six contiguous frames were automatically analysed, covering 24 mm of the 25 mm length of each specimen. Specimens were moved manually between frames using a purpose-built slide which restricted travel to only one axis aligned parallel to the camera axis. The fields were positioned to be reliably contiguous using an on-screen image alignment reference: a vertical bar of detected features captured from one extremity of a frame and translated by an on-screen distance equivalent to 4 mm in the axis of movement. This acted as a template allowing a 'live' image of the specimen to be realigned.

System parameters were adjusted to provide reliable detection of porespace, fibres and voids as discernible, distinct features. Low pass filtering was used to improve the signal/noise ratio of the image.

The following measurements were made:

- Areas ( $\text{mm}^2$ ) of individual features of *segmented* porespace.
- Count of total number of individual features of *segmented* porespace.
- Total void volume fraction.
- Individual void count with corresponding areas ( $\text{mm}^2$ ).

## RESULTS AND DISCUSSION

### Permeability measurements

Figure 5 shows the permeability results for the three fabrics<sup>27</sup>. The values on the diagonal are those for quasi-isotropic fabric lay-up sequences, *i.e.* cross-plyed warp directions in adjacent layers. Note that if the twill and Injectex are not cross-plyed they are anisotropic, due to a difference in warp and weft count in the former case, and the presence of flow-enhancing tows in the latter. Values off the diagonal are indicative of the extent of anisotropy of the materials.

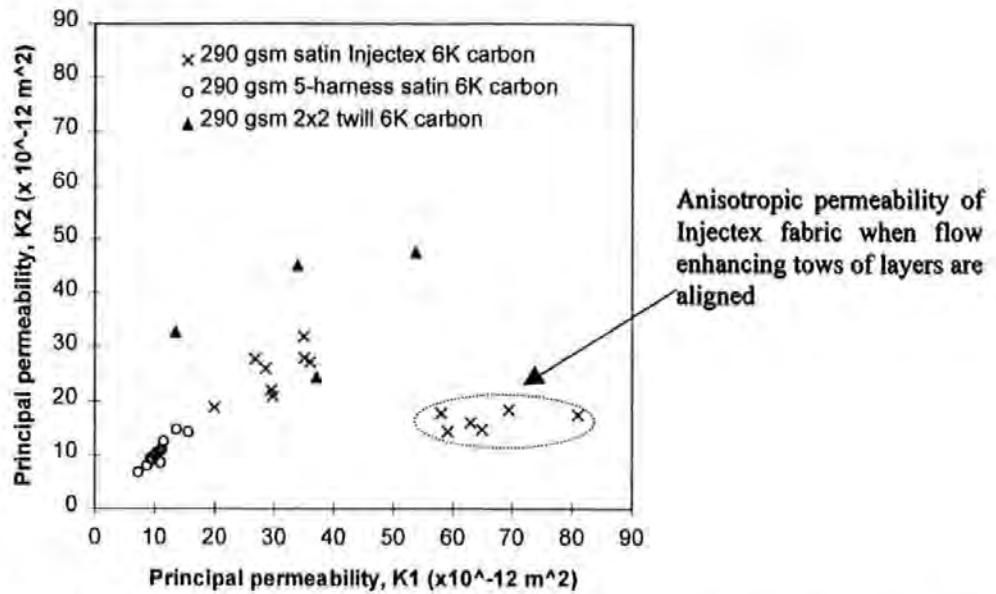


**Figure 5 Principal permeabilities of the twill, satin and Injectex fabrics**

Table 4 shows the range of measured permeabilities for quasi-isotropic lay-ups with fibre volume fractions of 49% and 54%. There is clearly a permeability ranking between the fabrics in the order: twill > Injectex > satin. This ranking must be a function of fabric architecture and its effect on porespace, as the results are derived from notionally identical experiments.

**Table 4 Range of measured permeabilities for quasi-isotropic lay-ups ( $\times 10^{-12} \text{ m}^2$ )**

<i>Fabric</i>	<i>Lower bound</i>	<i>Upper bound</i>
Twill	34.0	53.7
Injectex	18.9	36.1
Satin	8.1	17.9

### ILSS testing

The ILSS of samples of the three fabrics were measured to CRAG Specification 100<sup>26</sup>. Figure 6 shows the full set of results obtained from the thirty specimens tested (ten for each fabric). As with the permeability results, there is a clear ranking of the ILSS values, note however that the order is reversed: satin > Injectex > twill. The difference in ILSS between the twill and satin fabrics could be a result of variation in crimp. However, the difference between the satin and Injectex ILSS values must result from a change in porespace distribution, as the crimp of the two fabrics is the same (i.e. they are both satin weaves).

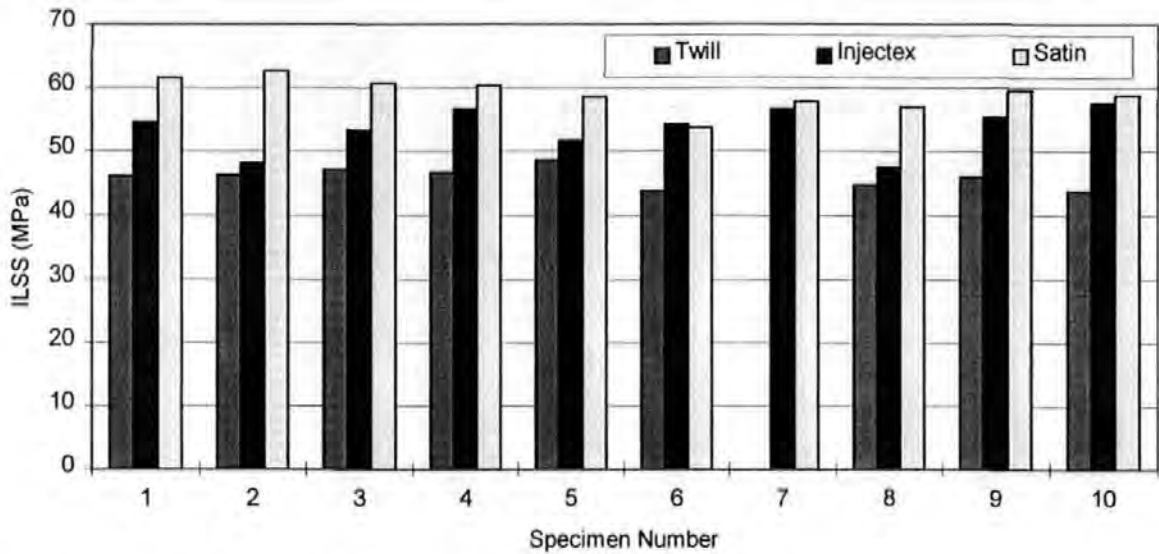


**Figure 6 ILSS of the twill, satin and Injectex fabrics**

#### **Microstructural image analysis**

The void volume fraction was measured for each of the thirty specimens. Figure 7 shows the full set of results obtained. It can be seen that there is no discernible relationship between void content and specimen location with respect to the injection ports. Therefore, there is no reason to suspect any influence on measured ILSS values due to specimen location.

The high void volume fraction for Injectex specimen 7 does not yield a correspondingly low ILSS value. The voids were located close to the specimen surface and hence would not be expected to cause a large decrease in the shear strength.

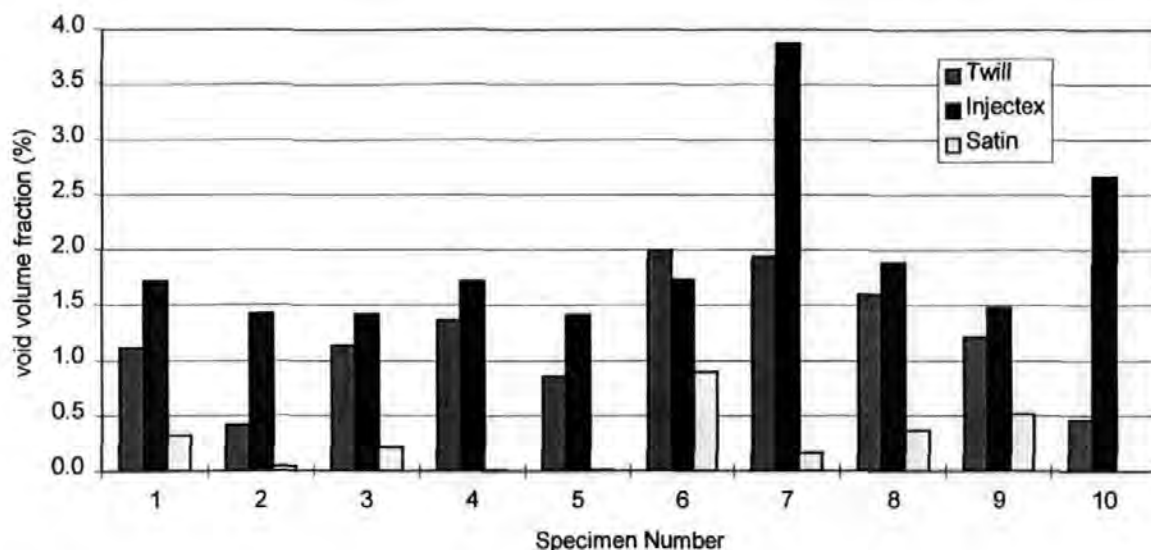


**Figure 7 Measured void volume fractions**

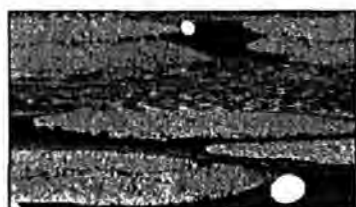


**Figure 8 Micrograph of twill fabric**



**Figure 9 Micrograph of satin fabric**



**Figure 10 Micrograph of injectex fabric**

Figures 8, 9 and 10 show micrographs of the three fabrics. The white features are voids which lie in the plane of the image and have been filled with magnesium silicate to enhance detection.

Qualitatively, variations can be seen in the size of porespace between the tows of the fabrics. The twill fabric has a higher crimp than the satin, as shown in Figure 1. This increases the amount by which the tows run out of plane, and therefore reduces the ability of the tows in adjacent layers to nest together. The bound tows of the Injectex fabric can be seen in Figure 10. The shape of bound and conventional tows clearly differ, the binding prevents the tows from flattening resulting in an increase in the size of porespace around them.

The size of the porespace which lies between the tows will affect the permeability of the fabrics, and is also believed to influence void formation and void volume fraction. Large areas of porespace will act as channels through which resin can flow. This will increase the permeability as channel flow is more rapid (at pressures commonly used in RTM) than the capillary flow which occurs within tows<sup>28-34</sup>. The differences in flow rate will result in transverse microflows occurring behind the flow front. Resin will be wicked into the tows, displacing the air within them, which will then form voids in the porespace around the tows.

It is thought that the size of the porespace will influence the degree of lead and lag between channel and capillary flow. It is sensible to assume that larger porespace will result in a greater difference, more air entrapment, and allow larger voids to coalesce.



With reference to Figure 7 it can be seen that the void volume fractions measured for the three fabrics are highest for the twill and Injectex. Both of these exhibit higher permeabilities than the satin, and have larger areas of porespace around tows.

#### Determination of porespace areas

Area measurements were made of the porespace features, and number of features, for the three fabrics (6 frames per specimen, 10 specimens per fabric). An automatic segmentation process was used to convert large areas of detected porespace into separate features when the areas necked below a set threshold. Interconnected large channels were therefore separated, and treated as distinct areas. Table 5 summarises the results obtained from all of the specimens. The minimum porespace area measured for all fabrics was set by a detection threshold equivalent to 3 pixels. As expected, the maximum porespace sizes for the twill and Injectex fabrics were larger than the value for the satin.

**Table 5 Porespace area measurements (mm<sup>2</sup>)**

<i>Fabric</i>	<i>Min.</i>	<i>Max.</i>	<i>Average</i>	<i>Number of areas</i>
Twill	0.000549	1.007446	0.053	1445
Injectex	0.000549	0.705078	0.056	2061
Satin	0.000549	0.319031	0.027	2498

Comparison of the results is most easily achieved by using a normalised plot of cumulative feature frequencies, as shown in Figure 11. The plot in Figure 11 is based upon the frequency of occurrence of areas which lie within a given range (bin). Figure 12 shows the frequency data upon which Figure 11 is based.

With reference to Figures 11 and 12, it can be seen that: The ranking of measured permeability values for the three fabrics corresponds directly with the ranking of the proportion of porespace areas greater than 0.25 mm<sup>2</sup>. The ranking of permeability also correlates inversely with number of porespace areas. There is no direct correlation to the total area of measured porespace. It is therefore necessary to consider the distribution of sizes of the pores.

The satin fabric has the greatest proportion of porespace areas up to 0.06 mm<sup>2</sup> (small flow areas). The flow enhancing tows in Injectex create a significant number of additional porespace areas in the range 0.08 mm<sup>2</sup> - 0.3 mm<sup>2</sup>, it is believed that these result in the increase in permeability compared to the satin. This range is similar to that previously identified for flow enhancing tows in a different set of twill weave fabrics (0.10-0.25 mm<sup>2</sup>)<sup>17</sup>. The twill fabric has a high proportion of porespace areas in the range up to 0.06 mm<sup>2</sup>, and a significant proportion of porespace areas over 0.5 mm<sup>2</sup> (very large flow areas). It is thought that the areas over 0.5 mm<sup>2</sup> give rise to the higher permeability of the twill.

#### Comparison of permeability and ILSS

The ILSS increases: twill < Injectex < satin, the permeability increases: satin < Injectex < twill (see Figure 13). The decrease in ILSS of the Injectex compared with that of the satin is thought to result from the increased size of porespace areas. The twill has the largest porespace areas and hence the highest permeability, however, the size of the large porespace areas causes a reduction in the ILSS.

With the fabrics currently available, a choice must be made between maximum properties or minimum processing time. There may be scope for development of advanced fabrics which produce a more structured / regular arrangement of porespace without creating large pores and hence resin rich areas.

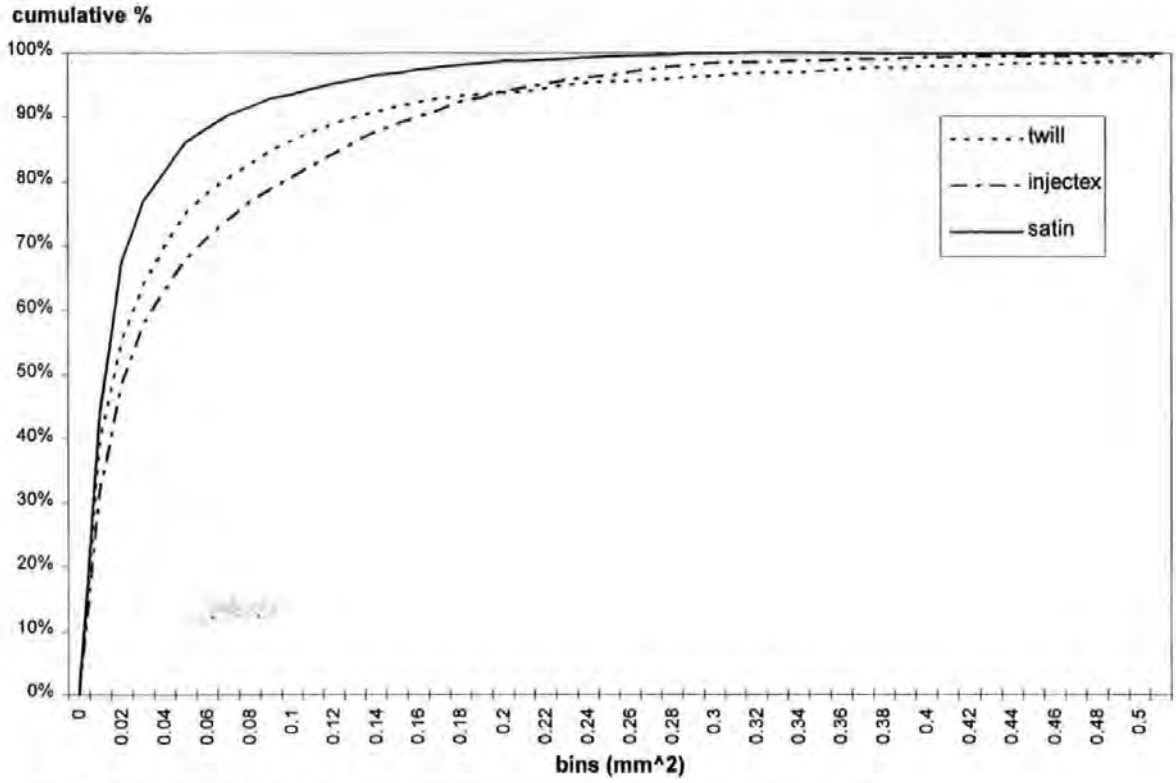


**Figure 11 Normalised plot of cumulative porespace area feature frequencies**

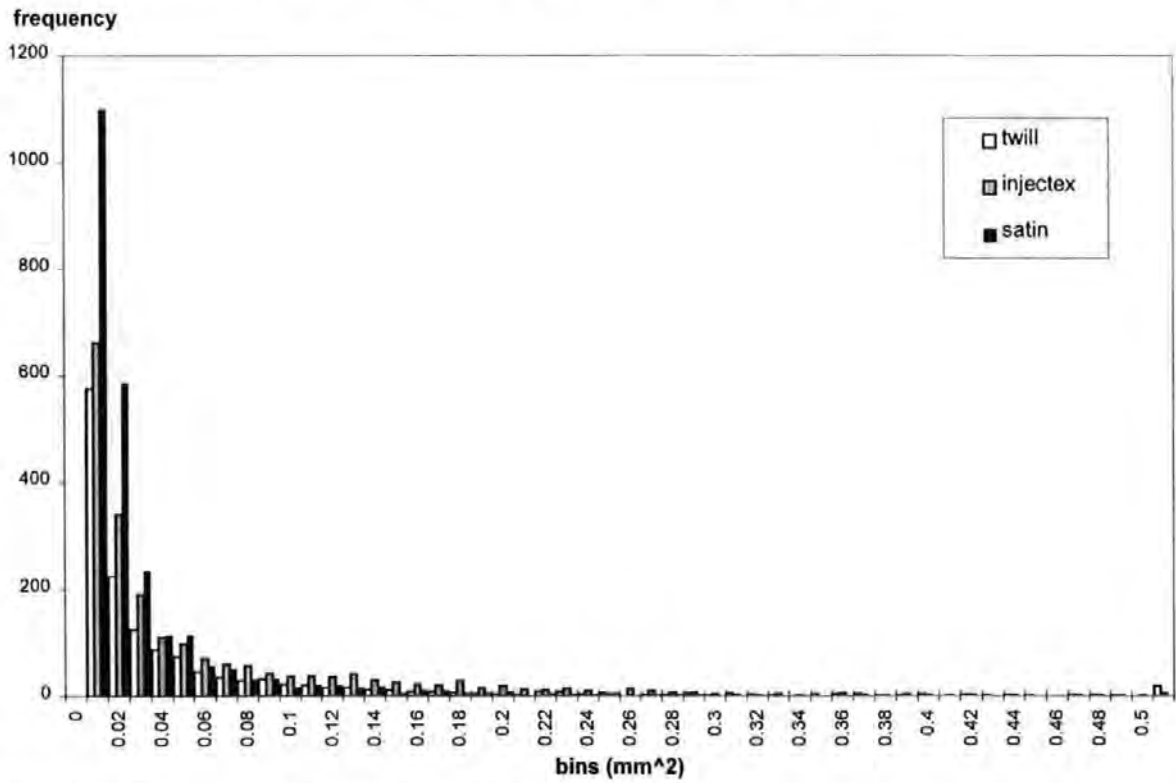


**Figure 12 Porespace area feature frequencies**

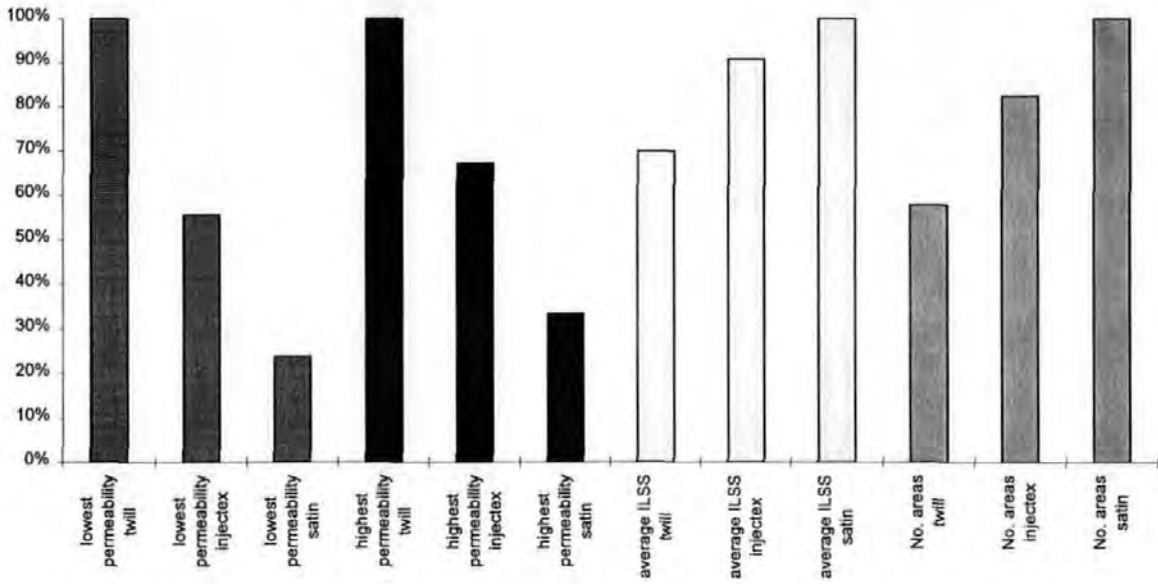


**Figure 13 Normalised permeabilities, ILSS and porespace feature count for twill, satin and Injectex**

## SUMMARY

Permeability experiments have been conducted on three fabrics: twill, satin and satin Injectex. The architecture of the fabrics differ, but fibre type, surface treatment and fibre volume fractions are equivalent. The measured permeabilities fall in a definite order: twill > Injectex > satin.

ILSS testing has also shown a definite ranking, but in reverse to that of the permeability: satin > Injectex > twill.

The satin fabric had the highest number, and highest proportion of small flow areas ( $< 0.06 \text{ mm}^2$ ), and very few areas of porespace  $> 0.25 \text{ mm}^2$ . This was thought to explain the lower permeability and higher ILSS measured.

Twill had the smallest number of flow areas but a significant number of large porespaces. The large porespaces were thought to result in the high permeability but low ILSS observed.

Unlike the satin and twill fabrics, the Injectex (flow enhanced satin) had a significant number of porespace areas in the range  $0.08 \text{ mm}^2 - 0.3 \text{ mm}^2$ . The porespaces in this range were thought to explain the increase in permeability and decrease in ILSS compared to the satin.

The permeabilities for the three fabrics were ranked in the same sequence as the proportion of larger porespaces, and ranked in the same order as descending ILSS.

## ACKNOWLEDGMENTS

The authors would like to acknowledge the support of EPSRC grants GR/J77405 and GR/K04699 and BRITE/EurAM II grant BRE2/CT92/0227 which have supported this work. Thanks are also due to Eddie Carter, Tony Fell and Patrick Griffin for conducting and analysing the permeability experiments, and to Paul Russell of UoP Department of Biological Sciences for assistance with the Quantimet.

## REFERENCES

1. van Harten. K., 'Production by resin transfer moulding', in Sheno, R.A. and Wellicome, J.F., (editors): "*Composite Materials in Maritime Structures*". Cambridge University Press, Cambridge, 1993, Chapter 4, 86-126
2. Tucker, C.L. and Dessenberger, R.B., 'Resin transfer moulding phenomena in polymeric composites', in Advani, S.G., (editor): "*Flow and Rheology in Polymer Composites Manufacturing*". Elsevier, Amsterdam, 1994, Chapter 8, 257-323.
3. Advani, S.G. and Brusckhe, M.V., 'Governing equations for flow and heat transfer in stationary fiber beds'. *Ibid*, Chapter 12, 465-515
4. Darcy, H.P.G., "*Les fontaines publiques de la ville de Dijon*". Dalmont, Paris, 1856.
5. Kozeny, J., 'Über die kapillare Leitung des Wassers in Boden'. *Sitzungsberichte Akademie der Wissenschaft Wien Math-naturw*, 1927, 136 (Kl.abt.IIa), 271-306.
6. Carman, P.C., 'Fluid flow through a granular bed'. *Trans. Institute of Chemical Engineers*, (London), 1937, 15, 150-166.
7. Blake, F.C., 'The resistance of packing to fluid flow'. *Trans. American Institute of Chemical Engineers*, 1922, 14, 415-421.
8. Williams, J.G., Morris, C.E.M. and Ennis, B.C., 'Liquid flow through aligned fibre beds'. *Polymer Engineering and Science*, 1974, 14(6), 413-419.
9. Summerscales, J., 'A model for the effect of fibre clustering on the flow rate in resin transfer moulding'. *Composites Manufacturing*, 1993, 4(1), 27-31.
10. Thirion, J.M., Girardy, H. and Waldvogel, U., 'New developments in resin transfer moulding of high-performance composite parts'. Materials Information Translations Service Series C: Engineered Materials, *Composites*, (Paris), 1988, 28(3), 81-84.
11. Guild, F.J., Davy, P.J. and Hogg, P.J., 'A model for unidirectional composites in longitudinal tension and compression'. *Composites Science and Technology*, 1989, 36(1), 7-26.
12. Basford, D.M., Griffin, P.R., Grove, S.M. and Summerscales, J., 'Research Report: Relationship between mechanical performance and microstructure in composites fabricated with flow-enhancing fabrics'. *Composites*, 1995, 26(9), 675-679.
13. Guild, F.J. and Summerscales, J., 'Microstructural image analysis applied to fibre composite materials: a review'. *Composites*, 1993, 24(5), 383-394.
14. Summerscales, J., Green, D. and Guild, F.J., 'Effect of processing dwell-time on the microstructure of a fibre-reinforced composite'. *Journal of Microscopy*, 1993, 169(2), 173-182.

15. Griffin, P.R., Grove, S.M., Guild, F.J., Russell, P. and Summerscales, J., 'The effect of microstructure on flow promotion in RTM reinforcement fabrics'. *Journal of Microscopy*, 1995, 177(3), 207-217.
16. Griffin, P.R., Grove, S.M., Russell, P., Short, D., Guild, F.J. and Taylor, E., 'The effect of reinforcement architecture on the long range flow in fibrous reinforcements'. *Composites Manufacturing*, 1995, 6(3/4), 221-235.
17. Summerscales, J., Griffin, P.R., Grove, S.M. and Guild, F.J., 'Quantitative microstructural examination of RTM fabrics designed for enhanced flow'. *Composite Structures*, 1995, 32, 519-529.
18. Guild, F.J., Pearce, N.R.L., Griffin, P.R. and Summerscales, J., 'Optimisation of reinforcement fabrics for the resin transfer moulding of high fibre volume fraction composites'. Proc. 7th European Conference on Composite Materials, London, 14-16 May 1996, 273-278.
19. Pearce, N.R.L., Griffin, P.R., Summerscales, J. and Guild, F.J., 'Optimisation of reinforcement fabrics for the resin transfer moulding of high fibre volume fraction composites'. Proc. 17th International Conference, SAMPE European Chapter, Basel CH, 28-30 May 1996, 225-236.
20. Adams, L., Russel, W.B. and Rebenfeld, L., 'Radial penetration of a viscous fluid into a planar anisotropic porous medium'. *Intl. Journal of Multiphase Flow*, 1988, 14(2), 203-215.
21. Chan, A.W. and Hwang, S. 'Anisotropic in-plane permeability of fabric media'. *Polymer Engineering and Science*, 1991, 13(16), 1233-1239.
22. Carter, E.J., Fell, A.W., Griffin, P.R. and Summerscales, J., 'Data validation procedures for the automated determination of the two-dimensional permeability tensor of a fabric reinforcement'. *Composites Part A: Applied Science and Manufacturing*, 1996, 27A(3), 255-261.
23. Carter, E.J., Fell, A.W. and Summerscales, J., 'A simplified model to calculate the permeability tensor of an anisotropic fibre bed'. *Composites Manufacturing*, 1995, 6(3/4), 228-235.
24. Pearce, N.R.L., Guild, F.J. and Summerscales, J., 'A study of the effects of convergent flow fronts on the properties of fibre-reinforced composites produced by RTM'. Verbal presentation at the 4th International Conference on Flow Processes in Composite Materials, Aberystwyth, September 1996. Composites Part A, in submission.
25. Judd, N.C.W. and Wright, W.W., 'Voids and their effects on the mechanical properties of composites - an appraisal', *SAMPE Journal*, January/February 1978, 14(1), 10-14.
26. Curtis, P.T., 'CRAG test methods for the determination of the engineering properties of fibre reinforced plastics'. Royal Aerospace Establishment Technical Report 88012, February 1988.
27. Carter, E.J., Fell, A.W., Griffin, P.R. and Summerscales, J. 'Final report on Sub-Task 1.2: The apparent permeability of reinforcement fabrics'. University of Plymouth report BE5477/UoP/FR/1.2/A/CC/1.0, January 1996.

28. Hayward, J.S. and Harris, B., 'Effect of process variables on the quality of RTM mouldings'. *SAMPE Journal*, 1990, **26**.
29. Hayward, J.S. and Harris, B., 'The effect of vacuum assistance in Resin Transfer Moulding'. *Composites Manufacturing*, 1990, **1**.
30. Parnas, R.S. and Phelan, F.R., 'The effect of heterogeneous porous media on mould filling in resin transfer moulding' *SAMPE Quarterly*, 1991, Jan, 53-60.
31. Chan, A.W. and Morgan, R.J., 'Modelling preform impregnation and void formation in resin transfer moulding of unidirectional composites'. *SAMPE Quarterly*, 1992, **23**(3), 48-52.
32. Lowe, J.R., Owen, M.J. and Rudd, C.D., 'Void formation in resin transfer moulding'. Proc. ICAC 95, Nottingham, 1995.
33. Williams, J.G., Morris, C.E.M. and Ennis, B.C., 'Liquid flow through aligned fibre beds'. *Polymer Engineering and Science*, 1974, June, 14(6), 413-419.
34. Bayramli, E. and Powell, R.L., 'The normal (transverse) impregnation of liquids into axially oriented fiber bundles'. *Journal of Colloid and Interface Science*, 1990, **138**(2), 346-353.

# A STUDY OF THE EFFECTS OF CONVERGENT FLOW FRONTS ON THE PROPERTIES OF FIBRE REINFORCED COMPOSITES PRODUCED BY RTM

NEIL PEARCE\*, FELICITY GUILD<sup>+</sup> AND JOHN SUMMERSCALES\*

\* School of Manufacturing, Materials and Mechanical Engineering,  
University of Plymouth, Plymouth, Devon PL4 8AA

+ Department of Materials Science and Engineering  
University of Surrey, Guildford, Surrey GU2 5XH

**Abstract:** The processing speed of resin transfer moulding (RTM) can be improved by using multiple injection ports. Out of necessity this results in the convergence of resin flow fronts. Such convergence can result in the entrapment of voids within the composite leading to a degradation of mechanical properties. A series of carbon/epoxy plates of differing weave styles were manufactured by RTM in a transparent mould with porting arrangements designed to cause resin flows to converge. The plates were analysed to determine the effect of injection strategy, injection temperature and differences in weave style. Analysis was performed by qualitative ultrasound scanning, quantitative image analysis and interlaminar shear strength testing. It has been shown that there is a marked increase in voidage in the areas where flows meet and this is correlated to a deterioration of mechanical properties.

## INTRODUCTION

Resin transfer moulding (RTM) involves the long range flow of resin through a fibre preform within a closed mould. The fibre volume fraction of the preform dictates both the rate at which the resin can fill the mould and also the mechanical performance of the resulting composite material. At higher fibre volume fractions (>50%), as is the case with high performance composites, there is a significant decrease in the permeability of the preform and hence reduced flow rates. In order to improve production times multi-port moulds can be used where resin is injected at a number of locations. This decreases the processing time but depending on the injection strategy can result in the convergence of resin flows and an increased expectancy of air entrapment and therefore voidage within the material.

Prior to investigating the influence of convergent flow on voidage, it is first necessary to understand the mechanisms with which voids form during non-convergent flow, and the ways in which this can be minimised. It is also necessary to note the influence of void content and void distribution on the properties of composite materials.

### Void Formation

The void content within a composite material produced by RTM will depend on the void content of the resin prior to injection and the extent of void formation and growth during mould filling and cure. Lundstrom et al<sup>1</sup> have shown that void formation during mould filling is most prevalent at the flow front and the void content is significantly higher in this area. This can be caused by obstructions to flow such as stitching in non crimp fabric, or globules of thermoplastic binder or size resulting in mechanical entrapment. Mechanical entrapment can also occur due to fingering<sup>2-8</sup> of the resin at the flow front.



Fingering occurs where the localised wetting flow is uneven due to differences in permeability between the fibre tows and the surrounding porespace. Capillary flow will occur within the tows and channel flow will occur within the porespace. Depending on injection pressure one flow is likely to lead the other. At low pressures (below those commonly used in RTM) capillary flow will lead, whilst at higher pressures (those typical to RTM) channel flow will lead. When the resin in the porespace leads that within the tows, complex transverse microflows occur, wicking resin from the porespace into the tows ahead of the capillary flow. This action forms voids within the tows. Further capillary flow causes the volume of the voids to reduce, increasing their internal pressure until equilibrium is reached.

Once a void has formed its volume can change due to the following effects<sup>9</sup>:

- a) Changes in vapour mass (solvents, condensation products) and the vapour transfer across the void/material interface.
- b) Pressure changes inside the void due to temperature and pressure changes in the material.
- c) Thermal expansion due to temperature gradients in the resin.

Models which take into account the first two of these effects, vapour transport and changes in temperature/pressure have been developed by Loos and Springer<sup>10,11</sup> and by Kardos et al<sup>12-14</sup>.

Voids can also form on curing of thermosetting resins by the reactions of residual solvent, catalyst, resin, binder or size, causing homogeneous or heterogeneous nucleation and growth throughout the material. However, this influence on void content is small in comparison to that of gas/vapour entrapment during flow.

#### **Effect of Vacuum on Void Formation**

Regardless of the type of reinforcement or resin and its viscosity, the void content of composites produced by RTM can be significantly reduced by the application of vacuum to the mould during injection<sup>2,3</sup>. For voids already present in the resin this influence can be simply explained by the increase in pressure gradient across the mould reducing void radius, therefore giving greater mobility<sup>1</sup>.

With the case of voids being formed at the flow front by mechanical entrapment, the fingering mechanism has been modelled<sup>15-17</sup>. It has been shown that if vacuum is applied in the porespace ahead of the flow, the voids formed will eventually collapse<sup>16</sup> as they will have no internal pressure to support them. It follows that voids will still occur by this mechanism unless full vacuum can be applied<sup>6</sup>.

Vacuum can have a beneficial influence on void content only if the mould is vacuum tight<sup>1</sup>. If this is not ensured, air will be drawn into the resin in the flow region that is below atmospheric pressure and the void content will be increased.

Vacuum can also have a deleterious effect with vinyl ester and unsaturated polyester resin systems causing voids to form, commonly attributed to the boiling of styrene within a heated mould<sup>6</sup>. However, Lundstrom et al<sup>1</sup> noted that pure styrene boils at 40°C at 90% vacuum, and 140°C at atmospheric pressure. Therefore in many practical instances of RTM this will not cause a problem.

## **Effects of Voids**

The presence of voids within fibre reinforced composites can adversely affect the materials appearance<sup>18</sup>, properties<sup>19-23</sup> and performance<sup>24</sup>. An extensive review of the effect of voids on mechanical performance was carried out by Judd and Wright<sup>19</sup>. They compiled the findings of 47 papers and indicated that voids reduce the following properties; interlaminar shear strength (ILSS), longitudinal and transverse flexural modulus, longitudinal and transverse tensile strength and modulus, compressive strength and modulus, fatigue resistance and high temperature resistance. It has also been shown that the dielectric strength of composites is reduced with increasing void content<sup>20</sup>.

Judd and Wright<sup>19</sup> reported that the first one percent of voidage can result in a decrease in strength of up to 30% in bending, 3% in tension, 9% in torsional shear, and 8% impact. They also noted that regardless of resin type, fibre type and fibre surface treatment that the ILSS of a composite will be reduced by approximately 7% for each 1% of voids up to a total void content of about 4%.

The relationship between voidage and ILSS has since been investigated by others. Ghiorse<sup>21</sup> found that for carbon fibre/epoxy composites each 1% of voids up to 5% decreased the flexural modulus by 5% and the flexural strength and ILSS by 10%. Bowles and Frimpong<sup>22</sup> found a 20% decrease at 5% voidage for a unidirectional carbon fibre composite (AS4/PMR-15).

As well as the effects noted above voids can also affect the long term performance of fibre reinforced composites by increasing moisture absorption resulting in a degradation of the fibre/matrix interface<sup>23</sup>. However it should be noted that voids are not always unwanted as they can improve some properties such as tensile strain to failure<sup>24</sup>. It may also be possible to predict failure in the case of high void content materials<sup>25</sup> as the Poisson ratio approaches zero at this point.

Stone and Clarke<sup>26</sup> correlated ultrasonic attenuation measurements on constant thickness panels of unidirectional CFRP with void content. A simple bilinear relationship was postulated. At low void content (less than 1.5%) the shape of voids tend to be spherical with a diameter of 5-20 $\mu$ m. At higher contents, the voids are cylindrical, their length being up to an order of magnitude more than the diameter quoted above and oriented parallel to the fibre axis.

The presence of voids in a composite can clearly have a marked detrimental influence, especially on matrix dominated failure modes such as bending and torsional shear. The level of voidage will determine the amount of reduction in properties compared with those predicted for a void free material. Furthermore the distribution of the voids will have a great effect on performance, as properties will be reduced locally to areas of higher voidage.

Problems associated with poor void distribution are believed to be more likely in the case of convergent flow. It is feasible that when two or more flow fronts meet, their driving pressures will cancel each other (either partly or wholly), causing flow to diminish or cease. The voids previously created by mechanical entrapment at the fronts will then remain in that region causing an area of high void content. This problem is also expected to be exacerbated by further void formation when the uneven, fingering flow fronts meet, creating isolated unwetted pockets.

A series of experiments have been conducted as part of a BRITE EurAM II project (BE5477) investigating flow behaviour inside moulds where flow fronts converged due to multiport injection. The experiments provided digitised video images for the validation of process simulation software. The resulting carbon fibre/epoxy resin plates were subsequently 'inherited' by an EPSRC research project and analysed to investigate the effect of flow convergence on mechanical properties.

## EXPERIMENTAL

### Experimental apparatus for flow experiments

The mould used for the multiport experiments had a flat aluminium base (500 mm x 500 mm x 50 mm), with nine universal inlet/outlet ports: at the centre, four corners and four mid-side points of a 400 mm x 400 mm square concentric to the base. The upper surface of the mould was two 10 mm thick glass cover plates, which allowed the progress of the resin to be monitored during the experiments. The mould cavity was created by means of ground flat steel stock spacers which were placed around the periphery of the base plate, raising the glass a known (and variable) distance above it. Vacuum integrity was provided by a rectangular section rubber seal positioned adjacent to the spacers. The glass was held in position by three steel clamps per edge, also located about the periphery.

Injection at elevated temperature was possible by heating elements attached to the underside of the aluminium base with temperature control provided by a PID controller. Constant pressure injection was used with the resin dispensed from a regulated pressure chamber.

During injection the flow front isochrones were monitored using a Minitron camera fitted with a Computar V1218 12.5 mm f1.8 C-mount lens (Optimum Vision Limited, Petersfield). The camera was mounted 1000 mm above the centre of the glass plate on a welded steel support frame. Illumination was provided by three 500W floodlights mounted to either side and behind the apparatus. The light was diffused by white fluted plastic sheets attached to the support frame.

The video signal was recorded as a series of grey-scale digital images using a Synapse video frame grabber and C\_Images software (Foster Findlay Associates, Newcastle-upon-Tyne). The frame grabber has a resolution of 768 x 512 pixels and thus can resolve lengths to less than 1 mm when focused on the full square flow region of 400 mm edge length (i.e. the error is of the order of  $\pm 1$  pixel or  $\pm 1$  mm). This is better than the resolution achievable when tracing the flow front isochrone onto an acetate sheet given the thickness of the drawn line, the time taken to trace the full flow front and the potential for parallax errors when working from an edge of the apparatus.

### Multiport experiments

A series of flow experiments were conducted at two mould temperatures; ambient and 65°C. Three fabrics were used: a twill, a 5 harness satin and a 5 harness satin Injectex, (Figures 1, 2 and 3). Three different multiport configurations were examined (Figures 4, 5 and 6).

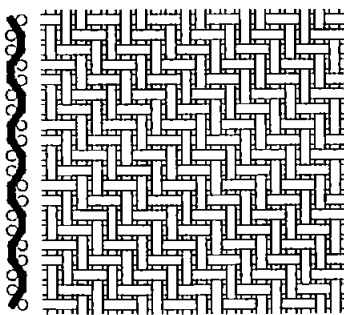


Figure 1 Schematic of 2x2 twill weave

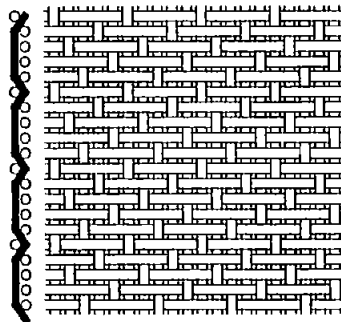


Figure 2 Schematic of 5-harness satin weave

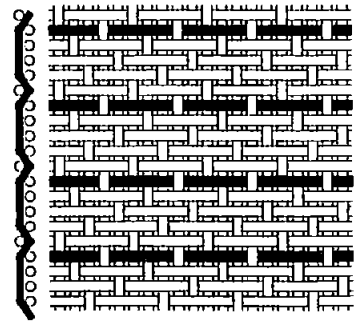
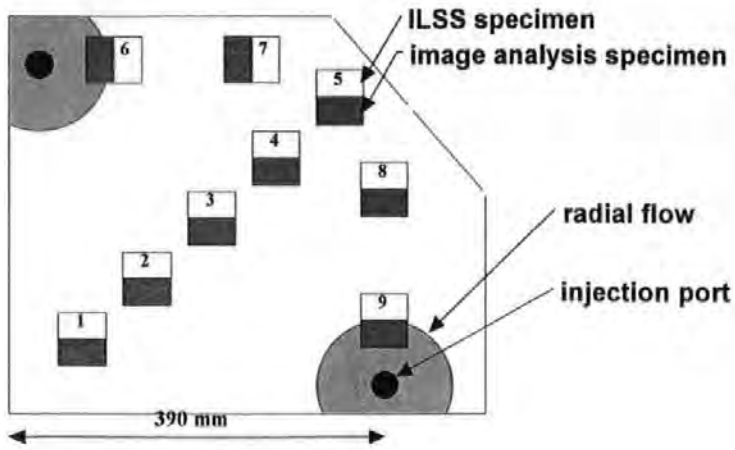
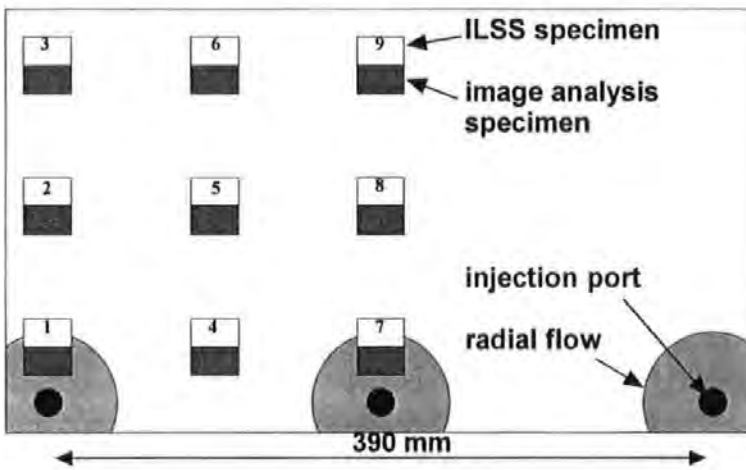


Figure 3 Schematic of 5-harness satin Injectex weave



**Figure 4 Injection at mid-side ports on two adjacent edges**



**Figure 5 Injection at three points along one edge**

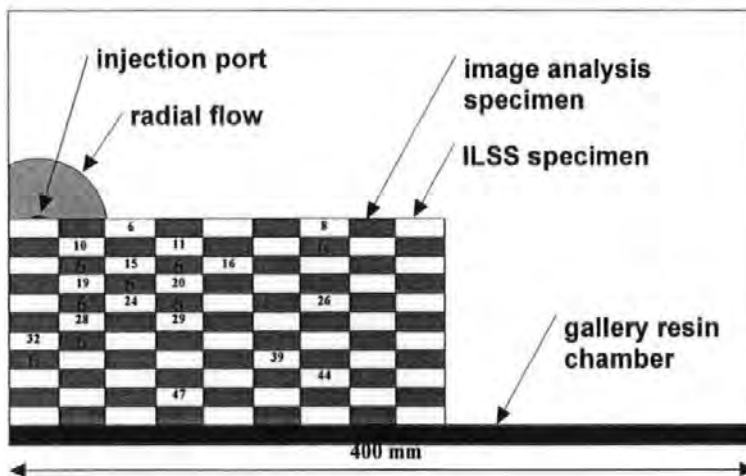


**Figure 6 Injection via a gallery along one edge and one mid-side port**

Figures 1-3 show the differences between the weave styles and indicate the tortuosity of the path the tows take through the fabric. The Injectex fabric has the same weave style as the satin but a modified architecture to improve its permeability. One in five tows are bound, (as shaded in Figure 3) this maintains the size of porespace around these tows when stacked with other layers within a mould.

The three fabrics were chosen as they provided factors which were deemed useful for facilitating comparisons:

- Their permeabilities had previously been characterised as part of the BRITE Euram project.
- All three fabrics had the same areal weight (283 gsm) and would provide the same fibre volume fraction for a given number of laminae with a given mould cavity thickness.
- All three fabrics were produced from the same batch of carbon fibre and had been processed in the same manner.
- The Injectex fabric is known to have an improved permeability over the satin but is expected to generate more voids due to increased fingering.

The experimental parameters are outlined in Table 1. The fabric lay-ups were all preformed to allow more accurate edges to be produced. To prevent edge effects dominating the flow, a 20 mm wide strip of 5-harness satin fabric was placed in two additional layers around the periphery of the fibre pack. The rubber sealing strip was used as a deformable barrier which, when compressed, moulded itself to the shape of the preform edge. A mould cavity of 3 mm depth was used for all the experiments giving a fibre volume fraction of 54%.

**Table 1 Experimental Parameters**

<i>Fabric</i>	<i>No. Layers</i>	<i>Fibre Vf (%)</i>	<i>Mould.temp</i>	<i>Atm.press (mbar)</i>	<i>Inj.press (bar)</i>
<i>Two ports on adjacent edges</i>					
<i>Twill</i>	10	54	21	1012.0	2
<i>Twill</i>	10	54	65	1021.8	2
<i>Satin</i>	10	54	17	1023.6	2
<i>Satin</i>	10	54	65	1031.4	2
<i>Injectex</i>	10	54	18	1021.8	2
<i>Injectex</i>	10	54	65	1022.4	2
<i>Three ports on one edge</i>					
<i>Twill</i>	10	54	23	997.9	2
<i>Twill</i>	10	54	65	988.3	2
<i>Satin</i>	10	54	ambient	997.7	2
<i>Satin</i>	10	54	65	1022.1	2
<i>Injectex</i>	10	54	ambient	1012.8	2
<i>Injectex</i>	10	54	65	1025.9	2
<i>Line gallery and edge port</i>					
<i>Twill</i>	10	54	28	1012.0	2
<i>Twill</i>	10	54	65	1016.2	2
<i>Satin</i>	10	54	22	1017.6	2
<i>Satin</i>	10	54	65	1027.2	2
<i>Injectex</i>	10	54	ambient	1019.9	2
<i>Injectex</i>	10	54	65	1026.9	2

The epoxy resin system (Ciba Composites LY564-1/HY2954) was mixed as detailed in the Ciba process sheet reference K6b (dated April 1991) in the ratio base-resin:hardener 100:35 parts by weight. In all experiments an injection pressure of 2 bar gauge was used at the pressure chamber and a rough vacuum (less than 10mbar: the resolution of the gauge) drawn at the outlet ports. Resin was supplied to the (heated) mould through 1.5 m long tubes at ambient temperature.

**Non-destructive evaluation using ultrasound C-scan equipment**

The ultrasound NDT C-scans were acquired on a 1989 Physical Acoustics Limited Ultrapac water-immersion system with a 5 MHz transducer powered by an Accutron 1010 pulser/receiver (serial number UPKEPR106) controlled by an Everex 286/16 PC (serial number 16E01-903-10702). The system parameters are given in Table 2.

The tank is 470 mm square and 305 mm deep. The mounting of the transducer does not permit acquisition of images from the whole area of the tank. This limits the scan area to 292 mm wide. The second dimension was limited to 178 mm or 216 mm as the acquisition time for the larger size is approximately 3 hours.

**Table 2 Parameters used for ultrasound C-scanning**

<i>Ultrapac/Everex</i>		<i>Pulser</i>	
Scan width (inches)	11.5	Rep rate	2
Scan depth (inches)	8.5	Energy	3
Step size (inches)	0.1	Attenuation (dB)	0+6
Delay (ms)	11.5	Gain (dB)	40
Gate (ms)	4	Damping	10
Parameters	M20-18MY	Switch	1

**Sectioning of plates for interlaminar shear strength (ILSS) and microscopical testing**

CRAG Specification 100<sup>27</sup> was chosen to determine the interlaminar shear strengths (ILSS) of the plates. The size of ILSS specimens being dependent on plate thickness: for the 3 mm thick plates, the specimens were 25 mm x 15 mm.

The minimum size of the microscopy specimens was constrained by the repeat cell size of the fabrics: that of the spacing between tows with identical positioning within the fabric architecture. It was necessary to meet or exceed this minimum to ensure that each microscopy specimen was truly representative of the material. The repeat sizes for the fabrics were measured and are reported in Table 3.

**Table 3 Unit cell sizes for the fabrics**

<i>Fabric</i>	<i>Repeat size (mm)</i>
Twill	12
Satin	7
Injectex	7

The maximum repeat distance was 12 mm, measured from the twill fabric. The dimensions of the microscopy specimens were made equal to those of the ILSS specimens (25 mm x 15 mm). This ensured at least twenty repeat cells per specimen (2 cells per layer x 10 layers) and made the sectioning process easier.

One plate from each of the three porting configurations was marked out to provide pairs of ILSS and microscopical test specimens along direct flow lines and along ‘knit’ lines produced by convergent flows. (Figures 4-6). These specimen locations were then mapped on to the remaining plates such that specimen locations were identical for all of the plates with similar porting configurations. The position at which flow fronts met did not coincide exactly between experiments. However, the specimen size was greater than the absolute point of convergence: a consistent plate position was sampled. The sink marks left by the ports on the injection face of the plates were used as datum points for the measurements.

The ILSS and microscopy specimens were marked out adjacent to one another to facilitate comparison. The edge of the microscopy specimen lying next to the ILSS specimen was identified so that this edge could be polished. It was assumed that the voidage would be similar in adjacent microscopical and ILSS samples for the purpose of the subsequent analysis.

The specimens were cut using a Tyslide diamond slitting saw (serial number MB1116) fitted with a specially constructed attachment designed to ensure repeatability of specimen dimensions. The edges of the specimens were found to be flat and smooth and required no further machining, therefore allowing the specimens to be cut to net size.

**ILSS testing**

The thickness and width of each specimen was measured using a Mitutoyo digital micrometer (serial number 293-766) with a resolution of 0.001 mm. The measurements were stored in a Microsoft Excel 5.0 spreadsheet.

ILSS testing was performed to CRAG specification 100 using an Instron 1175 Universal Testing Machine (serial number HO525) fitted with a 10 KN load cell (serial number UK833). Control of the Instron and data acquisition were achieved using a Strawberry Tree parallel port data acquisition system and 486DX100 PC. Load cell output voltage was automatically converted to force in Newtons and logged against time at a rate of 10 Hz. The data acquired from each specimen test was saved to disk for subsequent processing in the Excel spreadsheet.

**Preparation of specimens for optical microscopy**

Specimens were individually potted in polyester resin (Strand Resin A). They were then prepared using a Buehler 2000 Metpol Grinder/Polisher with Metlap Fluid Dispenser. All specimens were prepared following the procedure shown in Table 4.

**Table 4 Microscopical specimen preparation**

step	Platen				Head		time
	surface	abrasive	speed (rpm)	direction	speed (rpm)	force (lbs)	
1	SiC paper	240 grit	150	complementary	120	15	until plane
2	"	400 grit	"	"	"	20	2 min
3	"	600 grit	"	"	"	"	"
4	"	800 grit	"	"	"	"	"
5	nylon cloth	6µm diamond	50	contra	"	30	5 min
6	texmet cloth	1µm diamond	100	complementary	60	"	"
7	mastertex cloth	Al SiO2	50	contra	"	5	2 min



After polishing, the surface breaking voids were filled with a magnesium silicate (talc) powder to enhance the greyscale detection of these features whilst avoiding detection of other voids beneath the surface.

### **Quantitative microstructural analysis**

The microstructural analysis was achieved using a Quantimet 570 image analysis system. Images were acquired using a Kyowa STZ tri-nocular stereo zoom microscope (serial number 850101) and Fujitsu TCZ-230EA low light level black and white video camera (serial number 20006728). The process was performed in a darkened room using incident illumination from a Flexilux 150 HL Universal ring illuminator.

The magnification of the microscope was adjusted to give an on-screen field of view which encompassed the full (3 mm) thickness of a specimen, giving a linear resolution of 4662 nm/pixel. The system was calibrated using a 2 mm reference gauge and checked prior to each testing session.

The Quantimet was programmed to automatically analyse a 2 mm square frame centred within the field. Each specimen was therefore analysed to within 0.5 mm of the plate surfaces. This ensured that plate surface features were not found in the image frame and thus negated any possible problems associated with edge detection. Low pass filtering was used to improve the signal/noise ratio of the image. A minimum area mask of 12 pixels ( $2.596 \times 10^{-4} \text{ mm}^2$ ) was used to eliminate very small features in the image.

Three contiguous frames were automatically analysed for each specimen with manual movement between frames using a purpose-built slide which restricted travel to only one axis aligned parallel to the camera axis. The fields were positioned to be reliably contiguous using an on-screen image alignment reference: a vertical bar of detected features captured from one extremity of a frame and translated by an on-screen distance equivalent to 2 mm in the axis of movement. This acted as a template allowing a 'live' image of the specimen to be realigned.

The microscopical specimens were analysed for total void volume fraction and individual void count with measurements of the corresponding areas, aspect ratios and roundness. The latter two parameters have not been analysed

## **RESULTS AND DISCUSSION**

### **Flow front isochrones**

In the experiments conducted the whole area of the mould cavity was filled with a consistent number of layers of fabric, except where additional strips were laid to prevent easy flow paths between the ports. The fibre volume fraction is thus sensibly constant across the area examined.

Figures 7, 8 and 9 show images just prior to, or at the time of flow front convergence from representative experiments for each of the three injection strategies (injection times are not comparable). Darkened areas show the extent of resin flow, light grey the unwetted fabric. Prior to meeting, the shape of each flow front is that anticipated from previously conducted permeability experiments (*i.e.* circular in isotropic fabrics and elliptical in anisotropic fabrics). At this stage the shape of the isochrones can be predicted by simple line plotting techniques.

Figures 10, 11 and 12 are from the same experiments after the flow fronts have met.

With reference to Figures 7 and 10, the radial fronts met head-on, creating a large isolated pocket due to the constraint imposed by the corner of the mould. Injection was continued until the combined front had passed out of the fabric. Visually the pocket appeared to collapse, made possible by the vacuum. Nonetheless, void content was expected to be higher at the corner, and along a diagonal from the corner. The lowest void contents were expected close to the ports, away from the area of convergence.

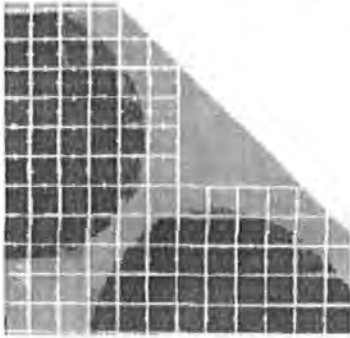


**Figure 7 Injection from two mid-side ports**



**Figure 8 Injection from three ports on one edge**

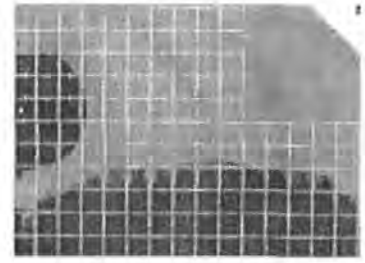


**Figure 9 Injection from a mid-side port and gallery**

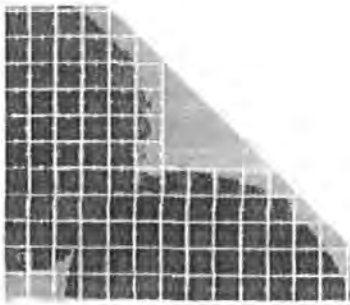


**Figure 10 Flow convergence from two mid-side ports**



**Figure 11 Flow convergence from three ports on one edge**

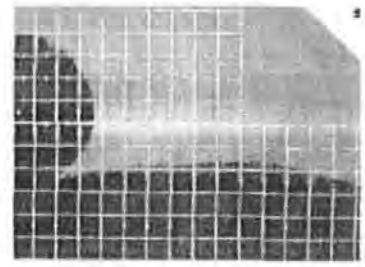


**Figure 12 Flow convergence from mid-side port/gallery**

Figure 8 shows that the flow fronts met at an acute angle at the lower edge of the preform. At this point, void formation by fingering of the resin would be expected to be increased compared with that from a single flow front. Figure 11 shows that the arcs formed by the initial radial flows formed obtuse angles to one another and the resin progressed as one front. Void content was expected to be higher at the mid points between the injection ports and to a lesser extent along the verticals going from the mid points. The lowest void content was expected closest to the ports.

Figures 9 and 12 show a similar convergence to that of Figures 7 and 10, although in this instance an isolated pocket of fabric did not form. Some retardation of flow is evident at the edges due to the higher volume fraction necessary to prevent edge effects dominating in this region. The acute angle between the two flows in Figure 12 would be expected to increase void formation from fingering. Void content was expected to be higher along a diagonal from the mid point between the injection port and the gallery, and lower closest to the injection points.

The anticipated void distribution dictated the locations chosen for the ILSS and microscopy specimens.

### Ultrasound C-scanning

Each plate was scanned in double through-transmission mode. System parameters were set to give comparable contrast for all plates and the same parameters used throughout. No international standards are known and hence calibration is not possible. The system is also subject to minor colour drift during extended periods of testing. The C-scan images are thus only qualitative. Figures 13, 14 and 15 show C-scans of the plates from Figures 7, 8 and 9 above, as an indication of the results obtained.



Figure 13



Figure 14



Figure 15

The greyscale images presented here have been converted from the colour originals. The greyscale level corresponds to the height of the A-scan signal (received voltage amplitude against time from pulse initiation) reflected from a glass plate beneath the composite. The A-scan signal is windowed to analyse only the peak height corresponding to the time of the first reflection from the plate glass. Black indicates the highest attenuation within that window: this may correspond to a thicker section, higher fibre volume fraction, poor fibre/matrix bonding or higher void content. White corresponds to the lowest attenuation within that window.

Figure 13 clearly shows a higher signal attenuation along a diagonal indicating higher voidage where the flow fronts converged. Figure 14 shows a relatively even signal attenuation and therefore a uniform distribution of voids (Note: the black bar toward the lower edge shows a piece of tape used for identification purposes). Figure 15 shows differences in attenuation indicating areas of varying void content, highest attenuation can be seen where the flow fronts met.

### Interlaminar shear strengths

The ILSS of samples taken from the cured plates were measured to CRAG Specification 100<sup>27</sup>. It is difficult to draw any conclusions regarding differences in results between individual specimen locations, as flows did not meet in exactly the same place in each of the experiments. For this reason mean values are reported (Figure 16 and Table 5) for specimens taken from convergent and direct flow areas for each of the experiments.

In every case the ILSS is higher from the direct flow area than the convergent indicating an increased void content where flows met. The inferred increase in void content is calculated based on the ILSS/Void relationship presented by Judd and Wright<sup>19</sup>.

The results also show a definite ascending ranking of ILSS between the weave styles: twill-Injectex-satin. This could be due to the differences in crimp, porespace and the effect of porespace on void formation/distribution.

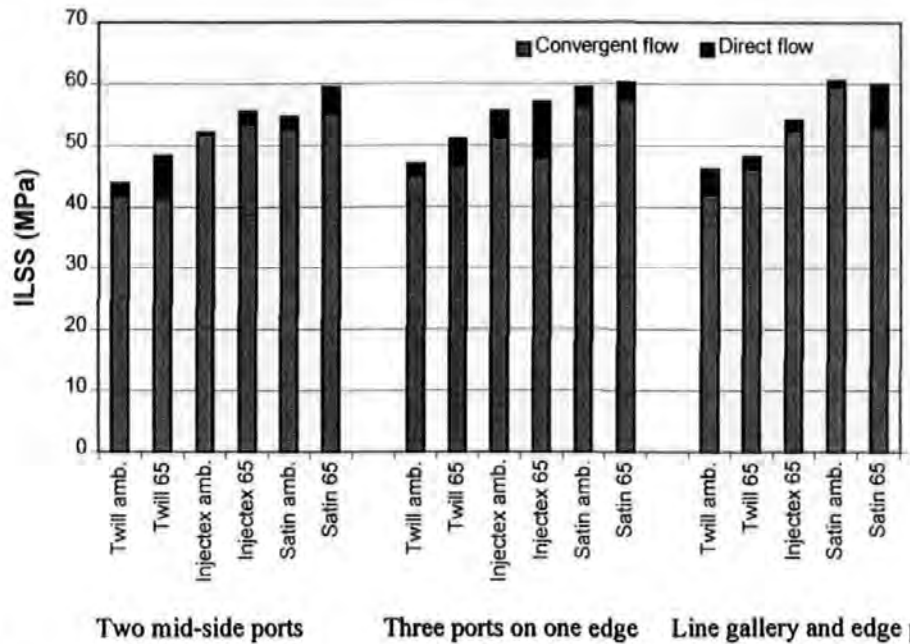


Figure 16 Averaged values of ILSS for specimens from convergent and direct flow areas

Table 5 Summary of Interlaminar Shear Strength (ILSS) results

		<u>Direct flow</u>	<u>Convergent flow</u>	
<i>Two ports on adjacent edges</i>				
		<i>Mean of 4 samples:</i>	<i>Mean of 5 samples:</i>	<i>Inferred</i>
<i>Weave</i>	<i>Inject.temp</i>	<i>6,7,8,9</i>	<i>1,2,3,4,5</i>	<i>void increase</i>
Twill	ambient	43.9	41.8	0.70%
Twill	65 C	48.3	41.4	2.00%
Satin	ambient	54.6	52.6	0.50%
Satin	65 C	59.4	55.1	1.00%
Injectex	ambient	52.1	51.7	0.10%
Injectex	65 C	55.5	53.4	0.50%
<i>Three ports on one edge</i>				
		<i>Mean of 6 samples:</i>	<i>Mean of 3 samples:</i>	<i>Inferred</i>
<i>Weave</i>	<i>Inject.temp</i>	<i>1,2,3,7,8,9</i>	<i>4,5,6</i>	<i>void increase</i>
Twill	ambient	47	45.1	0.60%
Twill	65 C	51	46.7	1.20%
Satin	ambient	59.4	56.2	0.80%
Satin	65 C	60.2	57.2	0.70%
Injectex	ambient	55.5	51.2	1.10%
Injectex	65 C	57.1	47.9	2.30%
<i>Line gallery and edge port</i>				
		<i>Mean of 5 samples:</i>	<i>Mean of 5 samples:</i>	<i>Inferred</i>
<i>Weave</i>	<i>Inject.temp</i>	<i>6,10,26,39,44</i>	<i>16,20,24,28,32</i>	<i>void increase</i>
Twill	ambient	46.2	42.1	1.30%
Twill	65 C	48.2	46.3	0.60%
Satin	ambient	60.6	59.7	0.20%
Satin	65 C	60	53.1	1.60%
Injectex	ambient	n/a	n/a	n/a
Injectex	65 C	54.2	52.5	0.50%

It was difficult to anticipate the influence the higher injection temperature would have. The reduced resin viscosity might exaggerate the fingering mechanism, therefore creating more voids, however, the voids would have a greater mobility due to the reduced viscosity and would be more likely to migrate through the wetted fabric, driven by the pressure gradient. From the results it is not possible to draw a conclusion.

The interlaminar shear strengths for satin and Injectex are compared with those reported by KTH<sup>28</sup> in Table 6. Note that the University of Plymouth (UoP) mean values are calculated as the average of the mean values for each plate/fabric/temperature combination and therefore include the ILSS values taken from positions where flow fronts meet. The KTH plates were produced without convergent flow. It is thus not unexpected that the KTH values are slightly higher.

**Table 6 Comparison of ILSS mean values reported by UoP and KTH**

Fabric	ILSS (MPa)		
	UoP	KTH	UoP/KTH
Satin	57.6	58.8	98%
Injectex	53.0	55.7	95%

**Quantitative microscopy for void content**

No conclusions can be drawn comparing the void volume fractions measured at specific locations. Flows did not meet in exactly the same place, therefore causing variations between notionally similar experiments. As with the ILSS results, mean values are reported from areas believed to represent convergent and non convergent flows (see Figure 20 and Table 7).

Figure 20 shows that the averaged void volume fractions measured from convergent flow areas are higher than all but two of those from direct flow areas. This is in agreement with the ILSS results indicating higher void content with convergent flow. However there is no consistent variation between fabrics as is the case with the averaged ILSS results. This can be explained as ILSS is not only dependent on void content but also the architecture of the weave and its influence on crimp and porespace. As the variation of ILSS between fabrics is so distinct, it follows that differences in fabric architecture may have a far greater effect on ILSS than the effect of variation in void content.

Figures 17, 18 and 19 show the variation of porespace (black and white areas) for the three fabrics (frame sizes consistent at 2 mm x 1.15 mm). The white areas are voids which lie in the plane of the image and have been filled with magnesium silicate to enhance detection. Figure 19 clearly shows the constrained tows of the satin Injectex fabric and the increase in size of porespace and voids compared with the satin in Figure 18.



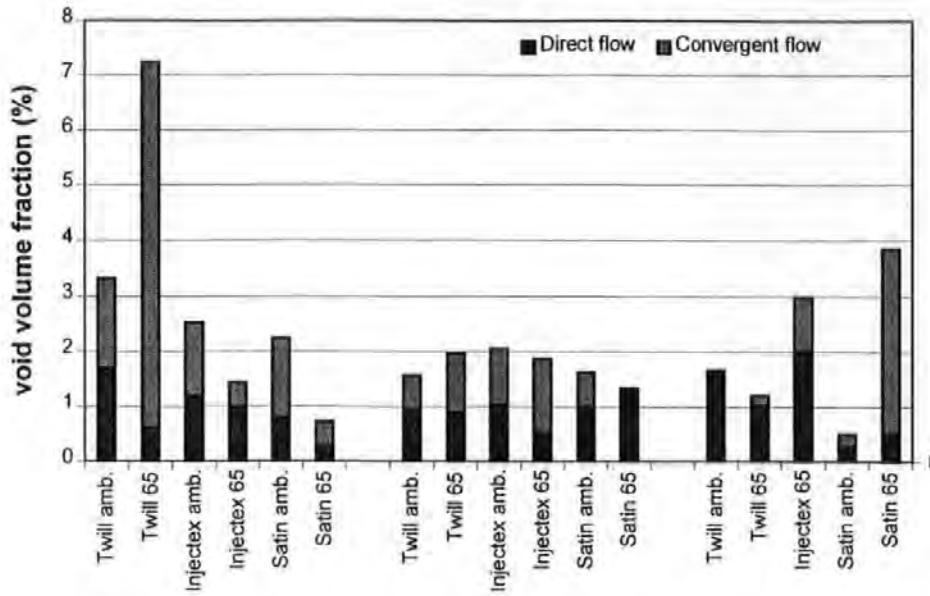
**Figure 17 Micrograph of twill fabric**



**Figure 18 Micrograph of satin fabric**



**Figure 19 micrograph of satin Injectex fabric**



Two mid-side ports      Three ports on one edge      Line gallery and edge port

Figure 20 Averaged void volume fractions for specimens from convergent and direct flow areas

Table 7 Summary of results for void volume fraction (%)

		<i>Direct flow</i>	<i>Convergent flow</i>
<i>Two ports on adjacent edges</i>			
		<i>Mean of 4 samples:</i>	<i>Mean of 5 samples:</i>
<i>Weave</i>	<i>Inject.temp</i>	<i>6,7,8,9</i>	<i>1,2,3,4,5</i>
Twill	ambient	1.70	3.32
Twill	65 C	0.61	7.23
Satin	ambient	0.81	2.25
Satin	65 C	0.28	0.73
Injectex	ambient	1.20	2.53
Injectex	65 C	0.98	1.44
<i>Three ports on one edge</i>			
		<i>Mean of 6 samples:</i>	<i>Mean of 3 samples:</i>
<i>Weave</i>	<i>Inject.temp</i>	<i>1,2,3,7,8,9</i>	<i>4,5,6</i>
Twill	ambient	0.95	1.57
Twill	65 C	0.90	1.97
Satin	ambient	0.99	1.62
Satin	65 C	1.34	0.66
Injectex	ambient	1.04	2.05
Injectex	65 C	0.54	1.88
<i>Line gallery and edge port</i>			
		<i>Mean of 5 samples:</i>	<i>Mean of 5 samples:</i>
<i>Weave</i>	<i>Inject.temp</i>	<i>6,10,26,39,44</i>	<i>16,20,24,28,32</i>
Twill	ambient	1.66	1.45
Twill	65 C	1.01	1.21
Satin	ambient	0.28	0.50
Satin	65 C	0.51	3.86
Injectex	ambient	n/a	n/a
Injectex	65 C	2.02	2.98

As an indication of the influence of injection strategy Table 8 shows fabric type and specimen location for the highest void volume fractions measured. Note that all of the values were measured from specimens taken from convergent flow areas.

**Table 8 Magnitude (%), fabric and specimen location of the highest void volume fractions measured**

Injection strategy	Highest	Second highest	Third highest
Two ports on adjacent edges	13.2 twill 1	8.4 twill 4	8.0 twill 2
Three ports on one edge	6.8 twill 4	4.8 Injectex 4	3.4 Injectex 4
Line gallery and edge port	5.0 satin 16	4.6 twill 19	4.4 satin 32

**Comparison of ILSS and Quantitative microscopy results**

It was assumed that the void volume fraction would be similar in adjacent ILSS and microscopy samples. The cutting of the respective samples inevitably resulted in a loss of up to 1 mm of material between the samples due to the width of the diamond saw blade and the polishing processes. The void content was derived from a planar measurement. The resulting volume fraction would therefore be dependent on the size and distribution of the voids. If the void distribution was irregular, an areal measurement could not be truly representative of the volume of material the specimen was taken from. Therefore, the assumption stated above will only be valid where there is a uniform distribution of voids, and must be called into question when isolated large voids are detected.

Nevertheless, in a number of cases there is a close correlation between the ILSS and voidage measurements at the same specimen locations (for example see Figure 21).

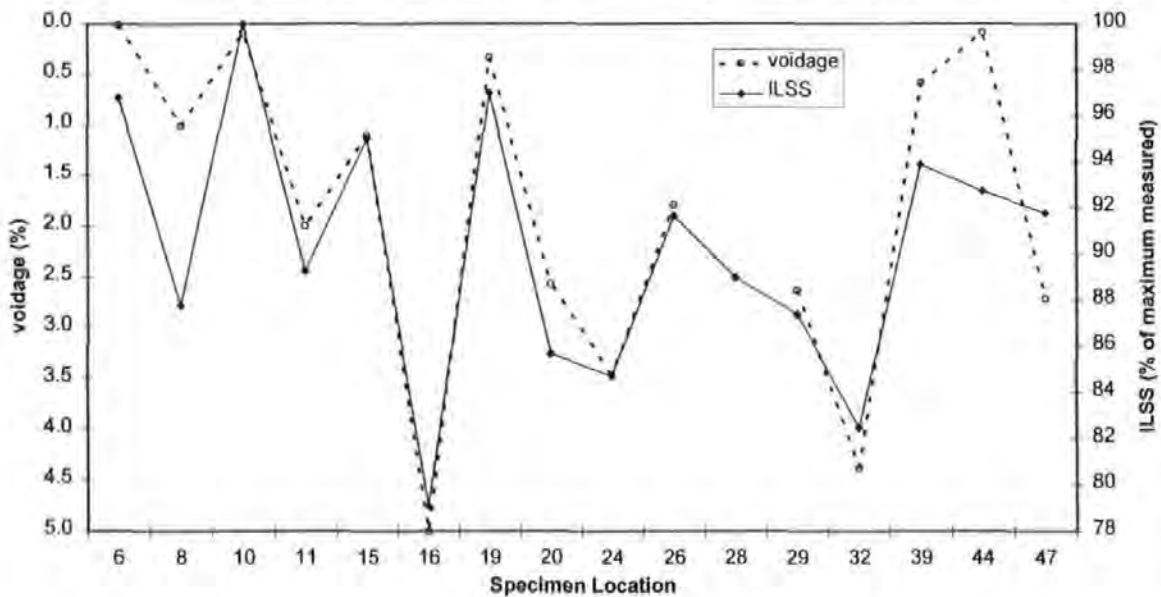


**Figure 21 Measured voidage / Normalised ILSS. Line and edge port injection. 5-Harness satin 65°C**

## SUMMARY

Prior to convergence, flow fronts act independently and in a manner which can be predicted, based on previously conducted permeability experiments.

The angle and location at which flows meet relative to mould edges affects the way in which they interact:

When flow fronts meet at a mould edge they merge and act as a single front.

When flow fronts meet head-on there will be increased voidage along the knit line and at any adjacent corners. Voids formed in the this manner may retain their position during subsequent flow due to the cancelling of driving pressures.

C-scan results can provide a useful indication of void distribution. However, in the absence of reference materials, they can only show relative quality, not known levels of voidage.

Void volume fractions were higher from areas of convergent flow and ILSS results consistently lower, indicating the adverse influence of flow convergence.

The injection strategy with two ports on adjacent edges resulted in the highest detected void volume fractions.

All of the experiments were conducted with vacuum drawn in the mould cavity. Without the positive influence of vacuum, the void volume fractions would be expected to be higher.

A good correlation can be found between ILSS and void volume fraction results taken from adjacent specimens, although this is highly dependent on void distribution.

The three fabrics tested show a clear ranking in terms of ILSS. This ranking is believed to be primarily due to the influence of fabric architecture on crimp, and porespace size and distribution.

There is a conflict between ILSS and processing requirements (see Table 9) based on previously determined values of permeability:

**Table 9 Generalised comparison of ILSS and Permeability results for the three fabrics**

<i>Weave</i>	<i>ILSS</i>	<i>Permeability</i>
Satin	highest	lowest
Injectex	intermediate	intermediate
Twill	lowest	highest

Finally, it is worth noting that multiport injection strategies are possible in which flows do not converge<sup>29</sup>. Resin can be introduced sequentially into a mould from injection ports which have been passed by the global flow front. This will maintain the pressure gradient between the active injection port and the flow front, and hence increase flow rate.



## ACKNOWLEDGEMENTS

This work was conducted within EU BRITE / EurAM II grant BRE2/CT92/0227 (Proposal BE 5477). The permission of the Partners (listed below) to submit for publication is gratefully acknowledged: British Aerospace Airbus Limited, (UK), Brochier SA (now Hexcel Composites, France), Inasco Hellas (GR), Inasmet (ES), Intracom SA (GR), Royal Institute of Technology (SW), Short Brothers plc (NI), SICOMP (SW), Sonaca SA (BE) and TNO Institute for Industrial Technology (NL). NRLP is supported by EPSRC grant GR/K04699 and EPSRC grant GR/J77405 enables the collaboration of FJG.

## REFERENCES

1. Lundstrom, T.S., Gebart, B.R. and Lundemo, C.Y., 'Void formation in RTM'. Proc. SPI Composite Institutes 47th Annual Conference, Cincinnati, 1992.
2. Hayward, J.S. and Harris, B., 'Effect of process variables on the quality of RTM mouldings'. *SAMPE Journal*, 1990, 26.
3. Hayward, J.S. and Harris, B., 'The effect of vacuum assistance in Resin Transfer Moulding'. *Composites Manufacturing*, 1990, 1.
4. Parnas, R.S. and Phelan, F.R., 'The effect of heterogeneous porous media on mould filling in resin transfer moulding' *SAMPE Quarterly*, 1991, Jan, 53-60.
5. Chan, A.W. and Morgan, R.J., 'Modelling preform impregnation and void formation in resin transfer moulding of unidirectional composites'. *SAMPE Quarterly*, 1992, 23(3), 48-52.
6. Lowe, J.R., Owen, M.J. and Rudd, C.D., 'Void formation in resin transfer moulding'. Proc. ICAC 95, Nottingham, 1995.
7. Williams, J.G., Morris, C.E.M. and Ennis, B.C., 'Liquid flow through aligned fibre beds'. *Polymer Engineering and Science*, 1974, June, 14(6), 413-419.
8. Bayramli, E. and Powell, R.L., 'The normal (transverse) impregnation of liquids into axially oriented fiber bundles'. *Journal of Colloid and Interface Science*, 1990, 138(2), 346-353.
9. Summerscales, J., 'Manufacturing defects in fibre-reinforced plastic composites'. *Insight* 1994, 36(12), 936-942.
10. Springer, G.S., 'A model of the curing process of epoxy matrix composites'. Proc. ICCM 4, Tokyo, October 1982, Vol. 1, 23-35.
11. Loos, A.C. and Springer, G.S., 'Curing of epoxy matrix composites'. *Journal of composite materials*, 1983, 17(2), 135-169.
12. Kardos, J.L., Dudukovic, M.P., McKague, E.L. and Lehman, M.W. 'Void formation and transport during composite laminate processing'. ASTM STP 797, 1983, 96-109.
13. Kardos, J.L., Dave, R. and Dudukovic, M.P., 'Void growth and resin transport during processing of thermosetting matrix composites'. *Advances in Polymer Science*, 1986, 80(4), 101-123.

14. Kardos, J.L., Dave, R. and Dudukovic, M.P., 'Voids in composites'. *Manufacturing International*, 1988, (IV), 41-48. *Proc. Manufacturing Science of Composites*, ASME, Atlanta, April 1988.
15. Patel, N. and Lee, L.J., 'Effect of capillary pressure on mold filling and fibre wetting in liquid composite molding'. *Proc. ASM/ESD 10th Annual Advanced Composite Conference*, Dearborn, MI, USA, 1994, 7-10 Nov., 325-333.
16. Chan, A.W. and Morgan, R.J., 'Tow impregnation during resin transfer molding of bi-directional nonwoven fabrics'. *Polymer Composites*, 1993, **14**(4), 335-340.
17. Parnas, R.S. Salem, A.J., Sadiq, T.A.K., Wang, H.P. and Advani, S.G., 'The interaction between microscopic and macroscopic flow in RTM preforms'. *Composite Structures*, 1994, **27**(1-2), 93-107.
18. Yamada, H., Mihata, I., Tomiyama, T. and Walsh, S.P., 'Investigation of the fundamental causes of pinholes in SMC mouldings', *Proc. SPI Composite Institutes 47th Annual Conference*, Cincinnati, 1992.
19. Judd, N.C.W. and Wright, W.W., 'Voids and their effects on the mechanical properties of composites - an appraisal', *SAMPE Journal*, January/February 1978, **14**(1), 10-14.
20. Paul, J.T. and Thomson, J.B., 'The importance of voids in the filament wound structure', *Proc. SPI Composite Institutes 20th Annual Conference*, Illinois, 1965.
21. Ghiorse, S.R., 'Effect of void content on the mechanical properties of carbon/epoxy laminates', *SAMPE Quarterly*, January 1993, **24**(2), 54-59.
22. Bowles, K.J. and Frimpong, S., 'Void effects on the interlaminar shear strength of unidirectional graphite fiber-reinforced composites', *Journal of Composite Materials*, 1992, **26**, 1487-1509.
23. Sheno, R.A. and Wellicome, J.F., 'Composite materials in marine structures, Vol. 1, Fundamental Aspects', Cambridge University Press, 1993.
24. Varna, J., Joffe, R., Berglund, L.A. and Lundstrom, T.S., 'Effect of voids on failure mechanisms in RTM laminates'. *Composite Science and Technology*, 1995, **53**, 241-249.
25. Summerscales, J. and Fry, S.A., 'Poisson's ratio in fibre-reinforced polymer composites with a high void content'. *Journal of Materials Science Letters*, 1994, **13**(12), 912-914.
26. Stone, D.E.W. and Clarke, B., 'Ultrasonic attenuation as a measure of void content in carbon-fibre reinforced plastics'. *Non-Destructive Testing*, 1975, **8**(3), 137-145.
27. Curtis, P.T., 'CRAG test methods for the determination of the engineering properties of fibre reinforced plastics'. Royal Aerospace Establishment Technical Report 88012, February 1988.
28. Private communication. Kungl Tekniska Hogskolan, (Royal Inst. Of Technology) Stockholm, Sweden.
29. Chan, A.W. and Morgan, R.J., 'Sequential multiple port injection for resin transfer moulding of polymer composites'. *SAMPE Quarterly*, 1992, **24**(1), 45-49.

# **THE USE OF AUTOMATED IMAGE ANALYSIS FOR THE INVESTIGATION OF FABRIC ARCHITECTURE ON THE PROCESSING AND PROPERTIES OF FIBRE REINFORCED COMPOSITES PRODUCED BY RTM**

N R L Pearce<sup>\*</sup>, F J Guild<sup>+</sup> and J Summerscales<sup>\*</sup>

<sup>\*</sup> School of Manufacturing, Materials and Mechanical Engineering,  
University of Plymouth, Plymouth, Devon PL4 8AA

<sup>+</sup> Department of Mechanical Engineering,  
Bristol University, Bristol, BS8 1TR

**Abstract:** The use of resin transfer moulding (RTM) as an economic means of producing high performance fibre-reinforced composites is critically limited by the permeability of the fabrics employed. Commercial fabrics are available where the architecture of their reinforcement is designed to cluster the fibres, giving higher permeabilities than conventional fabrics. This has been shown to improve processing times but there is evidence that such clustering is detrimental to mechanical performance.

The objective of this work was to relate variations in permeability, mechanical performance and microstructure. This was achieved by producing carbon/epoxy plates of differing weave styles by RTM in a transparent mould. Permeabilities were calculated. Interlaminar shear, tensile and compressive tests were performed and fractal analysis was carried out to obtain fractal dimensions for the three fabrics. Variations in permeabilities and mechanical properties can be related to observed differences in the microstructure.

## **INTRODUCTION**

Resin transfer moulding (RTM) is a process for producing polymer-matrix composites. A preform of dry reinforcement fibres is placed into a mould. The mould is closed and resin injected. Once cured, the near net-shape component is removed. RTM differs from other composite manufacturing processes as it involves long-range flow of resin through porespace surrounding the reinforcement fibres.

Darcy (1) found that the flow rate of a fluid through a porous medium was proportional to the pressure drop and inversely proportional to the bed length. The coefficient of proportionality is known as the permeability and must be either measured or predicted. Kozeny (2) and Carman (3) related the flow rate to the microstructure of the medium using the Blake concept (4) of the hydraulic radius of the bed (ratio between flow area and wetted perimeter). Williams et al (5) used a mean hydraulic radius which may only apply if fibres have either uniform or truly random packing.

Summerscales (6) used a specific hydraulic radius to model the effect of variations in the reinforcement architecture on the flow rate. Flow rate, under identical conditions, was predicted to be significantly greater with a clustered array of fibres than for a uniform distribution of individual fibres at the same fibre volume fraction. Thirion et al (7) have shown that the linear flow rate through similar commercial reinforcement fibres at the same fibre volume fraction was more rapid in fabrics when clustered flow-enhancing tows were present.

Uneven fibre distribution has been predicted to cause a degradation of the mechanical properties of continuous fibre reinforced laminates (8). This prediction has been confirmed by measurements (9) showing reductions in longitudinal compressive strength and interlaminar shear strengths (ILSS) by including flow enhancing tows in a 2x2 twill weave fabric. The resulting effect on flow rate from modifying the weave has been correlated to measured variations in microstructure (10-12).

The evaluation of real materials requires automated microstructural image analysis. Techniques suitable to fibre-reinforced composites have been reviewed by Guild and Summerscales (13). Summerscales et al (14) have used the Voronoi half-interparticle distance to study the microstructure of carbon fibre-reinforced composites processed by the vacuum-bag technique using different process dwell times.

Fractal analysis may provide a way forward for the quantitative evaluation of microstructures that are difficult to accommodate by more traditional methods. Worrall and Wells (15) used fractal-variance analysis to characterise differences in filamentisation between bundled and filamentised press-moulded long discontinuous glass-fibre/polyester resin composites. Changes in the slope of Richardson plots (measured length plotted against the size of the measure on a log-log scale) were used to identify changes in the composite structure using optical microscope images of polished sections.

A study (16,17) has been made on the relationship between permeability, ILSS and area measurement of porespace features for a twill, 5-harness satin and a flow enhanced 5-harness satin (Injectex). This paper extends the study to include tensile and compressive testing and the use of fractal analysis to determine the fractal dimension of the intra-tow porespace distribution for each of the three fabrics.

## EXPERIMENTAL

### Materials

The conventional and flow-enhanced carbon-fibre fabrics in this study were obtained from Brochier SA (now Hexcel Composites, Dagneux - France). All three fabrics had the same areal weight (290 gsm) and were woven from the same batch of fibre. As the fabrics were of equal areal weight, fibre volume fractions would be the same for a given number of laminae within a given mould cavity thickness. The fabrics are described in Table 1 and shown schematically in Figures 1-3.

**Table 1: Fabrics studied**

<i>Designation</i>	<i>Description</i>
E3853 G986	2x2 twill weave 6K carbon fibre
E3795	5-harness satin weave 6K carbon fibre fabric
E3833 G963	5-harness satin Injectex weave 6K carbon fibre fabric

Figures 1-3 show the differences between the weave styles and indicate the tortuosity of the path the tows take through the fabric (crimp). The Injectex fabric has the same weave style as the satin but a modified architecture to improve its permeability. One in five tows (as shaded) are spirally bound, with a light filament at 250 turns per metre, which maintains the size of porespace around these tows when stacked with other layers within a mould.

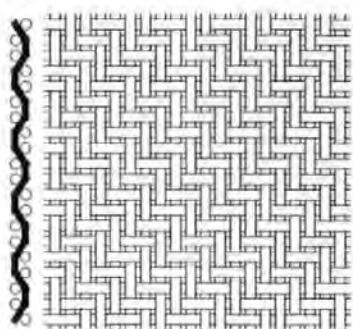


**Figure 1 Schematic of 2x2 twill weave**

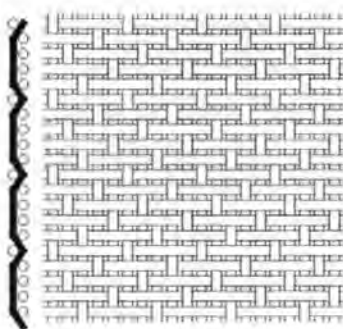


**Figure 2 Schematic of 5-harness satin weave**

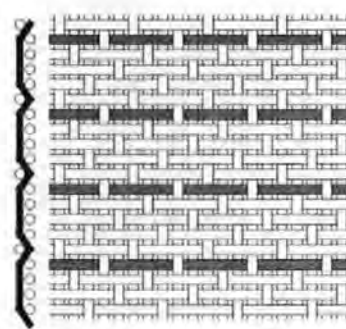


**Figure 3 Schematic of 5-harness satin Injectex weave**

The resin matrix system was Ciba-Geigy LY564-1/HY2954 epoxy. This has an initial viscosity of 500-700 mPas at 25°C and 80-125 mPas at 60°C (manufacturers data sheet K6B of April 1991). The NIP (non-injection point: time taken for the viscosity to rise to 1000 mPas, at which point flow effectively ceases) is 85 minutes at 25°C and 42 minutes at 65°C.

### **Permeability measurements**

Radial flow permeability experiments were conducted on each of the three fabrics at nominal fibre volume fractions of 49%, 54% and 60%. The varying volume fractions were achieved by using nine, ten or eleven layers of each fabric in a 400 mm square, 3.0 mm deep flat mould with a 20 mm thick glass top. Resin was introduced through a central inlet port and vacuum drawn through exit ports in each corner. A constant differential fluid pressure was used ranging from  $1.53\text{-}2.21 \times 10^5$  Pa between experiments.

The twill and satin fabrics were expected to have quasi-isotropic in-plane permeabilities and all layers were stacked with weft tows running across the width of the mould. Only the weft tows of the Injectex fabric were bound therefore two stacking sequences were used. One sequence with weft tows aligned across the width of the mould to give major and minor permeabilities, one sequence with alternate layers cross-plyed to give an effective quasi-isotropic permeability.

During injection the flow front isochrones were monitored using a Minitron CCD camera fitted with a Computar V1218 12.5 mm f1.8 C-mount lens. The camera was mounted 1000 mm above the centre of the glass plate on a steel support frame. Illumination was provided by three 500W floodlights mounted to either side and behind the apparatus. The light was diffused by opaque fluted plastic sheets attached to the support frame.

The video signal was recorded as a series of grey-scale digital images using a Synapse video frame grabber and C\_Images software (Foster Findlay Associates, Newcastle-upon-Tyne). The camera has a resolution of 768 x 512 pixels and thus can resolve lengths to less than 1mm when focused on the full square flow region of 400 mm edge length (i.e. the error is of the order of  $\pm 1$  pixel or  $\pm 1$  mm).

The flow front isochrones were recorded at equal intervals. The permeability values were calculated using the radial form of Darcy's equation. This approach is similar to that of Adams et al (18) and Chan and Hwang (19). Data validation routines have been described in the literature (20) and the theory is published (21).

### Preparation for mechanical and microscopical testing

Mechanical and microscopical specimens were aligned with tow direction and taken from quasi-isotropic plates manufactured at 54% fibre volume fraction. Tension and compression specimens were cut using a Parkson universal milling machine fitted with a diamond cutting disc. ILSS specimens were cut using a Tyslide diamond slitting saw. The edges of the specimens were found to be flat and smooth and required no further machining.

Mechanical testing was performed to CRAG (22) specifications. Plate thickness dictated the dimensions of the specimens. For the 3 mm thick plates the tension/compression specimens were 200 mm x 30 mm (100 mm gauge length between end tabs), and the ILSS specimens were 25 mm x 15 mm. The thickness and width of each specimen was measured using a Mitutoyo digital micrometer with a resolution of 0.001 mm.

The size of the microscopy specimens was dictated by the repeat cell size of the fabrics: that of the distance between tows with identical positioning within the fabric architecture. The approximate repeat sizes for the fabrics were measured and are reported in Table 2.

**Table 2: Approximate unit cell sizes for the fabrics**

Fabric	Repeat size (mm)
Twill	12
Satin	7
Injectex	7

The maximum repeat distance for the three fabrics was 12 mm, measured for the twill fabric. The dimensions of the microscopy specimens were made equal to those of the ILSS specimens (i.e. 25 mm x 15 mm) as this simplified sectioning. This gave at least two repeat cells for each of the ten fabric layers per specimen.

Specimens were individually potted in an epoxy casting resin and prepared using a Buehler 2000 Metpol grinder/polisher with Metlap fluid dispenser. All specimens were prepared following the procedure shown in Table 3.

**Table 3: Microscopical specimen preparation**

step	Platen				Head		time
	surface	abrasive	speed (rpm)	direction	speed (rpm)	force (lbs)	
1	SiC paper	240 grit	150	complementary	120	15	until plane
2	"	400 grit	"	"	"	20	2 min
3	"	600 grit	"	"	"	"	"
4	"	800 grit	"	"	"	"	"
5	nylon cloth	6µm diamond	50	contra	"	30	5 min
6	texmet cloth	1µm diamond	100	complementary	60	"	"
7	mastertex cloth	Al SiO <sub>2</sub>	50	contra	"	5	2 min

### Mechanical testing

Tension and compression tests were performed to CRAG specifications 302 and 401 respectively (22) using an Instron 8500 servo-hydraulic testing machine fitted with a 200 kN load cell. Strain measurements were made using 350 Ω strain gauges with 12.5 mm gauge length supplied by Vishay Measurements Group. ILSS tests were performed to CRAG specification 100 using an Instron 1175 universal testing machine fitted with a 10 kN load cell. Strain and load data were logged at a rate of 10 Hz using a Strawberry Tree parallel port data acquisition system and 486 DX4 100 PC.

### Determination of fractal dimension

Data for fractal-variance analysis were generated using a Quantimet 570 image analysis system. Images were acquired using a Kyowa STZ tri-nocular stereo zoom microscope and Fujitsu TCZ-230EA low light level black and white CCD camera. The process was performed in a darkened room using incident illumination from a Flexilux 150 HL Universal ring illuminator.

The Quantimet 570 has an adjustable image frame of 512 x 512 pixels maximum, with 256 grey levels (black = 0 and white = 255). A 480 pixel wide x 400 pixel high frame was defined and the magnification calibrated to include the full thickness of each specimen, giving an image frame 3.6 mm x 3.0 mm (10.8 mm<sup>2</sup>). System parameters were adjusted to provide reliable detection of tows and intra-tow porespace as discernible, distinct features. Three contiguous frames were automatically analysed per specimen, and ten specimens for each of the fabrics (total area 324 mm<sup>2</sup> per fabric). Table 4 shows details of the detection boxes used.

**Table 4: Details of detection boxes used for fractal analysis**

box edge (pixels)	2	3	4	7	9	15	19	39
box area (mm <sup>2</sup> )	0.000225	0.000506	0.000900	0.002756	0.004556	0.012656	0.020306	0.085556
boxes per frame	21333	12000	7680	3000	1920	750	480	120

## RESULTS AND DISCUSSION

### Permeability

Figure 4 shows the permeability results in the tow directions for the three fabrics (23) at 49% and 54% fibre volume fractions. The values on the diagonal are those for quasi-isotropic fabric lay-up sequences, *i.e.* cross-plyed warp directions in adjacent layers. Note that if the twill and Injectex are not cross-plyed they are anisotropic, due to a difference in warp and weft count in the former case, and the presence of flow-enhancing tows in the latter. Values off the diagonal are indicative of the extent of anisotropy of the materials.

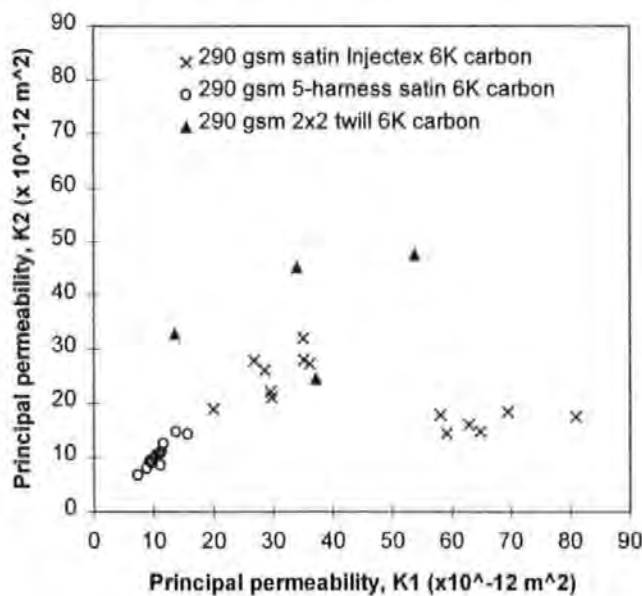


**Figure 4 Principal permeabilities of the twill, satin and Injectex fabrics**

Table 5 shows the range of measured permeabilities for quasi-isotropic lay-ups. There is clearly a permeability ranking between the fabrics in the order: twill > Injectex > satin. This ranking must be a function of fabric architecture and its effect on porespace distribution, as the results are derived from notionally identical experiments.

**Table 5: Range of measured permeabilities for quasi-isotropic lay-ups ( $\times 10^{-12} \text{ m}^2$ )**

<i>Fabric</i>	<i>Lower bound</i>	<i>Upper bound</i>
<i>Twill</i>	34	53.7
<i>Injectex</i>	18.9	36.1
<i>Satin</i>	8.1	17.9

### **ILSS**

Figure 5 shows the full set of results obtained from the thirty specimens tested (ten for each fabric). As with the permeability results, there is a clear ranking of the ILSS values, note however that the order is reversed: satin > Injectex > twill. The difference in ILSS between the twill and satin fabrics could be a result of variation in crimp. However, the difference between the satin and Injectex ILSS values must in part result from a change in porespace distribution, as the crimp of the two fabrics should be similar only exaggerated where tows cross flow-enhancing tows.

### **Tensile and compressive moduli and strengths**

Tensile and compressive moduli can be seen in Figure 6 and Figure 7 respectively. In both cases the ranking of the moduli is satin > twill > Injectex. Figure 8 and Figure 9 show the variation in failure strengths. Again the satin fabric has the highest properties with twill generally having marginally better properties than the Injectex. The compressive moduli and compressive strengths are lower than the tensile moduli and strengths for all fabrics as anticipated because of the prebuckling of fibres due to the crimp of the fabrics.

### **Fractal dimensions**

Qualitatively, variations can be seen in the size and distribution of porespace between the tows of the fabrics (uppermost row of images Figure 10). The twill fabric has a higher crimp than the satin. This increases the amount by which the tows run out of plane, and therefore reduces the ability of the tows in adjacent layers to nest together. The shape of the bound tows of the Injectex fabric clearly differ from that of the conventional tows. The binding prevents the tows from flattening, resulting in an increase in the size of porespace around them.

The second row of images in Figure 10 show the porespace detected from the images in the first row. The fractal detection of porespace is illustrated for four of the eight different sized boxes in rows 3-6 (boxes of 2, 4, 15 and 39 pixel edges respectively). The fractal dimensions (slope of Richardson plot, denoted as  $\delta$ ) for the satin, twill and Injectex fabrics are 0.424, 0.364 and 0.356 respectively and can be seen in Figure 11.

### **Comparison of properties and microstructure parameters**

Table 6 summarises the ranking of the permeabilities, mechanical properties and fractal dimensions for the three cross-plyed fabric laminates. The satin fabric provides the best mechanical properties but has the lowest permeability. The twill fabric has generally better mechanical design properties (ILSS is not recommended as a parameter for design prediction) than the Injectex fabric and higher permeability when the fabrics are cross-plyed. The slopes of the Richardson plots are ranked in the reverse sequence to tensile and compressive moduli and strengths.



**Table 6: Summary of results for all tests showing ranking of fabrics**

<i>Property</i>	<i>Ranking</i>				
Permeability	satin	<	Injectex	<	twill
ILSS	satin	>	Injectex	>	twill
Tensile strength	satin	>	twill	>	Injectex
Compressive strength	satin	>	twill	>	Injectex
Tensile modulus	satin	>	twill	>	Injectex
Compressive modulus	satin	>	twill	>	Injectex
Fractal dimension	satin	>	twill	>	Injectex

**SUMMARY**

For the fabrics tested the satin weave style provided the best mechanical properties, but the lowest permeability. The cross-plyed Injextex weave (enhanced satin) exhibited a higher permeability than the satin but at the expense of mechanical performance. The twill fabric had significantly higher permeability than both the satin and Injextex fabrics, whilst, with the exception of ILSS, possessing slightly better mechanical properties than the Injextex.

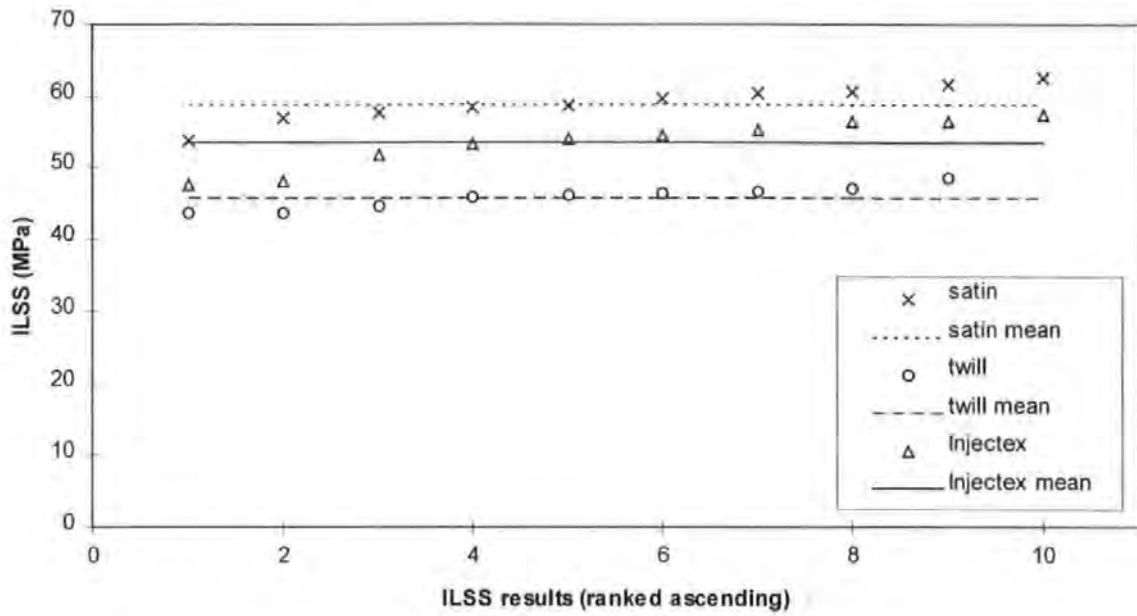


Figure 5 ILSS of the twill, satin and Injectex fabrics

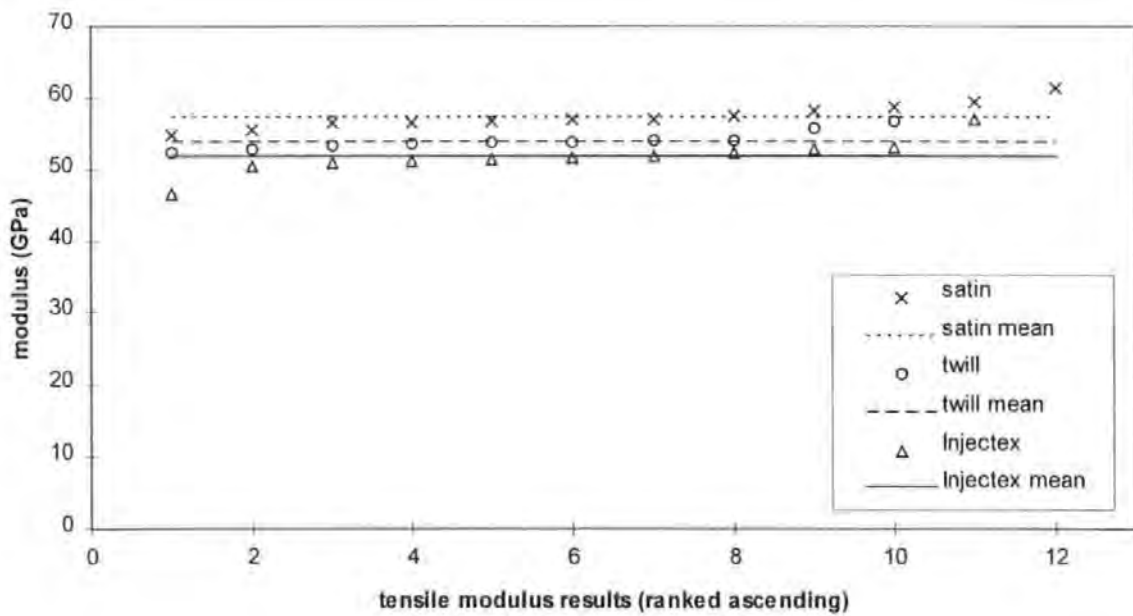
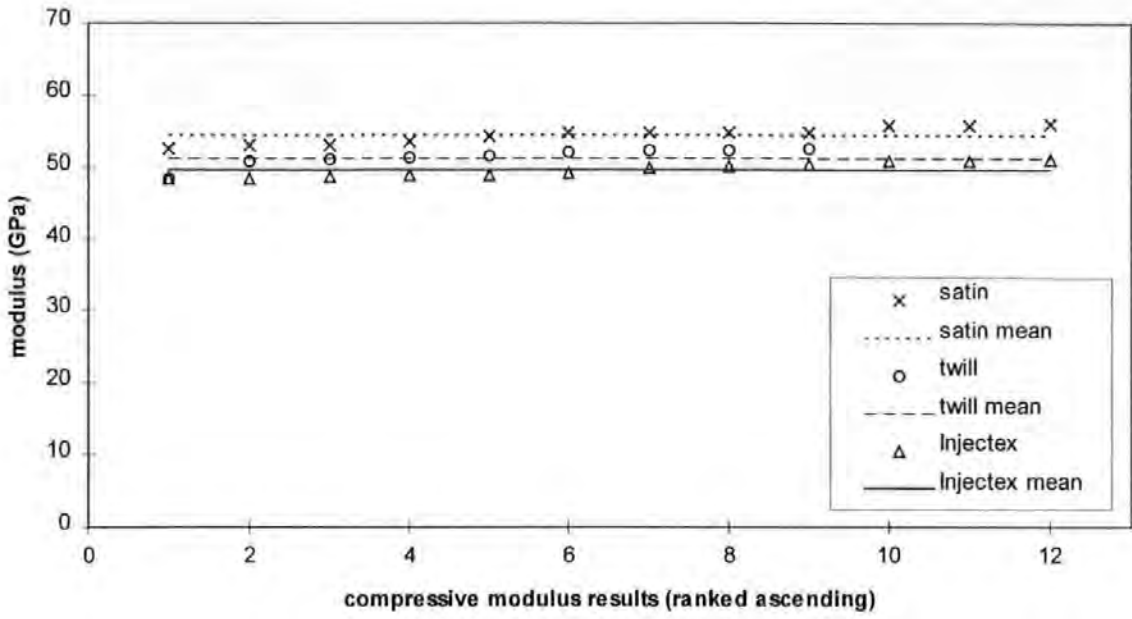
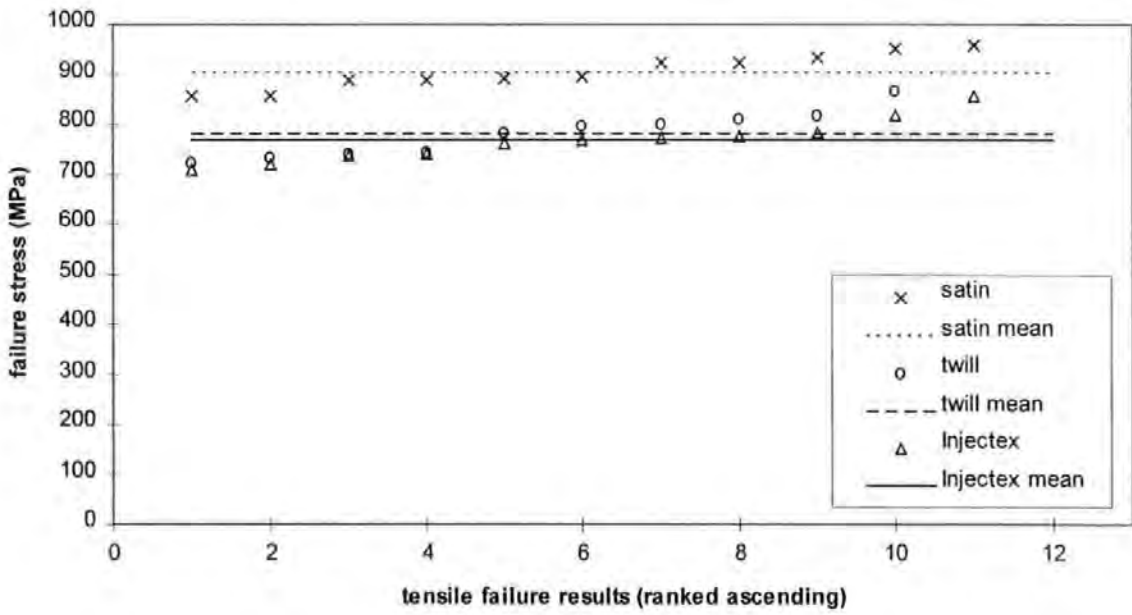


Figure 6 Tensile secant moduli of the twill, satin and Injectex fabrics



**Figure 7 Compressive secant moduli of the twill, satin and Injectex fabrics**



**Figure 8 Tensile failure stress**

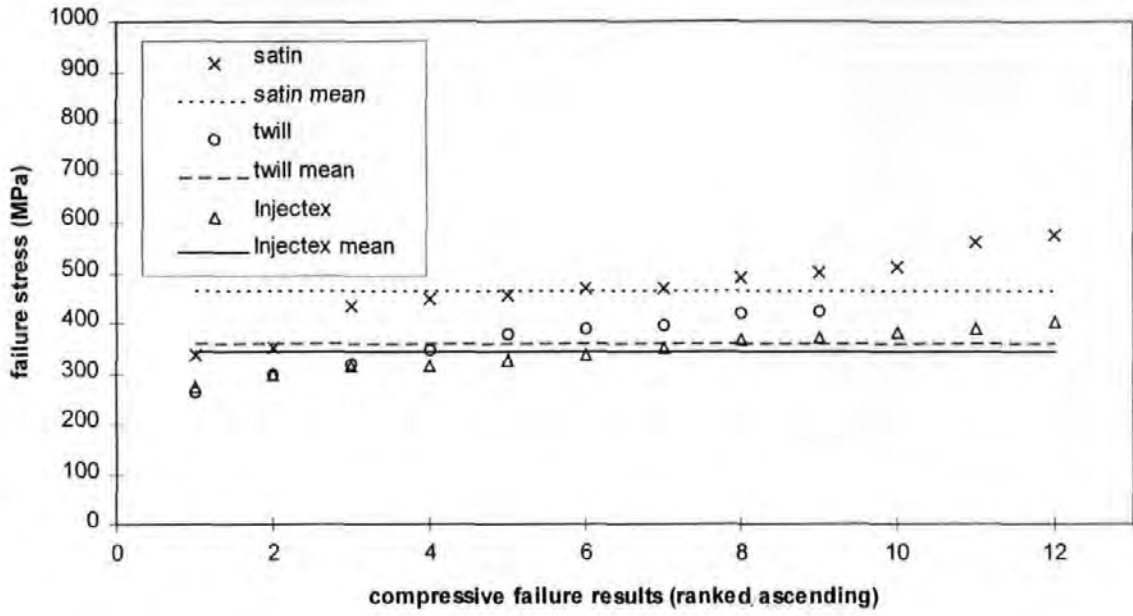
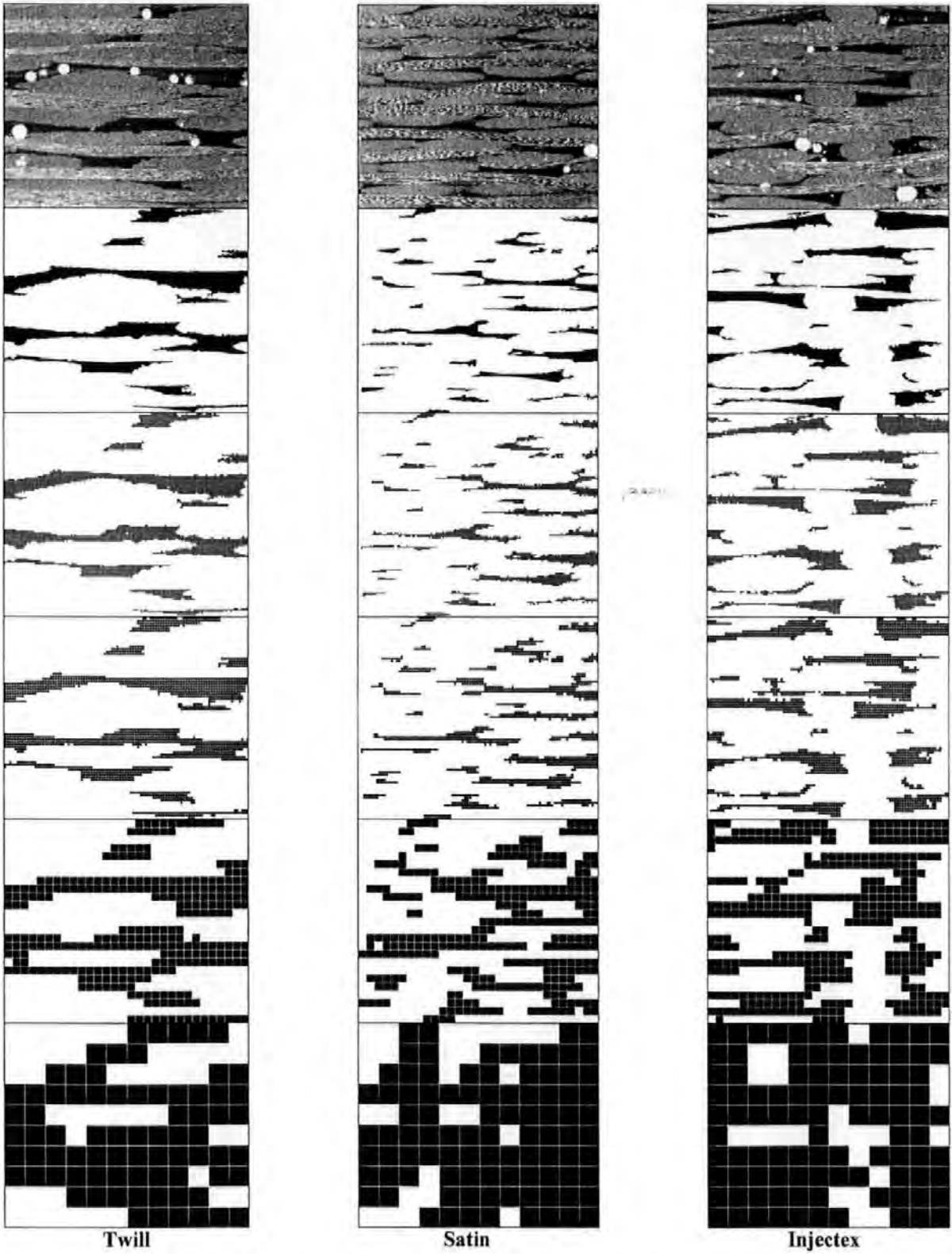
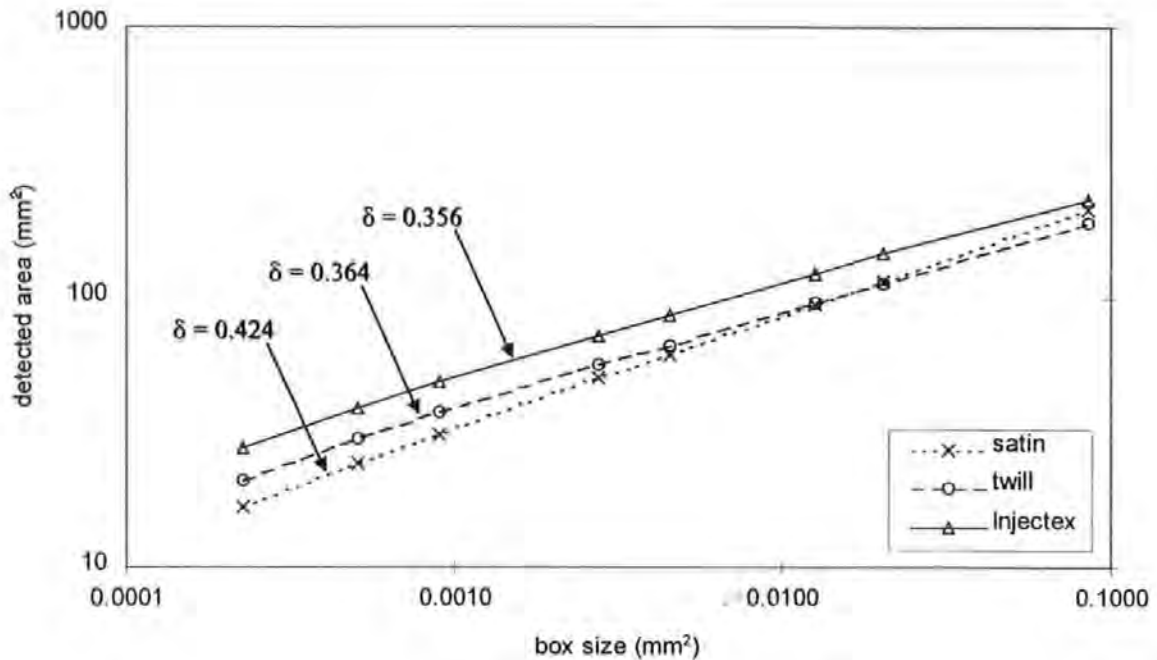


Figure 9 Compressive failure stress



**Figure 10** Representative images showing selective stages of fractal data generation



**Figure 11 Richardson plot showing fabric fractal dimensions**

## ACKNOWLEDGMENTS

The authors would like to acknowledge the support of EPSRC grants GR/J77405 and GR/K04699 and BRITE/EurAM II grant BRE2/CT92/0227 for this work. Thanks are also due to Eddie Carter, Tony Fell and Patrick Griffin of UoP School of Manufacturing, Materials and Mechanical Engineering for conducting and analysing the permeability experiments, and to Paul Russell of UoP Department of Biological Sciences for assistance with the Quantimet.

## REFERENCES

1. Darcy, H.P.G., "*Les fontaines publiques de la ville de Dijon*". Dalmont, Paris, 1856.
2. Kozeny, J., 'Über die kapillare Leitung des Wassers in Boden'. *Sitzungsberichte Akademie der Wissenschaft Wien Math-naturw*, 1927, **136** (Kl.abt.IIa), 271-306.
3. Carman, P.C., 'Fluid flow through a granular bed'. *Trans. Institute of Chemical Engineers*, (London), 1937, **15**, 150-166.
4. Blake, F.C., 'The resistance of packing to fluid flow'. *Trans. American Institute of Chemical Engineers*, 1922, **14**, 415-421.
5. Williams, J.G., Morris, C.E.M. and Ennis, B.C., 'Liquid flow through aligned fibre beds'. *Polymer Engineering and Science*, 1974, **14**(6), 413-419.
6. Summerscales, J., 'A model for the effect of fibre clustering on the flow rate in resin transfer moulding'. *Composites Manufacturing*, 1993, **4**(1), 27-31.

7. Thirion, J.M., Girardy, H. and Waldvogel, U., 'New developments in resin transfer moulding of high-performance composite parts'. Materials Information Translations Service Series C: Engineered Materials, *Composites*, (Paris), 1988, **28**(3), 81-84.
8. Guild, F.J., Davy, P.J. and Hogg, P.J., 'A model for unidirectional composites in longitudinal tension and compression'. *Composites Science and Technology*, 1989, **36**(1), 7-26.
9. Basford, D.M., Griffin, P.R., Grove, S.M. and Summerscales, J., 'Research Report: Relationship between mechanical performance and microstructure in composites fabricated with flow-enhancing fabrics'. *Composites*, 1995, **26**(9), 675-679.
10. Griffin, P.R., Grove, S.M., Guild, F.J., Russell, P. and Summerscales, J., 'The effect of microstructure on flow promotion in RTM reinforcement fabrics'. *Journal of Microscopy*, 1995, **177**(3), 207-217.
11. Griffin, P.R., Grove, S.M., Russell, P., Short, D., Guild, F.J. and Taylor, E., 'The effect of reinforcement architecture on the long range flow in fibrous reinforcements'. *Composites Manufacturing*, 1995, **6**(3/4), 221-235.
12. Summerscales, J., Griffin, P.R., Grove, S.M. and Guild, F.J., 'Quantitative microstructural examination of RTM fabrics designed for enhanced flow'. *Composite Structures*, 1995, **32**, 519-529.
13. Guild, F.J. and Summerscales, J., 'Microstructural image analysis applied to fibre composite materials: a review'. *Composites*, 1993, **24**(5), 383-394.
14. Summerscales, J., Green, D. and Guild, F.J., 'Effect of processing dwell-time on the microstructure of a fibre-reinforced composite'. *Journal of Microscopy*, 1993, **169**(2), 173-182.
15. Worrall, C.M. and Wells, G.M. "Fibre distribution in discontinuous fibre reinforced plastics: characterisation and effect on material performance". Proc. 7th European Conference on Composite Materials, London, 14-16 May 1996, 247-252.
16. Pearce, N.R.L., Guild, F.J. and Summerscales, J., 'A study of the effects of convergent flow fronts on the properties of fibre-reinforced composites produced by RTM'. *Composites Part A*, 1998, **29A** (1/2), 141-152.
17. Pearce, N.R.L., Guild, F.J. and Summerscales, J., 'A study of the effects of convergent flow fronts on the properties of fibre-reinforced composites produced by RTM'. *Composites Part A*, 1998, **29A** (1/2), 19-27.
18. Adams, L., Russel, W.B. and Rebenfeld, L., 'Radial penetration of a viscous fluid into a planar anisotropic porous medium'. *Intl. Journal of Multiphase Flow*, 1988, **14**(2), 203-215.
19. Chan, A.W. and Hwang, S. 'Anisotropic in-plane permeability of fabric media'. *Polymer Engineering and Science*, 1991, **13**(16), 1233-1239.
20. Carter, E.J., Fell, A.W. and Summerscales, J., 'A simplified model to calculate the permeability tensor of an anisotropic fibre bed'. *Composites Manufacturing*, 1995, **6**(3/4), 228-235.

21. Carter, E.J., Fell, A.W., Griffin, P.R. and Summerscales, J., 'Data validation procedures for the automated determination of the two-dimensional permeability tensor of a fabric reinforcement'. *Composites Part A: Applied Science and Manufacturing*, 1996, **27A**(3), 255-261.
22. Curtis, P.T., 'CRAG test methods for the determination of the engineering properties of fibre reinforced plastics'. Royal Aerospace Establishment Technical Report 88012, February 1988.
23. Carter, E.J., Fell, A.W., Griffin, P.R. and Summerscales, J. 'Final report on Sub-Task 1.2: The apparent permeability of reinforcement fabrics'. University of Plymouth report BE5477/UoP/FR/1.2/A/CC/1.0, January 1996.



# IMPROVING THE RESIN TRANSFER MOULDING PROCESS FOR FABRIC-REINFORCED COMPOSITES BY MODIFICATION OF THE FABRIC ARCHITECTURE

NRL Pearce, J Summerscales  
Department of Mechanical and Marine Engineering,  
University of Plymouth, Plymouth PL4 8AA, United Kingdom

and FJ Guild  
Department of Mechanical Engineering,  
University of Bristol, Bristol BS8 1TR, United Kingdom.

## ABSTRACT

The use of resin transfer moulding (RTM) as an economic and efficient means of producing high-performance fibre-reinforced composites is critically limited by the permeability of the fabrics employed. Commercial fabrics are available where the architecture of the reinforcement is designed to cluster the fibres giving higher permeabilities than conventional fabrics. This has been shown to improve processing times, but there is evidence that such clustering is detrimental to the mechanical performance of the resulting composite material.

The objective of this work was to relate variations in permeability, and in the laminate mechanical properties, to differences in microstructure. A series of experimental carbon fibre fabrics woven to incorporate a novel flow enhancement concept (use of 3K tows in a 6K fabric) were used to manufacture plates by RTM in a transparent mould. The progress of the resin front was recorded to computer disc during injection, thus allowing the permeabilities of the fabrics to be calculated.

The manufactured plates were subsequently sectioned for mechanical testing (moduli and strengths in tension and compression) and automated image analysis. Relationships were sought between measured permeabilities, mechanical properties and microstructures using a Quantimet 570 automatic image analyser to determine fractal dimensions from polished sections. It has been shown that variations in the microstructures can be related to the permeability and mechanical property values obtained. Further the deterioration of mechanical properties for the novel fabrics with reduced fibre volume fractions is less than has been reported for fabrics with clustered flow-enhancing tows at constant fibre volume fraction.

## INTRODUCTION

Resin transfer moulding (RTM) is a process for manufacturing polymer-matrix composites [1-5]. A preform of dry reinforcement fibres is placed into a mould. The mould is closed and resin injected. Once cured, the near net-shape component is removed. RTM differs from other composite manufacturing processes as it involves long-range flow of resin through porespace surrounding the reinforcement fibres.

Darcy's equation [6] predicts that the flow rate of a fluid through a porous medium is proportional to the pressure drop and inversely proportional to the bed length. The coefficient of proportionality is known as the permeability and must be either measured or predicted. Kozeny [7] and Carman [8] related the flow rate to the microstructure of the medium using the Blake concept [9] of the hydraulic radius of the bed (ratio between flow area and wetted perimeter). Williams et al [10] used a *mean* hydraulic radius to model liquid flow through aligned fibre beds. This may only apply if fibres have either uniform or truly random packing.

Summerscales [11] used a *specific* hydraulic radius to model the effect of variations in the reinforcement architecture on the flow rate. Under identical conditions, flow rate was predicted to be significantly greater with a clustered array of fibres than for a uniform distribution of individual fibres at the same fibre volume fraction. Similar results from experimental work by Thirion et al [12] have shown that the flow rate through commercial reinforcement fabrics was more rapid in fabrics with clustered flow-enhancing tows than in fabrics without the enhancement under otherwise identical conditions at the same fibre volume fraction.

Uneven fibre distribution has been predicted to cause a degradation of the mechanical properties of continuous fibre reinforced laminates [13]. This prediction has been confirmed by measurements [14] showing reductions in longitudinal compressive strength and interlaminar shear strengths (ILSS) associated with spiral bound tows included in a 2x2 twill weave fabric to promote flow enhancement. The resulting effect on flow rate due to modification of the weave has been correlated to measured variations in microstructure [15-19].

The evaluation of real materials requires automated microstructural image analysis. Techniques suitable to fibre-reinforced composites have been reviewed by Guild and Summerscales [20]. Summerscales *et al* [21] have used the Voronoi half-interparticle distance to study the microstructure of carbon fibre-reinforced composites processed by the vacuum-bag technique using different process dwell times.

Fractal analysis may provide a way forward for the quantitative evaluation of microstructures that are difficult to accommodate by more traditional methods. Worrall and Wells [22] used fractal-variance analysis to characterise differences in filamentisation between bundled and filamentised press-moulded long discontinuous glass-fibre/polyester resin composites. Changes in the slope of Richardson plots (measured length plotted against the size of the measure on a log-log scale) were used to identify changes in the composite structure examined as optical microscope images of polished sections.

Pearce *et al* [23-25] studied the relationship between fabric permeability, mechanical performance and microstructure for twill, 5-harness satin and enhanced 5-harness satin (Injectex) fabrics from Brochier SA (France). The results [23] showed that fabric permeability is significantly increased by the presence of inter-tow flow channels in the range 0.08 - 0.3 mm<sup>2</sup> (area measured normal to the direction of flow) and that there is a marked deterioration of mechanical performance when channels of 0.5 mm<sup>2</sup> or larger are present. The fractal dimension (slope of the Richardson plot) was ranked in the same sequence as the tensile and compressive moduli and strengths [25]. The microstructure of 'normal' and flow-enhanced satin fabrics is illustrated in Figure 1. Note the more pronounced pore-space in the latter fabric.

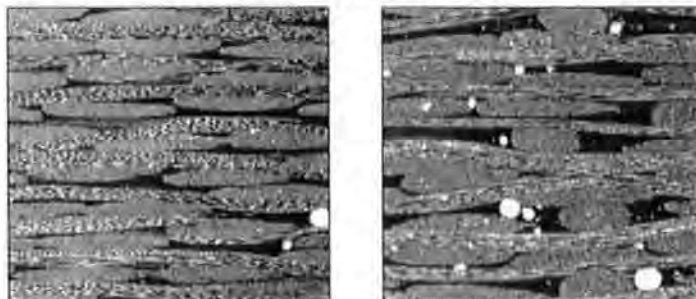


Figure 1: Micrographs of sections from 'normal' (left) and flow-enhanced (right) satin fabrics at the same fibre volume fraction

This paper reports a study of novel fabrics (variations on a 6k tow twill weave) woven in an attempt to optimise flow-enhancing fabrics for the process-performance dilemma. Four fabrics, three of which have been modified by including varying proportions of 3k tows in place of 6k tows in the weft direction only are analysed. Previous reports of the measurement of permeability [26, 27] and mechanical properties [28] for these fabrics are integrated in this paper.

### EXPERIMENTAL: Materials

Four carbon-fibre fabrics were woven specifically for this study by Carr Reinforcements Limited using a 372 g/m<sup>2</sup> 2x2 twill weave as the reference fabric (Table 1). The fabrics were all woven from the same two batches of fibres (one each for the 3k and for the 6k fibres). More comprehensive description of the fabrics is withheld for commercial reasons at the request of the weaver. The resin matrix was SP Systems Ampreg 26 epoxy with Ampreg 26SL slow hardener. This has an initial viscosity of 310 cps at 25°C and a gel time at this temperature of 230 minutes. Permeability values were derived from the first 20 minutes of each experiment when changes in viscosity were minimal.

**Table 1: Fabrics studied**

Fabric Code	Areal Weight (g/m <sup>2</sup> )	% of 3k tows to 6k tows			Change in areal weight with respect to Fabric D	Fibre volume fraction in the laminate
		warp	weft	total	%	%
A	340	nil	33%	17%	- 8.6 %	40.8%
B	353	nil	20%	10%	- 5.1 %	42.4%
C	358	nil	14%	7%	- 3.8 %	43.0%
D	372	nil	nil	nil	0	44.7%

Square laminates of 440 mm edge were manufactured using five layers of fabric (all warp fibres aligned) in a 2.35 mm cavity at a controlled temperature of 25°C. The mould is an integral part of the University of Plymouth radial flow permeability apparatus [29, 30] enhanced by:

- a thicker glass top to minimise mould cavity changes due to pressure/vacuum levels (a laminate of two 25mm toughened float glass sheets supplied by Hayes Laminate Glass, West Drayton UK).
- solenoid valve control of the pressure in the resin reservoir to 2000 +12/-0 mbar absolute using a solid state relay with TTL logic.

Resin was introduced through a central inlet port in the mould base and full vacuum (<1 mbar absolute) drawn through exit ports in each corner. The resin reservoir pressure was held at 2000 mbar absolute. Upon completion of mould fill, the vacuum lines were clamped and 300 mbar positive pressure was maintained on the resin chamber to reduce the size of any retained voids. Plates were demoulded 24 hours after mould fill, then ramped at 0.5°C/min to 80°C and post-cured for 5 hours.

The progress of the flow front was monitored using a Minitron CCD camera fitted with a Computar V1218 12.5 mm f1.8 C-mount lens. The camera has a resolution of 768x512 pixels and can thus resolve lengths to less than 1 mm when focused on the full square flow region of 400 mm edge length (*ie* the error is of the order of ±1 pixel or ±1 mm). The camera was calibrated against a reference image of 280 mm overall length. Illumination was provided by fluorescent light tubes along the edges of the glass plate.

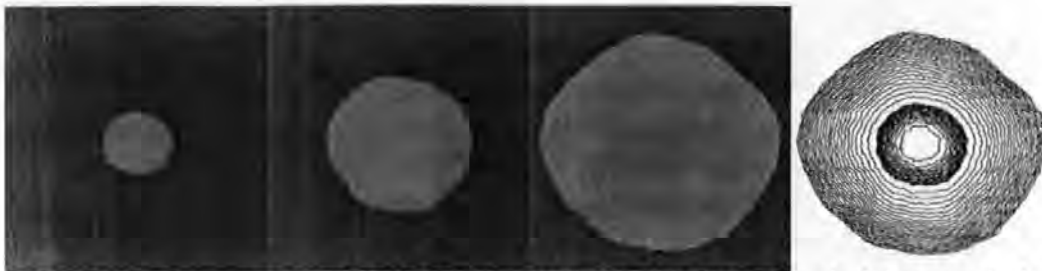


**Figure 2: Flow front images at 36, 201 and 653 seconds (first to third box from the left respectively) and a composite of the detected flow front for 45 frames (right).**

The digitised video signal was recorded in FFA-format, converted to TIF-format and analysed using the Quantimet 570 image analyser. Data acquired for each time-frame included x- and y-flow front radii, flow front radii every five degrees, flow front aspect ratio, equivalent circle diameter, roundness, area and x- and y- centres of gravity. Sample images are shown in Figure 2. Permeability was calculated from the video images captured during the first ~20 minutes of radial flow using the radial form of the Darcy equation [30].

### **EXPERIMENTAL: Mechanical and microscopical testing**

Microscopical, tension and compression specimens were cut using a Parkson universal milling machine fitted with a diamond cutting disc. The edges of the mechanical test specimens were found to be flat and smooth and required no further machining. Three microscopical specimens (each 21.75 mm long) in each of warp and weft directions per fabric were individually potted in an epoxy casting resin. All specimens for microscopical analysis were prepared as described in reference 25.

Mechanical testing was performed to CRAG [31] specification. Five tension and five compression specimens were cut in each of warp and weft directions for all four fabrics (eighty specimens in total). The specimens were 200 mm x 23.5 mm as dictated by the plate thickness with 100 mm gauge length between end tabs. The thickness and width of each specimen was checked using a Mitutoyo digital micrometer with a resolution of 0.001 mm.

Tension tests were performed to CRAG specification 302 at 5 mm/min using an Instron 1175 screw-driven universal testing machine fitted with a 100 kN load cell. Compression tests were performed to CRAG specification 401 at 2.4 mm/min using an Instron 8500 servo-hydraulic testing machine fitted with a 200 kN load cell. Strain measurements were made using 350  $\Omega$  strain gauges with 12.5 mm gauge length (type N2A-06-500BL-350 from Vishay Measurements Group, UK). Strain and load data were logged at a rate of 10 Hz using a Strawberry Tree parallel port data acquisition system and a 486 DX4 100 PC. The secant moduli were calculated at an axial strain of 2500  $\mu\epsilon$ .

### **EXPERIMENTAL: Determination of fractal dimension**

Data for fractal-variance analysis were generated using a Quantimet 570 image analysis system. Images were acquired using a Kyowa STZ tri-nocular stereo zoom microscope and Fujitsu TCZ-230EA low light level black and white CCD camera. The process was performed in a darkened room using incident illumination from a Flexilux 150 HL Universal ring illuminator.

The Quantimet 570 has an adjustable image frame of 512 x 512 pixels maximum, with 256 grey levels (black = 0 and white = 255). A 480 pixel wide x 480 pixel high frame was defined and the magnification calibrated to include the full thickness of each specimen, giving an image frame 2.2 mm x 2.2 mm (4.84 mm<sup>2</sup>). System parameters were adjusted to provide reliable detection of tows and intra-tow porespace as discernible, distinct features. Four contiguous frames were automatically analysed per specimen giving twelve frames in each of warp and weft per fabric (total detection area of 58.08 mm<sup>2</sup>). Figure 3 shows selective images captured during the fractal data generation process.



Figure 3: Representative images showing the stages of fractal data generation for a Brochier twill fabric

The images were analysed by detecting the inter-tow porespace and converting the grey-scale image to binary (black or white). This binary image was overlaid with an grid of boxes and the boxes overlaying porespace were 'flagged'. The porespace area was measured from 'flagged' area as a proportion of the whole area analysed. A range of box sizes were used (Table 2). The flagged area was plotted against box area on a log-log scale. The slope of this plot is the fractal dimension ( $\delta$ ).

Table 2: Detection boxes used for fractal analysis

box edge (pixels)	2	3	4	7	9	15	19	39
box area (mm <sup>2</sup> )	0.00008	0.00019	0.00034	0.00103	0.00170	0.00473	0.00758	0.03195
boxes per frame	25600	14400	9216	3600	2304	900	576	144

## RESULTS AND DISCUSSION

### Permeabilities

The permeability results are summarised in Figure 4. Each data point represents a single experiment.  $K_{ecd}$  is the effective in-plane permeability (equivalent to the same flow rate through an isotropic medium) and is derived from a measurement of wetted area. Note that D is the reference fabric. The increase in permeability of the fabrics is not consistent with the proportion of 3k tows included to promote flow-enhancement.

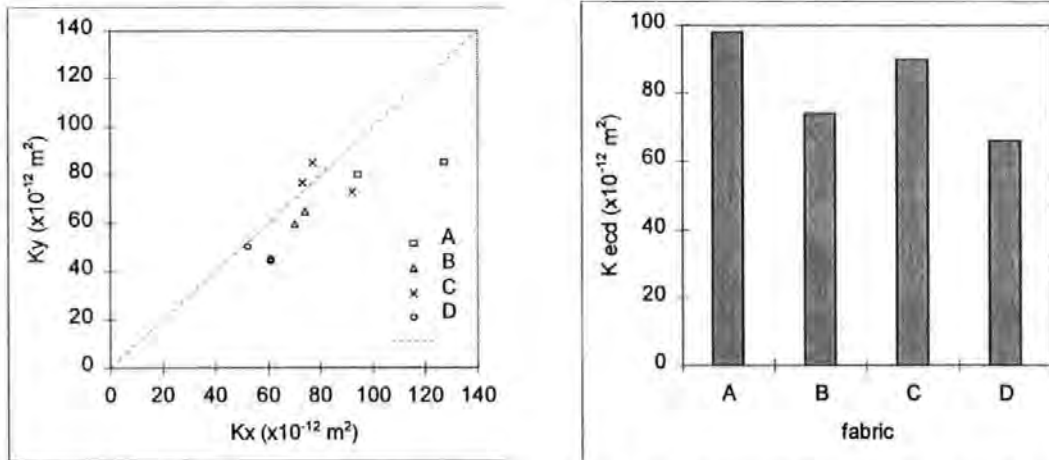


Figure 4: Fabric Permeabilities (left: directional values, right: effective isotropic in-plane value).

## Tensile and compressive moduli and strengths

The results for tensile/compressive moduli/strengths are shown in Figures 5 and 6. The standard deviations for all moduli and for compression strengths are <2% and for all tensile strengths are <5% [28]. Figure 5 shows that the base fabric D has similar moduli in warp and weft for both tensile and compressive loading. The moduli in the warp direction (all 6k tows) are relatively constant for all four of the fabrics (Figure 5). Moduli in compression are marginally lower than those in tension. This is believed to be due to the crimp of the fabric straightening in tension or increasing in waviness during compression.

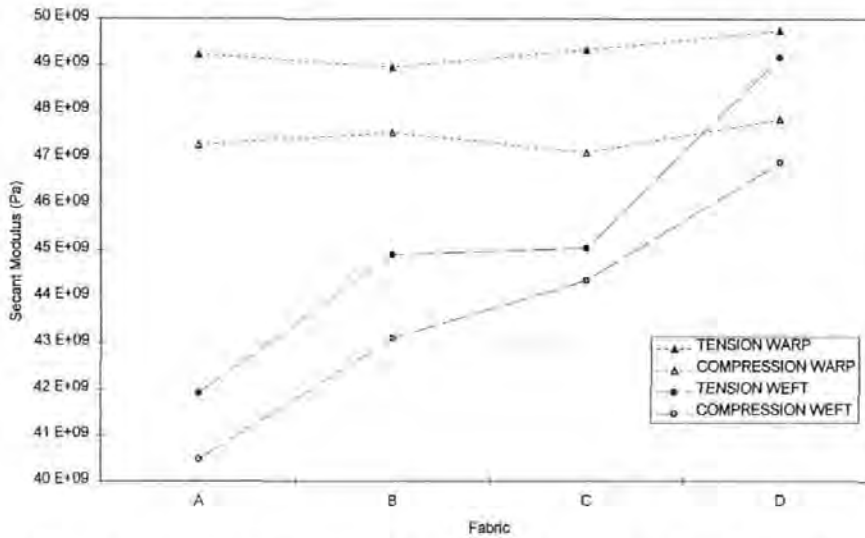


Figure 5. Averaged Tensile and Compressive Moduli in Warp and Weft

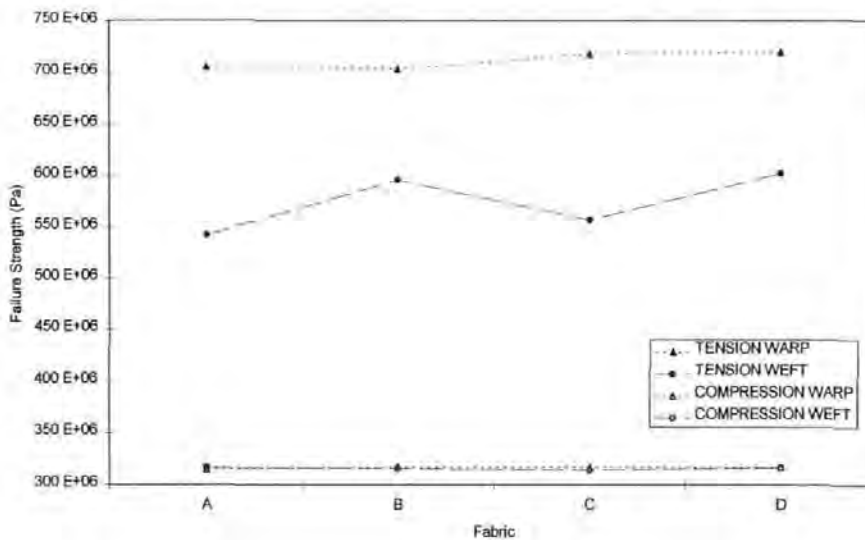


Figure 6. Averaged Tensile and Compressive Strengths in Warp and Weft

The weft direction has lower moduli than the warp direction in both tension and compression. There is a strong correlation between both tensile and compressive moduli and fibre volume fraction in the weft direction as the smaller 3k tows are substituted. The rate at which modulus decreases with increasing proportion of 3k tows is broadly consistent with the change in volume fraction of fibres in the test direction.

The compression strengths are unaffected by the change in fibre architecture. Figure 6 shows that the compressive strengths are sensibly constant for each fabric direction.

The tensile strength in the weft direction is typically 80% of that in the warp direction. The weft direction tensile strengths do not correlate to the proportion of 3k tows but are ranked in the same sequence as the fractal dimension (see below).

The warp direction compression strengths are consistently reduced to ~45% of those in tension. The weft direction compression strengths are reduced by ~50-60% compared to those in tension. Note that the weft direction tensile strength is considerably reduced relative to that in the warp, whilst the compressive strengths are essentially similar in both warp and weft directions. As the 3K tows are likely to experience lower crimp than the 6K tows it is probable that failure of the latter dominates the tensile strength performance of these fabrics.

### Microstructural image analysis

The fractal dimensions are the slopes of the Richardson plots shown in Figures 7 and 8. The fractal dimensions and the linearity of the data upon which they are based are shown in Table 3. A strong correlation between permeability and fractal dimensions is shown in Figures 9 and 10.

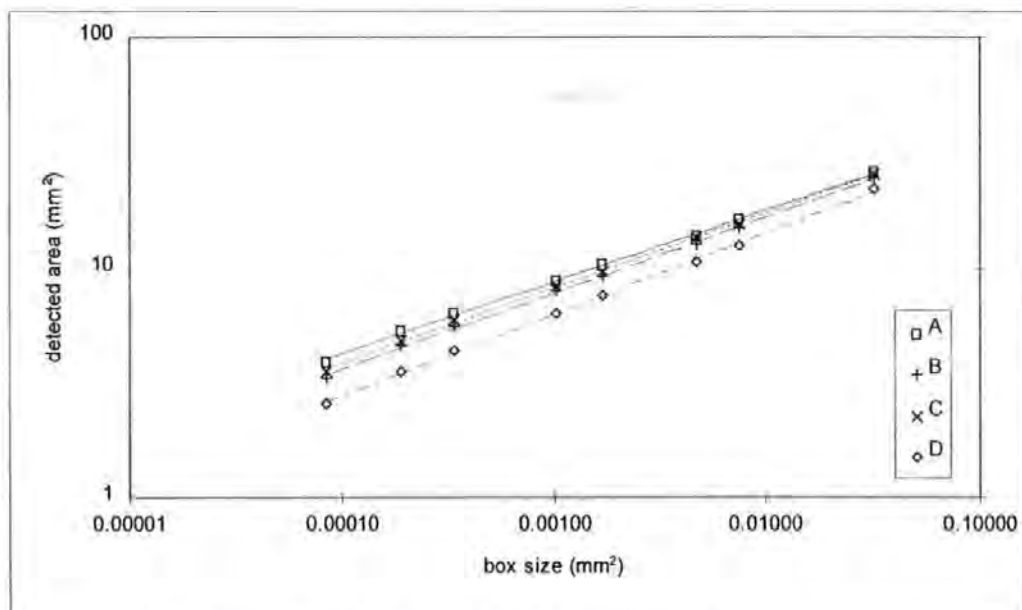


Figure 7: Richardson plot showing fabric fractal dimensions measured in the weft direction

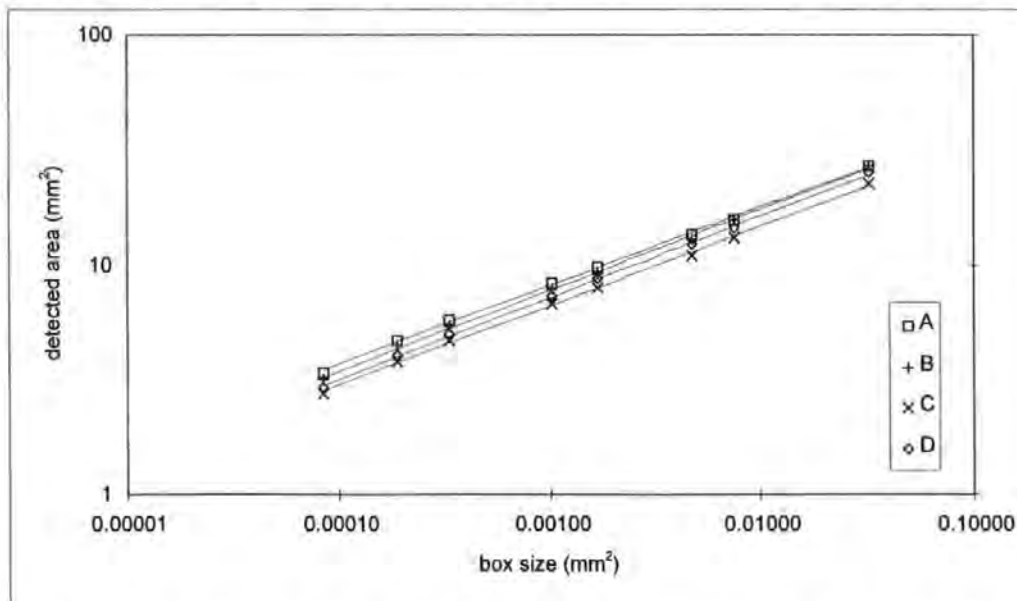
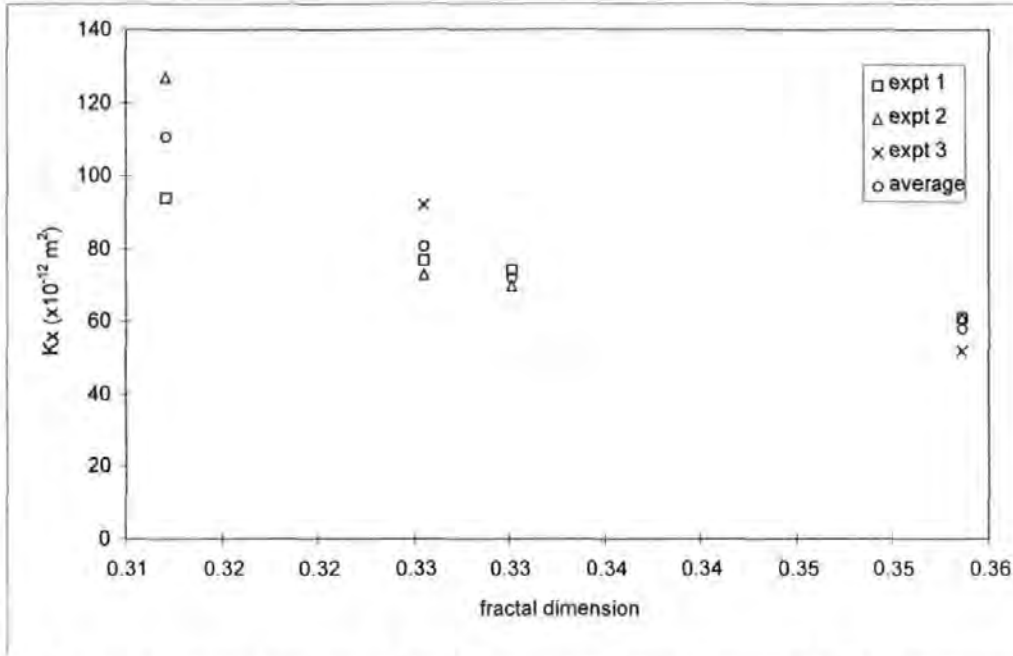


Figure 8: Richardson plot showing fabric fractal dimensions measured in the warp direction

**Table 3: Fractal dimensions and linearity**

fabric	fractal dimension		linearity	
	warp	weft	warp	weft
A	0.3397	0.3120	0.9994	0.9995
B	0.3504	0.3301	0.9993	0.9995
C	0.3443	0.3255	0.9993	0.9995
D	0.3539	0.3536	0.9996	0.9995



**Figure 9: Fractal dimensions plotted against permeability (both measured in the weft direction)**

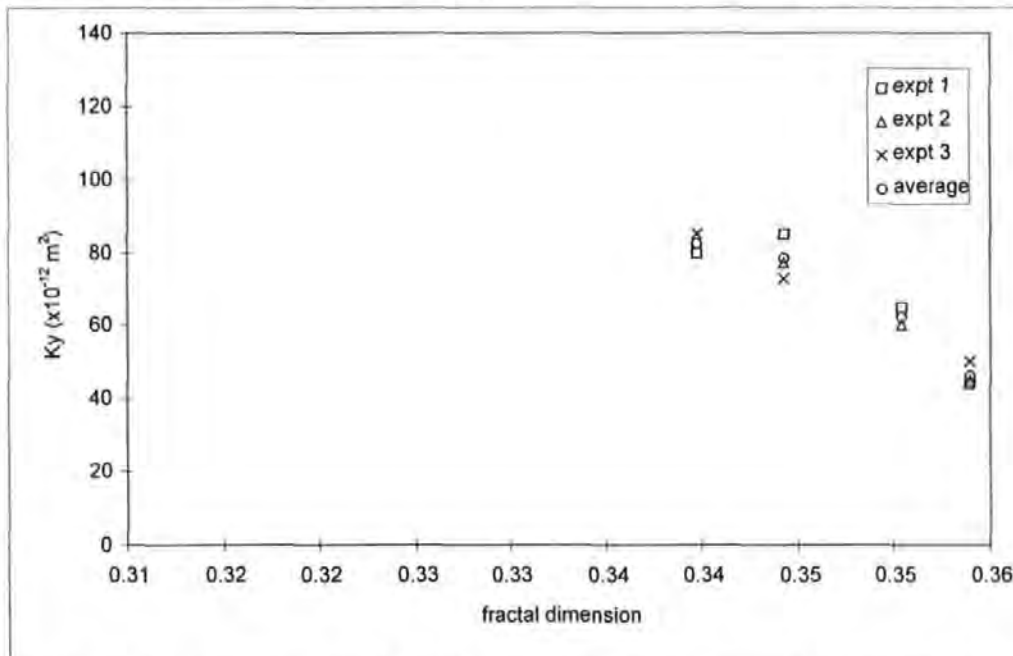


**Figure 10: Fractal dimensions plotted against permeability (both measured in the warp direction), plotted on the same scale as Figure 9.**



The weft direction tensile strengths do not correlate to the proportion of 3k tows but are ranked in the same sequence as the fractal dimension (Table 4).

**Table 4: Ranking of weft tensile strength and fractal dimension**

Fabric	Fractal dimension	Strength (MPa)
A	0.3120	542
C	0.3255	556
B	0.3301	595
D	0.3536	602

## DISCUSSION

The permeability of the fabrics containing differing proportions of flow enhancing tows has been shown to *not* be directly proportional to the proportion of modified tows introduced. Higher permeability is found for the fabric containing 7% modified tows than for the fabric containing 10% modified tows. This result is surprising since increased permeability arises from increased pore space. More pore space, perhaps of more favourable size and as separate pores, must be present in the fabric containing the lower proportion of modified tows. The results of the image analysis support this observation, with the ranking of the values of fractal dimension being identical to the ranking of the values of permeability.

The measurement of mechanical properties demonstrated some interesting results. The measured values of stiffness can be correlated with the change in fibre volume fraction arising from the replacement of tows. The compression strengths were found to be unaffected by the changes in fabric architecture. This result is not surprising for these woven fabrics since compression strength can be related to the maximum curvature in the axial direction; the maximum value would be unchanged with the introduction of these flow enhancing tows. However, the values of tensile strength in the weft direction (the direction containing the flow enhancing tows) is found to be dependent on the architecture. The strength for the fabric containing 7% modified tows is lower than the strength for the fabric containing 10% modified tows. This result can be correlated with both the results from the permeability measurements and the microscopical examination. The reduction in strength for this fabric is measurable, but small.

These results show that the new fabrics have improved permeability achieved by the introduction of a low percentage of flow enhancing tows (with a lower tow count than the normal tows). The stiffness of the laminate is reduced by the change in the fibre volume fraction, but this reduction is far smaller than that introduced if a large percentage of similar modified tows is used.

## SUMMARY

Novel fabrics with differing proportions of flow enhancing tows (3k tows in the weft direction only within a standard 6k fabric) have been woven which offer increased permeability, whilst reductions in mechanical properties are in line with the change in fibre volume fraction. The increase in permeability is not consistent with the proportion of flow-enhancing tows, but can be ranked in the same sequence as the fractal dimension derived from polished sections.

The compression strengths are unaffected by the change in tow size. The weft direction has lower moduli in both tension and compression. The rate at which modulus decreases with increasing proportion of 3k tows is broadly consistent with the change in volume fraction of fibres in the test direction. The weft tensile strength is ranked in the same sequence as the fractal dimension.

## ACKNOWLEDGMENTS

The authors gratefully acknowledge the support of EPSRC grants GR/J77405 and GR/K04699 for support of this work. Thanks are also due to Carr Reinforcements Limited [32] for weaving the special fabrics and to Mr P Russell of the UoP Department of Biological Sciences for assistance with the Quantimet.

## REFERENCES

1. van Harten, K., 'Production by resin transfer moulding', in Shenoi, R.A. and Wellicome, J.F., (editors): "*Composite Materials in Maritime Structures*". Cambridge University Press, Cambridge, 1993, Chapter 4, 86-126.
2. Potter, K., "*Resin Transfer Moulding*", Chapman & Hall, London, 1997, ISBN 0-412-72570-3.
3. Rudd, C.D., Long, A.C., Kendall, K.N. and Mangin, C.G.E., "*Liquid Composite Moulding*", Woodhead Publishing, Cambridge, 1997, ISBN 1-85573-242-4.
4. Kruckenberg, T.M. and Paton, R. (editors), "*Resin Transfer Moulding for Aerospace Structures*", Kluwer Academic Publishers, Dordrecht NL, 1998, ISBN 0-412-73150-9.
5. Benjamin, W.P. and Beckwith, S.W., "*Resin Transfer Moulding*", SAMPE Monograph 3, Covina CA, 1999, ISBN 0-938-99483-2.
6. Darcy, H.P.G., "*Les fontaines publiques de la ville de Dijon*". Dalmont, Paris, 1856.
7. Kozeny, J., 'Über die kapillare Leitung des Wassers in Boden'. *Sitzungsberichte Akademie der Wissenschaft Wien Math-naturw*, 1927, **136** (Kl.abt.IIa), 271-306.
8. Carman, P.C., 'Fluid flow through a granular bed'. *Trans. Institute of Chemical Engineers*, (London), 1937, **15**, 150-166.
9. Blake, F.C., 'The resistance of packing to fluid flow'. *Trans. American Institute of Chemical Engineers*, 1922, **14**, 415-421.
10. Williams, J.G., Morris, C.E.M. and Ennis, B.C., 'Liquid flow through aligned fibre beds'. *Polymer Engineering and Science*, 1974, **14**(6), 413-419.
11. Summerscales, J., 'A model for the effect of fibre clustering on the flow rate in resin transfer moulding'. *Composites Manufacturing*, 1993, **4**(1), 27-31.
12. Thirion, J.M., Girardy, H. and Waldvogel, U., 'New developments in resin transfer moulding of high-performance composite parts'. Materials Information Translations Service Series C: Engineered Materials, *Composites*, (Paris), 1988, **28**(3), 81-84.
13. Guild, F.J., Davy, P.J. and Hogg, P.J., 'A model for unidirectional composites in longitudinal tension and compression'. *Composites Science and Technology*, 1989, **36**(1), 7-26.
14. Basford, D.M., Griffin, P.R., Grove, S.M. and Summerscales, J., 'Research Report: Relationship between mechanical performance and microstructure in composites fabricated with flow-enhancing fabrics'. *Composites*, 1995, **26**(9), 675-679.
15. Griffin, P.R., Grove, S.M., Russell, P., Short, D., Guild, F.J. and Taylor, E., 'The effect of reinforcement architecture on the long range flow in fibrous reinforcements'. *Composites Manufacturing*, 1995, **6**(3/4), 221-235.
16. Summerscales, J., Griffin, P.R., Grove, S.M. and Guild, F.J., 'Quantitative microstructural examination of RTM fabrics designed for enhanced flow'. *Composite Structures*, 1995, **32**, 519-529.

17. Griffin, P.R., Grove, S.M., Guild, F.J., Russell, P. and Summerscales, J., 'The effect of microstructure on flow promotion in RTM reinforcement fabrics'. *Journal of Microscopy*, 1995, **177**(3), 207-217.
18. Guild, F.J., Pearce, N.R.L., Griffin, P.R. and Summerscales, J., 'Optimisation of reinforcement fabrics for the resin transfer moulding of high fibre volume fraction composites'. Proc. 7th European Conference Composite Materials, London, 14-16 May 1996, 273-278.
19. Pearce, N.R.L., Griffin, P.R., Summerscales, J. and Guild, F.J., 'Optimisation of reinforcement fabrics for the resin transfer moulding of high fibre volume fraction composites'. Proc. 17th International Conference, SAMPE European Chapter, Basel CH, 28-30 May 1996, 225-236.
20. Guild, F.J. and Summerscales, J., 'Quantitative microstructural analysis for continuous fibre composites'. In J Summerscales (editor): *Microstructural Characterisation of Fibre-Reinforced Composites*, Woodhead Publishing, Cambridge, 1998, Chapter 6, 179-203.
21. Summerscales, J., Green, D. and Guild, F.J., 'Effect of processing dwell-time on the microstructure of a fibre-reinforced composite'. *Journal of Microscopy*, 1993, **169**(2), 173-182.
22. Worrall, C.M. and Wells, G.M., 'Fibre distribution in discontinuous fibre reinforced plastics: characterisation and effect on material performance', Proc. 7th European Conference on Composite Materials, London, 14-16 May 1996, 247-252
23. Pearce, N.R.L., Guild, F.J. and Summerscales, J., 'An investigation into the effects of fabric architecture on the processing and properties of fibre reinforced composites produced by RTM'. *Composites Part A*, 1998, **29A**(1/2), 19-27.
24. Pearce, N.R.L., Guild, F.J. and Summerscales, J., 'A study of the effects of convergent flow fronts on the properties of fibre-reinforced composites produced by RTM'. *Composites Part A*, 1998, **29A**(1/2), 141-152.
25. Pearce, N.R.L., Summerscales, J. and Guild, F.J., 'The use of automated image analysis for the investigation of fabric architecture on the processing and properties of fibre-reinforced composites produced by RTM'. *Composites Part A*, 1998, **29A**(7), 829-837.
26. Summerscales, J., Guild, F.J. and Pearce N.R.L., 'The use of fractal dimensions to analyse fabric architecture for fibre reinforced composites produced by RTM', Fourth International Conference on Microscopy of Composite Materials, Institute of Materials, Cirencester, 6-8 April 1998, verbal presentation only.
27. Pearce, N.R.L., Summerscales, J. and Guild, F.J., 'The modification of fabric architecture to improve the processing of continuous fibre reinforced composites manufactured by RTM', Seventh International Conference on Fibre-Reinforced Composites (FRC '98), University of Newcastle-upon-Tyne, 15-17 April 1998, verbal presentation only.
28. Pearce, N.R.L., Guild, F.J. and Summerscales, J., 'The effect of flow-enhancement tows on the mechanical properties of composites produced by the RTM process'. Fifth International Conference on Deformation and Fracture of Composites, Institute of Materials, London, 18-19 March 1999, pp 101-110.
29. Carter, E.J., Fell, A.W., Griffin, P.R. and Summerscales, J., 'Data validation procedures for the automated determination of the two-dimensional permeability tensor of a fabric reinforcement'. *Composites Part A: Applied Science and Manufacturing*, 1996, **27A**(3), 255-261.

30. Carter, E.J., Fell, A.W. and Summerscales, J., 'A simplified model to calculate the permeability tensor of an anisotropic fibre bed'. *Composites Manufacturing*, 1995, **6**(3/4), 228-235.
31. Curtis, P.T., 'CRAG test methods for the measurement of the engineering properties of fibre reinforced plastics', Royal Aerospace Establishment Technical Report 88 012, Farnborough, February 1988.
32. Carr Reinforcements Limited, Unit 1A Heapriding Business Park, Ford Street, Chestergate, Stockport, SK3 0BT UK. ☎ 0161.429.9380 📠 0161.480.5822.

## Voronoi cells, fractal dimensions and fibre composites

John Summerscales<sup>1</sup>, Felicity Guild<sup>2</sup>, Neil Pearce<sup>3</sup> and Paul Russell<sup>4</sup>

<sup>1</sup> *Department of Mechanical and Marine Engineering, University of Plymouth*

<sup>2</sup> *Department of Mechanical Engineering, University of Bristol*

<sup>3</sup> *Devonport Management Limited, Plymouth*

<sup>4</sup> *Department of Biological Sciences, University of Plymouth*

### Abstract

The use of fibre-reinforced polymer matrix composite materials is growing at a faster rate than GDP in many countries. An improved understanding of their processing and mechanical behaviour would extend the potential applications of these materials. For unidirectional composites, it is predicted that localised absence of fibres is related to longitudinal compression failure. The use of woven reinforcements permits more effective manufacture than for unidirectional fibres. It has been demonstrated experimentally that compression strengths of woven composites are reduced when fibres are clustered. Summerscales predicted that clustering of fibres would increase the permeability of the reinforcement and hence expedite the processing of these materials. Commercial fabrics are available which employ this concept using flow-enhancing bound tows. The net effect of clustering fibres is to enhance processability whilst reducing the mechanical properties.

The effects reported above were qualitative correlations. To improve the design tools for reinforcement fabrics we have sought to quantify the changes in the micro-/meso-structure of woven reinforcement fabrics. Gross differences in the appearance of laminate sections are apparent for different weave styles. The use of automated image analysis is essential for the quantification of subtle changes in fabric architecture. This paper considers Voronoi tessellation and fractal dimensions for the quantification of the microstructures of woven fibre-reinforced composites. It reviews our studies in the last decade of the process-property-structure relationships for commercial and experimental fabric reinforcements in an attempt to resolve the processing *versus* properties dilemma. A new flow-enhancement concept has been developed which has a reduced impact on laminate mechanical properties.

### Introduction

The manufacture of fibre reinforced composites has been reviewed by Åström (1997) [1], Gutowski (1997) [2] and Davé and Loos (1999) [3]. Resin Transfer Moulding (RTM) (van Harten, 1993. Potter, 1997. Rudd *et al.*, 1997. Kruckenberg and Paton, 1998. Benjamin and Beckwith, 1999) [4-8] is emerging as the most probable route to mass production for composite components of complex shape. In RTM a mould is loaded with dry fibres, resin then flows into the dry fabric stack and the resin cures to produce a solid component. The success of the process is critically dependent on the rate at which the resin percolates through the fibres. The Darcy (1856) equation [9] is commonly used for simulation of the process. For a fixed geometry, the flow rate is proportional to the pressure gradient and inversely proportional to the resin viscosity. The constant of proportionality is known as the permeability of the porous medium. Summerscales (1993b) [10] predicted that clustering of fibres would increase the resin flow rate in the reinforcement and hence expedite the processing of these materials. Thirion *et al.* (1988) [11] have reported commercial fabrics which employ this concept using flow-enhancing bound tows.

Unidirectional (UD) fibres offer the highest mechanical performance when stresses are primarily in either tension or compression along the fibre axis. For more uniformly distributed stresses, it is common to use cross/angle-ply UD fibre composites. However, the absence of transverse reinforcement within each layer makes these materials liable to splitting parallel to the fibres. For applications where high stiffness and high strength are required together with toughness, woven composites can provide a reasonable balance of stiffness, strength and toughness whilst offering improved processability.

For unidirectional composites, the finite element method (FEM) has been used to predict that the type of packing (Wisnom, 1990) [12] or the degree of randomness (Guild *et al.*, 1990) [13] affects the transverse modulus. Further, FEM has indicated that localised absence of fibres is related to longitudinal compression failure (Guild *et al.*, 1989) [14]. Basford *et al.* (1995) [15] have demonstrated experimentally that compression strengths of woven composites were reduced when fibres were more clustered. The net effect of clustering fibres is generally to enhance processability whilst reducing the mechanical properties.

The effects reported above were qualitative correlations. To improve the design tools for reinforcement fabrics we have sought to quantify the changes in the micro-/meso-structure of woven reinforcement fabrics. Gross differences in the appearance of materialographic sections are apparent for different weave styles. For subtle variations within a single weave style, the eye cannot easily discern changes. The use of automated image analysis (Guild and Summerscales, 1993. Summerscales, 1998) [16, 17] is essential for the quantification of subtle changes in fabric

architecture.

The microstructure of fibre reinforced composites is normally defined by specifying the form of the reinforcement and quantified by measuring the fibre volume fraction and the fibre length/orientation distributions. This data may be insufficient where clustering of fibres occurs. The classification of structured populations can be achieved by a variety of parameters. Early techniques included nearest-neighbour analysis (Clark and Evans, 1954) [18], chi-squared analysis for point patterns (Davis, 1974) [19], quadrat analysis (Greig-Smith, 1952) [20], mean free path and mean random spacing (Cribb, 1978) [21], space auto-correlograms (Mirza, 1970) [22], area fraction variance analysis and mean intercept length analysis (Li *et al.*, 1992) [23] and (for hybrid composites) contiguity index (Short and Summerscales, 1984) [24]. More recently the classification of the structures within composite materials has used either tessellation techniques (Summerscales *et al.*, 1993a. Pyrz, 1994, Ghosh *et al.*, 1997. Pyrz, 2000a. Pyrz, 2000b) [25-29] or fractal dimensions (Taya *et al.*, 1991. Cross, 1994. Worrall and Wells, 1996) [30-32].

This paper will consider Voronoi tessellation and fractal dimensions for quantification of the microstructures of woven fibre-reinforced composites and will review the process-property-structure relationships for commercial and experimental fabric reinforcement materials studied experimentally in an attempt to resolve the processing *versus* properties dilemma.

## EXPERIMENTAL

### Materials

Three sets of woven carbon fibre reinforcement fabrics were studied in the following temporal sequence:

- Carr Reinforcements twill fabric with bound Flow-Enhancing Tows (FET)
- Brochier twill, satin and Injectex FET satin
- Carr Reinforcements twill fabric with new concept FET

### Carr fabrics with bound FET

The Carr fabrics with bound FET were based on a 380 g/m<sup>2</sup> 6K carbon 2x2 twill fabric (Figure 1). The flow enhancement was achieved by binding regularly spaced weft tows to constrain these tows to remain approximately elliptical under compression, thereby creating large porespaces adjacent to the FET. There were four variants plus the reference base fabric:

- fabric twill = normal
- fabric 156 = 12½% FET (1 in 8)
- fabric 150 = 17% FET (1 in 6)
- fabric 148 = 25% FET (1 in 4)
- fabric 126 = 50% FET (1 in 2)

The permeating fluids were Scott Bader Resin E (initial ambient viscosity (IAV): 4600 mPa.s [1 mPa.s = 1 centipoise]) and Jotun 4210 (IAV = 2600 mPa.s) unsaturated polyester resins. The results have been reported more fully elsewhere (Griffin *et al.*, 1995a/b. Guild *et al.*, 1996. Summerscales *et al.*, 1995) [33-36].



Figure 1: Schematics of Carr fabrics

### Brochier fabrics

The Brochier fabrics were all 290 g/m<sup>2</sup> 6K carbon fibre fabrics (Figure 2):

- 2x2 twill (designated E3853/G986)
- normal 5-harness satin (designated E3833/G963)
- flow-enhanced Injectex 5-harness satin (every fifth tow bound in one direction, designated E3795)

The permeating fluid was Ciba-Geigy LY564-1/HY2954 epoxy resin (IAV ~600 mPa.s). The results have been reported more fully elsewhere (Pearce *et al.*, 1998a/b) [37, 38].

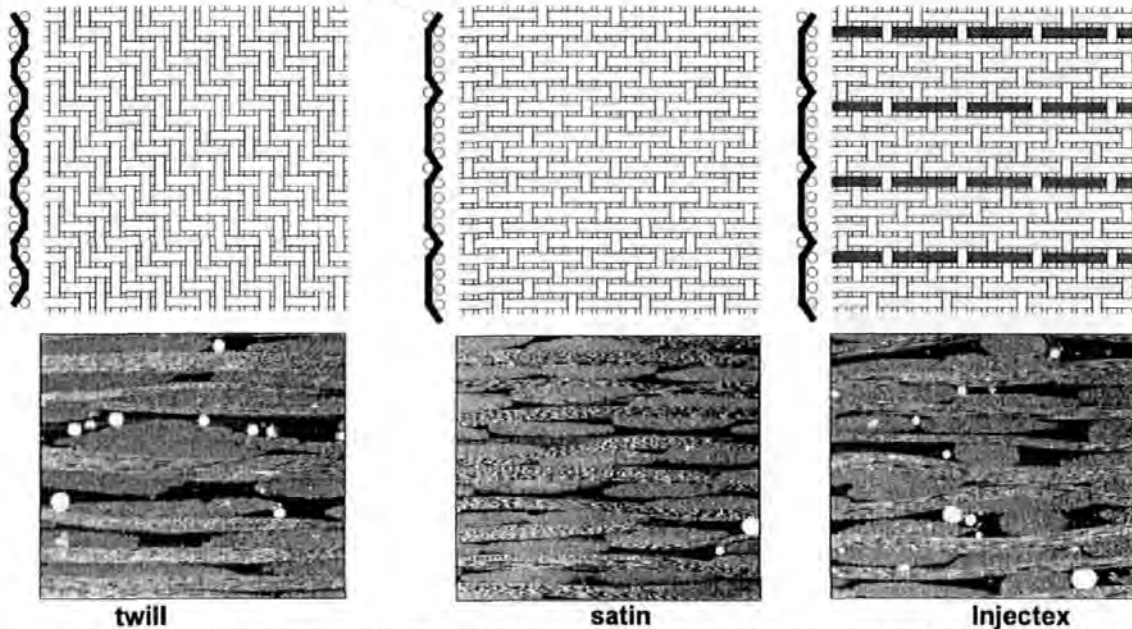


Figure 2: Schematics and transverse micrographs of Brochier weaves. Image frame is 3.6 x 3.0 mm.

### New concept Carr fabrics

The new concept Carr fabrics are based on a 372 g/m<sup>2</sup> 6K carbon 2x2 twill fabric. Flow enhancement is achieved by substitution of some 6K weft tows by 3K tows with a consequent reduction in fabric areal weight:

- | Fabric | Description      | Areal weight         |
|--------|------------------|----------------------|
| D      | normal twill     | 372 g/m <sup>2</sup> |
| C      | 14% FET (1 in 6) | 358 g/m <sup>2</sup> |
| B      | 20% FET (1 in 4) | 353 g/m <sup>2</sup> |
| A      | 33% FET (1 in 2) | 340 g/m <sup>2</sup> |

It is not possible to discern differences between these fabrics with the unaided eye either for dry fabric or sectioned composites. The permeating fluid was SP Ampreg 26 epoxy resin with slow hardener (IAV = 310 mPa.s). The results have been reported more fully elsewhere (Pearce *et al.*, 2000) [39].

### Measurement of permeability/fabrication of test plates

The composite plates were manufactured during radial flow permeability experiments conducted in a glass topped aluminium mould with controlled cavity depth. The apparatus and technique, as used for the Brochier fabrics, has been described elsewhere (Carter *et al.*, 1996) [40] and is subject to progressive refinement. Figure 3 shows frame grabbed images of the advancing flow front during a typical determination of permeability. The images were taken at 36, 201 and 653 seconds into mould fill. Carter *et al.* (1995) [41] have published the theory used for calculation of the permeability.



Figure 3: Frame-grabbed images of a typical radial flow permeability experiment at 36, 201 and 653 seconds. The square mould has an edge length of 440 mm.

## Microscopical analysis

### Preparation

The woven fabric composites were sampled in both warp and weft directions. Individual pieces of full specimen thickness by up to 25 mm length were mounted by casting in cylindrical pots. Each block was polished in six stages to 1  $\mu\text{m}$  and finished with  $\text{AlSiO}_2$  for 2 min (Pearce *et al.*, 1998a/b, Pearce *et al.*, 2000) [37-39].

### Image analysis

Image analysis was undertaken using a Quantimet 570 image analysis system. The following features were measured: individual void areas, numbers of voids, total void area, counts and areas of porespace.

Dirichlet tessellations are constructed such that any point within a cell is closer to the centre of gravity of the feature within that cell than the centre of gravity of any other cell. The boundaries between Dirichlet cells are straight lines which are in effect the perpendicular bisectors between the centres of gravity of features. Dirichlet tessellation characterises clustering from the positions of the features

We have used a specific form of tessellation known as the Voronoi cell to characterise the clustering of the features. The features are "grown" until the surfaces meet and fill the whole space. This normally results in non-linear boundaries between cells. Characterisation of clustering by growing techniques is strongly influenced by the size and shape of the features as well as their positions. A rigorous treatment of the spatial statistics is given in Cressie (1993) [42]. Figure 4a illustrates how, for individual filaments within a bundle, each point in space is assigned to the nearest particle and Figure 4b shows the boundaries constructed from this information. The cells of the tessellation are then analysed to characterise the regions influenced by the non-overlapping particles. The parameters recorded were area, maximum width (horizontal feret), maximum height (vertical feret), perimeter and *x*- and *y*- centres of gravity.

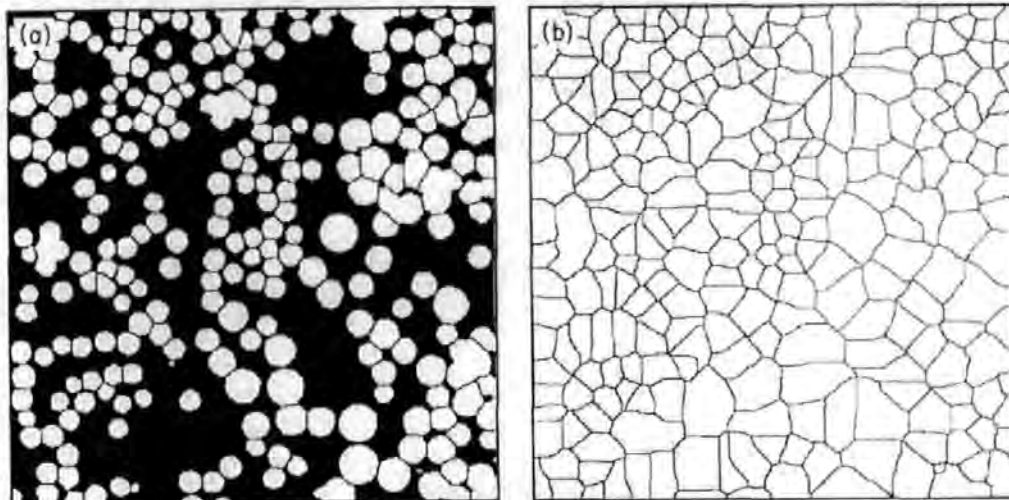


Figure 4: Voronoi tessellation of a section of glass fibre composite (fibre diameters  $\sim 10\text{-}30 \mu\text{m}$ )

To determine the fractal dimension, the microscope image is recorded with 256 grey levels. For example, in Figure 5 we use a double threshold. Surface breaking voids are filled with talc and appear white to permit them to be quantified separately. They are then converted to black along with all the other (darker) intertow porespace by careful selection of threshold levels. The tows are then represented by white. The whole image is mapped with a grid of boxes and those boxes containing any porespace are flagged (Figure 5). A range of square box sizes is used. In each case, the porespace area is measured as the total 'flagged' area. The log (area of filled boxes) is plotted against log (box size). This is known as a Richardson plot. The slope of the graph is the fractal dimension ( $\delta$ ) and gives a unique measurement of the porespace size and distribution. The raw value returned by this process is reported here (note that this value is 0 for a line and 1 for an area. For more conventional representations of dimensions it is necessary to increase this number by unity). The measurement details are summarised in Table 1.

Table 1: Details of image analysis for determination of fractal dimensions

	Brochier [37]	Brochier [38]	Carr new concept [39]
Published reference	Pearce <i>et al.</i> , 1998a	Pearce <i>et al.</i> , 1998b	Pearce <i>et al.</i> , 2000
Pixel frame	512 x 400	480 x 400	480 x 480
Analysis frame area (mm)	4 x 3.125	3.6 x 3.0	2.2 x 2.2
Linear resolution (nm/pixel)	7812	7500	4583
Contiguous frames per sample	six	three	four
Measured area (mm)	24 x 3.125	10.8 x 3	8.8 x 2.2
Specimens per fabric	one	ten	three
Total area per fabric	75 mm <sup>2</sup> /fabric	324 mm <sup>2</sup> /fabric	58 mm <sup>2</sup> /fabric



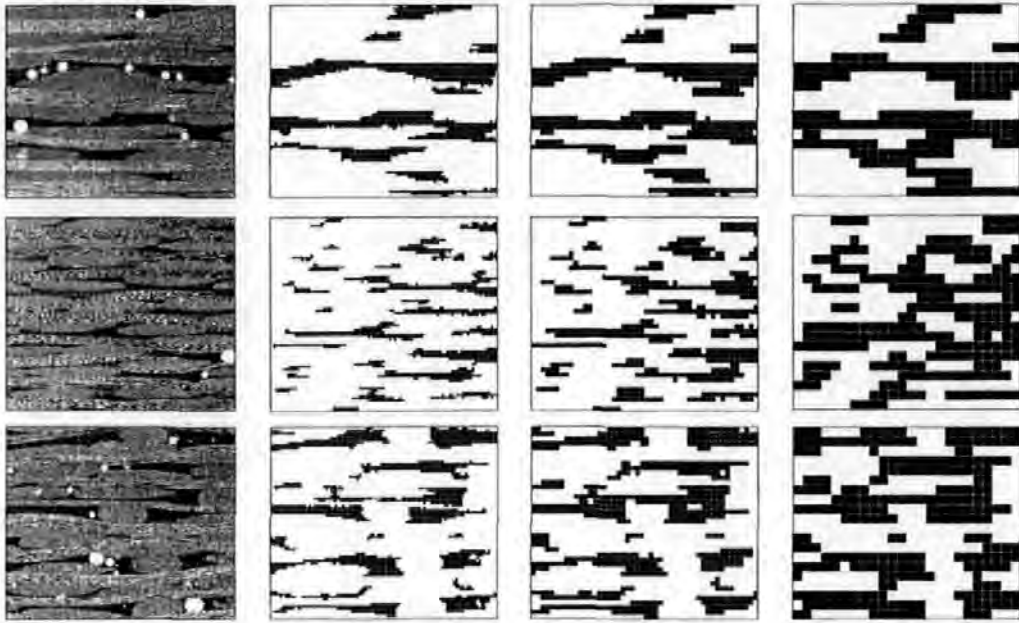


Figure 5: Sections of Brochier weaves with sample frames from the determination of fractal dimensions. Top row: twill, middle row: satin, bottom row: Injectex. Image frame is 3.6 x 3.0 mm. column 1: 480x400 pixel grey image, column 2: 4x4 pixel boxes, column 3: 9x9 pixel boxes, column 4: 19x19 pixel boxes

### Mechanical testing

Mechanical testing was conducted using CRAG test methods (Curtis, 1988) [43]:

- Tensile properties were measured using CRAG method 302 at 5 mm/min crosshead displacement in an Instron 1175 screw-driven universal testing machine with a 100 kN load cell.
- Compression properties were measured using CRAG method 401 at an actuator displacement speed of 2.4 mm/min in an Instron 8500 servo-hydraulic universal testing machine with a 200 kN load cell.

except where otherwise stated (*i.e.* Carr bound FET). All specimens were monitored with TMG 350  $\Omega$  12.5 mm strain gauges fed to a Strawberry Tree data logger recording at 10 Hz. Secant moduli were calculated at 2500  $\mu\epsilon$ .

## RESULTS

### Carr bound tow FET fabrics

Initial attempts to quantify the microstructure of woven fabrics were conducted on Carr fabrics with bound FET. The areas of pore space were collected and histograms were drawn: for example, fabric 126 data is shown in figure 6a. Comparing the histograms, it was apparent that different shapes of histograms were associated with the different fabrics. The differences in the data is clearest when the cumulative curves are plotted as the number of zones *less* than a given size. These cumulative curves, for all 5 fabrics, are shown in figure 6b. The cumulative number has been 'normalised' to account for the small differences in total area measured for the different fabrics. This plot is truncated at small porespace areas corresponding to  $\sim 2\%$  of the area of a typical tow. The relative separation of the plots at around  $0.05 \text{ mm}^2$  appears to correlate with the relative values of permeability (Figure 7), albeit that the range of flow areas chosen is somewhat arbitrary.

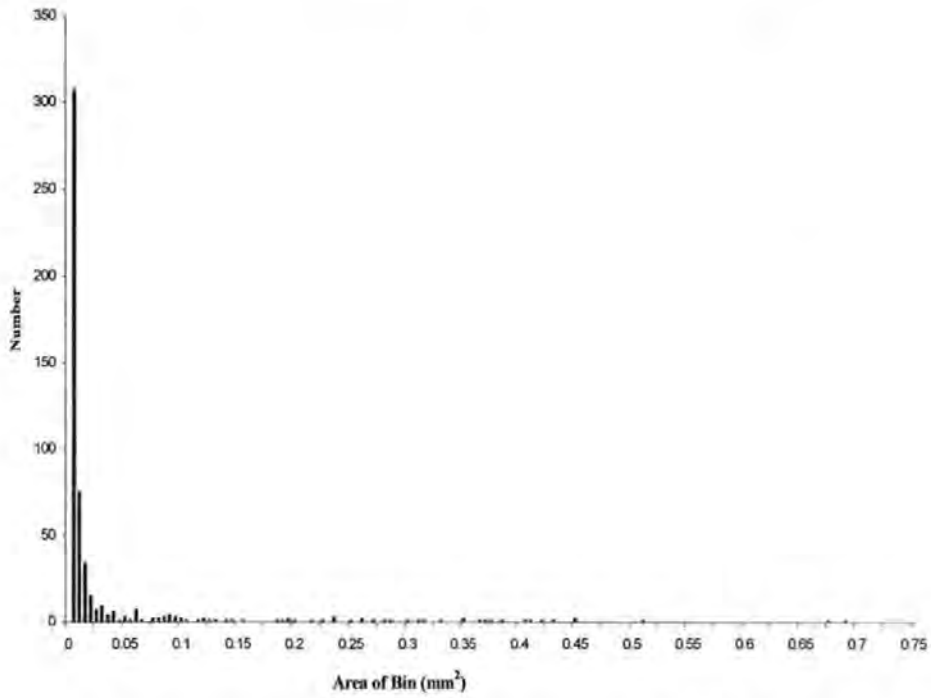


Figure 6a: Histogram of pore space areas for Carr fabric 126

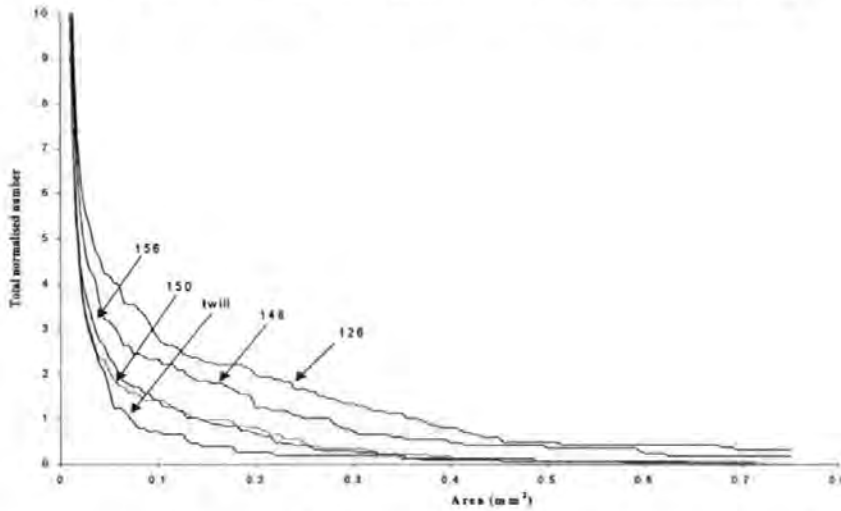


Figure 6b: Cumulative curve of pore space zones less than a given value for Carr fabrics

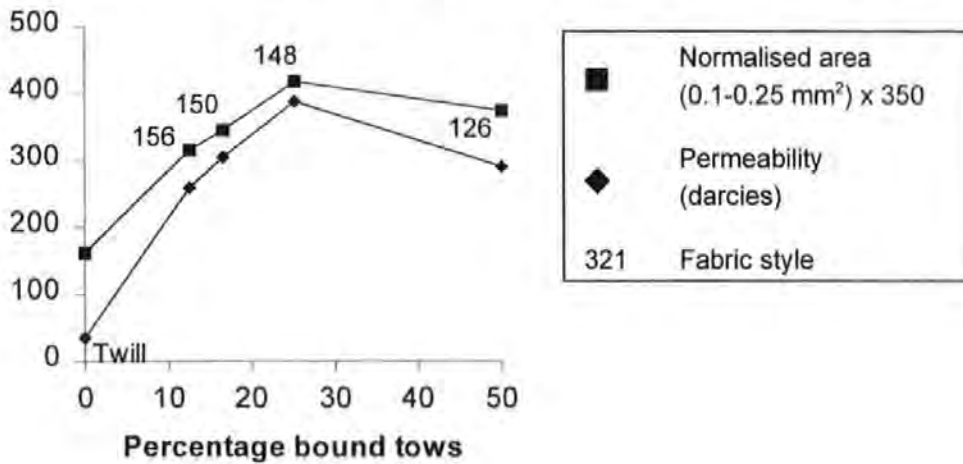


Figure 7: Flow area and permeability plotted against percentage FET for Carr bound tow FET

Basford *et al.* (1995) [15] measured mechanical properties for these composites at constant fibre volume fraction in the Instron 1175 screw-driven test machine. Both the compression strengths (CRAG method 401 at 2 mm/min) and the apparent interlaminar shear strengths (CRAG method 100 at 1 mm/min) decreased with increasing proportion of flow-enhancing tows at constant fibre volume fraction (~43%). The mean values for six specimens of each type are shown in Figure 8. The maximum standard deviation was 26 MPa for compression strengths and 5.2 MPa for ILSS.

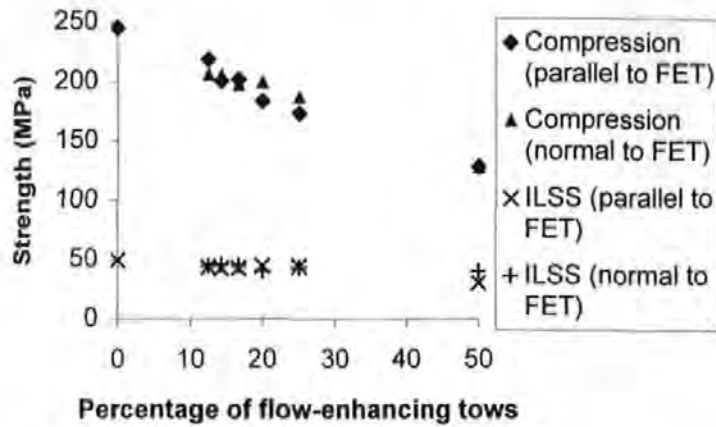


Figure 8: Strengths of Carr fabrics plotted against proportion of flow-enhancing tows in the weft.

**Brochier fabrics**

The use of fractal dimensions to analyse the porespace features normal to the flow enhancing tows clearly differentiates between the structures of the Brochier fabrics: Injectex FET ( $\delta = 0.356$ ), twill ( $\delta = 0.364$ ) and satin without FET ( $\delta = 0.424$ ). The weave style influences porespace distribution (and hence permeability) and fibre crimp (and hence mechanical properties). The relative permeabilities of the fabrics are shown in Figure 9 and the mechanical properties are presented in Table 2. The ranked experimental results (Table 3) for the Brochier fabrics clearly show that a conflict exists between processing (satin is the worst fabric) and mechanical properties (satin is the best fabric).

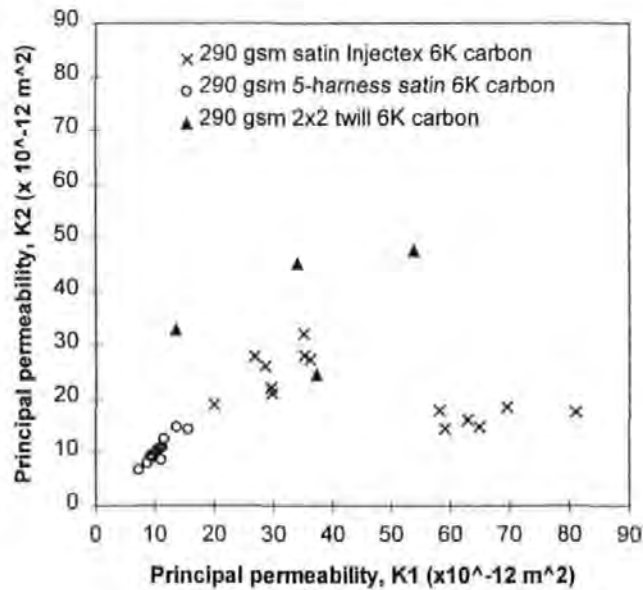


Figure 9: Principal in-plane permeabilities in x (K1) and y (K2) of the Brochier fabrics (units of permeability are  $\times 10^{-12} \text{ m}^2$ )

Table 2: Mechanical properties of Brochier fabrics normal to the FET

	Compression	Tension
<b>Young's moduli (GPa)</b>		
Injectex	50 ± 1.0	52 ± 2.4
Satin	54 ± 1.1	57 ± 1.3
Twill	51 ± 1.3	54 ± 1.3
<b>Strengths (MPa)</b>		
Injectex	339 ± 37.2	767 ± 42.7
Satin	458 ± 66.2	906 ± 34.3
Twill	360 ± 56.5	781 ± 46.2

**Table 3: Ranking of measured properties and quantified microstructures normal to the FET**

	Lowest	Middle	Highest
<i>Processing</i>			
Permeability	satin	Injectex	twill
<i>Mechanical properties</i>			
Tensile Strength/Moduli	Injectex	twill	satin
Compressive Strength/Moduli	Injectex	twill	satin
<i>Fractal analysis</i>			
Inter-tow porespace area	satin	twill	Injectex
Fractal dimension ( $\delta$ )	Injectex	twill	satin

**New concept Carr fabrics**

For the new concept Carr fabrics, the permeabilities and fractal dimensions are both ranked in the sequence ACBD (Figure 10). The fractal dimension ( $\delta$ ) of the base fabric (D) is essentially the same in warp and weft. The value of  $\delta$  is similar for the warp direction for all fabrics.

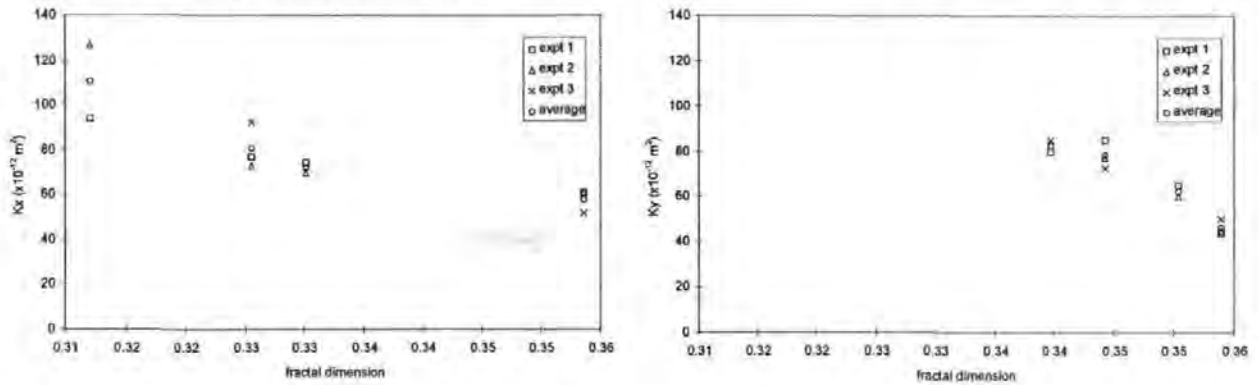


Figure 10:

Permeability plotted against fractal dimension for weft (left) and warp (right) new concept Carr fabrics

The mechanical properties of the new concept Carr fabrics are very similar and show very low scatter for all directions without FET; both warp and weft in the base fabric and the warp direction in FET fabrics (Table 4). The higher scatter in the tensile strength is attributed to the alignment of the mechanical grips in the screw-driven machine being less accurate than that of the hydraulic grips in the servo-hydraulic machine.

**Table 4: Mechanical properties of new concept Carr fabrics**

Secant moduli (GPa)				
	Compression		Tension	
	Warp	Weft	Warp	Weft
A	47 ± 1.10%	40 ± 0.75%	49 ± 0.89%	42 ± 0.37%
B	48 ± 1.02%	43 ± 0.58%	49 ± 1.34%	45 ± 0.82%
C	47 ± 1.24%	44 ± 0.38%	49 ± 0.70%	45 ± 1.25%
D	48 ± 0.51%	47 ± 0.44%	50 ± 0.38%	49 ± 0.84%
%SD	0.58%	5.28%	0.58%	5.70%
Strengths (MPa)				
	Compression		Tension	
	Warp	Weft	Warp	Weft
A	315 ± 1.01%	317 ± 0.25%	706 ± 4.49%	542 ± 3.41%
B	317 ± 0.14%	316 ± 0.86%	704 ± 2.88%	595 ± 3.51%
C	317 ± 0.23%	314 ± 1.55%	718 ± 4.08%	556 ± 4.97%
D	317 ± 0.22%	317 ± 0.18%	720 ± 4.93%	602 ± 3.44%
%SD	0.24%	0.33%	1.01%	4.43%

The weft compression and weft tension moduli decrease broadly in line with the expectations from rule-of-mixtures. The weft tension strength decreases in the same sequence as the fractal dimension (Figure 11). The compression and warp tension strengths are barely affected by the presence of the FET.

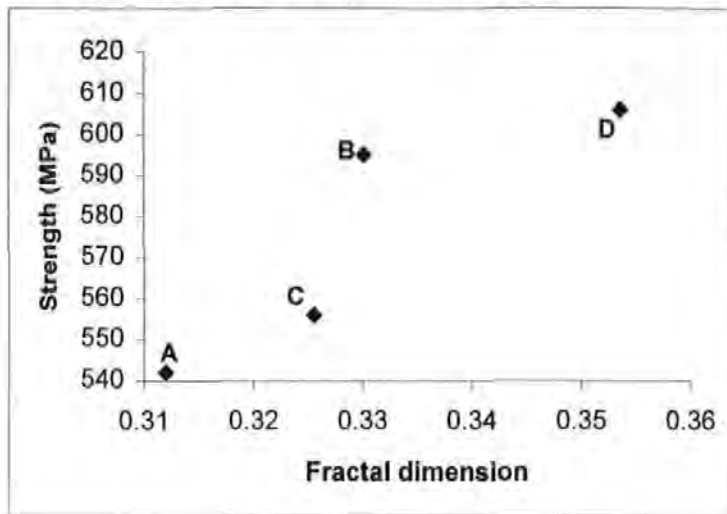


Figure 11: Weft tensile strength plotted against fractal dimension for new concept Carr fabrics

#### Comparison of different fabric sets

Table 5 and Figure 12 present the fractal dimensions and measured permeabilities of the Brochier and new concept Carr FET fabrics. The point at the right-hand end of the twill fabric line is for Brochier material of a lower areal weight, whilst the other points are for new concept Carr fabrics. Note that both the Brochier satin and the new concept Carr fabrics can have permeability doubled by the insertion of flow-enhancement tows.

Table 5: Fractal dimensions and permeabilities for two sets of fabric

Fabric	Fractal dimensions	Permeability ( $10^{-12} \text{ m}^2$ )
<i>Brochier fabrics: 290 gsm</i>		
Satin (no FET)	0.424	8-18
Twill	0.364	34-54
Injectex FET	0.356	19-36
<i>Carr fabrics: 340-372 gsm</i>		
D (base twill)	0.354	41-61
B (20% FET)	0.330	54-75
C (14% FET)	0.326	67-92
A (33% FET)	0.312	72-126

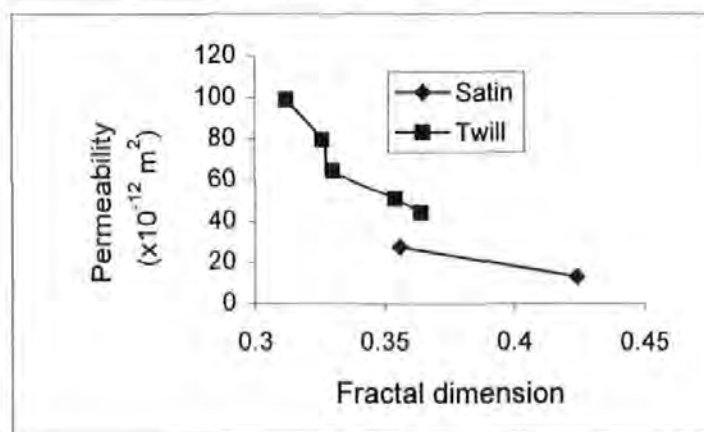


Figure 12: Permeability plotted against fractal dimension for Brochier and new concept Carr fabrics

#### Summary

In this paper we have considered routes to permit the microstructural features of woven composites to be quantified. These techniques have been applied to real woven reinforcement materials. Certain processing and mechanical properties can be correlated to the quantified microstructures, even when no differences can be discerned by eye. New concept Carr fabrics have been developed which appear to achieve appropriate process-property-structure relationships for commercial application, *i.e.* flow enhancement with minimal reduction in mechanical properties.

## Acknowledgements

The authors wish to express their gratitude to the European Union for BRITE/EurAM II grant BE5477 and to EPSRC for research grants GR/J77405 and GR/K04699 which funded this work. Especial thanks are due to Carr Reinforcements Limited (Stockport) for weaving fabrics specifically for this research. Thanks are due to colleagues Eddie Carter, Tony Fell, Patrick Griffin, Eirian Jones, Rana Moyeed, Tim Searle for their helpful discussions and/or assistance with the experimental work. We are also grateful to the anonymous referees for their respective comments on the manuscript.

## References

- Åström, B.T. (1997), *Manufacturing of Polymer Composites*, Chapman & Hall, London. ISBN 0-412-81960-0.
- Basford, D.M., Griffin, P.R., Grove, S.M. and Summerscales, J. (1995), The relationship between mechanical performance and microstructure in composites with flow-enhancing tows, *Composites*, 26(9), 675-679.
- Benjamin, W.P. and Beckwith, S.W. (1999), *Resin Transfer Moulding*, SAMPE Monograph 3, Covina CA. ISBN 0-938-99483-2.
- Carter, E., Fell, A.W. and Summerscales, J. (1995), A simplified model for the derivation of the permeability tensor of an anisotropic fibre bed, *Composites Manufacturing*, 6(3/4), 228-235.
- Carter, E., Fell, A.W., Griffin, P.R. and Summerscales, J. (1996), Data validation procedures for the automated determination of the two-dimensional permeability tensor of a fabric reinforcement, *Composites Part A: Applied Science and Manufacturing*, 27A(4), 255-261.
- Clark, P.J. and Evans, F.C. (1954), Distance to the nearest neighbour as a measure of spatial relationships in population, *Ecology*, 35(4), 445-453.
- Cressie, N.A.C. (1993), *Statistics for Spatial Data*, John Wiley, New York. ISBN 0-471-00255-0.
- Cribb, W.R. (1978), Quantitative metallography of polyphase microstructures, *Scripta Metallurgica*, 12, 893-898.
- Cross, S.S. (1994), The application of fractal geometric analysis to microscopic images, *Micron*, 25(1), 101-113.
- Curtis, P.T. (1988), CRAG test methods for the measurement of the engineering properties of fibre reinforced plastics, *Royal Aerospace Establishment Technical Report RAE TR 88 012*.
- Darcy, H.P.G. (1856), *Les Fontaines Publiques de la Ville de Dijon*, Dalmont, Paris.
- Davé, R.S. and Loos, A.C. (1999), *Processing of Composites*, Hanser Publishers, Munich. ISBN 1-56990-226-7.
- Davis, P. (1974), Data description and presentation, Chapter 3 in *Describing Point Patterns*, Oxford University Press, Oxford, 29-35.
- Ghosh, S., Nowak, Z. and Lee, K. (1997), Tessellation-based computational methods for the characterization and analysis of heterogeneous microstructures, *Composites Science and Technology*, 57(9), 1187-1210.
- Greig-Smith, P. (1952), The use of random and contiguous quadrats in the study of plant communities, *Annals of Botany - London*, NS16, 293-316.
- Griffin, P.R., Grove, S.M., Guild, F.J., Russell, P.M., and Summerscales, J. (1995a), The effect of microstructure on flow promotion in resin transfer moulding reinforcement fabrics, *Journal of Microscopy*, 177(3), 207-217.
- Griffin, P.R., Grove, S.M., Russell, P.M., Short, D., Summerscales, J., Guild, F.J. and Taylor, E. (1995b), The effect of reinforcement architecture on the long-range flow in fibrous reinforcements, *Composites Manufacturing*, 6(3/4), 221-228.
- Guild, F.J., Davy, P.J. and Hogg, P.J. (1989), A model for unidirectional composites in longitudinal tension and compression, *Composites Science and Technology*, 36(1), 7-26.
- Guild, F.J., Davy, P.J. and Hogg, P.J. (1990), A predictive model for the mechanical behaviour of transverse fibre composites, *4th International Conference on Fibre-Reinforced Composites*, Liverpool, 89-99.
- Guild, F.J. and Summerscales, J. (1993), Microstructural image analysis applied to fibre composite materials – a review, *Composites*, 24(5), 383-394.
- Guild, F.J., Pearce, N.R.L., Griffin, P.R. and Summerscales, J. (1996), Optimisation of reinforcement fabrics for the resin transfer moulding of high fibre volume fraction composites, *7th European Conference on Composite Materials*, London, volume 1, pp 273-278.
- Gutowski, T.G. (1997), *Advanced Composites Manufacturing*, John Wiley, New York. ISBN 0-471-15301-x.
- Kruckenberg, T.M. and Paton, R. (editors) (1998), *Resin Transfer Moulding for Aerospace Structures*, Kluwer Academic Publishers, Dordrecht NL. ISBN 0-412-73150-9.
- Q F Li, Q.F., Smith, R. and McCartney, D.G. (1992), Quantitative evaluation of fiber distributions in a continuously reinforced aluminium alloy using automatic image analysis, *Materials Characterization*, 28(3), 189-203.
- Mirza, K. S. M. A. (1970), A statistical study of the structure of mixtures of particulate solids, PhD thesis, University of Exeter.
- Pearce, N.R.L., Summerscales, J. and Guild, F.J. (1998a), An investigation into the effects of fibre architecture on the processing and properties of fibre reinforced composites produced by resin transfer moulding, *Composites Part A: Applied Science and Manufacturing*, 29A(1), 19-27 and 29A(5/6), 707.
- Pearce, N.R.L., Summerscales, J. and Guild, F.J. (1998b), The use of automated image analysis for the investigation of fibre architecture on the processing and properties of fibre reinforced composites made by RTM, *Composites Part A: Applied Science and Manufacturing*, 29A(7), 829-837.

- Pearce, N.R.L., Summerscales, J. and Guild, F.J. (2000), Improving the resin transfer moulding process for fabric-reinforced composites by modification of the fibre architecture *Composites Part A: Applied Science and Manufacturing*, 31A(12), 1433-1441.
- Potter, K. (1997), *Resin Transfer Moulding*, Chapman & Hall, London. ISBN 0-412-72570-3.
- Pyrz, R. (1994), Quantitative description of the microstructure of composites, Part 1: morphology of unidirectional composite systems, *Composites Science and Technology*, 50(2), 197-208.
- Pyrz, R. (2000a), Morphological Characterization of Microstructures, *Comprehensive Composite Materials Encyclopædia, vol. 1: Fiber Reinforcements and General Theory of Composites*, Elsevier, Oxford, pp 465-478.
- Pyrz, R. (2000b), The Application of Morphological Methods to Polymer Matrix Composites, *Comprehensive Composite Materials Encyclopædia, vol. 2: Polymer Matrix Composites*, Elsevier, Oxford, pp 553-576.
- Rudd, C.D., Long, A.C., Kendall, K.N. and Mangin, C.G.E. (1997), *Liquid Composite Moulding*, Woodhead Publishing, Cambridge. ISBN 1-85573-242-4.
- Short, D. and Summerscales, J. (1984), The definition of microstructures in hybrid reinforced plastics, 5th *European Conference of the Society for the Advancement of Materials and Process Engineering*, Montreux.
- Summerscales, J., Green, D. and Guild, F.J. (1993a), Effect of processing dwell time on the microstructure of a fibre reinforced composite, *Journal of Microscopy*, 169(2), 173-182.
- Summerscales, J. (1993b), A model for the effect of fibre clustering on the flow rate in resin transfer moulding, *Composites Manufacturing*, 4(1), 27-31.
- Summerscales, J., Griffin, P.R., Grove, S.M. and Guild, F.J. (1995), Quantitative microstructural examination of RTM fabrics designed for enhanced flow, *Composite Structures*, 32(1-4), 519-529.
- Summerscales, J. (editor) (1998), *Microstructural Characterisation of Fibre-Reinforced Composites*, Woodhead, Cambridge. ISBN 1-85573-240-8.
- Taya, M., Muramatsu, K., Lloyd, D.J. and Watanabe, R. (1991), Determination of distribution patterns of fillers in composites by micromorphological parameters, *JSME International Journal Series I*, 34(2), 198-206.
- Thirion, J.-M., Girardy, H. and Waldvogel, U. (1988), New developments in resin transfer moulding of high-performance composite parts, *Institute of Metals Materials Information Translation of Composites (Paris)*, 28(3), 81-84.
- van Harten, K. (1993), Production by resin transfer moulding, in R A Sheno and J F Wellicome (editors): *Composite Materials in Maritime Structures*, Cambridge University Press, Cambridge, Chapter 4, 86-126.
- Wisnom, M.R. (1990), Factors affecting the transverse tensile strength of unidirectional continuous silicon carbide fibre reinforced 6061 aluminium, *Journal of Composite Materials*, 24(7), 707-726.
- Worrall, C.M. and Wells, G.M. (1996), Fibre distribution in discontinuous fibre reinforced plastic: characterisation and effect on material performance, 7th *European Conference on Composite Materials*, London, vol. 1, pp 247-252.

## References

- 1 B T Åström, *Manufacturing of Polymer Composites*, Chapman & Hall, London, 1997. ISBN 0-412-81960-0.
- 2 T G Gutowski, *Advanced Composites Manufacturing*, John Wiley, New York, 1997. ISBN 0-471-15301-x.
- 3 R S Davé and A C Loos, *Processing of Composites*, Hanser Publishers, Munich, 1999. ISBN 1-56990-226-7.
- 4 K van Harten, 'Production by resin transfer moulding', in R A Sheno and J F Wellicome (editors): *Composite Materials in Maritime Structures*, Cambridge University Press, Cambridge, 1993, Chapter 4, 86-126.
- 5 K Potter, *Resin Transfer Moulding*, Chapman & Hall, London, 1997, ISBN 0-412-72570-3.
- 6 C D Rudd, A C Long, K N Kendall and C G E Mangin, *Liquid Composite Moulding*, Woodhead Publishing, Cambridge, 1997, ISBN 1-85573-242-4.
- 7 T M Kruckenberg and R Paton (editors), *Resin Transfer Moulding for Aerospace Structures*, Kluwer Academic Publishers, Dordrecht NL, 1998, ISBN 0-412-73150-9.
- 8 W P Benjamin and S W Beckwith, *Resin Transfer Moulding*, SAMPE Monograph 3, Covina CA, 1999, ISBN 0-938-99483-2.
- 9 H P G Darcy, *Les Fontaines Publiques de la Ville de Dijon*, Dalmont, Paris, 1856.
- 10 J Summerscales, *Composites Manufacturing*, 1993, 4(1), 27-31.
- 11 J M Thirion *et al*, *Composites (Paris)*, 1988, 28(3), 81-84.
- 12 M R Wisnom, *Journal of Composite Materials*, 1990, 24(7), 707-726.
- 13 F J Guild *et al*, 4th Int Conf Fibre-Reinforced Composites, Liverpool, 1990, 89-99.
- 14 F J Guild *et al*, *Composites Science and Technology*, 1989, 36(1), 7-26.
- 15 D M Basford *et al*, *Composites*, 1995, 26(9), 675-679.
- 16 F J Guild and J Summerscales, *Composites*, 1993, 24(5), 383-394.
- 17 J Summerscales (ed), *Microstructural Characterisation of Fibre-Reinforced Composites*, Woodhead, Cambridge, 1998. ISBN 1-85573-240-8.
- 18 P J Clark and F C Evans, *Ecology*, 1954, 35(4), 445-453.
- 19 P Davis, Chapter 3 in *Describing Point Patterns*, OUP, Oxford, 1974, 29-35.
- 20 P Greig-Smith, *Annals of Botany - London*, 1952, NS16, 293-316.
- 21 W R Cribb, *Scripta Metallurgica*, 1978, 12, 893-898.
- 22 K S M A Mirza, PhD thesis, University of Exeter, 1970.
- 23 Q F Li, R Smith and D G McCartney, *Materials Characterization*, 1992, 28(3), 189-203.
- 24 D Short & J Summerscales, 5th European Conference, SAMPE, Montreux, June 1984.
- 25 J Summerscales, D Green and F J Guild, *Journal of Microscopy*, February 1993, 169(2), 173-182.
- 26 R Pyrz, *Composites Science and Technology*, 1994, 50(2), 197-208.
- 27 S Ghosh, Z Nowak and K Lee, *Composites Science and Technology*, 1997, 57(9), 1187-1210.
- 28 R Pyrz, Morphological Characterization of Microstructures, *Comprehensive Composite Materials, vol. 1: Fiber Reinforcements and General Theory of Composites*, Elsevier, Oxford, 2000, Chapter 16, pp 465-478.
- 29 R Pyrz, The Application of Morphological Methods to Polymer Matrix Composites, *Comprehensive Composite Materials, vol. 2: Polymer Matrix Composites*, Elsevier, Oxford, 2000, Chapter 15, pp 553-576.
- 30 M Taya, K Muramatsu, D J Lloyd and R Watanabe, *JSME International Journal Series I*, 1991, 34(2), 198-206.
- 31 S S Cross, *Micron*, 1994, 25(1), 101-113.
- 32 C M Worrall and G M Wells, 7th European Conference on Composite Materials, London, May 1996, vol. 1, pp 247-252.
- 33 P R Griffin, S M Grove, P M Russell, D Short, J Summerscales and F J Guild, *Composites Manufacturing*, 1995, 6(3/4), 221-228.
- 34 P R Griffin, S M Grove, F J Guild, P M Russell and J Summerscales, *Journal of Microscopy*, March 1995, 177(3), 207-217.
- 35 F J Guild, N R L Pearce, P R Griffin and J Summerscales, 7th European Conference on Composite Materials, London, May 1996, volume 1, pp 273-278.
- 36 J Summerscales, P R Griffin, S M Grove and F J Guild, *Composite Structures*, 1995, 32(1-4), 519-529.
- 37 N R L Pearce, J Summerscales and F J Guild, *Composites*, 1998, 29A(1), 19-27.
- 38 N R L Pearce, J Summerscales and F J Guild, *Composites*, 1998, 29A(7), 829-837.
- 39 N R L Pearce, J Summerscales and F J Guild, Fifth International Conference on Flow Process in Composite Materials, Plymouth, 12-14 July 1999, pp 303-310. ISBN 1-870918-01-0. *Composites Part A*, 2000, 31A(12), 1433-1441.
- 40 E Carter, A W Fell, P R Griffin and J Summerscales, *Composites*, 1996, 27A(4), 255-261.
- 41 E Carter, A W Fell and J Summerscales, *Composites Manufacturing*, 1995, 6(3/4), 228-235.
- 42 N A C Cressie, *Statistics for Spatial Data*, John Wiley, New York, 1993. ISBN 0-471-00255-0.
- 43 P T Curtis, CRAG test methods for the measurement of the engineering properties of fibre reinforced plastics, Royal Aerospace Establishment Technical Report RAE TR 88 012, February 1988.



## APPENDIX B1

### Reinforcements fabrics tested for permeability in University of Plymouth programmes

**Appendix B1-1: Carr Reinforcements twisted tow flow-enhancing 2x2 twill fabrics**

Designation	Areal weight (gsm)	Description	% bound tows
38166	382	normal 2x2 twill fabric	0
156	382	one bound tow in each eight tows	12.5
150	382	one bound tow in each six tows	16.7
148	382	one bound tow in each four tows	25
126	382	one bound tow in each two tows	50

**Appendix B1-2: Fabrics supplied for BRITE EurAM II programme BE5477**

	Code A	Code B	Areal weight (gsm)	Fabric description
Brochier	E3910	G947	160	unidirectional 3K CF
Brochier	E3836	E3836	160	unidirectional 6K CF
Brochier	E3909	G904	190	plain weave 3K CF
Brochier	E3853	G986	290	2x2 twill weave 6K CF
Brochier	E3833	G963	290	5-harness satin 6K CF
(BAe Airbus Ltd)	no code	no code	290	5-harness satin 6K CF
Brochier	E3795	E3795	290	5-harness Injectex satin 6K CF
Brochier	EF630	EF630	630	Injectex glass fibre fabric
Brochier	7781	7781	300	Satin weave glass fibre fabric
Vetrotex	Unifilo	Unifilo	450	random-swirl continuous GF

**Appendix B1-3: Carr Reinforcements new concept flow-enhancing fabrics**

Designation	unsized Toray 3K	twisted Toray 6K	Toray 6K	Areal weight gsm
DWO-313A	x2		x1	313
DWO-313	x1		x2	340
DWO-314	x1		x4	353
DWO-315	x1		x6	358
DWO-316A		x2	x1	372
DWO-316		x1	x2	372
DWO-317		x1	x4	372
DWO-318		x1	x6	372
384000 (Russian) 6K weft mixed with Toray (lots of size).				374

The permeabilities of the fabrics with twisted Toray 6K tows were measured, but no statistically significant difference was found.

## **Appendix B2: Procedure for the conduct of a permeability experiment**

1. Confirm temperature constant at 25°C in the laboratory.
2. Replace the tubes at the resin inlet and the vacuum ports.
3. Apply release agent to the mould and the glass top.
4. Cut the fabric (number of layers appropriate to the required fibre volume fraction) using the template.
5. Place the fabric onto mould within the area defined by the O-ring seal.
6. Lower the glass top into place and release the vacuum lifting grips.
7. Draw full vacuum between the inner and the outer O-ring seals.
8. Position and tighten the clamping framework.
9. Position the lighting frame and switch-on the fluorescent tubes.
10. Position the removable opaque screens on the front and the side of the enclosure to complete the light-tight box.
11. Power-up the Viglen computer and launch C:\RUN.EXE.
12. Enter the initialisation data for the frame grabber.
13. Power-on the XEN computer and the DATAshuttle and launch PERM.WBB.
14. Set up the data acquisition / control system.
15. Mix the resin.
16. Place the resin inside the pressure pot and tighten the lid with the inlet tubing above the surface of the resin.
17. Pull full vacuum at the resin outlet ports to evacuate the mould and degas the resin.
18. Degas for two minutes (sufficient time for pressure pot and resin trap to equalise to within 2 mbar pressure).
19. Slide the resin feed tube further through lid to below the resin surface.
20. Immediately start the process control / data acquisition / frame grabbing systems.
21. Observe the flow front on the frame-grabber monitor until the flow front reaches the mould edge.
22. Stop data acquisition.
23. Stop frame grabbing and remove the opaque screens.
24. Allow the mould to fill.
25. Clamp off the vacuum ports.
26. Apply 300 mbar consolidation pressure at the pressure pot.
27. Save the process data (temperatures and pressures) to a file (file names characteristic to the experiment).
28. Backup / transfer the flow front images as described in Appendix B4.
29. Demould the plate after 24 hours and clean mould surfaces ready for next experiment.

### **The following pages include:**

- Figure B2.1: Schematic diagram of the permeability apparatus.
- Figure B2.2: DATA shuttle worksheet for permeability testing
- Figure B2.3: DATA shuttle display during permeability testing
- DATAshuttle channel/control settings and calculations for permeability testing

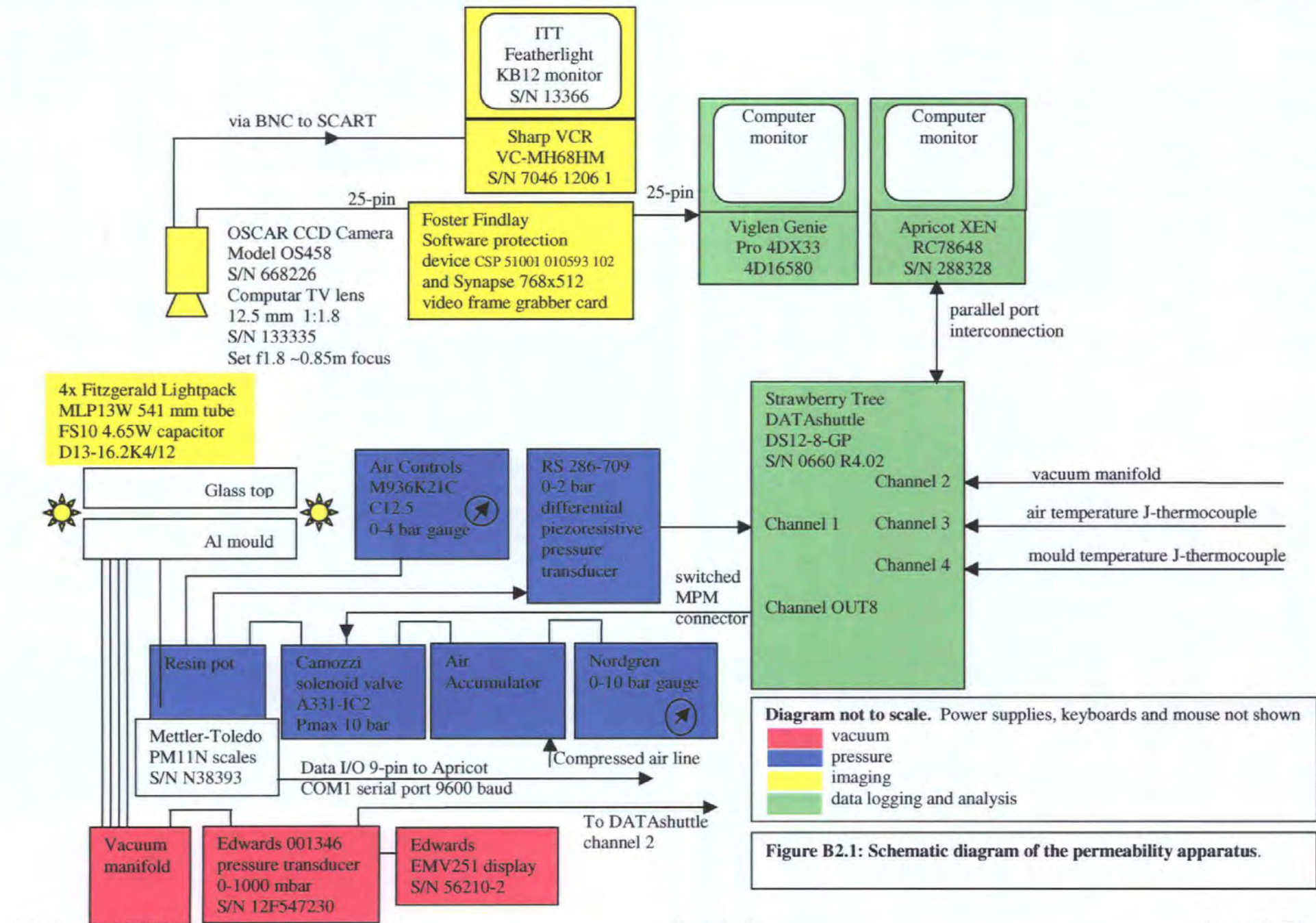


**Figure B2.1: Schematic diagram of the permeability apparatus.**

Figure B2.2: DATA shuttle worksheet for permeability testing

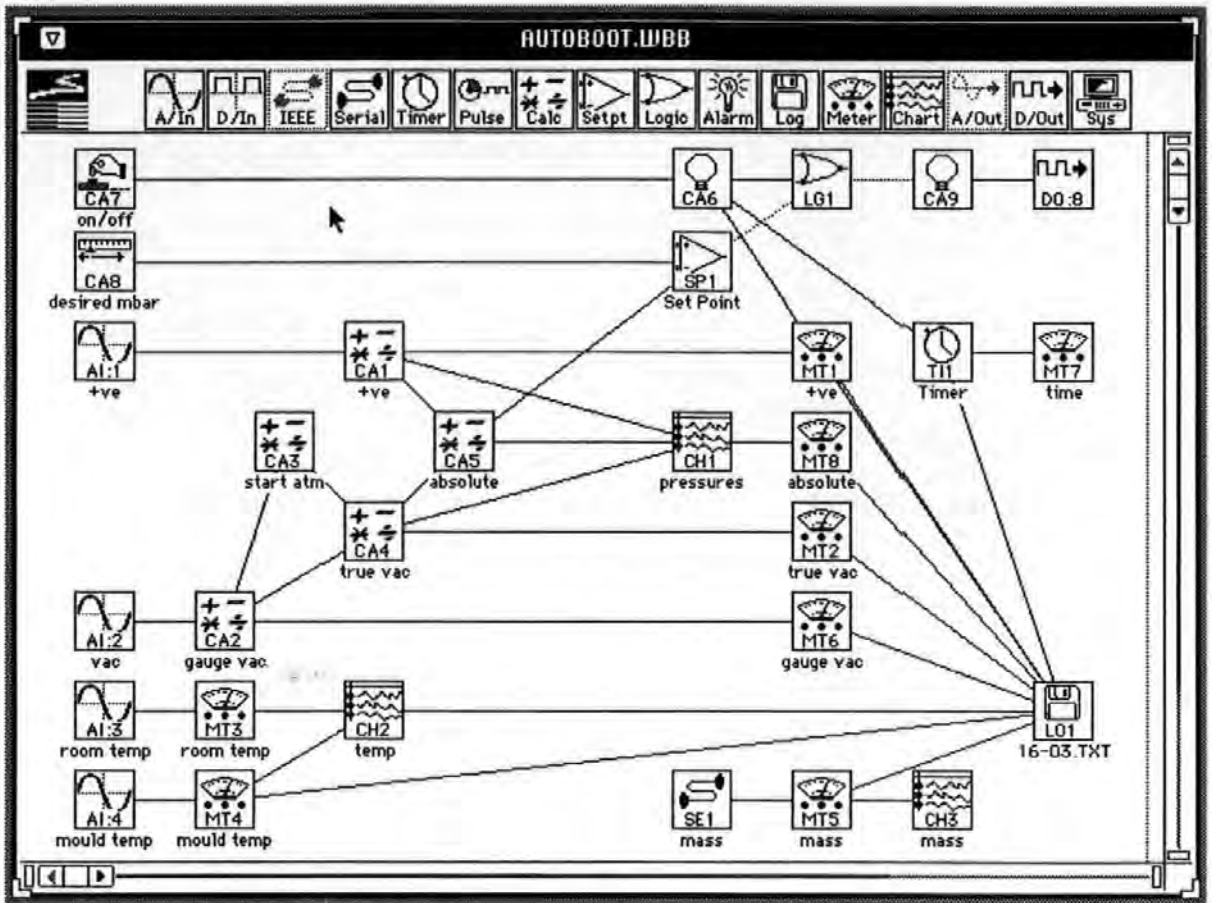
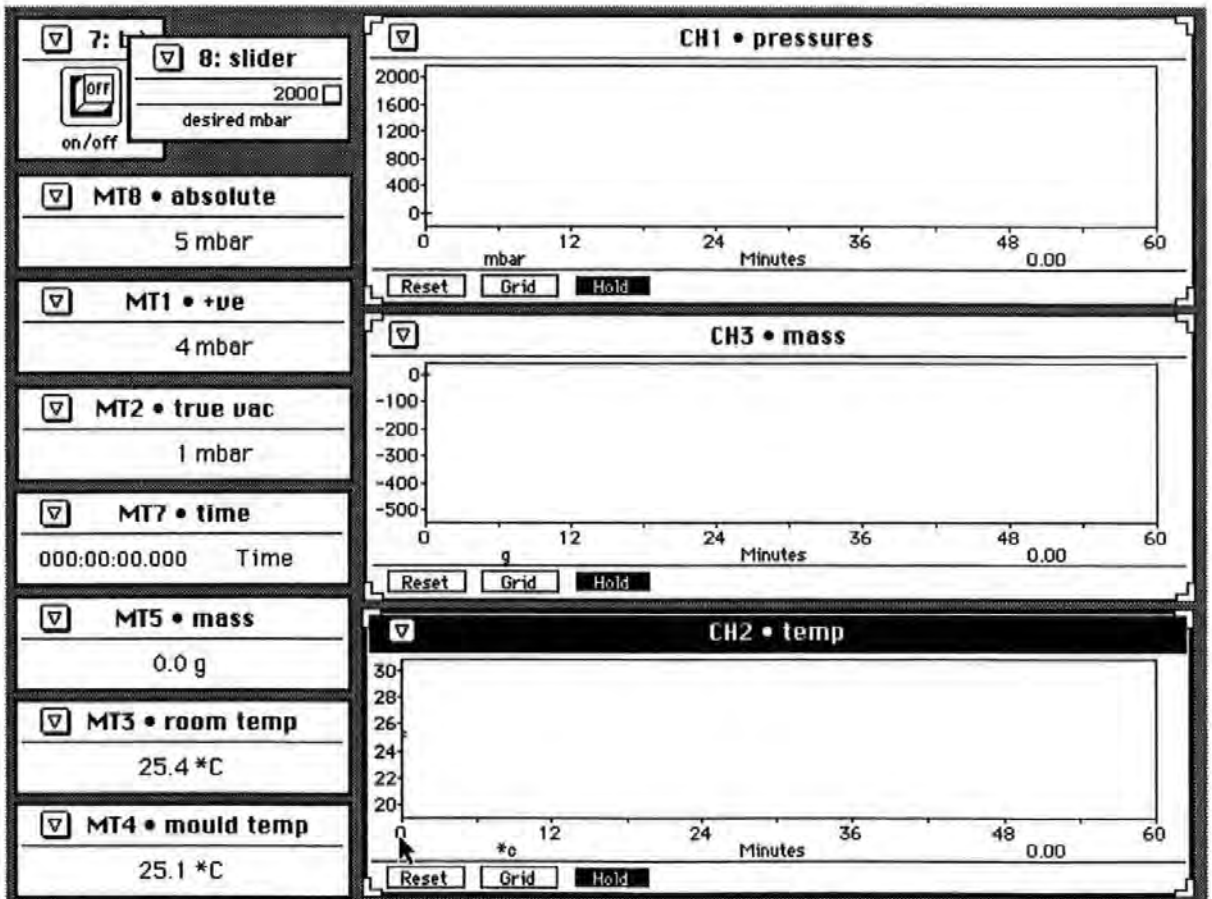


Figure B2.3: DATA shuttle display during permeability testing



**DATASHUTTLE channel/control settings and calculations for permeability testing**

**Abbreviations**

AI Analog input  
AO Analog output (not used)  
CA Calculation  
CH Channel  
CT Counter timer (not used)  
DI Digital input (not used)  
DIO Digital input/output (not used)  
DO Digital output  
LG Logic  
LO Logging file  
MT Meter  
SE Serial connection  
SP Set point  
TI Timer

**Worksheet Name:** PERM.WBB

Hardware list:

Name	AIs	AOs	DIOs	CTs	Dis	DOs
DS-12-8-GP	8	0	8	1	0	0

Maximum icons: 624  
Grid size: 16  
Snap to grid: enabled  
Report Unsynch: < disabled >  
Fast Mode: < disabled >  
Fast Mode samples: 1000  
Fast Mode rate: 1.0 KiloHertz  
Trigger level: -10.0  
Trigger source: Positive  
Trigger slope: Analog  
Trigger mode: None  
Pre-trigger samples: 0  
Com ports: 2

Port: COM 1  
Baud rate: 9600  
Data bits: 7  
Stop bits: 2  
Duplex: Full  
Parity: Even  
XonXoff: < disabled >  
Echo wait: < disabled >  
Line delay: < disabled >

Port: COM 2  
Comment: Mouse connected

IEEE: < disabled >

**Type: Analog Input**

Name: AI:1 +ve  
Card Type: DS-12-8-GP  
Channel Number: 1  
Range: +/-250 mV  
Resolution: Lo Noise (17ms)  
Output Type: Voltage  
Sample rate: 20.0 Hertz  
Fast Mode: < disabled >  
Inputs: < None >  
Outputs: CA1 +ve

Name: AI:2 vac  
Card Type: DS-12-8-GP  
Channel Number: 2  
Range: 500 mV  
Resolution: Lo Noise (17ms)  
Output Type: Voltage  
Sample rate: 20.0 Hertz  
Fast Mode: < disabled >  
Inputs: < None >  
Outputs: CA2 gauge vac

Name: AI:3 room temp  
Card Type: DS-12-8-GP  
Channel Number: 3  
Range: J Type T/C 50 mV  
Resolution: Lo Noise (17ms)  
Output Type: Celcius  
Sample rate: 10.0 Seconds  
Fast Mode: < disabled >  
Inputs: < None >  
Outputs: MT3 room temp

Name: AI:4 mould temp  
Card Type: DS-12-8-GP  
Channel Number: 4  
Range: J Type T/C 50 mV  
Resolution: Lo Noise (17ms)  
Output Type: Celcius  
Sample rate: 10.0 Seconds  
Fast Mode: < disabled >  
Inputs: < None >  
Outputs: MT4 mould temp

**Type: Timer**

Name: TI1 Timer  
Inputs: CA6  
Outputs: MT7 time  
LO1 TRIAL-01.TXT

**Type: Calculation**

Name: CA1 +ve  
Function: aX + bY  
X input: AI:1 +ve  
Y input: 0.0  
"a" constant: 30290.0  
"b" constant: 0.0  
"c" constant: 0.0  
Inputs: AI:1 +ve  
Outputs: MT1 +ve  
CH1 pressures  
CA5 absolute

Name: CA2 gauge vac  
Function: aX + bY  
X input: AI:2 vac  
Y input: 0.0  
"a" constant: 10090.0  
"b" constant: 0.0  
"c" constant: 0.0  
Inputs: AI:2 vac  
Outputs: CA3 start atm  
CA4 true vac  
MT6 gauge vac

Name: CA3 start atm  
 Function: Max(X) for last (a) seconds  
 X input: CA2 gauge vac  
 Y input: 0.0  
 "a" constant: 1.0e+08  
 "b" constant: 0.0  
 "c" constant: 0.0  
 Inputs: CA2 gauge vac  
 Outputs: CA4 true vac

Name: CA4 true vac  
 Function: aX + bY  
 X input: CA3 start atm  
 Y input: CA2 gauge vac  
 "a" constant: 1.0  
 "b" constant: -1.0  
 "c" constant: 0.0  
 Inputs: CA3 start atm  
 CA2 gauge vac  
 Outputs: CH1 pressures  
 MT2 true vac  
 CA5 absolute

Name: CA5 absolute  
 Function: X + Y  
 X input: CA4 true vac  
 Y input: CA1 +ve  
 "a" constant: 0.0  
 "b" constant: 0.0  
 "c" constant: 0.0  
 Inputs: CA4 true vac  
 CA1 +ve  
 Outputs: SP1 Set Point  
 CH1 pressures  
 MT8 absolute

Name: CA6  
 Function: LED indicator  
 X input: CA7 on/off  
 Y input: 0.0  
 "a" constant: 0.0  
 "b" constant: 0.0  
 "c" constant: 0.0  
 Inputs: CA7 on/off  
 Outputs: TI1 Timer  
 LG1 LO1 TRIAL-01.TXT

Name: CA7 on/off  
 Function: Button(a:type)  
 X input: 0.0  
 Y input: 0.0  
 "a" constant: 2.0  
 "b" constant: 0.0  
 "c" constant: 0.0  
 Inputs: < None >  
 Outputs: CA6

Name: CA8 desired mbar  
 Function: Slider(a..b)  
 X input: 0.0  
 Y input: 0.0  
 "a" constant: 0.0  
 "b" constant: 2000.0  
 "c" constant: 0.0  
 Inputs: < None >  
 Outputs: SP1 Set Point

Name: CA9  
 Function: LED indicator  
 X input: LG1  
 Y input: 0.0  
 "a" constant: 0.0  
 "b" constant: 0.0  
 "c" constant: 0.0  
 Inputs: LG1  
 Outputs: DO:8

**Type: Set Point**

Name: SP1 Set Point  
 Function: X > Y  
 X input: CA8 desired mbar  
 Y input: CA5 absolute  
 Dead Band: 0.0  
 Inputs: CA8 desired mbar  
 CA5 absolute  
 Outputs: LG1

**Type: Logic**

Name: LG1  
 Function: X AND Y  
 X input: SP1 Set Point  
 Y input: CA6  
 Inputs: SP1 Set Point  
 CA6  
 Outputs: CA9

**Type: Log**

Name: LO1 TRIAL-01.TXT  
 Log Status: enabled  
 Sample Rate: 1.0 Minutes  
 Gate: CA6  
 Data Format:  
 Heading: trial test 1 59% vf twill x 4 layers  
 plus fabric 16a x 2 2bar desired  
 File Path: F:\  
 File Name: TRIAL-01.TXT  
 Date Stamp: < disabled >  
 Time Stamp: < disabled >  
 Inputs: TI1 Timer  
 MT1 +ve  
 MT2 true vac  
 MT3 room temp  
 MT4 mould temp  
 MT5 mass  
 MT6 gauge vac  
 MT8 absolute CA6  
 Outputs: < None >



**Type: Meter**

Name: MT1 +ve  
Output Type: Fixed Point  
Units: mbar  
Integer: 9  
Decimal: 0  
Inputs: CA1 +ve  
Outputs: LO1 TRIAL-01.TXT

Name: MT2 true vac  
Output Type: Fixed Point  
Units: mbar  
Integer: 9  
Decimal: 0  
Inputs: CA4 true vac  
Outputs: LO1 TRIAL-01.TXT

Name: MT3 room temp  
Output Type: Fixed Point  
Units: \*C  
Integer: 8  
Decimal: 1  
Inputs: AI:3 room temp  
Outputs: CH2 temp  
LO1 TRIAL-01.TXT

Name: MT4 mould temp  
Output Type: Fixed Point  
Units: \*C  
Integer: 8  
Decimal: 1  
Inputs: AI:4 mould temp  
Outputs: CH2 temp  
LO1 TRIAL-01.TXT

Name: MT5 mass  
Output Type: Fixed Point  
Units: g  
Integer: 8  
Decimal: 1  
Inputs: SE1 mass  
Outputs: CH3 mass  
LO1 TRIAL-01.TXT

Name: MT6 gauge vac  
Output Type: Fixed Point  
Units: mbar  
Integer: 9  
Decimal: 0  
Inputs: CA2 gauge vac  
Outputs: LO1 TRIAL-01.TXT

Name: MT7 time  
Output Type: Time  
Units: < None >  
Integer: 6  
Decimal: 3  
Inputs: TI1 Timer  
Outputs: < None >

Name: MT8 absolute  
Output Type: Fixed Point  
Units: mbar  
Integer: 9  
Decimal: 0  
Inputs: CA5 absolute  
Outputs: LO1 TRIAL-01.TXT

**Type: Chart**

Name: CH1 pressures  
Chart Color: White  
X Axis Label: Minutes  
X Axis Min: 0.0  
X Axis Max: 30.0  
Y Axis Label: mbar  
Y Axis Min: 0.0  
Y Axis Max: 2000.0  
Inputs: CA5 absolute  
CA1 +ve  
CA4 true vac  
Outputs: < None >

Name: CH2 temp  
Chart Color: White  
X Axis Label: Hours  
X Axis Min: 0.0  
X Axis Max: 30.0  
Y Axis Label: +c  
Y Axis Min: 20.0  
Y Axis Max: 30.0  
Inputs: MT3 room temp  
MT4 mould temp  
Outputs: < None >

Name: CH3 mass  
Chart Color: White  
X Axis Label: Minutes  
X Axis Min: 0.0  
X Axis Max: 30.0  
Y Axis Label: g  
Y Axis Min: -500.0  
Y Axis Max: 0.0  
Inputs: MT5 mass  
Outputs: < None >

**Type: Digital Output**

Name: DO:8  
Card Type: DS-12-8-GP  
Channel Number: 8  
Inputs: CA9  
Outputs: < None >

**Type: Serial**

Name: SE1 mass  
Sample Rate: 10.0 Seconds  
Port: COM 1  
Trigger: < disabled >  
Initialize with: < None >  
Run Commands: INPUT  
REMOVE (LNN)  
REMOVE (TNN)  
REMOVE (WHITESPACE)   
Terminate With: < None >  
Inputs: < None >  
Outputs: MT5 mass

## Appendix B3:

### Mathematics for calculation of anisotropic permeability from a radial flow experiment

The composite plates were manufactured during radial flow permeability experiments conducted in a glass topped aluminium mould with controlled cavity depth. The apparatus and technique, as used for the Brochier fabrics, has been described elsewhere [B3-1] and has been subject to progressive refinement. These enhancements include tighter control of pressure levels (Appendix B2) and of cavity depth through the use of a 53 mm laminate of two 25 mm glass plates for the mould top. Figure B3-1 shows frame grabbed images of the advancing flow front during a typical flow experiment. The images were taken at 36, 201 and 653 seconds into mould fill. Chan and Hwang [B3-2] proposed a method to calculate the anisotropic permeability using Darcy's law in polar co-ordinates. Carter *et al.* [B3-3] modified this method to eliminate the need for scaling of the inlet diameter: this approach has been used for the permeabilities reported in this paper. Weitzenböck *et al.* [B3-4] have reported that this modified approach “significantly improves the accuracy of the calculated anisotropic permeability because no scaling of the inlet diameter is done”.



Figure B3-1: Frame-grabbed images of a typical radial flow permeability experiment at 36, 201 and 653 seconds. The square mould has an edge length of 440 mm.

This work is a development of the papers by Adams, Russel and Rebenfield [B3-5] and by Chan and Hwang [B3-2], referred to hereafter as papers 1 and 2, respectively. The first paper described a new model. The second paper derived a more easily applied model, achieved by incorporating novel ideas into the work of the first paper. Both papers have been successfully tested against experiment. The work in the two papers above has been unified and simplified using first principles. The equations presented can be used to calculate the values of the permeability tensor from observations of the expanding two-dimensional radial flow front.

#### *The mathematical model*

*Practical considerations and assumptions.* The model considers the radial flow of resin into a fibre bed constrained between parallel plates. The resin is assumed to flow according to Darcy's law. The assumptions made in papers 1 and 2 apply to this model. These assumptions include the following important points:

- i. The resin is incompressible;
- ii. The resin has constant viscosity and constant temperature whilst flowing;
- iii. The fibre bed is homogeneous and inelastic;
- iv. Edge, gravitational and surface tension effects are not significant;
- v. The resin pressure at the inlet is constant; and
- vi. The resin pressure at the flow front is zero.

Note that (ii) implies that the resin does not react chemically as it flows. That is, flow and cure are considered to be independent processes occurring sequentially in time.

The good agreement between the models of papers 1 and 2 and their respective experimental results shows that these assumptions are reasonable.

In practice, the resin will be made to flow from a circular entry port into a fibre bed in a mould. Vacuum will be applied to the mould cavity. The mould must be properly dimensioned and have well controlled heating. Care must be taken when laying up the fibre bed as the model is unable to address local irregularities within the bed. These irregularities may be due to poor manufacture, poor loading or poor cutting of the fibre mat. A circular entry port permits the ingress of resin into the fibre bed. Clustering of the fibres has been shown to be of particular significance in the determination of flow rates [B3-6].

*Theoretical considerations: isotropic flow.* The authors of papers 1 and 2 above used resin as the flowing fluid. This was due to their interest in resin transfer moulding. The model works for any fluid satisfying the assumptions. For generality, the word fluid will be used throughout the rest of this Appendix.

When the fibre bed is isotropic, the fluid flows out equally in all directions from the entry port. In this case, the Darcy law becomes:

$$-v_r = \frac{k}{\mu} \frac{dP}{dr} \quad (\text{Eq. 1})$$

By continuity:  $2\pi r_0 v_0 = 2\pi r v_r$  (Eq. 2)

The symbols used in equations (Eq. 1) and (Eq. 2) relate to physical properties as follows:

- $k$  the constant of permeability for the fibre bed;
- $r_0$  radius of the inlet port;
- $r$  radial distance from the centre of the inlet port;
- $v_0$  superficial fluid velocity at the boundary of the inlet port;
- $v_r$  superficial fluid velocity at radial position  $r$ ;
- $\mu$  fluid viscosity;
- $dP/dr$  the radial pressure gradient in the fluid at  $r$ ;  
the gradient is positive in the direction of flow.

The superficial velocity  $v_r$  is defined by:

$$v_r = \varepsilon v_f \quad (\text{Eq. 3})$$

where  $\varepsilon$  is the void fraction (porosity) and  $v_f$  is the flow front velocity at radial distance  $r$ .

Rearranging equation (Eq. 2) gives

$$v_r = \frac{r_0 v_0}{r} \quad (\text{Eq. 4})$$

Substituting equation (Eq. 4) into equation (Eq. 1) and rearranging we have:

$$\frac{k}{\mu} dP = -\frac{r_o v_o}{r} dr \quad (\text{Eq. 5})$$

The pressure at the flow front is zero (since vacuum is applied and continuity of pressure is maintained across the front). The integral of the reciprocal of  $r$  with respect to  $r$  is  $\ln(r)$ , hence integrating over the area of fluid flow we have:

$$\frac{k}{\mu} P_o = r_o v_o \ln\left(\frac{r}{r_o}\right) \quad (\text{Eq. 6})$$

Substituting equation (Eq. 4) into equation (Eq. 6) gives

$$\frac{k}{\mu} P_o = r v_r \ln\left(\frac{r}{r_o}\right) \quad (\text{Eq. 7})$$

From equation (Eq. 3):

$$v_f = \frac{v_r}{\varepsilon} \quad (\text{Eq. 8})$$

Since the front has velocity equal to the local rate of change of  $r$  with time ( $t$ ) then:

$$\frac{v_r}{\varepsilon} = \frac{dr}{dt} \quad (\text{Eq. 9})$$

Substituting equation (Eq. 9) into equation (Eq. 7) we have:

$$\frac{kP_o}{\varepsilon\mu} dt = r \ln\left(\frac{r}{r_o}\right) dr \quad (\text{Eq. 10})$$

Where  $r$  now represents the radial distance to the flow front from the centre of the inlet port. Integrating equation (Eq. 10) we have:

$$\frac{kP_o}{\varepsilon\mu} \int_{t=0}^T dt = \int_{r=r_o}^R r \ln\left(\frac{r}{r_o}\right) dr \quad (\text{Eq. 11})$$

where  $T$  is the time taken to fill to radial distance  $R$ .

Using the product rule for integration (integration by parts) in equation (Eq. 11) we have:

$$\frac{kP_o}{\varepsilon\mu} \int_{t=0}^T dt = \int_{r=r_o}^R \ln\left(\frac{r}{r_o}\right) d\left(\frac{r^2}{2}\right) \quad (\text{Eq. 12})$$

Therefore

$$\frac{kP_o}{\varepsilon\mu} T = \left[ \frac{r^2}{2} \ln \frac{r}{r_o} \right]_{r_o}^R - \int_{r=r_o}^R \frac{r^2}{2} \frac{d}{dr} \ln\left(\frac{r}{r_o}\right) dr \quad (\text{Eq. 13})$$

$$\frac{kP_o}{\varepsilon\mu}T = \left[ \frac{r^2}{2} \ln \frac{r}{r_o} \right]_{r_o}^R - \int_{r=r_o}^R \frac{r^2}{2} \frac{1}{r} dr \quad (\text{Eq. 14})$$

or

$$\frac{kP_o}{\varepsilon\mu}T = \frac{R^2}{2} \ln \left( \frac{R}{r_o} \right) - \frac{R^2}{4} + \frac{r_o^2}{4} \quad (\text{Eq. 15})$$

On rearranging equation (Eq. 15) we have:

$$\frac{R^2}{4} \left[ 2 \ln \left( \frac{R}{r_o} \right) - 1 \right] + \frac{r_o^2}{4} = \frac{kP_o}{\varepsilon\mu}T \quad (\text{Eq. 16})$$

Equation (Eq. 16) becomes non-dimensional by substituting  $\rho = R/r_o$  and then dividing through by  $r_o^2$ . Denoting the right-hand side of the new equation by  $\Phi$  we have:

$$\rho^2 (2 \ln \rho - 1) + 1 = \frac{4kP_o}{\varepsilon\mu r_o^2}T = \Phi \quad (\text{Eq. 17})$$

where  $\Phi$  can be viewed as a dimensionless time, and  $\rho$  can be viewed as a dimensionless length.

In this dimensionless form, equation (Eq. 17) is the same result as obtained in paper 1. It has been obtained from first principles rather than from the construction and solution of the Laplace equation in polar co-ordinates.

*Theoretical considerations: anisotropic flow.* In this case the flow will not have a circular flow front but rather an elliptical one. This is a consequence of Darcy's law which now takes the form:

$$-\bar{\mathbf{v}} = \frac{\bar{\mathbf{K}}}{\mu} \text{grad}P \quad (\text{Eq. 18})$$

The mass flux continuity equation generalises to:

$$\text{div} \bar{\mathbf{v}} = 0 \quad (\text{Eq. 19})$$

where  $\bar{\mathbf{v}}$  is the fluid superficial velocity vector at some point within the region of flow and  $\text{grad}P$  is the pressure gradient experienced by the fluid at the same point. The flow can be considered to be two-dimensional in the plane of the mould. This is the same as the plane of the principal axes (see paper 1). Thus the permeability tensor  $\bar{\mathbf{K}}$  becomes a 2x2 matrix and  $\text{grad}P$  and  $\bar{\mathbf{v}}$  both become 2x1 vectors.

The governing equation is now derived. Let the first and second principal axes be the x- and y-axes, respectively. Within this axes system the permeability tensor  $\bar{\mathbf{K}}$  is given by

$$\bar{\mathbf{K}} = \begin{pmatrix} K_{11} & 0 \\ 0 & K_{22} \end{pmatrix} \quad (\text{Eq. 20})$$

and

$$\text{grad } P = \begin{pmatrix} \partial P / \partial x \\ \partial P / \partial y \end{pmatrix} \quad (\text{Eq. 21})$$

The diagonal terms,  $K_{11}$  and  $K_{22}$ , of equation (Eq. 20) are the principal permeabilities in the direction of the first and second principal axes (directions), respectively.

Substituting equations (Eq. 20) and (Eq. 21) into equation (Eq. 18), and taking the divergence of both sides, gives:

$$\text{div} \left[ \begin{pmatrix} K_{11} & 0 \\ 0 & K_{22} \end{pmatrix} \begin{pmatrix} \partial P / \partial x \\ \partial P / \partial y \end{pmatrix} \right] = 0 \quad (\text{Eq. 22})$$

Expanding equation (Eq. 22) gives:

$$K_{11} \frac{\partial^2 P}{\partial x^2} + K_{22} \frac{\partial^2 P}{\partial y^2} = 0 \quad (\text{Eq. 23})$$

Since it is the relative magnitudes of  $K_{11}$  and  $K_{22}$  that determine the aspect ratio of the flow front, we set:

$$\alpha = \frac{K_{22}}{K_{11}} \quad (\text{Eq. 24})$$

And obtain the governing equation:

$$\frac{\partial^2 P}{\partial x^2} + \alpha \frac{\partial^2 P}{\partial y^2} = 0 \quad (\text{Eq. 25})$$

When  $\alpha = 1$  the fibre bed is isotropic and flow is then governed by the Laplace equation. We showed in the previous section that it was not necessary to solve the Laplace equation for isotropic flow. In this section, we shall now show that it is also not necessary to solve equation (Eq. 25) for anisotropic flow.

As in paper 1, we make the substitution

$$x^* = \alpha^{1/4} x \quad (\text{Eq. 26})$$

$$y^* = \alpha^{-1/4} y \quad (\text{Eq. 27})$$

into equation (Eq. 25) to obtain

$$\frac{\partial^2 P}{\partial x^{*2}} + \frac{\partial^2 P}{\partial y^{*2}} = 0 \quad (\text{Eq. 28})$$

Which is, of course, the Laplace equation. However, we know that the Laplace equation is the governing equation for isotropic flow. Thus, in the domain  $(x^*, y^*)$ , the anisotropic flow transforms to an equivalent isotropic flow with a circular flow front about the centre

of the inlet port. Thus, at some time  $t$  into the flow:

$$(x^*)^2 + (y^*)^2 = R^2 \quad (\text{Eq. 29})$$

Where  $R$  is the radius of the flow front at time  $t$ .

Substituting equations (Eq. 26) and (Eq. 27) into (Eq. 29) gives:

$$x^2 \alpha^{1/2} + y^2 \alpha^{-1/2} = R^2 \quad (\text{Eq. 30})$$

or

$$\frac{x^2}{R^2 \alpha^{-1/2}} + \frac{y^2}{R^2 \alpha^{1/2}} = 1 \quad (\text{Eq. 31})$$

Equation (Eq. 31) is the equation of an ellipse with major and minor axes  $a$  and  $b$ , where:

$$\frac{a^2}{b^2} = \frac{R^2 \alpha^{-1/2}}{R^2 \alpha^{1/2}} \quad (\text{Eq. 32})$$

That is

$$\alpha = \frac{b^2}{a^2} \quad (\text{Eq. 33})$$

Equation (Eq. 33) relates the ratio of the principal permeabilities to the aspect ratio of the expanding elliptical flow front. At any flow time  $t$ , the volume of fluid flowed can be calculated in either the  $(x,y)$  or the  $(x^*,y^*)$  system. Since both describe the same physical situation the same value will be obtained in each case, and we therefore have

$$\pi ab = \pi R^2 \quad (\text{Eq. 34})$$

and the radius of the circular flow front in the isotropic case is given by:

$$R = \sqrt{ab} \quad (\text{Eq. 35})$$

The permeability relating to the equivalent isotropic flow is defined by the equivalent permeability (denoted by  $k$ ) given by the equation:

$$k = \sqrt{K_{11} K_{22}} \quad (\text{Eq. 36})$$

The derivation of this equation is given below.  $K_{11}$  and  $K_{22}$  represent the principal permeabilities. For convenience they are also referred to respectively as  $k_x$  and  $k_y$  in the work which follows. That is, we set:

$$K_{11} = k_x \quad (\text{Eq. 37})$$

$$K_{22} = k_y \quad (\text{Eq. 38})$$

And hence from equation (Eq. 24):

$$\alpha = \frac{k_y}{k_x} \quad (\text{Eq. 39})$$



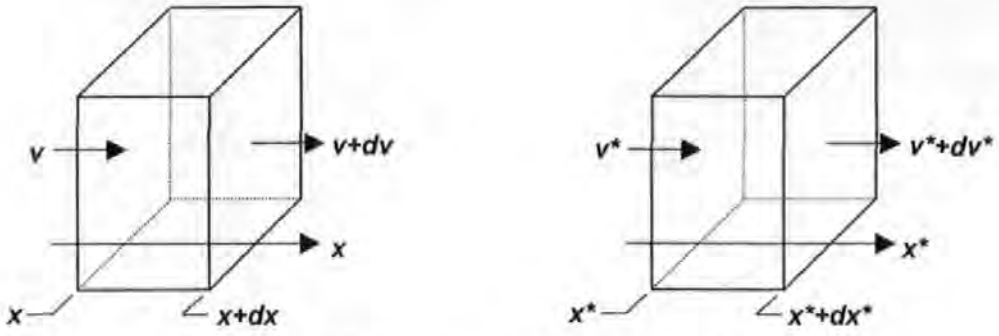


Figure B3-2: Flow through an elemental volume.

*Derivation of  $k = \sqrt{k_x k_y}$ .* The left-hand side of Figure B3-2 shows an elemental volume situated at some point on the principal x-axis within the anisotropic flow regime. The right-hand side of Figure B3-2 shows the transformed situation within the equivalent isotropic flow regime.

Equation (Eq. 26) relates  $x^*$  to  $x$  by a simple stretch. The axes  $x^*$  and  $x$  will coincide and have a common origin at the centre of the inlet port. Also, the pressure at  $x^*$  will equal the pressure at  $x$  and the pressure at  $x^* + dx^*$  will equal the pressure at  $x + dx$ . Thus the increments in pressure will also be equal. That is:

$$dP^* = dP \quad (\text{Eq. 40})$$

By Darcy's law: 
$$-\mu \frac{dx^*}{dt} = k \frac{dP^*}{dx^*} \quad (\text{Eq. 41})$$

and 
$$-\mu \frac{dx}{dt} = k_x \frac{dP}{dx} \quad (\text{Eq. 42})$$

Substituting equation (Eq. 40) into equation (Eq. 41) and dividing the resulting equation by equation (Eq. 42) gives:

$$\frac{dx^*}{dx} = \frac{k}{k_x} \frac{dx}{dx^*} \quad (\text{Eq. 43})$$

But the transformation is a stretch, therefore:

$$dx^* = \alpha^{1/4} dx \quad (\text{Eq. 44})$$

Substituting equation (Eq. 44) into equation (Eq. 43) and rearranging we have:

$$\frac{k}{k_x} = \alpha^{1/2} = \left( \frac{k_y}{k_x} \right)^{1/2} \quad (\text{Eq. 45})$$

Rearranging equation (Eq. 45) we have:

$$k = \sqrt{k_x k_y} \quad (\text{Eq. 46})$$

*Anisotropic permeabilities.* We are now in a position to obtain the principal permeabilities and, by application of Darcy's law, to extend the analysis to obtain the general permeability tensor. This tensor will relate to the experimental co-ordinate system. The co-ordinate axes of this system shall have their origin at the centre of the inlet port and may be rotated through some angle  $\theta$  with respect to the principal  $x$ -axis.

It would be simpler to align the general co-ordinate system with the principal axis. In practice this cannot be done, of course, as the directions of the principal axes are not necessarily known until after the experiment has been carried out.

The next section closely follows the work of Chan and Hwang [B3-2]. However, no use is made of eigenvalue theory. Instead, Darcy's law is applied to obtain the same results.

From equations (Eq. 17), (Eq. 33) and (Eq. 46) and experimental observation of the progress of the flow front, the principal permeabilities may easily be found.

- (i) Plot the simultaneous values of  $b$  against  $a$ , where  $b$  is the length of the minor axis of the elliptical flow front and  $a$  is the length of the major axis.
- (ii) The slope of the regression line through the origin for the graph obtained in (i) is equal to  $\sqrt{\alpha}$  by equation (Eq. 33), i.e.

$$slope_{(1)} = \frac{\sqrt{k_y}}{\sqrt{k_x}} \quad (\text{Eq. 47})$$

- (iii) Use equation (Eq. 26) to convert the data for the increase of the major axis of the elliptical flow front with time from the anisotropic flow regime to the equivalent isotropic flow regime. These converted data now relate to the radial increase with time of a circular flow front in an isotropic medium. Equation (Eq. 17) now applies.
- (iv) Plot  $\Phi$  of equation (Eq. 17) against time of fill (note that in equation (Eq. 17) the symbol  $T$  is used to denote this time). The slope of the regression line for this plot is

$$slope_{(2)} = \frac{4P_o k}{\mu \epsilon_o^2} \quad (\text{Eq. 48})$$

- (v) Substituting equation (Eq. 46) into equation (Eq. 48) we have:

$$slope_{(2)} = \frac{4P_o \sqrt{k_x} \sqrt{k_y}}{\mu \epsilon_o^2} \quad (\text{Eq. 49})$$

- (vi) From equation (Eq. 47) we have:

$$\sqrt{k_y} = \sqrt{k_x} slope_{(1)} \quad (\text{Eq. 50})$$

Substituting equation (Eq. 50) into equation (Eq. 49) we have:

$$slope_{(2)} = \frac{4P_o \sqrt{k_x} \sqrt{k_x} slope_{(1)}}{\mu \epsilon_o^2} = \frac{4P_o k_x slope_{(1)}}{\mu \epsilon_o^2} \quad (\text{Eq. 51})$$

Rearranging equation (Eq. 51) we have:

$$k_x = \frac{\mu \sigma_o^2 \text{slope}_{(2)}}{4P_o \text{slope}_{(1)}} \quad (\text{Eq. 52})$$

(vii)  $k_y$  is obtained by substituting  $k_x$  into equation (Eq. 39).

It now remains to obtain the full permeability tensor using the values of  $k_x$  and  $k_y$  and the angle between the chosen experimental axes and the principal axes (the principal axes are aligned with the major and minor axes of the elliptical flow front). This can be achieved using the anisotropic form of Darcy's law and the frame independence of vector results.

Consider pressure gradient acting along the principal  $x$ -direction, then:

$$\bar{V} = -\frac{k_x}{\mu} \frac{dP}{dx} \quad (\text{Eq. 53})$$

Expressing the fluid pressure gradient along the principal axis in both the principal and experimental co-ordinate systems, using Darcy's law and equating the results we have:

$$\bar{K}\bar{V} = k_x \bar{V} \quad (\text{Eq. 54})$$

where  $K$  is the full permeability tensor. Let this be given in the experimental axes system by:

$$\bar{K} = \begin{pmatrix} k_{11} & k_{12} \\ k_{21} & k_{22} \end{pmatrix} \quad (\text{Eq. 55})$$

Also, let  $\bar{V}$  have components  $v_1$  and  $v_2$  in the experimental axes system.

The tensor  $K$  is known to be symmetrical (i.e.  $k_{12} = k_{21}$ ). Equation (Eq. 54) can therefore be written as:

$$\begin{pmatrix} k_{11} & k_{12} \\ k_{12} & k_{22} \end{pmatrix} \begin{pmatrix} v_1 \\ v_2 \end{pmatrix} = k_x \begin{pmatrix} v_1 \\ v_2 \end{pmatrix} \quad (\text{Eq. 56})$$

Expanding equation (Eq. 56) we obtain the following simple simultaneous equations:

$$k_{11}v_1 + k_{12}v_2 = k_x v_1 \quad (\text{Eq. 57})$$

and 
$$k_{12}v_1 + k_{22}v_2 = k_x v_2 \quad (\text{Eq. 58})$$

Rearranging equations (Eq. 57) and (Eq. 58) we have:

$$(k_x - k_{11})v_1 = k_{12}v_2 \quad (\text{Eq. 59})$$

and 
$$(k_x - k_{22})v_2 = k_{12}v_1 \quad (\text{Eq. 60})$$

Alternatively, equations (Eq. 59) and (Eq. 60) can be written as:

$$\frac{v_2}{v_1} = \frac{k_x - k_{11}}{k_{12}} = \frac{k_{12}}{k_x - k_{22}} = \tan \theta \quad (\text{Eq. 61})$$

where  $\theta$  is the (acute) angle between the principal and the experimental axes.

Cross-multiplying in equation (Eq. 61) and rearranging gives:

$$k_x^2 - (k_{11} + k_{22})k_x + k_{11}k_{22} - k_{12}^2 = 0 \quad (\text{Eq. 62})$$

Solving equation (Eq. 62) for  $k_x$  by the usual quadratic formula with  $a = 1$ ,  $b = -(k_{11} + k_{22})$

and  $c = k_{11}k_{22} - k_{12}^2$  gives:

$$k_x = \frac{k_{11} + k_{22}}{2} + \sqrt{\left(\frac{k_{11} - k_{22}}{2}\right)^2 + k_{12}^2} \quad (\text{Eq. 63})$$

Note that an identical result would have been obtained for  $k_y$  had the principal  $y$ -axis been chosen. But the flow front is elliptical and hence:

$$k_x \neq k_y \quad (\text{Eq. 64})$$

In fact, since permeability is greater in the direction of the major axis:

$$k_x > k_y \quad (\text{Eq. 65})$$

Therefore the permeability on the principal  $x$ -axis (i.e. the major axis of the elliptical front) will be given by:

$$k_x = \frac{k_{11} + k_{22}}{2} + \sqrt{\left(\frac{k_{11} - k_{22}}{2}\right)^2 + k_{12}^2} \quad (\text{Eq. 66})$$

And the permeability on the principal  $y$ -axis (i.e. the minor axis of the elliptical front) will be given by:

$$k_y = \frac{k_{11} + k_{22}}{2} - \sqrt{\left(\frac{k_{11} - k_{22}}{2}\right)^2 + k_{12}^2} \quad (\text{Eq. 67})$$

where the positive square root has been taken throughout.

Adding equations (Eq. 66) and (Eq. 67) gives:

$$k_x + k_y = k_{11} + k_{22} \quad (\text{Eq. 68})$$

From equation (Eq. 61)

$$\tan \theta = \frac{k_{12}}{k_x - k_{22}} \quad (\text{Eq. 69})$$

and 
$$\tan \theta = \frac{k_x - k_{11}}{k_{12}} \quad (\text{Eq. 70})$$

Multiplying equation (Eq. 69) by equation (Eq. 70) gives:

$$\tan^2 \theta = \frac{k_x - k_{11}}{k_x - k_{22}} \quad (\text{Eq. 71})$$

Now: 
$$\tan 2\theta = \frac{2 \tan \theta}{1 - \tan^2 \theta} \quad (\text{Eq. 72})$$

Substituting equations (Eq. 69) and (Eq. 71) into equation (Eq. 72) gives:

$$\tan 2\theta = \frac{2k_{12} / k_x - k_{22}}{1 - \frac{k_x - k_{11}}{k_x - k_{22}}} \quad (\text{Eq. 73})$$

and 
$$\tan 2\theta = \frac{2k_{12}}{(k_x - k_{22})(k_{11} - k_{22})} (k_x - k_{22}) \quad (\text{Eq. 74})$$

i.e. 
$$\tan 2\theta = \frac{2k_{12}}{k_{11} - k_{22}} \quad (\text{Eq. 75})$$

and 
$$k_{12} = \frac{k_{11} - k_{22}}{2} \tan 2\theta \quad (\text{Eq. 76})$$

Substituting for  $k_{12}$  and for  $k_{11} + k_{22}$  into equation (Eq. 66) gives:

$$k_x = \frac{k_x + k_y}{2} + \frac{k_{11} - k_{22}}{2} \sqrt{1 + \tan^2 2\theta} \quad (\text{Eq. 77})$$

where the positive square root must be taken.

However: 
$$\sec^2 2\theta = \frac{1}{\cos^2 2\theta} = 1 + \tan^2 2\theta \quad (\text{Eq. 78})$$

Substituting equation (Eq. 78) into equation (Eq. 77) gives:

$$2k_x = k_x + k_y + \frac{k_{11} - k_{22}}{\cos 2\theta} \quad (\text{Eq. 79})$$

or 
$$k_x - k_y = \frac{k_{11} - k_{22}}{\cos 2\theta} \quad (\text{Eq. 80})$$

From equation (Eq. 76)

$$k_{11} - k_{22} = \frac{2k_{12}}{\tan 2\theta} \quad (\text{Eq. 81})$$

Substituting equation (Eq. 81) into equation (Eq. 80) we have:

$$k_{12} = \frac{k_x - k_y}{2} \sin 2\theta \quad (\text{Eq. 82})$$

Rearranging equation (Eq. 80) gives:

$$k_{11} - k_{22} = (k_x - k_y) \cos 2\theta \quad (\text{Eq. 83})$$

But: 
$$k_{11} + k_{22} = k_x + k_y \quad (\text{Eq. 68})$$

Adding equations (Eq. 83) and (Eq. 68) gives:

$$k_{11} = \frac{k_x + k_y}{2} + \frac{k_x - k_y}{2} \cos 2\theta \quad (\text{Eq. 84})$$

Substituting equation (Eq. 84) into equation (Eq. 68) gives:

$$k_{22} = \frac{k_x + k_y}{2} - \frac{k_x - k_y}{2} \cos 2\theta \quad (\text{Eq. 85})$$

The permeability tensor is now completely specified by equations (Eq. 82), (Eq. 84) and (Eq. 85). Its values can be obtained once  $k_x$  and  $k_y$  have been determined experimentally and  $\theta$  has been measured.

## Summary

The resin transfer moulding (RTM) process involves the long-range flow of resin through a bed of reinforcement. Modelling of the RTM process requires a knowledge of the permeability tensor of the reinforcement. The equations used for calculation of the values of the permeability tensor from a two-dimensional radial flow experiment have been derived in a simplified form. The equations should be used with careful attention to the fact that the volume of fluid collected is the volume of the combined media (reinforcement and pore space) multiplied by the porosity. The analysis presented here is specific to the case where the advance of the flow front is observed in the combined media.

The analysis presented here follows the work of Chan and Hwang [B3-2] with several simplifications. Chan and Hwang take their theory from Bear [B3-7] using:

$$\alpha = b^2 / a^2 \quad (\text{Eq.33})$$

$$\kappa = \sqrt{\kappa_x \kappa_y} \quad (\text{Eq.46})$$

This approach has been replaced by a scaling of variables to transform a circle to an ellipse as in Adams *et al* [B3-5] together with a short first-principles derivation of Equation 46.

In order to obtain the full permeability tensor from a knowledge of the principal permeabilities, Chan and Hwang resorted to an eigenvalue formulation. A simpler approach using Darcy's equation in the principal directions and the frame of invariance of vectors is used in this work. The resulting equations are essentially the same. The manipulation of these equations is not presented by Chan and Hwang, but is included here for reasons of completeness.

## References

- B3-1 E Carter, A W Fell, P R Griffin and J Summerscales, Data validation procedures for the automated determination of the two-dimensional permeability tensor of a fabric reinforcement, *Composites Part A: Applied Science and Manufacturing*, 1996, 27A(4), 255-261.
- B3-2 AW Chan and S-T Hwang, Anisotropic in-plane permeability of fabric media, *Polymer Engineering and Science*, 1991, 13(16), 1233-1239.
- B3-3 E Carter, A W Fell and J Summerscales, A simplified model to calculate the permeability tensor of an anisotropic fibre bed, *Composites Manufacturing*, 1995, 6(3/4), 228-235.
- B3-4 JR Weitzenböck, RA Shenoii and PA Wilson, Radial flow permeability measurement. Part B: application, *Composites Part A: Applied Science and Manufacturing*, 1999, 30A(6), 797-813.
- B3-5 KL Adams, WB Russell and L Rebenfeld, Radial penetration of a viscous fluid into a planar anisotropic porous medium, *International Journal of Multiphase Flow*, 1988, 14(2), 203-215.
- B3-6 J Summerscales, A model for the effect of fibre clustering on the flow rate in resin transfer moulding, *Composites Manufacturing*, March 1993, 4(1), 27-31.
- B3-7 J Bear, *Dynamics of Fluids in Porous Media*, American Elsevier, 1972. Republished by Dover Publications, Mineola NY, 1988.

**Appendix B4** Software for interrogation of flow front images and calculation of permeability.

*Page B4-1 Program to capture flow front isochrone images during a radial flow experiment*

*Page B4-43 Program to copy files from Viglen to XEN and prepare files to be read by the Quantimet 570*

*Page B4-44 Quantimet program to retrieve isochrone data from images*

*Page B4-48 Excel spreadsheet (permcals.xls) on XEN used to calculate permeabilities from isochrone data. The mathematics for this are presented in Appendix B3.*

-----  
*Program to capture flow front isochrone images during a radial flow experiment*

```
#include <graph.h>
#include "file3.h"
#include <dos.h>
#include <stdlib.h>
#include <stdio.h>
#include <stdarg.h>
#include <conio.h>
#include <string.h>
#include <math.h>
#include <time.h>
#include "cimmsc7.h"
#include "cimages.h"
#include "brdspec.h"
#include "lowlevel.h"
#include "timer1.h"

#define DATE 1
#define FABRIC 2
#define LAYUP 3
#define VOLUME_FRACTION 4
#define AREAL_WEIGHT 5
#define NO_OF_LAYERS 6
#define PRESSURE 7
#define COMMENTS 8
#define X_CENTRE 95
#define Y_CENTRE 96
#define X_CALIB_FACTOR 97
#define Y_CALIB_FACTOR 98
#define TIME 99
#define NUM_OF_SPOKES 24
#define ELEMENTS 200
#define PI 4.0*atan(1.0)

/* Structures for system configuration and chart environment. */
struct videoconfig vc;

/* Variable used to track control and screen position. */
struct screeninfo si;

/* Colors of menus and prompts. */
struct menucolors co;

/* Arrays of strings used by the Menu function. The first string is the
menu title. The next non-null strings are the menu selections. A null
string indicates the end of the list. */
char *mainmenu[] =
```

```

        { "Main Menu", "File and Disk Actions Menu", "Calibration Menu",
          "Acquisition Menu", "Processing Menu", "Quit", "" };
char *fdactions_menu[]=
    { "File and Disk Actions Menu", "1False", "2False", "3False", ""};
char *calibration_routines_menu[]=
    { "Calibration Menu", "Focus Camera", "Enter Header Information",
      "Calibrate Image", "Save Calibration Image", "Get Calibration
      Image", "Reinitialise Program", ""};
char *acquisition_menu[]=
    { "Acquisition Cycle", "Initial Frames", "Frame Delay",
      "Begin Frame Acquisition", ""};
char *header_options[]=
    { "Options", "Fabric", "Layup", "Volume Fraction", "Areal Weight",
      "Number of Layers", "Pressure (Nominal)", "Comments", "Review
      Header Information", ""};
char *edit_header_options[]=
    { "Edit Options", "Fabric", "Layup", "Volume Fraction", "Areal
      Weight", "Number of Layers", "Pressure (Nominal)", "Comments", ""};
char *post_processing_menu[]=
    { "Processing Options", "Display Single Image", "Image Playback",
      "Manual Post Processing", "Automatic Post Processing", ""};
char *manual_post_processing_menu[]=
    { "Manual", "Calibration Image", "Set Threshold Level", "Image
      Analysis", "Reinitialise All Data", ""};
char *process_image_menu[]=
    { "Image Options", "Frame Number", "Array Index", "Process Image",
      "Save Results", "Results to File", ""};

/* Variables to manage menus. */
int menulevel = 0;          /* Current menu level */
char *menutitles[10];     /* Stack of menu titles */
char *two_choice_titles[4];

int integer1=1;
double double1=0.0;
char *our_string="This a temporary string to prove the point of the
exercise";

image framestore;
image binary;
uchar lut[768];          /* lookup table */

fg_dimensions framestore_dimensions;
#define WID framestore_dimensions.vidwid
#define HT  framestore_dimensions.vidht

ci_handle hInst = 0;     /* Instance handle for Windows compatibility */
ci_handle hWnd = 0;     /* Window handle for Windows compatibility */

point centre_point;
pointset roi, roi_bound;
object roi_obj;

rgb col;    /* Binary overlay colour */

FILE *file_ptr;

double radii[NUM_OF_SPOKES];
double angle[NUM_OF_SPOKES];
point point_array[NUM_OF_SPOKES], end_point[NUM_OF_SPOKES];
pointset ps_array[NUM_OF_SPOKES];

double time_and_radii[ELEMENTS][NUM_OF_SPOKES+1];

```



```

int calib_image_flag=FALSE;
int save_calib_flag=FALSE;
int run_flag=FALSE;
int focus_flag=FALSE;
int get_calib_flag=FALSE;
int set_threshold_flag=FALSE;
int roi_defined=FALSE;
int break_loop=0;
int initial_frames=20;
int frame_delay=5;
int thresh_val;
int frame_index=1;
int array_index=0;

char time_buffer[20];
char filename[13];
char name[6]="image";
char ext[4]="ffa";
char fabric_buffer[51];
char layup_buffer[51];
char comment_buffer[51];
char areal_weight_buffer[17];
char volume_fraction_buffer[17];
char nominal_pressure_buffer[17];
char num_layers_buffer[9];
char x_factor_buffer[17];
char y_factor_buffer[17];
char x_point_buffer[17];
char y_point_buffer[17];
char date_buffer[17];

char temp_fabric[51];
char temp_layup[51];
char temp_comment[51];
char temp_areal_weight[17];
char temp_volume_fraction[17];
char temp_nominal_pressure[17];
char temp_num_layers[9];
char temp_x_factor[17];
char temp_y_factor[17];
char temp_x_point[17];
char temp_y_point[17];
char temp_date[17];

char emptystr[4];
double x_factor, y_factor;
double last_time;
double frame_time;
double areal_weight=0.0;
double volume_fraction=0.0;
double nominal_pressure=0.0;
int num_layers=1;

time_t timer;
struct tm *time_ptr;
unsigned char far *str;

void false1(void);
void false2(void);
void false3(void);
void focus(void);
void calibration_routines(void);

```

```

void calibration_header(void);
void save_calibration_image(void);
void edit_calibration_image(void);
void file_and_disk_actions(void);
void acquire(void);
int find_video_mode( struct videoconfig vc );
void initialize(void);
void main_menu(void);
BOOL set_graph_mode(int mode);
int two_choice_menu(char *title, char *choice1, char *choice2);
void clear_form(void);
void clear_help(void);
void display_error_message(char *error_message);
void help(char *error_message, short color);
int input_char(char *prompt, char *accept);
int input_int(char *prompt, int old, int min, int max);
double input_double( char *prompt, double old );
char *input_string(char *prompt, char *old);
BOOL in_range(int value, int min, int max);
int menu(char *menulist[]);
void pop_title(void);
void print_at(int row, int column, char far *string, short color);
void print_char(int row, int column, char character, short color);
void push_title(char *title);
void set_display_colors(void);
void write_form(int ybottom);
char *make_filename(char *output_buffer, char *name_buffer, char
*ext_buffer, int number);
void double_to_string( double value, int precision, char *output_buffer);
void print_frame_data( int frame_number);
void review_header_information(void);
void init(void);
void grab_video(void);
void calibrate_image(imptr im, ptptr centre_point, double *x_factor_ptr,
double *y_factor_ptr);
void free_image_text(imptr image_ptr);
double snap_and_save(int frame_number);
void reset_prog(void);
void post_processing_routines(void);
void retrieve_single_image(void);
void image_playback(void);
void set_threshold_level(void);
void define_roi(psptr ps);
void manual_post_processing(void);
void analyse_image(void);
void generate_points(ptptr centre_point, ptptr ptarray, int
num_of_spokes);
void draw_radii(imptr im, ptptr centre_point, ptptr ptarray, int
num_of_spokes);
void gen_spokes(ptptr centre_point, ptptr ptarray, psptr psarray, int
num_of_spokes);
void get_spoke_end(imptr im, psptr psspoke, ptptr end_point, int
num_of_spokes);
void draw_cross(imptr im, ptptr ptarray, int num_of_spokes);
void calc_coords(ptptr centre_point, ptptr end_point, double *rad);
void initialise_array(void);
void process_image(void);
void save_results(void);
void sprintf_at(int row, int col, char *fmt, ... );
void print_frame_results();
void file_results(void);

void main(void)

```

```

(
    if (INIT_COMMS())
    {
        if (BRD_INIT()) /* Initialise for particular board */
        {
            switch(LIB_CONFIG()) /* Initialise the library for
board */
            {
                case 0:
                    printf("\n Library configuration failed ");
                    printf("\n Error No = %lx: %s \n", (sword)
ci_get_val(GS_ERRNO, 0),
                    ci_errmess(hInst, (uint) ci_get_val(GS_ERRNO, 0)));
                    break;

                case -1:
                    printf("\n Please attach software security device \n");
                    break;

                default:
                    init(); /* initialise images */
                    initialize();
                    main_menu();

                    /* Reset the video mode and screen colors prior to
leaving. */
                    _setvideomode( _DEFAULTMODE );
                    _settextcolor( co.infocolor );
                    _clearscreen( _GCLEARSCREEN );

                    ci_clear_fg(&framestore);
                    free_image_text(&framestore);
                    ci_finit(hInst); /* terminate C_IMAGES */
            }
            BRD_FINIT();
        }
        else printf("Board Initialisation failed\n Error %s",
                    ci_errmess(hInst, (uint) ci_get_val(GS_ERRNO, 0)));
        FINIT_COMMS();
    }
    else printf("Comms Initialisation failed\n");
}

void false1(void)
{
    help("Enter an integer in range 1-20.", co.inputcolor);
    integer1=input_int("Integer? ", integer1, 1, 20);
}

void false2(void)
{
    help("Enter a double", co.inputcolor);
    double1=input_double("Double? ", double1);
}

void false3(void)
{
    help("Enter a string", co.inputcolor);
    input_string("String? ", our_string);
}

void focus(void)
{

```

```

int cross_colour=0, break_loop=0;
point point1, point2, point3, point4;
point1.X=0;                point1.Y=HT>>1;
point2.X=WID-1;           point2.Y=HT>>1;
point3.X=WID>>1;         point3.Y=0;
point4.X=WID>>1;         point4.Y=HT-1;

clear_form();
help("Press \"B\" for Black or \"W\" for White cross hairs",
co.inputcolor);

if(input_char("Black or White Cross Hairs ", "BW")== 'W')
{
    cross_colour=255;
}

write_form(16);
print_at(1, 20, "Permeability Measurement Program", co.titlecolor );
print_at(si.mid, 5, "Focus camera image and align axes",
co.inputcolor);
help("Press ESC to continue", co.inputcolor);

do
{
    ci_live(&framestore);
    ci_draw_line(&point1, &point2, &framestore, cross_colour);
    ci_draw_line(&point3, &point4, &framestore, cross_colour);
    ci_live(&framestore);

    if(kbhit())
    {
        if(getch()==ESCAPE)
        {
            break_loop=1;
        }
    }
}
while(!break_loop);

ci_clear_fg(&framestore);
focus_flag=TRUE;
}

void reset_prog(void)
{
    calib_image_flag=FALSE;
    save_calib_flag=FALSE;
    run_flag=FALSE;
    focus_flag=FALSE;

    strcpy(date_buffer, emptystr);
    strcpy(fabric_buffer, emptystr);
    strcpy(layup_buffer, emptystr);
    strcpy(volume_fraction_buffer, emptystr);
    strcpy(areal_weight_buffer, emptystr);
    strcpy(num_layers_buffer, emptystr);
    strcpy(nominal_pressure_buffer, emptystr);
    strcpy(comment_buffer, emptystr);
    strcpy(x_factor_buffer, emptystr);
    strcpy(y_factor_buffer, emptystr);
    strcpy(x_point_buffer, emptystr);
    strcpy(y_point_buffer, emptystr);
}

```

```

clear_form();
    help("Reinitialising internal data", co.inputcolor);
    input_char("Press ESC to continue. ", "\x1b");
}
void calibration_header(void)
{
    int choice;
    push_title( header_options[0] );
    while( (choice = menu( header_options )) != ESCAPE )
    {
        switch( choice )
        {
            /* Set appropriate header strings. */

            case 1:
                help("Enter a string of 50 characters or less.",
co.inputcolor);
                input_string("Fabric? ", fabric_buffer);
                break;

            case 2:
                help("Enter a string of 50 characters or less.",
co.inputcolor);
                input_string("Layup? ", layup_buffer);
                break;

            case 3:
                help("Enter the volume fraction of the fibre bed.",
co.inputcolor);
                volume_fraction=input_double("Volume Fraction? ",
volume_fraction);
                double_to_string(volume_fraction, 2, volume_fraction_buffer);
                break;

            case 4:
                help("Enter the fabric areal weight in grams",
co.inputcolor);
                areal_weight=input_double("Areal weight (g)? ",
areal_weight);
                double_to_string(areal_weight, 2, areal_weight_buffer);
                break;

            case 5:
                help("Enter the number of layers in the fibre bed.",
co.inputcolor);
                num_layers=input_int("Number of layers? ", num_layers, 1,
100);
                itoa(num_layers, num_layers_buffer, 10);
                break;

            case 6:
                help("Enter the nominal inlet pressure in bars",
co.inputcolor);
                nominal_pressure=input_double("Nominal Pressure (bar)? ",
nominal_pressure);
                double_to_string(nominal_pressure, 2,
nominal_pressure_buffer);
                break;

            case 7:
                help("Enter comment string of 50 characters or less.",
co.inputcolor);
                input_string("Comments? ", comment_buffer);

```

```

        break;

    case 8:
        review_header_information();
        break;
    }
}
pop_title();
}

void review_header_information(void)
{
    int break_loop=0;
    write_form(21);
    print_at(1, 20, "Permeability Measurement Program", co.titlecolor );
    help("Hit ESC to continue", co.inputcolor);
    print_at(8, 5, "Fabric: ", co.inputcolor);
    print_at(9, 5, "Layup: ", co.inputcolor);
    print_at(10, 5, "Volume Fraction: ", co.inputcolor);
    print_at(11, 5, "Areal Weight: ", co.inputcolor);
    print_at(12, 5, "Number of Layers: ", co.inputcolor);
    print_at(13, 5, "Nominal Pressure: ", co.inputcolor);
    print_at(14, 5, "Comment: ", co.inputcolor);
    print_at(15, 5, "X Factor: ", co.inputcolor);
    print_at(16, 5, "Y Factor: ", co.inputcolor);
    print_at(17, 5, "Centre X Pixel: ", co.inputcolor);
    print_at(18, 5, "Centre Y Pixel: ", co.inputcolor);
    print_at(8, 25, fabric_buffer, co.infocolor);
    print_at(9, 25, layup_buffer, co.infocolor);
    print_at(10, 25, volume_fraction_buffer, co.infocolor);
    print_at(11, 25, areal_weight_buffer, co.infocolor);
    print_at(12, 25, num_layers_buffer, co.infocolor);
    print_at(13, 25, nominal_pressure_buffer, co.infocolor);
    print_at(14, 25, comment_buffer, co.infocolor);
    print_at(15, 25, x_factor_buffer, co.infocolor);
    print_at(16, 25, y_factor_buffer, co.infocolor);
    print_at(17, 25, x_point_buffer, co.infocolor);
    print_at(18, 25, y_point_buffer, co.infocolor);

    do
    {
        if(kbhit())
        {
            if(getch()==ESCAPE)
            {
                break_loop=1;
            }
        }
    }
    while(!break_loop);
}

void save_calibration_image(void)
{
    if(!calib_image_flag || save_calib_flag)
    {
        if(!save_calib_flag)
        {
            clear_form();
            help("Image has not been calibrated", co.inputcolor);
            input_char("Press ESC to continue. ", "\x1b");
            return;
        }
    }
}

```

```

        else
        {
            clear_form();
            help("Resaving of image not permitted", co.inputcolor);
            input_char("Press ESC to continue. ", "\x1b");
            return;
        }
    }

    grab_video();
    ci_add_imtext(&framestore, date_buffer, DATE);
    ci_add_imtext(&framestore, fabric_buffer, FABRIC);
    ci_add_imtext(&framestore, layup_buffer, LAYUP);
    ci_add_imtext(&framestore, volume_fraction_buffer, VOLUME_FRACTION);
    ci_add_imtext(&framestore, areal_weight_buffer, AREAL_WEIGHT);
    ci_add_imtext(&framestore, num_layers_buffer, NO_OF_LAYERS);
    ci_add_imtext(&framestore, nominal_pressure_buffer, PRESSURE);
    ci_add_imtext(&framestore, comment_buffer, COMMENTS);
    ci_add_imtext(&framestore, x_point_buffer, X_CENTRE);
    ci_add_imtext(&framestore, y_point_buffer, Y_CENTRE);
    ci_add_imtext(&framestore, x_factor_buffer, X_CALIB_FACTOR);
    ci_add_imtext(&framestore, y_factor_buffer, Y_CALIB_FACTOR);
    ci_write_discim("calib.ffa", &framestore, FFA, NO_PACK);
    ci_string_to_im(date_buffer, &framestore, 5, 5, 1, -1);
    ci_string_to_im(fabric_buffer, &framestore, 5, 25, 1, -1);
    ci_string_to_im(layup_buffer, &framestore, 5, 45, 1, -1);
    ci_string_to_im(volume_fraction_buffer, &framestore, 5, 65, 1, -1);
    ci_string_to_im(areal_weight_buffer, &framestore, 5, 85, 1, -1);
    ci_string_to_im(num_layers_buffer, &framestore, 5, 105, 1, -1);
    ci_string_to_im(nominal_pressure_buffer, &framestore, 5, 125, 1, -1);
    ci_string_to_im(comment_buffer, &framestore, 5, 145, 1, -1);
    ci_string_to_im(x_point_buffer, &framestore, 5, 165, 1, -1);
    ci_string_to_im(y_point_buffer, &framestore, 5, 185, 1, -1);
    ci_string_to_im(x_factor_buffer, &framestore, 5, 205, 1, -1);
    ci_string_to_im(y_factor_buffer, &framestore, 5, 225, 1, -1);

    clear_form();
    help("Calibration image saved successfully", co.inputcolor);
    input_char("Press ESC to continue. ", "\x1b");
    free_image_text(&framestore);
    ci_clear_fg(&framestore);
    save_calib_flag=TRUE;
}

void edit_calibration_image(void)
{
    int tag, n=0;
    int choice;
    if(!ci_read_discim("calib.ffa", &framestore, FFA))
    {
        clear_form();
        help("Image not read successfully", co.inputcolor);
        input_char("Press ESC to continue. ", "\x1b");
        return;
    }

    tag=DATE;
    str=(unsigned char far*) ci_get_imtext(&framestore, &tag, &n);
    strcpy(temp_date, str);
    tag=FABRIC;
    str=(unsigned char far*) ci_get_imtext(&framestore, &tag, &n);
    strcpy(temp_fabric, str);
    tag=LAYUP;
}

```

```

    str=(unsigned char far*) ci_get_imtext(&framestore, &tag, &n);
strcpy(temp_layup, str);
    tag=VOLUME_FRACTION;
    str=(unsigned char far*) ci_get_imtext(&framestore, &tag, &n);
strcpy(temp_volume_fraction, str);
    tag=AREAL_WEIGHT;
    str=(unsigned char far*) ci_get_imtext(&framestore, &tag, &n);
strcpy(temp_areal_weight, str);
    tag=NO_OF_LAYERS;
    str=(unsigned char far*) ci_get_imtext(&framestore, &tag, &n);
strcpy(temp_num_layers, str);
    tag=PRESSURE;
    str=(unsigned char far*) ci_get_imtext(&framestore, &tag, &n);
strcpy(temp_nominal_pressure, str);
    tag=COMMENTS;
    str=(unsigned char far*) ci_get_imtext(&framestore, &tag, &n);
strcpy(temp_comment, str);
    tag=X_CENTRE;
    str=(unsigned char far*) ci_get_imtext(&framestore, &tag, &n);
strcpy(temp_x_point, str);
    tag=Y_CENTRE;
    str=(unsigned char far*) ci_get_imtext(&framestore, &tag, &n);
strcpy(temp_y_point, str);
    tag=X_CALIB_FACTOR;
    str=(unsigned char far*) ci_get_imtext(&framestore, &tag, &n);
strcpy(temp_x_factor, str);
    tag=Y_CALIB_FACTOR;
    str=(unsigned char far*) ci_get_imtext(&framestore, &tag, &n);
strcpy(temp_y_factor, str);

free_image_text(&framestore);
push_title( edit_header_options[0] );
while( (choice = menu( edit_header_options )) != ESCAPE )
{
    switch( choice )
    {
        /* Set appropriate header strings, */
        case 1:
            help("Enter a string of 50 characters or less.",
co.inputcolor);
            input_string("Fabric? ", temp_fabric);
            break;

        case 2:
            help("Enter a string of 50 characters or less.",
co.inputcolor);
            input_string("Layup? ", temp_layup);
            break;

        case 3:
            help("Enter the volume fraction of the fibre bed.",
co.inputcolor);
            volume_fraction=input_double("Volume Fraction? ",
volume_fraction);
            double_to_string(volume_fraction, 2, temp_volume_fraction);
            break;

        case 4:
            help("Enter the fabric areal weight in grams",
co.inputcolor);
            areal_weight=input_double("Areal weight (g)? ",
areal_weight);
            double_to_string(areal_weight, 2, temp_areal_weight);

```



```

        break;

    case 5:
        help("Enter the number of layers in the fibre bed.",
co.inputcolor);
        num_layers=input_int("Number of layers? ", num_layers, 1,
100);
        itoa(num_layers, temp_num_layers, 10);
        break;

    case 6:
        help("Enter the nominal inlet pressure in bars",
co.inputcolor);
        nominal_pressure=input_double("Nominal Pressure (bar)? ",
nominal_pressure);
        double_to_string(nominal_pressure, 2, temp_nominal_pressure);
        break;

    case 7:
        help("Enter comment string of 50 characters or less.",
co.inputcolor);
        input_string("Comments? ", temp_comment);
        break;
    }
}
pop_title();
ci_add_intext(&framestore, temp_date, DATE);
ci_add_intext(&framestore, temp_fabric, FABRIC);
ci_add_intext(&framestore, temp_layup, LAYUP);
ci_add_intext(&framestore, temp_volume_fraction, VOLUME_FRACTION);
ci_add_intext(&framestore, temp_areal_weight, AREAL_WEIGHT);
ci_add_intext(&framestore, temp_num_layers, NO_OF_LAYERS);
ci_add_intext(&framestore, temp_nominal_pressure, PRESSURE);
ci_add_intext(&framestore, temp_comment, COMMENTS);
ci_add_intext(&framestore, temp_x_factor, X_CALIB_FACTOR);
ci_add_intext(&framestore, temp_y_factor, Y_CALIB_FACTOR);
ci_write_discim("calib.ffa", &framestore, FFA, NO_PACK);
clear_form();
help("Calibration image resaved successfully", co.inputcolor);
input_char("Press ESC to continue. ", "\x1b" );
free_image_text(&framestore);
ci_clear_fg(&framestore);
}

void retrieve_calibration_image(void)
{
    int tag, n=0;
    if(!ci_read_discim("calib.ffa", &framestore, FFA))
    {
        clear_form();
        help("Image not read successfully", co.inputcolor);
        input_char("Press ESC to continue. ", "\x1b");
        return;
    }

    tag=DATE;
    str=(unsigned char far*) ci_get_intext(&framestore, &tag, &n);
    strcpy(date_buffer, str);
    tag=FABRIC;
    str=(unsigned char far*) ci_get_intext(&framestore, &tag, &n);
    strcpy(fabric_buffer, str);
    tag=LAYUP;
    str=(unsigned char far*) ci_get_intext(&framestore, &tag, &n);

```

```

strcpy(layup_buffer, str);
tag=VOLUME_FRACTION;
str=(unsigned char far*) ci_get_imtext(&framestore, &tag, &n);
strcpy(volume_fraction_buffer, str);
tag=AREAL_WEIGHT;
str=(unsigned char far*) ci_get_imtext(&framestore, &tag, &n);
strcpy(areal_weight_buffer, str);
tag=NO_OF_LAYERS;
str=(unsigned char far*) ci_get_imtext(&framestore, &tag, &n);
strcpy(num_layers_buffer, str);
tag=PRESSURE;
str=(unsigned char far*) ci_get_imtext(&framestore, &tag, &n);
strcpy(nominal_pressure_buffer, str);
tag=COMMENTS;
str=(unsigned char far*) ci_get_imtext(&framestore, &tag, &n);
strcpy(comment_buffer, str);
tag=X_CENTRE;
str=(unsigned char far*) ci_get_imtext(&framestore, &tag, &n);
strcpy(x_point_buffer, str);
tag=Y_CENTRE;
str=(unsigned char far*) ci_get_imtext(&framestore, &tag, &n);
strcpy(y_point_buffer, str);
tag=X_CALIB_FACTOR;
str=(unsigned char far*) ci_get_imtext(&framestore, &tag, &n);
strcpy(x_factor_buffer, str);
tag=Y_CALIB_FACTOR;
str=(unsigned char far*) ci_get_imtext(&framestore, &tag, &n);
strcpy(y_factor_buffer, str);

volume_fraction=atof(volume_fraction_buffer);
areal_weight=atof(areal_weight_buffer);
nominal_pressure=atof(nominal_pressure_buffer);
x_factor=atof(x_factor_buffer);
y_factor=atof(y_factor_buffer);
centre_point.X=atoi(x_point_buffer);
centre_point.Y=atoi(y_point_buffer);

ci_string_to_im(date_buffer, &framestore,5,5,1,-1);
ci_string_to_im(fabric_buffer, &framestore,5,25,1,-1);
ci_string_to_im(layup_buffer, &framestore,5,45,1,-1);
ci_string_to_im(volume_fraction_buffer, &framestore,5,65,1,-1);
ci_string_to_im(areal_weight_buffer, &framestore,5,85,1,-1);
ci_string_to_im(num_layers_buffer, &framestore,5,105,1,-1);
ci_string_to_im(nominal_pressure_buffer, &framestore,5,125,1,-1);
ci_string_to_im(comment_buffer, &framestore,5,145,1,-1);
ci_string_to_im(x_point_buffer, &framestore,5,165,1,-1);
ci_string_to_im(y_point_buffer, &framestore,5,185,1,-1);
ci_string_to_im(x_factor_buffer, &framestore,5,205,1,-1);
ci_string_to_im(y_factor_buffer, &framestore,5,225,1,-1);

clear_form();
help("Calibration image retrieved successfully", co.inputcolor);
input_char("Press ESC to continue. ", "\x1b" );
free_image_text(&framestore);
ci_clear_fg(&framestore);
get_calib_flag=TRUE;
}

void retrieve_single_image(void)
{
int tag, n=0;
int frame_number=1;
char temp[17];

```

```

help("Enter number of frame to retrieve.", co.inputcolor);
frame_number=input_int("Number of Frame? ", frame_number, 1, 0);
make_filename(filename, name, ext, frame_number);

if(!ci_read_discim(filename, &framestore, FFA))
{
    clear_form();
    clear_help();
    help("Image not read successfully", co.inputcolor);
    input_char("Press ESC to continue. ", "\x1b");
    return;
}

tag=TIME;
str=(unsigned char far*) ci_get_imtext(&framestore, &tag, &n);
strcpy(time_buffer, str);
frame_time=atof(time_buffer);
itoa(frame_number, temp, 10);

ci_string_to_im("Frame Number  ", &framestore,5,5,1,-1);
ci_string_to_im(temp, &framestore,110,5,1,-1);
ci_string_to_im("Frame Time    ", &framestore,5,25,1,-1);
ci_string_to_im(time_buffer, &framestore,110,25,1,-1);
clear_form();
clear_help();
help("Image retrieved successfully", co.inputcolor);
input_char("Press ESC to continue. ", "\x1b" );
free_image_text(&framestore);
ci_clear_fg(&framestore);
}

void image_playback(void)
{
    int tag=TIME, n=0;
    int count;
    int frame_number=1;
    int break_loop=0;
    int response;

    char temp[17];

    write_form(20);
    print_at(1, 20, "Permeability Measurement Program", co.titlecolor );
    help("Press ESC to break out or \"P\" to pause. ", co.inputcolor);

    do
    {
        make_filename(filename, name, ext, frame_number);

        if(!ci_read_discim(filename, &framestore, FFA))
        {
            clear_form();
            clear_help();
            help("End of image sequence", co.inputcolor);
            input_char("Press ESC to continue. ", "\x1b");
            free_image_text(&framestore);
            ci_clear_fg(&framestore);
            return;
        }

        str=(unsigned char far*) ci_get_imtext(&framestore, &tag,
&n);
        strcpy(time_buffer, str);

```

```

        itoa(frame_number, temp, 10);

        ci_string_to_im("Frame Number  ", &framestore, 5, 5, 1, -1);
        ci_string_to_im(temp, &framestore, 110, 5, 1, -1);
        ci_string_to_im("Frame Time    ", &framestore, 5, 25, 1, -1);
        ci_string_to_im(time_buffer, &framestore, 110, 25, 1, -1);

        frame_number++;

        if(kbhit())
        {
            response=toupper(getch());

            if(response==ESCAPE)
            {
                break_loop=1;
            }
            else
            {
                if(response=='P')
                {
                    clear_form();
                    clear_help();
                    input_char("Press ESC to continue.", "\x1b" );
                    clear_form();
                    help("Press ESC to break out or \"P\" to pause.
", co.inputcolor);
                }
            }
        }
        for(count=0; count<=20000; count++)0;
    }
    while(!break_loop);

    free_image_text(&framestore);
    ci_clear_fg(&framestore);
}

void calibration_routines(void)
{
    int choice;
    push_title( calibration_routines_menu[0] );
    while( (choice = menu( calibration_routines_menu )) != ESCAPE )
    {
        switch( choice )
        {
            /* Branch to the appropriate menu. */
            case 1:
                focus();
                break;

            case 2:
                calibration_header();
                break;

            case 3:
                /* calibrate image*/
                calibrate_image(&framestore, &centre_point, &x_factor,
&y_factor);
                break;

            case 4:

```

```

        save_calibration_image();
        break;

    case 5:
        edit_calibration_image();
        break;

    case 6:
        reset_prog();
        break;
    }
}
pop_title();
}

void post_processing_routines(void)
{
    int choice;
    initialise_array();
    generate_points(&centre_point, point_array, NUM_OF_SPOKES);
    gen_spokes(&centre_point, point_array, ps_array, NUM_OF_SPOKES);
    push_title( post_processing_menu[0] );
    while( (choice = menu( post_processing_menu )) != ESCAPE )
    {
        switch( choice )
        {
            /* Branch to the appropriate menu. */
            case 1:
                retrieve_single_image();
                break;

            case 2:
                image_playback();
                break;

            case 3:
                manual_post_processing();
                break;

            case 4:
                break;
        }
    }
    pop_title();
}

void manual_post_processing(void)
{
    int choice;
    push_title( manual_post_processing_menu[0] );
    while( (choice = menu( manual_post_processing_menu )) != ESCAPE )
    {
        switch( choice )
        {
            /* Branch to the appropriate menu. */
            case 1:
                retrieve_calibration_image();
                break;

            case 2:
                set_threshold_level();
                break;
        }
    }
}

```

```

        case 3:
            process_image();
            break;

        case 4:
            initialise_array();
            break;
    }
}
pop_title();
}

void process_image(void)
{
    int choice;
    if(!get_calib_flag || !set_threshold_flag)
    {
        if(!get_calib_flag)
        {
            clear_form();
            help("Calibration image has not been retrieved",
co.inputcolor);
            input_char("Press ESC to continue. ", "\x1b");
        }

        if(!set_threshold_flag)
        {
            clear_form();
            help("A threshold level has not been set",
co.inputcolor);
            input_char("Press ESC to continue. ", "\x1b");
        }
        return;
    }

    push_title( process_image_menu[0] );
    while( (choice = menu( process_image_menu )) != ESCAPE )
    {
        switch( choice )
        {
            /* Branch to the appropriate menu. */
            case 1:
                help("Set number of frame to analyse.",
co.inputcolor);
                frame_index=input_int("Frames Number? ",
frame_index, 1, 0);
                break;

            case 2:
                help("Set index of storage array (must be less <=
current index).", co.inputcolor);
                array_index=input_int("Array Index? ",
array_index, 0, array_index+1);
                break;

            case 3:
                analyse_image();
                break;

            case 4:
                /*save_results*/
                save_results();
                break;
        }
    }
}

```

```

        case 5:
            /*save_results*/
            file_results();
            break;
        }
    }
    pop_title();
}

void save_results(void)
{
    int count;
    if(array_index<=ELEMENTS)
    {
        time_and_radii[array_index][0]=frame_time;
        for(count=0; count<NUM_OF_SPOKES; count++)
        {
            time_and_radii[array_index][count+1]=radii[count];
        }
        frame_index++;
        array_index++;
    }
    else
    {
        clear_form();
        clear_help();
        help("Array index out of bounds", co.inputcolor);
        input_char("Press ESC to continue. ", "\x1b");
        return;
    }
}

void file_results(void)
{
    int count1=0, count2;
    if((file_ptr=fopen("RESULTS.DAT", "w"))==NULL)
    {
        clear_form();
        help("Unable to open results file", co.inputcolor);
        input_char("Press ESC to continue. ", "\x1b");
        return;
    }

    fprintf(file_ptr, "\t\tBRITE Permeability Measurement
Program\n\n");
    fprintf(file_ptr, "Date                : %s\n",
date_buffer);
    fprintf(file_ptr, "Fabric                : %s\n",
fabric_buffer);
    fprintf(file_ptr, "Fabric Layup         : %s\n",
layup_buffer);
    fprintf(file_ptr, "Volume Fraction      : %s\n",
volume_fraction_buffer);
    fprintf(file_ptr, "Areal weight        : %s\n",
areal_weight_buffer);
    fprintf(file_ptr, "Number of Layers     : %s\n",
num_layers_buffer);
    fprintf(file_ptr, "Nominal Inlet Pressure (Bar): %s\n",
nominal_pressure_buffer);
    fprintf(file_ptr, "Comments             : %s\n\n\n",
comment_buffer);
}

```

```

fprintf(file_ptr, "\n");

do
{
    if((time_and_radri[count1][0]!=0) & (count1<=ELEMENTS))
    {
        fprintf(file_ptr, "%7.3f ", time_and_radri[count1][0]);
        for(count2=1; count2<=NUM_OF_SPOKES; count2++)
        {
            fprintf(file_ptr, "%7.3f ",
time_and_radri[count1][count2]);
        }
        fprintf(file_ptr, "\n");
    }
    else
    {
        clear_form();
        help("End of data array reached", co.inputcolor);
        input_char("Press ESC to continue. ", "\x1b");
    }
}
while(time_and_radri[count1++][0]!=0);

fclose(file_ptr);
}

void initialise_array(void)
{
    int count;
    frame_index=1;
    array_index=0;
    for(count=0; count<=ELEMENTS-1; count++)
    {
        time_and_radri[count][0]=0;
    }

    get_calib_flag=FALSE;
    set_threshold_flag=FALSE;
}

void file_and_disk_actions(void)
{
    int choice;
    push_title( fdactions_menu[0] );
    while( (choice = menu( fdactions_menu )) != ESCAPE )
    {
        switch( choice )
        {
            /* Branch to the appropriate menu. */
            case 1:
                false1();
                break;

            case 2:
                false2();
                break;

            case 3:
                false3();
                break;
        }
    }
    pop_title();
}

```



```

}
/*void acquire(void)
{
    int choice;
    push_title( acquisition_menu[0] );
    choice = menu( acquisition_menu );
    if( choice != ESCAPE )
    {
        switch( choice )
        {
            case 1:
                choice = two_choice_menu( "False1", "A", "B" );

                break;

            case 2:
                choice = two_choice_menu( "False2", "A", "B" );

                break;

        }
        if( choice != ESCAPE)
            pop_title();
    }
    pop_title();
}
*/

void acquire_frames(void)
{
    int break_loop=0, response;
    unsigned long int count;
    if(!save_calib_flag || run_flag)
    {
        if(!save_calib_flag)
        {
            clear_form();
            help("Calibration image has not been saved",
co.inputcolor);
            input_char("Press ESC to continue. ", "\x1b");
            return;
        }
        else
        {
            clear_form();
            help("Frame acquisition not permitted", co.inputcolor);
            input_char("Press ESC to continue. ", "\x1b");
            return;
        }
    }

    clear_form();
    response=input_char("Press \"A\" to acquire frames or ESC to quit.
", "Aa\x1b");

    if(response==ESCAPE) return;
    write_form(25);
    print_at(1, 20, "BRITE Permeability Measurement Program",
co.titlecolor );
    help("Hit ESC to quit acquisition cycle", co.inputcolor);
    run_flag=TRUE;
    start_clock();
}

```

```

do
{
    if(frame_index<=initial_frames)
    {
        last_time=snap_and_save(frame_index);
        print_frame_data( frame_index);
        for(count=1;count<=50000;count++);
        frame_index++;
    }
    else
    {
        if((elapsed_time()-last_time)>frame_delay)
        {
            last_time=snap_and_save(frame_index);
            print_frame_data( frame_index);
            frame_index++;
        }
    }

    if(kbhit())
    {
        if(getch()==ESCAPE)
        {
            break_loop=1;
        }
    }
}
while(!break_loop);
stop_clock();
ci_clear_fg(&framestore);
/* Reset frame count */
frame_index=1;
}

void acquire(void)
{
    int choice;
    push_title( acquisition_menu[0] );
    while( (choice = menu( acquisition_menu )) != ESCAPE )
    {
        switch( choice )
        {
            case 1:
                /* Get number of initial frames */
                help("Enter integer number of frames in range 1-50.",
co.inputcolor);
                initial_frames=input_int("Number of Initial Frames? ",
initial_frames, 1, 50);
                break;

            case 2:
                /* Get delay between frames */
                help("Enter delay between frames in range.", co.inputcolor);
                frame_delay=input_int("Delay between Frames (secs)? ",
frame_delay, 1, 0);
                break;

            case 3:
                acquire_frames();
                break;
        }
    }
}
pop_title();

```

```

)
/* find_video_mode - Finds the "best" video mode for the adaptor in use.
 * Params: vc - structure of type struct videoconfig
 * Returns: Best mode
 */
int find_video_mode( struct videoconfig vc )
(
    switch( vc.adapter )
    {
        case _CGA:
        case _OCGA:
            return _HRESBW;
        case _EGA:
        case _OEGA:
            return( vc.monitor == _MONO ) ? _ERESNOCOLOR : _ERESCOLOR;
        case _VGA:
        case _OVGA:
        case _MCGA:
            return _VRES16COLOR;
        case _HGC:
            return _HERCMONO;
        default:
            return _DEFAULTMODE;
    }
)

/* initialize - Does various initialization tasks.
 * Params: None
 */
void initialize( void )
(
    /* Initialize screen mode */
    _getvideoconfig( &vc );
    /* Find the best available mode for display.
     * Don't set 256 color, medium resolution ( _MRES256COLOR ).
     */
    si.mode = find_video_mode( vc );

    if( si.mode == _TEXTMONO )
    {
        _clearscreen( _GCLEARSCREEN );
        _outtext( "No graphics available. Can't run chart demo." );
        exit( 1 );
    }

    set_display_colors();
    set_graph_mode( si.mode );
    _setvideomode( _DEFAULTMODE );
)

/* main_menu - Manages the main menu.
 * Params: None
 */
void main_menu( void )
(
    int choice;
    char response = 'Y';
    char verify;
    push_title( mainmenu[0] );

    do
    {

```

```

/* If the user selects Quit, choice will contain 4. If the
 * user presses ESCAPE, choice will be ESCAPE, which is
 * equal to 27. In any case, we can test both conditions
 * by checking to see whether choice is less than 4.
 */
while( (choice = menu( mainmenu )) < 5 )
{
    /* Get main menu selection. */
    switch( choice )
    {
        case 1:
            /* File and Disk Action */
            file_and_disk_actions();
            break;

        case 2:
            /* Calibration */
            calibration_routines();
            break;

        case 3:
            /* Acquire */
            acquire();
            break;

        case 4:
            /* Post Process*/
            post_processing_routines();
            break;
    }
}

/* If the user is trying to leave the program using the ESCAPE
 * key, verify the choice to prevent exiting at an unanticipated
point.
 */
if( choice == ESCAPE )
{
    help( "Press \"Q\" to Quit", co.inputcolor );
    putchar( BEEP );
    _settextposition( si.help - 1, 32 );
    verify = getch();
    if( tolower( verify ) != 'q' )
        choice = 0;
    else
        choice = 5;
}
} while( choice !=5 );
pop_title();
}

/* set_graph_mode - Tests the specified graphics mode and sets the xmax
 * and ymax values in the si (Screen Information) structure.
 * Params: mode number
 * Return: FALSE if mode invalid, TRUE if valid
 */
BOOL set_graph_mode(int mode)
{
    if (!_setvideomode( mode ) )
        return FALSE;
    else
    {
        _getvideoconfig ( &vc );
    }
}

```

```

        if( !vc.numxpixels )
            return FALSE;
        si.xmax = vc.numxpixels;
        si.ymax = vc.numypixels;
        si.mode = mode;
        /* Set flag to indicate whether multiple colors are available.
*/
        si.color = iscolor( mode );
        return TRUE;
    }
}

/* two_choice_menu - Gets responses to two specified choices.
 * Params: title - Menu title string
 *         choicel - Selection 1 string
 *         choice2 - Selection 2 string
 * Return: Number of choice, or ESCAPE
 */
int two_choice_menu( char *title, char *choicel, char *choice2 )
{
    int choice;
    /* Initialize title and selections. */
    two_choice_titles[0] = title;
    two_choice_titles[1] = choicel;
    two_choice_titles[2] = choice2;
    two_choice_titles[3] = "\0";
    push_title( two_choice_titles[0] );

    while( TRUE )
    {
        /* Accept only first letter of either selection, or ESC. */
        choice = menu( two_choice_titles );
        switch( choice )
        {
            case 1:
            case 2:
            case ESCAPE:
                return(choice);
        }
    }
}

/* clear_form - Clears the center of the screen form.
 * Params: None
 */
void clear_form(void)
{
    /* Set partial screen window and clear it, then reset full screen.
*/
    _settextwindow( si.top, 1, si.bot, 80 );
    _clearscreen( _GWINDOW );
    _settextwindow( 1, 1, 25, 80 );
}

/* Clear_help - Clears the current help line.
 * Params: None
 */
void clear_help(void)
{
    /* Decrement the help line counter and clear the line. */
    _settextwindow( --si.help, 1, si.help, 80 );
    _clearscreen( _GWINDOW );
    _settextwindow( 1, 1, 25, 80 );
}

```

```

)

/* display_error_message - Displays an error message.
 * Params: error_message - error message string
 */
void display_error_message( char *error_message )
{
    /* Beep, set error color, and display error message and continue
    prompt. */
    putchar( BEEP );
    help( error_message, co.errorcolor );
    help( "Press any key to continue.", co.errorcolor );

    /* Wait for keypress and clear help lines. */
    getch();
    clear_help();
    clear_help();
}

/* help - Displays a help line on the screen.
 * Params: error_message - error message string
 *         color - color for message
 */
void help( char *error_message, short color )
{
    struct rccoord cursor_coords;
    /* Save current cursor position. */
    cursor_coords = _gettextposition();
    /* Print out help line and increment Helpline position variable.*/
    print_at(si.help++, 5, error_message , color );
    /* Restore cursor position. */
    _settextposition( cursor_coords.row, cursor_coords.col );
}

/* input_char - Prompts for and returns a character of input.
 * Params: prompt - Prompt string
 *         accept - String of acceptable characters (case insensitive)
 * Return: Character entered
 */
int input_char( char *prompt, char *accept )
{
    int response;
    char *chptr;

    /* Display prompt. */
    print_at(si.mid, 10, prompt, co.inputcolor );

    /* Loop until response is valid. */
    while( TRUE )
    {
        response = toupper( getch() );
        chptr=strchr( accept, response);

        /* Display and return if acceptable character, or beep if not.
        */
        if( chptr!=NULL )
        {
            _settextcolor( co.infocolor );
            putchar( response );
            return( response );
        }
        else
            putchar( BEEP );
    }
}

```

```

    )
}

/* input_int - Prompts for and returns an integer value within a
 * specified range.
 * Params: prompt - Prompt string
 *         old - Previous value
 *         min - Minimum value of range
 *         max - Maximum value of range
 * Return: integer input by user
 */
int input_int( char *prompt, int old, int min, int max )
{
    int i;
    char temp[70];

    /* Prompt for a string input and convert to an integer until a
     * value in the specified range is given. Then return the value.
     */
    do
    {
        input_string( prompt, itoa( old, temp, 10) );
        i = atoi( temp );
    } while( !in_range( i, min, max) );
    return( i );
}

/* input_double - Prompts for and returns a double value.
 * Params: prompt - Prompt string
 *         old - Previous value
 * Return: double input by user
 */
double input_double( char *prompt, double old )
{
    char temp[51];

    /* Prompt for a string input and convert to a double. */
    sprintf( temp, "%f", old );
    input_string( prompt, temp );
    return( atof( temp ) );
}

/* input_string - Prompts for a string. Displays the previous string
 * until the first character is given. Then replaces it with new
 * entry.
 * Params: prompt - Prompt string
 *         old - Character buffer containing previous string; it
 *             must be long enough to hold new string
 * Return: pointer to old, which now contains new string
 */
char *input_string( char *prompt, char *old )
{
    char temp[81];
    int x = 5, y = si.mid, ch;
    /* Display prompt in center of form. */
    clear_form();
    print_at( y, x, prompt, co.inputcolor );
    x += strlen( prompt );
    /* Print the old value for reference. */
    _settextcolor( co.infocolor );
    _outtext( old );
    _settextposition( y, x );
    /* Wait for input. When received, clear old string. */

```

```

while( !(ch = kbhit()) );
memset( temp, ' ', 80 );
temp[80] = '\0';
print_at(y, x, temp, -1 );
/* Get new string. If string entered, return it. If null string
 * (ENTER key pressed), return old value. */
_settextcolor( co.infocolor );
_settextposition( y, x );
temp[0] = 50;      /* Maximum length to be read */

cgets( temp );
if( temp[1] > 0 )      /* Are any characters read? */
{
    strcpy( old, &temp[2] );
    return( &temp[2] );
}
else
{
    _settextposition( y, x );
    return( old );
}
}

/* in_range - Checks an integer to see if it is in a specified range.
 *
 * Params: value - Integer to check
 *         min - Minimum value of range
 *         max - Maximim value of range
 * Return: TRUE if in range, FALSE if not
 */
BOOL in_range( int value, int min, int max )
{
    /* Check range and return true if valid, false if not. Note that
     * (min >= max) is taken as a signal to check only the minimum
     * value; there is no maximum.
     */
    if((value>=min) & ((value<=max)|| (min >= max)))
    {
        return( TRUE );
    }
    else
    {
        display_error_message( "Invalid value." );
        return( FALSE );
    }
}

/* menu - Draws menu on screen and returns choice number.
 * Params: array of menu strings
 * Return: number corresponding to the choice made from the menu
 */
int menu( char *menulist[] )
{
    int index, item_count, ypos, xpos = 10;
    int response;

    /* Count menu items. */
    for( item_count = 1; *menulist[item_count]; item_count++ );
    --item_count;

    /* Clear the form and print the items in the menu. */
    write_form( 10 + item_count );
    for( index = 1, ypos = 8; index <= item_count; index++, ypos++ )

```



```

    {
        print_at(ypos, xpos, menulist[index], co.inputcolor );
        print_char( ypos, xpos, menulist[index][0], co.hilitecolor );
    }
    ++ypos;

    /* Display prompt and help. */
    if( strcmpi( menulist[0], "main menu" ) ) /* If not the main menu
*/
        help( "Type the first letter of your selection or ESC to back up.",
            co.inputcolor );
    else
        help( "Type the first letter of your selection or \"Q\" to quit.",
            co.inputcolor );

    print_at(ypos, xpos += 5, "Choice? ", co.infocolor );
    xpos += 8;

    /* Loop until a valid choice is made. Beep at invalid choices. */
    while( TRUE )
    {
        _settextposition( ypos, xpos );
        response = toupper( getch() );

        /* Back up for ESC. */
        if( response == 27 )
        {
            clear_help();
            return( ESCAPE );
        }

        /* Search first letters of choices for a match. If found, return
        * choice and clear help line.
        */
        for( index = 1; index <= item_count; index++ )
        {
            if( response == toupper( menulist[index][0] ) )
            {
                putchar( response );
                clear_help();
                return( index );
            }
        }

        /* If we get here, no valid choice was found, so beep and repeat.
*/
        putchar( BEEP );
    }
}

/* pop_title - Pops a menu title from the menu stack.
* Params: None
*/
void pop_title()
{
    menutitles[--menulevel] = "";
}

/* print_at - Prints a string at the row/column coordinates
* specified, in the specified color.
* Params: row - row at which to begin output of string
* col - column at which to begin output of string
* string - zero (null) terminated string

```

```

*          color          - color in which to output string (-1 if
*                          print_at should leave color alone)
*/
void print_at(int row, int column, char far *string, short color )
(
    if( color != -1 )
        _settextcolor( color );
        _settextposition( row, column );
        _outtext( string );
)

/* print_char - Prints a character at the row/column coordinates
*              specified, in the specified color.
*
* Params: row          - row at which to begin output of string
*         col          - column at which to begin output of string
*         character    - character to print
*         color        - color in which to output string (-1 if
*                          print_char should leave color alone)
*/
void print_char(int row, int column, char character, short color)
(
    char temp[2];

    temp[0] = character;
    temp[1] = '\0';
    print_at(row, column, temp, color );
)

/* push_title - Pushes a menu title on to the menu stack.
*
* Params: title - title string to push
*/
void push_title( char *title )
(
    menutitles[menulevel++] = title;
)

/* set_display_colors - Set the colors to values appropriate to the
display
*                      adaptor being used.
* Params: None
*/
void set_display_colors()
(
    if( ismono( si.mode ) )
    (
        co.inputcolor   = M_INPUTCOLOR;
        co.hilitecolor  = M_HILITECOLOR;
        co.formcolor    = M_FORMCOLOR;
        co.titlecolor   = M_TITLECOLOR;
        co.errorcolor   = M_ERRORCOLOR;
        co.infocolor    = M_INFOCOLOR;
    )
    else
    (
        co.inputcolor   = C_INPUTCOLOR;
        co.hilitecolor  = C_HILITECOLOR;
        co.formcolor    = C_FORMCOLOR;
        co.titlecolor   = C_TITLECOLOR;
        co.errorcolor   = C_ERRORCOLOR;
        co.infocolor    = C_INFOCOLOR;
    )
)

```

```

)

/* write_form - Displays screen form.
 * Params: ybottom - Row number of the bottom row
 */
void write_form( int ybottom )
{
    int i;
    char temp[81];

    /* Print message in upper right. */
    _clearscreen( _GCLEARSCREEN );
    print_at(1, 20, "BRITE Permeability Measurement Program",
co.titlecolor );

    /* Clear the top separator line. */
    memset( temp, ' ', 79 );
    temp[79] = 0;

    /* Display each level of the menu title. */
    _settextposition( 5, 5 );
    for( i = 0; i < menulevel; i++ )
    {
        if( i )
            _outtext( " - " );
        _outtext( menutitles[i] );
    }

    /* Display the top separator line. */
    memset( temp, 196, 80 );
    temp[80] = 0;
    print_at(6, 1, temp, co.formcolor );

    /* Display the bottom separator line. */
    print_at(ybottom, 1, temp, co.formcolor );

    /* Set the global screen variables. */

    si.help = ybottom + 1;
    si.top = 7;
    si.bot = ybottom - 1;
    si.mid = (si.top + si.bot) / 2;
}

double snap_and_save(int frame_number)
{
    double frame_time;

    grab_video();
    frame_time=elapsed_time();
    double_to_string(frame_time, 4, time_buffer);
    ci_add_intext(&framestore, time_buffer, TIME);
    ci_add_intext(&framestore, fabric_buffer, FABRIC);
    ci_add_intext(&framestore, date_buffer, DATE);
    make_filename(filename, name, ext, frame_number);
    ci_write_discim(filename, &framestore, FFA, NO_PACK);
    free_image_text(&framestore);
    return(frame_time);
}

char *make_filename(char *output_buffer, char *name_buffer, char
*ext_buffer, int number)
{

```

```

char *filename_string;
filename_string=output_buffer;
do
{
    *(output_buffer++)=*(name_buffer++);
}
while(*name_buffer!='\0');
itoa(number, output_buffer, 10);
strcat(filename_string, ".");
strcat(filename_string, ext_buffer);
return(filename_string);
}

void print_frame_data( int frame_number )
{
    int y = si.mid;
    char temp[11];

    /* Display data at centre of form.    */
    print_at(y-2, 17, "Frame number", co.hilitecolor );
    print_at(y-2, 37, "Elapsed time (secs)", co.hilitecolor );
    y+=2;
    print_at(y, 22, (char far *)itoa(frame_number, temp, 10),
co.infocolor );
    print_at(y, 40, (char far *)time_buffer, co.infocolor );
}

void double_to_string( double value, int precision, char *output_buffer)
{
    char *input_buffer;
    int decimal, sign;
    input_buffer=fcvt(value, precision, &decimal, &sign);
    if(sign!=0) *(output_buffer++)='-';
    *(output_buffer++)=*(input_buffer++);
    *(output_buffer++)='.';
    if(*input_buffer=='\0')
    {
        *(output_buffer++)='0';
    }
    else
    {
        do
        {
            *(output_buffer++)=*(input_buffer++);
        }
        while(*input_buffer!='\0');
    }
    *(output_buffer++)='E';

    itoa((decimal-1), output_buffer, 10);
}

/*-----
---*/
/* Grab a live image from the video camera if it is set up */
/*-----
---*/

void grab_video(void)
{
    unsigned int i;
    ci_live(&framestore); /* Take live video images */
    for(i=0;i<49000;i++); /* Empty loop overcomes hardware fault */
}

```

```

    ci_photo(&framestore);/* Freezes image store framestore */
}

/*-----
--*/
/* Define and initialise images in framestore and disk */
/*-----
--*/

void init(void)
{
/* Read the framegrabber dimensions structure for image sizes, etc. */

    ci_fg_data(hInst, BOARD, 0, &framestore_dimensions);

/* Define framestore */

    if(!ci_def_vidim(hInst, &framestore, framestore_dimensions.grey[0].x,
framestore_dimensions.grey[0].y,
                                WID,
                                HT,
framestore_dimensions.grey[0].lsb,
                                UCHAR))
    {
        printf("\n Grey video image definition failed");
        printf("\n Error No = %lx: %s \n", (sword) ci_get_val(GS_ERRNO,
0),
            ci_errmess(hInst, (uint) ci_get_val(GS_ERRNO, 0)));
        exit(0);
    }

/* Set output LUT's for normal grey level display */

    ci_set_lin_out(&framestore, 0, &lut[0]);

    if(!ci_def_vidim(hInst, &binary,    framestore_dimensions.bin[0].x,
framestore_dimensions.bin[0].y,
                                WID,
                                HT,
framestore_dimensions.bin[0].lsb,
                                BIT))
    {
        printf("\n Binary image definition failed");
        printf("\n Error No = %lx: %s \n", (sword) ci_get_val(GS_ERRNO,
0),
            ci_errmess(hInst, (uint) ci_get_val(GS_ERRNO, 0)));
        exit(0);
    }

/* display grey image on monitor */
    if(!ci_display(&framestore))
    {
        printf("\n Image display failed");
        printf("\n Error No = %lx: %s \n", (sword) ci_get_val(GS_ERRNO,
0),
            ci_errmess(hInst, (uint) ci_get_val(GS_ERRNO, 0)));
        exit(0);
    }
}

void calibrate_image(imptr image_ptr, ptrptr ctr_point, double
*x_factor_ptr, double *y_factor_ptr)
{

```

```

point initial_point, x_point, y_point, x_axis_point, y_axis_point;

int button, break_loop=0;
int x_length=1, y_length=1;

if(calib_image_flag || !focus_flag)
{
    if(calib_image_flag)
    {
        clear_form();
        help("Recalibration not permitted", co.inputcolor);
        input_char("Press ESC to continue. ", "\x1b");
        return;
    }
    else
    {
        clear_form();
        help("Camera not focused", co.inputcolor);
        input_char("Press ESC to continue. ", "\x1b");
        return;
    }
}

/* Set initial point to centre of framestore */
initial_point.X=WID>>1;
initial_point.Y=HT>>1;
grab_video();

ci_define_cursor(hWnd, &initial_point, image_ptr, ARROW_CURSOR, 1);

clear_form();
write_form(12);
print_at(1, 20, "BRITE Permeability Measurement Program",
co.titlecolor );
print_at(8, 10, "Use LEFT mouse button to define centre of flow
region",
co.infocolor);
print_at(9, 10, "Click RIGHT mouse button to terminate action",
co.infocolor);
help("Follow instructions.", co.inputcolor);

do
{
    if((button=ci_roam_cursor(&initial_point, image_ptr)) &
LEFT_HIT)
    {
        *ctr_point=ci_where_cursor();
        ci_draw_cross(ctr_point, image_ptr, 5,0);
    }
}
while(button & LEFT_HIT);

itoa(ctr_point->X, x_point_buffer, 10);
itoa(ctr_point->Y, y_point_buffer, 10);

ci_draw_cursor(&initial_point, image_ptr);
ci_undraw_cursor(&initial_point, image_ptr);
ci_undefine_cursor();
x_axis_point.X=WID-1;
x_axis_point.Y=ctr_point->Y;
y_axis_point.X=ctr_point->X;
y_axis_point.Y=HT-1;
ci_draw_line(ctr_point, &x_axis_point, image_ptr, 0);

```

```

ci_draw_line(ctr_point,&y_axis_point,image_ptr,0);
ci_trans_char_to_im('X', image_ptr, WID-20, ctr_point->Y-20,1,0);
ci_trans_char_to_im('Y', image_ptr, ctr_point->X-10-20, HT-20,1,0);
ci_define_cursor(hWnd,&initial_point,image_ptr,ARROW_CURSOR,1);

clear_form();
write_form(12);
    print_at(1, 20, "BRITE Permeability Measurement Program",
co.titlecolor );
    print_at(8, 10, "Use LEFT mouse button to define known distance on X
axis",
                co.infocolor);
print_at(9, 10, "Click RIGHT mouse button to terminate action",
        co.infocolor);
help("Follow instructions.", co.inputcolor);

do
{
LEFT_HIT)
    if((button=ci_roam_cursor(&initial_point, image_ptr)) &
    {
        x_point=ci_where_cursor();
        ci_draw_cross(&x_point, image_ptr, 5,0);
    }
}
while(button & LEFT_HIT);
ci_draw_cursor(&initial_point,image_ptr);
ci_undraw_cursor(&initial_point, image_ptr);
ci_undefine_cursor();

clear_form();
write_form(11);
    print_at(1, 20, "Permeability Measurement Program", co.titlecolor
);
help("Enter known distance on X axis", co.inputcolor);
x_length=input_int("Distance on X axis? ", x_length, 1, 1000);
*x_factor_ptr = (double)x_length/((double)(x_point.X - ctr_point-
>X));

double_to_string(*x_factor_ptr, 4, x_factor_buffer);

clear_form();
write_form(12);
    print_at(1, 20, "Permeability Measurement Program", co.titlecolor
);
    print_at(8, 10, "Use LEFT mouse button to define known distance on Y
axis",
                co.infocolor);
print_at(9, 10, "Click RIGHT mouse button to terminate action",
        co.infocolor);
help("Follow instructions.", co.inputcolor);

do
{
LEFT_HIT)
    if((button=ci_roam_cursor(&initial_point, image_ptr)) &
    {
        y_point=ci_where_cursor();
        ci_draw_cross(&y_point, image_ptr, 5,0);
    }
}
while(button & LEFT_HIT);

```

```

    ci_draw_cursor(&initial_point, image_ptr);
    ci_undraw_cursor(&initial_point, image_ptr);
    ci_undefine_cursor();

    clear_form();
    write_form(11);
    print_at(1, 20, "Permeability Measurement Program", co.titlecolor
);
    help("Enter known distance on Y axis", co.inputcolor);
    y_length=input_int("Distance on Y axis? ", y_length, 1, 1000);

    *y_factor_ptr = y_length/((double)(y_point.Y - ctr_point->Y));

    double_to_string(*y_factor_ptr, 4, y_factor_buffer);

    clear_form();
    write_form(12);
    print_at(1, 20, "BRITE Permeability Measurement Program",
co.titlecolor );
    print_at(8, 10, "X calibration factor: ", co.inputcolor);
    print_at(9, 10, "Y calibration factor: ", co.inputcolor);
    print_at(8, 35, x_factor_buffer, co.infocolor);
    print_at(9, 35, y_factor_buffer, co.infocolor);
    help("Hit ESC to continue", co.inputcolor);

    do
    {
        if(kbhit())
        {
            if(getch()==ESCAPE)
            {
                break_loop=1;
            }
        }
    }
    while(!break_loop);

    /* Set current date in date_buffer */
    time(&timer);
    time_ptr=localtime(&timer);
    strftime(date_buffer, 16, "%d %B %Y",time_ptr);

    ci_clear_fg(image_ptr);
    calib_image_flag=TRUE;
}

void free_image_text(imptr image_ptr)
{
    ci_free_imtext(image_ptr);
    image_ptr->TDCOUNT=0;
}

/*****
*****
    FUNCTION: void DefROI(psptr ps)
    PURPOSE: Interactively define Region of Interest within pointset *ps
    *****/
void define_roi(psptr ps)
{
    point initial_point; /* Initial position of mouse & cursor */
    int ok;

```



```

    /* Set mouse to the middle of screen */
    initial_point.X = WID >> 1;
    initial_point.Y = HT >> 1;

    do
    {
        if(roi_defined)
        {
            ci_divest_obj(&roi_obj);
        }

/* The binary image must be cleared to enable us to define an ROI in it
*/
        ci_black_im(&binary);

/* Overlay binary image with random colour overlay
*/

        col.r = rand(); col.g = rand(); col.b = rand();
        ci_overlay(&binary, &col);

/* Reduce window size by 1 pixel all around. This allows neighbourhood
*/
/* operations including object detection, and the resulting ROI can then
*/
/* be used for neighbourhood operations in the image. */

        ci_reduce_ps(&binary.WHOLE, 1, 1);

        clear_form();
        write_form(13);
        print_at(1, 20, "BRITE Permeability Measurement Program",
co.titlecolor );
        print_at(8, 10, "Define a region of interest using mouse",
co.infocolor);
        print_at(9, 10, "Click LEFT mouse button to start drawing",
co.infocolor);
        print_at(10, 10, "Click either mouse button to terminate action",
co.infocolor);
        help("Follow instructions.", co.inputcolor);

/* Define cursor. The cursor is restricted to binyim.WHOLE
*/
        ci_define_cursor(hWnd, &initial_point, &binary, ARROW_CURSOR, 1);

/* Draw with mouse and generate object as boundary and interior pointsets
*/

        if (ok = ci_draw_gen_obj(&binary.WHOLE, &binary, &roi_obj))
        {
            roi = roi_obj.interior;          /* Set the ROI to object
just drawn */
            ci_draw(&roi, &binary, 0);      /* Clear the ROI
*/
        }
        else
        {
            clear_form();
            clear_help();
            help(ci_errmess(hInst, (uint) ci_get_val(GS_ERRNO, 0)),
co.inputcolor);
            input_char("Press ESC to continue. ", "\x1b");
        }

```

```

        ci_undefine_cursor(); /* Remove the cursor from the image */
        ci_reset_im(&binary); /* Reset binary.WHOLE */
        ci_overkill(hInst); /* Turn off overlay */
        roi_defined=TRUE;
    }
    while (!ok);
}

void set_threshold_level(void)
{
    dyn hgram;
    int frame_number=1;
    help("Enter number of frame to retrieve.", co.inputcolor);
    frame_number=input_int("Number of Frame? ", frame_number, 1, 0);
    make_filename(filename, name, ext, frame_number);

    if(!ci_read_discim(filename, &framestore, FFA))
    {
        clear_form();
        clear_help();
        help("Image not read successfully", co.inputcolor);
        input_char("Press ESC to continue. ", "\x1b");
        return;
    }

    ci_black_im(&binary);
    define_roi(&binary.WHOLE);

    if (ci_im_histo(&roi, &framestore, &hgram)) /* Generate a histogram
of image values over a pointset */
    {
        point p; /* Starting point for cursor */
        pointset box; /* Window in which to display histogram */
        pointset cursor; /* Pointset to be used as cursor */
        pointset cursline; /* Pointset in which to roam cursor */

#define CURS_HT 10 /* Height of cursor */
        int ox = WID - 256 >> 1;
        int oy = HT >> 2;
        int hy = oy + (HT >> 1);

        /* Define the window in which the cursor can move */
        ci_def_window(&cursline, ox, hy, 256, CURS_HT);

        /* Define a single pixel wide vertical line as a cursor */
        ci_def_window(&cursor, ox, hy, 1, CURS_HT);

        /* Define the box in which histogram will be displayed */
        ci_def_window(&box, ox, oy, 256, HT >> 1);
        col.r = 255; col.g = 127; col.b = 0;
        ci_overlay(&binary, &col);
        ci_draw_histo(&box, &binary, &hgram); /* Draw the histogram */
        ci_divest_dyn(&hgram); /* Release dynamic data */

        /* Place a tick at the lower end of the cursor range to indicate lower
value for thresholding. */
        cursor.PSORIGX--;
        ci_draw(&cursor, &binary, -1);
        cursor.PSORIGX++;
        p.X = ox + 128; /* Set mouse position to middle of range */
        p.Y = hy;
    }
}

```

```

/* Use the cursor pointset to indicate the position in the histogram. The
call to ci_define_cursor restricts cursor movement to binary.WHOLE, so
this must be set to the pointset cursline. By using NO_CURSOR, no other
pointer will be displayed in the image */

```

```

        binary.WHOLE = cursline;
        ci_define_cursor(hWnd, &p, &binary, NO_CURSOR, 1);
            clear_form();
            write_form(12);
            print_at(1, 20, "Permeability Measurement Program",
co.titlecolor);
            print_at(8, 10, "Select the level at which to threshold ",
                co.infocolor);
            print_at(9, 10, "Click RIGHT mouse button to terminate
action",
                co.infocolor);
            help("Follow instructions.", co.inputcolor);

        ci_roam_ps(&cursor, &binary); /* Put curser in roam mode */
        ci_undefine_cursor();          /* Undefine the cursor */
        thresh_val = cursor.PSORIGX - ox;
        cursor.PSORIGX = ox - 1;
        ci_draw(&cursor, &binary, 0); /* Clear low-level marker */
        ci_reset_im(&binary); /* Reset binary.WHOLE to the entire image
*/
        ci_draw(&box, &binary, 0); /* Clear histogram
*/
        /* Threshold the grey image into the binary image
*/
        ci_slice(&roi, &framestore, &binary, 0, thresh_val);
    }
    else
    {
        clear_form();
        clear_help();
        help("Unable to threshold", co.inputcolor);
        input_char("Press ESC to continue. ", "\x1b");
        free_image_text(&framestore);
        ci_overkill(hInst);
        ci_clear_fg(&framestore);
        ci_clear_fg(&binary);
        return;
    }

    clear_form();
    clear_help();
    help("", co.inputcolor);
    input_char("Press ESC to continue. ", "\x1b" );
    free_image_text(&framestore);
    ci_overkill(hInst);
    ci_clear_fg(&framestore);
    ci_clear_fg(&binary);
    set_threshold_flag=TRUE;
}

```

```

void generate_points(ptptr centre_point, ptptr ptarray, int
num_of_spokes)
{
    int count;
    double alpha, beta, gamma, delta;
    ptptr wrkptr;
    wrkptr=ptarray;

```

```

    alpha=atan((double)centre_point->Y/(double)(WID-1-centre_point-
>X));
    beta=PI-atan((double)centre_point->Y/(double)centre_point->X);
    gamma=PI+atan((double)(HT-1-centre_point->Y)/(double)centre_point-
>X);
    delta=2*PI-atan((double)(HT-1-centre_point->Y)/(double)(WID-1-
centre_point->X));

    for(count=0; count<num_of_spokes; count++)
    {
        angle[count]=(2*PI*count)/(double)num_of_spokes;

        if(((angle[count]>=0)&(angle[count]<=alpha))||((angle[count]>delta)
&(angle[count]<=2*PI)))
        {
            wrkptr->X=WID-1;
            wrkptr->Y=centre_point->Y-(int)((WID-1-centre_point-
>X)*tan(angle[count]));
        }
        else
        {
            if((angle[count]>alpha)&(angle[count]<=beta))
            {
                wrkptr->X=centre_point->X+(int)(centre_point-
>Y*tan(PI/2-angle[count]));
                wrkptr->Y=0;
            }
            else
            {
                if((angle[count]>beta)&(angle[count]<=gamma))
                {
                    wrkptr->X=0;
                    wrkptr->Y=centre_point->Y-
(int)(centre_point->X*tan(PI-angle[count]));
                }
                else
                {
                    if((angle[count]>gamma)&(angle[count]<delta))
                    {
                        wrkptr->X=centre_point->X-(int)((HT-
1-centre_point->Y)*tan((3*PI)/2-angle[count]));
                        wrkptr->Y=HT-1;
                    }
                    else
                    {
                        printf("Theta out of range\n");
                    }
                }
            }
        }
    }
    wrkptr++;
}

```

```

void draw_radii(imptr im, ptptr centre_point, ptptr ptarray, int
num_of_spokes)
{
    int count;
    ptptr wrkptr;
    wrkptr=ptarray;
    for(count=0; count<num_of_spokes; count++)
    {

```

```

        ci_draw_line(centre_point, wrkptr, im);
        wrkptr++;
    }
}

void gen_spokes(ptptr centre_point, ptptr ptarray, psptr psarray, int
num_of_spokes)
{
    int count;
    ptptr wrkptptr;
    psptr wrkpsptr;
    wrkptptr=ptarray;
    wrkpsptr=psarray;

    for(count=0; count<num_of_spokes; count++)
    {
        ci_arc_gen(centre_point, wrkptptr, wrkpsptr);
        wrkptptr++;
        wrkpsptr++;
    }
}

void get_spoke_end(imptr im, psptr psspoke, ptptr end_point, int
num_of_spokes)
{
    dyn profile;
    ptptr wrkptptr;
    psptr wrkpsptr;
    int found=0, x;
    int count;
    uchptr data;

    wrkptptr=end_point;
    wrkpsptr=psspoke;

    for(count=0; count<num_of_spokes; count++)
    {
        if(ci_im_sample(wrkpsptr, im, &profile))
        {
            if(ci_reset_ps(wrkpsptr))
            {
                if(CI_LOCKDYN(&profile))
                {
                    x=0;
                    data=profile.ptr;

                    do
                    {
                        if (data[x]==0)
                        {
                            /* found edge of flow */
                            found=1;
                            *wrkptptr=wrkpsptr->WRKPT;
                            ci_divest_dyn(&profile);
                            break;
                        }

                        x++;
                    }
                    while(ci_next_pt(wrkpsptr));
                    CI_UNLOCKDYN(&profile);
                }
                CI_UNLOCKPS(&wrkpsptr);
            }
        }
    }
}

```

```

        }
    }

    wrkptptr++;
    wrkpsptr++;
    found=0;
}
}

void draw_cross(imptr im, ptptr ptarray, int num_of_spokes)
{
    int count;
    ptptr wrkptr;
    wrkptr=ptarray;

    for(count=0; count<num_of_spokes; count++)
    {
        ci_draw_cross(wrkptr, im, 5, 5, 0);
        wrkptr++;
    }
}

void calc_coords(ptptr centre_point, ptptr end_point, double *rad)
{
    int count;
    double *wrkptr_rad;
    ptptr wrkptptr;
    wrkptr_rad=rad;
    wrkptptr=end_point;

    for(count=0; count<NUM_OF_SPOKES; count++)
    {
        *wrkptr_rad=sqrt(pow(fabs((double)(wrkptptr->X-centre_point-
>X)*x_factor),2.0)
+ pow(fabs((double)(wrkptptr->Y-centre_point->Y)*y_factor),2.0));
        wrkptr_rad++;
        wrkptptr++;
    }
}

void analyse_image(void)
{
    int num_of_spokes=NUM_OF_SPOKES;
    int tag, n=0;
    char temp[17];
    make_filename(filename, name, ext, frame_index);

    if(!ci_read_discim(filename, &framestore, FFA))
    {
        clear_form();
        clear_help();
        help(ci_errmess(hInst, (uint) ci_get_val(GS_ERRNO, 0)),
co.inputcolor);
        input_char("Press ESC to continue. ", "\x1b");
        return;
    }

    tag=TIME;
    str=(unsigned char far*) ci_get_imtext(&framestore, &tag, &n);
    strcpy(time_buffer, str);
    frame_time=atof(time_buffer);

    itoa(frame_index, temp, 10);
}

```

```

ci_string_to_im("Frame Number  ", &framestore,5,5,1,-1);
ci_string_to_im(temp, &framestore,110,5,1,-1);
ci_string_to_im("Frame Time    ", &framestore,5,25,1,-1);
ci_string_to_im(time_buffer, &framestore,110,25,1,-1);

define_roi(&binary.WHOLE);

/* Threshold the grey image into the binary image */
ci_slice(&roi, &framestore, &binary, 0, thresh_val);

/* generate_points(&centre_point, point_array, num_of_spokes); */
/* gen_spokes(&centre_point, point_array, ps_array, num_of_spokes); */
*/

get_spoke_end(&binary, ps_array, end_point, num_of_spokes);
col.r= col.g= col.b = 255;

draw_radii(&framestore, &centre_point, end_point, num_of_spokes);
draw_cross(&framestore, end_point, num_of_spokes);
calc_coords(&centre_point, end_point, radii);

clear_form();
clear_help();
help("Analysis completed.", co.inputcolor);
input_char("Press ESC to continue. ", "\x1b" );

print_frame_results();
free_image_text(&framestore);
ci_clear_fg(&framestore);
ci_clear_fg(&binary);
}

/*
 * Params: None
 */
void print_frame_results()

{
int row = 5, count;
static char *cont =
    "Press any key to return to the menu.";
clearscreen( _GCLREASCREEN );
strprint_at(row, 20, "Results for Frame Number %d", frame_index);
strprint_at(row+=2, 1, "Frame time %.3f", frame_time );
strprint_at(row+=2, 1, "Angle (Rads.)      Radius (mm)
Angle (Rads.)      Radius (mm)");
for(count=1;count<=NUM_OF_SPOKES;count+=2)
    {
strprint_at(++row, 1, "%3.3f %3.2f %3.3f %3.2f",
angle[count-1], radii[count-1], angle[count], radii[count]);
strprint_at(row+=2, 1, cont);
if( getch() == ESCAPE )
return;
}

/* strprint_at - Format a string, using sprintf() and output to screen
using print_at().
*
* Params: row - Row at which to begin display
*          col - Column at which to begin display
*          fmt - Format string (see run-time library documentation for
*          correct formation of a format string)

```

```
*          = Variables to output
*/
void strprint_at(int row, int col, char *fmt, ... )
{
    char temp[81];
    va_list marker;
    va_list save_marker;
    va_start( marker, fmt );
    save_marker = marker;
    vsprintf( temp, fmt, marker );
    va_end( marker );
    print_at(row, col, temp, -1 );
}
```



*Program to copy files from Viglen to XEN  
and prepare files to be read by the Quantimet 570*

```
CLS
F:
CD F:\PERM\FFA-TIG
CLS
@ECHO OFF
ECHO.
ECHO          *** about to delete all old TIG images from XEN ***
ECHO.
ECHO          *** have files been processed ? ***
ECHO.
ECHO          *** have files been backed up ? ***
ECHO.
PAUSE
DEL F:\PERM\DOWNLOAD\*.TIG

CLS
ECHO.
ECHO          *** copying *.TIF images from Viglen I-drive to XEN F-drive***
ECHO.
COPY I:\NP\RUN\*.TIF F:\PERM\DOWNLOAD

CLS
REN F:\PERM\DOWNLOAD\IMAGE1.TIF IMAGE01.TIF
REN F:\PERM\DOWNLOAD\IMAGE2.TIF IMAGE02.TIF
REN F:\PERM\DOWNLOAD\IMAGE3.TIF IMAGE03.TIF
REN F:\PERM\DOWNLOAD\IMAGE4.TIF IMAGE04.TIF
REN F:\PERM\DOWNLOAD\IMAGE5.TIF IMAGE05.TIF
REN F:\PERM\DOWNLOAD\IMAGE6.TIF IMAGE06.TIF
REN F:\PERM\DOWNLOAD\IMAGE7.TIF IMAGE07.TIF
REN F:\PERM\DOWNLOAD\IMAGE8.TIF IMAGE08.TIF
REN F:\PERM\DOWNLOAD\IMAGE9.TIF IMAGE09.TIF
IF EXIST F:\PERM\DOWNLOAD\IMAGE09.TIF ECHO
    *** images renamed, now sorted numerically as two digit numbers ***
ECHO.
ECHO          *** about to enter cropping phase ***
ECHO.
PAUSE
ECHO          *** starting windows ***
ECHO.
E:\WIN-APPS\TIFF-KIT\CROPEXE F:\PERM\DOWNLOAD\*.TIF,
F:\PERM\DOWNLOAD\*.TIF, F:\PERM\FFA-TIG\CROP.TXT, 1
ECHO.

CLS
ECHO.
ECHO          *** batch process *.TIF images in PSP to save as uncompressed ***
ECHO.
PAUSE

WIN E:\WIN-APPS\PSP\PSP.EXE
REN F:\PERM\DOWNLOAD\*.TIF *.TIG
ECHO.
ECHO          *** *.TIF now renamed to *.TIG ***
ECHO.
DEL F:\PERM\DOWNLOAD\IMAGE01.TIG
COPY I:\NP\CALIB\SIZE\IMAGE01.TIG F:\PERM\DOWNLOAD
ECHO.
ECHO          *** calibration file (IMAGE01.TIG) copied to XEN ***
ECHO.
```

**Quantimet program to retrieve isochrone data from flow images (FLOW.QBA)**

```
10 clearimages
20 BINCLEAR-1
30 BINCLEAR 15
40 CLEARPLANE-1
50 ferets 64
60 INPUT 'Name of file please neil? 'n$
70 open#1 'C:\neil\'+'n$+'.any'
80 open#2 'C:\neil\'+'n$+'.map'
90 open#3 'C:\neil\'+'n$+'.inj'
100 open#4 'C:\neil\'+'n$+'.cog'
110 open#5 'C:\neil\'+'n$+'.1st'
120 PRINT#1: 'FRAME', 'LENGTH', 'BREADTH', 'L-CAL-O', 'B-CAL-O'
130 PRINT#2: 'FRAME', 'WE', 'ENE', 'NE', 'NEN', 'NS', 'NWN', 'NW', 'WNW'
140 PRINT#3: 'FRAME', 'LENGTH', 'CALC-O', 'X', 'Y'
150 PRINT#4: 'FRAME', 'LENGTH', 'CALC O'
160 PRINT#5: 'FRAME', '0 DEG', '90
DEG', 'EAST', 'WEST', 'NORTH', 'SOUTH', 'MAXL/2', 'ECD/2', 'AREA', 'ROUND', 'AR', '
YCG-INJ', 'XCG-INJ'
170 mframe 0 0 512 512
180 iframe 0 0 512 512
190 K=0.583333 REM riasettings 'cal_value' k in mm
200 c=1
210 n=0
220 o=0
230 o$=str$(o)
240 c$=str$(c)
250 loadbin 9 'c:\bin\neilins'
260 loadbin 10 'c:\bin\neilmask'
270 loadimage 10 'c:\neil\image02.tig'
280 loadimage 0 "C:\neil\IMAGE"+o$+c$+".TIG"
290 rem grey 10=image01
300 greysub 0 10 1
310 greydetect 1 75 88 4 1 0
320 binopen 1 2 256 2
330 fillholes 2 3
340 setftrpar "2,3,1,8,33,15,28,29,4,5,9,12,21,24,22,25,23,20,32,34"
350 ftrgrey 1 : measfeat 3 1 1300 300000 : clraccept
360 acceptxfer 3 4
370 RFEATNUM N(1)
380 if c=1 goto 1530
390 if n(1)=0 goto 1530
400 FOR F=0 TO N(1)-1
410 RFEATRES F 1 a(1)
420 AREA=A(1)*K*K REM THIS AREA WILL BE PRINTED TO FILE 5 *.1ST
430 RFEATRES F 8 L(1)
440 RFEATRES F 9 B(1)
450 RFEATRES F 12 MO(1)
460 RFEATRES F 32 CO(1)
470 RFEATRES F 33 AR(1)
480 ASPECT=AR(1)/1000
490 RFEATRES F 15 R(1)
500 ROUND = R(1)/1000
510 RFEATRES F 28 X(1)
520 XCG=X(1)
530 RFEATRES F 29 Y(1)
540 YCG=Y(1)
550 RFEATRES F 4 WE(1)
560 RFEATRES F 34 EQDIA(1)
570 RADIUS=(EQDIA(1)*K)/2
580 RFEATRES F 5 NS(1)
590 RFEATRES F 20 ENE(1)
```

```

600 RFEATRES F 21 NE(1)
610 RFEATRES F 22 NEN(1)
620 RFEATRES F 23 NWN(1)
630 RFEATRES F 24 NW(1)
640 RFEATRES F 25 WNW(1)
650 PRINT#1:C,L(1)*K,B(1)*K,CO(1),MO(1)
660
PRINT#2:C,WE(1)*K,ENE(1)*K,NE(1)*K,NEN(1)*K,NS(1)*K,NWN(1)*K,NW(1)*K,WNW(
1)*K
670 next f
680 rfeatres n 28 x(2)
690 x=x(2)/1000
700 rfeatres n 29 y(2)
710 y=y(2)/1000
720 print x,y
730 position 5 x y
740 drawline 510 y
750 position 5 x y
760 drawline 0 y
770 position 5 x y
780 drawline x-200 y-200
790 position 5 x y
800 drawline x+200 y+200
810 position 5 x y
820 drawline x 510
830 position 5 x y
840 drawline x 0
850 position 5 x y
860 drawline x+200 y-200
870 position 5 x y
880 drawline x-200 y+200
890 BINGET 5 5
900 chrpoint 5 7 1
910 binx 5 7 7 3 0 0
920 rfeatnum n(2)
930 if n(2)>0 n=n(1)
940 print c,n
950 n=0
960 binx 4 7 8 1 0 0
970 setftrpar "2,3,8,1,11,28,29,32"
980 ftrgrey 1 : measfeat 8 1 4 300000 : clraccept
990 acceptfeat 8 5.18889 4980
1000 acceptxfer 8 22
1010 rfeatnum n(1)
1020 for f=0 to n(1)-1
1030 rfeatres f 8 l(1)
1040 L=L(1)+2
1050 rfeatres f 32 co(1)
1060 rfeatres f 28 x(1)
1070 rfeatres f 29 y(1)
1080 print#3:C,l*k,co(1),x(1)/1000,y(1)/1000
1090 next f
1100 binclear 11
1110 binx 10 4 11 1 0 0
1120 setftrpar "2,3,8,1,9,32,11"
1130 ftrgrey 1 : measfeat 11 1 4 300000 : clraccept
1140 acceptxfer 11 12
1150 rfeatnum n(1)
1160 for f=0 to n(1)-1
1170 rfeatres f 8 l(1)
1180 LL=L(1)+2
1190 rfeatres f 9 b(1)
1200 rfeatres f 11 o(1)

```

```

1210 rfeatres f 32 co(1)
1220 print#4: C,LL*k,co(1)
1230 next f
1240 CO=-225
1250 ML=0
1260 YC=Y-230:YD=Y+230
1270 XC=X-CO:XD=X+CO
1280 binclear 3
1290 clearplane 3
1300 POSITION 3 XC YC
1310 DRAWLINE XD YD
1320 binclear 13
1330 BINGET 3 13
1340 binx 4 13 14 1 0 0
1350 setftrpar "2,3,8,1,11,32"
1360 ftrgrey 1 : measfeat 14 1 4 300000 : clraccept
1370 acceptxfer 14 22
1380 rfeatnum n(1)
1390 for f=0 to n(1)-1
1400 rfeatres f 32 co(1)
1410 rfeatres f 8 l(1)
1420 IF ML<L(1) THEN ML=L(1)
1430 next f
1440 PRINT#4:C,ML*K,CO(1),'MAX'
1450 Co=Co+20
1460 IF co>247 GOTO 1480
1470 GOTO 1270
1480 XC=X-230:XD=X+230
1490 CY=CO-460
1500 YC=Y+CY:YD=Y-CY
1510 IF CO>694 GOTO 1580 REM NO REPEATS YET
1520 GOTO 1280
1530 PRINT#1:C
1540 PRINT#2:C
1550 PRINT#3:C
1560 PRINT#4:C
1570 PRINT#5:C
1580 c=c+1
1590 if c=10 o$=''
1600 if c>44 goto 2060 rem c=c+4=<1DEG C=C+20=<5DEG
1610 bindilate 9 16 66 272
1620 bindilate 9 17 24 271
1630 binx 16 4 18 1 0 0
1640 binx 17 4 19 1 0 0
1650 binx 18 9 20 1 0 1
1660 binx 19 9 21 1 0 1
1670 setftrpar "2,3,8,1,11"
1680 ftrgrey 1 : measfeat 19 1 4 300000 : clraccept
1690 acceptxfer 19 22
1700 RFEATNUM N(1)
1710 FOR F=0 TO N(1)-1
1720 RFEATRES F 8 L0(1)
1730 L0=L0(1)*K/2
1740 NEXT F
1750 setftrpar "2,3,8,1,11"
1760 ftrgrey 1 : measfeat 18 1 4 300000 : clraccept
1770 acceptxfer 18 22
1780 RFEATNUM N(1)
1790 FOR F=0 TO n(1)-1
1800 RFEATRES F 8 L90(1)
1810 L90=L90(1)*K/2
1820 NEXT F
1830 setftrpar "2,3,8,1,11"

```

```
1840 ftrgrey 1 : measfeat 21 1 4 300000 : clraccept
1850 acceptxfer 21 22
1860 RFEATNUM N(1)
1870 FOR F=0 TO N(1)-1
1880 RFEATRES F 8 L(1)
1890 IF F=0 LOL=(L(1)+.5)*K
1900 IF F=1 LOR=(L(1)+.5)*K
1910 NEXT F
1920 setftrpar "2,3,8,1,11"
1930 ftrgrey 1 : measfeat 20 1 4 300000 : clraccept
1940 acceptxfer 20 22
1950 RFEATNUM N(1)
1960 FOR F=0 TO N(1)-1
1970 RFEATRES F 8 L(1)
1980 IF F=0 LON=(L(1)+.5)*K
1990 IF F=1 LOS=(L(1)+.5)*K
2000 NEXT F
2010
PRINT#5:C,L0,L90,LOL,LOR,LON,LOS,ML*K/2,RADIUS,AREA,ROUND,ASPECT,(XCG/100
0)-256,(YCG/1000)-256
2020 outline 4 6
2030 binx 15 6 15 2 0 0
2040 print time$
2050 goto 240
2060 CLOSE#1:CLOSE#2:CLOSE#3:CLOSE#4:CLOSE#5
2070 SAVEBIN 15 'C:\NEIL\'+'N$+'.TIF'
2080 END
```

---

Excel spreadsheet (permcals.xls) on XEN used to calculate permeabilities from isochrone data.  
 The mathematics for this are presented in Appendix B3.

$\varepsilon$	FRAME	TIME (s)	X (m)	Y (m)	$x^*$ (m)	$y^*$ (m)	$\rho$	t	A26	X/Y	1	$x^*/y^*$	X-Y (m)	$x^*-y^*$ (m)
0.500	1	43.5	0.0495	0.0388	0.042	0.046	15	44	1030	1.28	1.00	0.91	0.011	0.004
$\mu$ 31.000 $\text{Nsm}^{-2}$	2	144.5	0.0772	0.0579	0.065	0.068	24	145	3013	1.34	1.00	0.96	0.019	0.003
	3	245.3	0.0946	0.0709	0.080	0.084	29	245	4861	1.33	1.00	0.96	0.024	0.004
	4	346.2	0.1099	0.0804	0.093	0.095	34	346	6908	1.37	1.00	0.98	0.030	0.002
$r_o$ 0.00275 (m)	5	447.2	0.1209	0.0897	0.102	0.106	37	447	8622	1.35	1.00	0.96	0.031	0.004
	6	548.1	0.1313	0.0975	0.111	0.115	40	548	10441	1.35	1.00	0.96	0.034	0.004
	7	649	0.1429	0.1053	0.121	0.124	44	649	12688	1.36	1.00	0.97	0.038	0.004
$P_o$ 200000 ( $\text{N/m}^2$ )	8													
	9													
	10				<b>For Frame 1</b>									
slope 1 0.7156	11			$x^*$ (m)	=D2*POWER(\$A\$15,0.25)									
	12			$y^*$ (m)	=E2*POWER(\$A\$15,-0.25)									
$\alpha$ 0.5121	13			$\rho$	=F2/A\$7									
	14			A26	=H2*H2*(2*LN(H2)-1)+1									
slope 2 18.966	15													
	16													
$k_x$ 3883.4 ( $\times 10^{-12} \text{m}^2$ )	17													
	18													
	19													
$k_y$ 1988.6 ( $\times 10^{-12} \text{m}^2$ )	20													
	21													
	22													

## Appendix B5: Procedure for preparation of polished sections

Specimens were individually potted in an epoxy casting resin and prepared using a Buehler 2000 Metpol grinder/polisher with Metlap fluid dispenser. All specimens were prepared following the procedure shown in Table B5-1.

**Table B5-1: Microscopical specimen preparation**

<i>step</i>	<i>Platen</i>				<i>Head</i>		<i>time</i>
	<i>surface</i>	<i>abrasive</i>	<i>speed (rpm)</i>	<i>direction</i>	<i>speed (rpm)</i>	<i>force (lbs)</i>	
1	SiC paper	240 grit	150	complementary	120	15	until plane
2	"	400 grit	"	"	"	20	2 min
3	"	600 grit	"	"	"	"	"
4	"	800 grit	"	"	"	"	"
5	nylon cloth	6 $\mu$ m diamond	50	contra	"	30	5 min
6	texmet cloth	1 $\mu$ m diamond	100	complementary	60	"	"
7	mastertex cloth	Al SiO <sub>2</sub>	50	contra	"	5	2 min

**Appendix B6:  
Software for quantification of microstructural features (Quantimet 570)**

**A NRLPVOID**

This program detects and measures white objects (magnesium silicate filled surface breaking voids) from contiguous image fields to permit determination of void volume fraction.

**B NRLPZOOM**

This program detects and measures inter-tow porespace as an area fraction and as individual features from six contiguous images.

**C FRACNEIL**

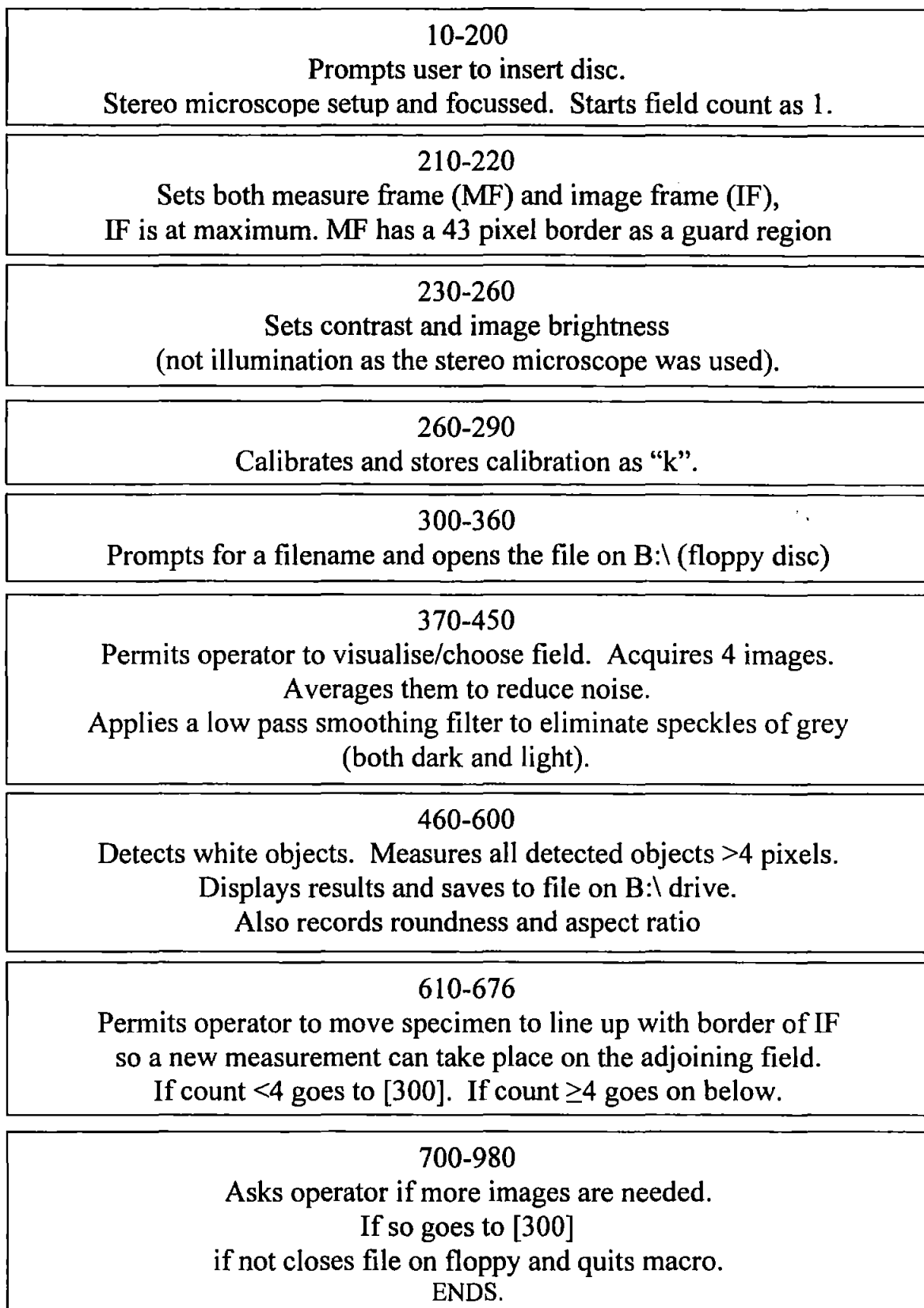
This program detects inter-tow porespace, and in conjunction with program 'NPLDBIN', produces data permitting the determination of a fractal dimension.

**D NPLDBIN**

This program is used in conjunction with the program 'FRACNEIL' and creates the pixel boxes used to 'map' images in the determination of a fractal dimension



**NRLPVOID (IF = Image frame, MF = Measure Frame)**



## NRLPVOID

```
10 panel 0,0,80,79,1,14,3"WELCOME":coltext 44:
   coltext 33:coltext 1
20 postext 12,14
30 print "Place 3.5 disc in bottom drive
   then press space bar"
40 g$=inkey$:if g$="" then 40
50 test g$=" " then 60 else 40
60 cls
70 panel 0,0,80,79,1,14,3"SET UP":coltext 45:
   coltext 32:coltext 1
80 postext 12,15
90 rem WHAT MICROSCOPE, MAG AND ILLUMINATION??????????????
100 PRINT "PLACE B&W CAM ON STEREO X2.5 ZOOM OBJECTIVE
   AND 2.5 EYEPIECE TO"
110 postext 13,26
120 PRINT "FOCUS AND POSITION OBJECT "
130 postext 14,26
140 PRINT " "
150 postext 15,26:COLTEXT 35
160 print "WHEN READY PRESS SPACE BAR"
170 r$=inkey$:if r$="" then 170
180 TEST R$=" " THEN 190 ELSE 170
190 CLS
200 c=1
210 mframe 43 43 427 427
220 iframe 0 0 512 512
230 camera 1
240 scanner 35.53 1.95
250 setlamps 0.0 0
260 QMENU 'IMAGE_SETUP'
270 calibrate 5, 'I'
280 QMENU 'CALIBRATE'
290 riasettings 'cal_value' k
300 panel 0,0,80,79,1,14,3"FILE":coltext 44:
   coltext 33:coltext 1
310 postext 14,5
320 input "PLEASE TYPE THE NAME OF THE FILE
   YOU WISH TO SAVE THIS IMAGE UNDER ",N$
330 open#1 "b:"+n$+".prn"
340 postext 16,5
360 CLS
370 qmenu 'image_setup'
380 panel 0,0,80,79,1,14,3"WORK":coltext 44:
   coltext 33:coltext 1
390 POSTEXT 12,23
400 PRINT "PLEASE WAIT I'M WORKING ON "N$ ", FIELD "C"!"
410 POSTEXT 13,28
420 PRINT "I WILL BE ABOUT 5 SECS"
430 REM
440 multiacquire 5 0 4
450 greyfill 0 1 2 2
460 greydetect 1 47 160 1 1 0
```

```

470 setftrpar "15,33,2,3,1"
480 ftrgrey 3 : measfeat 1 1 4 300000 : clraccept
490 acceptxfer 1 2
500 qmenu 'feature_results'
510 PAUSETEXT 2"ERE THEY BE!"
520 qmenu 'feature_results'
530 rem transform, detect, amend, measure, display
540 rfeatnum n(1)
550 for f=0 to n(1)-1
560 rfeatres f 1 a(1)
570 RFEATRES F 15 R(1)
580 RFEATRES F 33 AR(1)
590 print #1:c,n(1),k*k*a(1),R(1)/1000,AR(1)/1000
600 next f
610 iframe 43 43 427 427
620 qmenu 'measure_field'
630 greyshift 1 8 0 427
640 greydetect 8 47 73 1 1 0
650 display 0 1 0 2
655 qmenu 'display'
660 c=c+1
670 if c=4 goto 710
676 goto 370
700 rem
710 panel 0,0,80,79,1,14,3"THE END":coltext 44: coltext 33:
    coltext 1
720 panel 20,5,40,12,4,14,2"COPYRIGHT":coltext 41:
    coltext 33: coltext 1
730 POSTEXT 8,33
740 PRINT "PPPPP      RRRRR"
750 POSTEXT 9,33
760 PRINT "P    P      R    R"
770 POSTEXT 10,33
780 PRINT "PPPPP      RRRRR"
790 POSTEXT 11,33
800 PRINT "P                RR  "
810 POSTEXT 12,33
820 PRINT "P                R R"
830 POSTEXT 13,33
840 PRINT "P                R   R"
850 panel 20,18,40,6,5,4,2""
860 postext 19,32
870 coltext 1:coltext 32:coltext 45
880 print"Wasn't that fun!"
890 postext 20,32
900 print "That is " n$ " done"
910 postext 21,22:COLTEXT 35
920 print "Do you wish to do another?  y or n"
930 a$=inkey$:if a$="" then 930
940 test a$='y' then 320 else 950
950 coltext 0
960 close#1
970 cls
980 end

```

**NEILZOOM** (IF = Image frame, MF = Measure Frame)

10-70

Starts field count as 1.  
Sets grey images 1 & 2 to white (255) using B&W camera (low gain).  
Illumination is set to 0 as required for stereo microscope. Sets calibration.

80-100

Sets up a full width IF & MF.  
IF height is 45 pixel and MF height is 15 pixel.  
Enters image set-up permitting specimen to be aligned with frames.

110-120

Sets both measure frame (MF) and image frame (IF).  
IF set to maximum.  
MF has a 31 pixel border both W & E and a 61 pixel border N.  
Thus, MF is a square 450 pixel box resting on the S border



130-150

Acquires 4 images and averages images to reduce noise.  
Detects both black and grey objects.

160-210

Erodes binary image and then re-builds (to remove small objects).  
Horizontally erodes and re-builds (to remove slim vertical objects).  
Remaining objects are smoothed by a partial closing which is also vertically applied.

230-310

Detects white objects then removes small areas.  
Opens out areas (breaking any minor networking between objects).  
The resulting separated objects are dilated to return them to the original size.  
The resulting plane is added to the plane at the end of procedure (160-210).  
Only objects in BOTH planes are kept in resulting plane 16

320-360

Plane 16 is segmented to separate any slightly touching objects  
(and remove very small objects).  
Then the operator makes a choice on the images possible as to which one is measured.  
So No.=L170, 1=L150, 2=L170, 3=L180, 4=L200, 5=L210, 10=L250, 12=L270, 16=L310.

370-420

Area fraction of selected plane is measured.  
Individual areas are measured and displayed to screen to be stored if required.

430-560

The whole program is repeated to process six contiguous images.  
A translated part of the stored image  
is superimposed to facilitate alignment of the next live image.

## NEILZOOM

```
10 c=0
20 greyset 255 1
30 greyset 255 2
40 camera 1
50 scanner 16.80 0.00
60 setlamps 0.00 0
70 qmenu 'calibrate'
80 mframe 0 75 512 15
81 iframe 0 60 512 45
100 qmenu 'image_setup'
110 mframe 31.61 450 450
120 iframe 0 0 512 512
130 multiacquire 5 0 4
140 greydetect 0 90 165 4 1 0
150 qmenu 'detect'
160 binerode 1 2 256 2
170 build 1 2
180 edgefeat 2 3
190 binerode 2 4 24 10
200 build 2 4
210 binclose 4 5 24 4
220 greydetect 0 132 227 1 1 0
230 qmenu 'detect'
240 binerode 1 10 0 2
250 build 1 10
260 binopen 10 11 0 2
270 bindilate 11 12 0 6
280 binx 12 5 13 1 0 0
290 bindilate 13 14 24 2
300 build 12 14
310 binx 14 5 16 2 0 0
320 pausetext 2 'Segment bin 16 to bin 17 by 1 filter &
1 cycle'
330 qmenu 'segment'
340 pausetext 1 'You have the choice of taking the whole
area from any binary image'
350 pausetext 2 '1=orig pore, 2=smoothed orig, 3=edgefeat
removed, 4=small areas removed'
360 pausetext 3 '5=4 smoothed, 10=white areas, 12= holes,
16=holes+pore, 17=segmented ver'
370 qmenu 'measure_field'
380 qmenu 'measure_feature'
390 pausetext 1 ''
400 pausetext 2 ''
410 pausetext 3 ''
420 qmenu 'feature_results'
```

```
430 bingreymove 16 1 7
440 c=c+1
450 if c=6 goto 550
460 qmenu 'image_setup'
470 f=c*64
480 setblock 0 0 512 512
490 zoomblock 1 2 f 128 0 ,-8
500 greyshift 0 3 0 500
510 greydetect 3 0 126 1 1 0
520 display 0 1 3 2
530 qmenu 'display'
540 goto 80
550 qmenu 'acquire'
560 end
```

## FRACNEIL

10-70

Prompts for a filename to save to "neil" directory on the C: drive.  
Starts field count as 1. Illumination adjusted for contrast  
with B&W camera with stereo microscope. Image visible on screen.

80-140

Sets measure frame (MF) and image frame (IF),  
to give a 400 pixel square box.  
This allows all subsequent binary fractals to be 'complete'  
i.e. divisible into 400.  
Acquires image, then performs a white detect for magnesium silicate.

150-250

Removes small objects, detects pores (black), cleans image  
and combines with magnesium silicate plane.  
Permits operator to manually edit if necessary.

260-660

Takes processed image plane and sequentially superimposes fractal boxes  
generated from NPLDBIN, counts boxes that overlay porespace.  
Records total area of boxes.  
Each data set (count and area) is saved as a new line to the same file

670-760

Repeats 4 times and shifts image each time to facilitate congruity.  
ENDS

## FRACNEIL

```
10 input "File name? "n$
20 c=1
30 open#1 'c:\neil\'+n$+".prn"
40 camera 1
50 scanner 32.21 0.00
60 setlamps 0.00 0
70 qmenu 'image_setup'
80 mframe 0 81 480 400
90 iframe 0 81 480 400
100 qmenu 'frames'
110 multiacquire 5 0 4
120 greydetect 0 77 255 1 1 0
130 pausetext 2 "detect talc"
140 qmenu 'detect'
150 binerode 1 2 256 3
160 build 1 2
170 greydetect 0 77 212 4 1 0
180 pausetext 2 "detect pore space"
190 qmenu 'detect'
200 pausetext 2 ""
210 binopen 1 10 0 3
212 binopen 10 11 0 4
214 build 10 11
220 bindilate 2 3 0 2
230 binx 1 3 4 2 0 0
240 pausetext 2 'INPUT 4 OUTPUT 4 USE COVER & DELETE'
242 setftrpar "1,2,3,5,4"
243 ftrgrey 0 : measfeat 4 1 99 300000 : clraccept
244 acceptxfer 4 15
246 binmove 15 4
250 qmenu 'bin_edit'
260 pausetext 2 ''
270 binx 4 12 10 1 0 0
280 build 12 10
290 measfield 10
300 rfieldres a(1)
310 print #1:a(1),a(5),c
320 binx 4 13 10 1 0 0
330 build 13 10
340 measfield 10
350 rfieldres a(1)
360 print #1:a(1),a(5)
370 binx 4 14 10 1 0 0
380 build 14 10
390 measfield 10
400 rfieldres a(1)
410 print #1:a(1),a(5)
420 binx 4 15 10 1 0 0
430 build 15 10
440 measfield 10
450 rfieldres a(1)
460 print #1:a(1),a(5)
```



```

470 binx 4 16 10 1 0 0
480 build 16 10
490 measfield 10
500 rfieldres a(1)
510 print #1:a(1),a(5)
520 binx 4 17 10 1 0 0
530 build 17 10
540 measfield 10
550 rfieldres a(1)
560 print #1:a(1),a(5)
570 binx 4 18 10 1 0 0
580 build 18 10
590 measfield 10
600 rfieldres a(1)
610 print #1:a(1),a(5)
620 binx 4 19 10 1 0 0
630 build 19 10
640 measfield 10
650 rfieldres a(1)
660 print #1:a(1),a(5)
670 c=c+1
675 if c=4 goto 750
680 qmenu 'image_setup'
690 greyshift 0 3 0 460
700 greydetect 3 0 126 1 1 0
710 display 0 1 3 2
720 qmenu 'display'
740 goto 70
750 close#1
760 end

```

### **NPLDBIN.QBA**

```

10 loadbin 12 '3.bin'
20 loadbin 13 '4.bin'
30 loadbin 14 '5.bin'
40 loadbin 15 '8.bin'
50 loadbin 16 '10.bin'
60 loadbin 17 '16.bin'
70 loadbin 18 '20.bin'
80 loadbin 19 '40.bin'
100 end

```

This loads binary 12 with 3 pixel box through to bin 19 with a 40 pixel box. Each box separated by a 1-pixel break. Once done for the session the next program is loaded and uses these binary planes to superimpose the boxes on to the binary plane of interest.

**End of Appendix B6.**

## Appendix B7

Selective images taken during the production and testing of mechanical test specimens

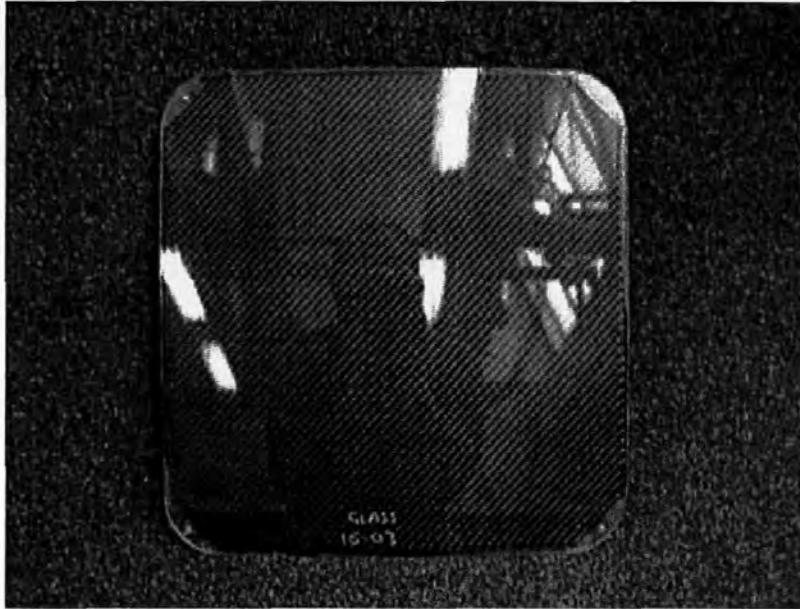


Figure B7-1: Demoulded plate following permeability experiment

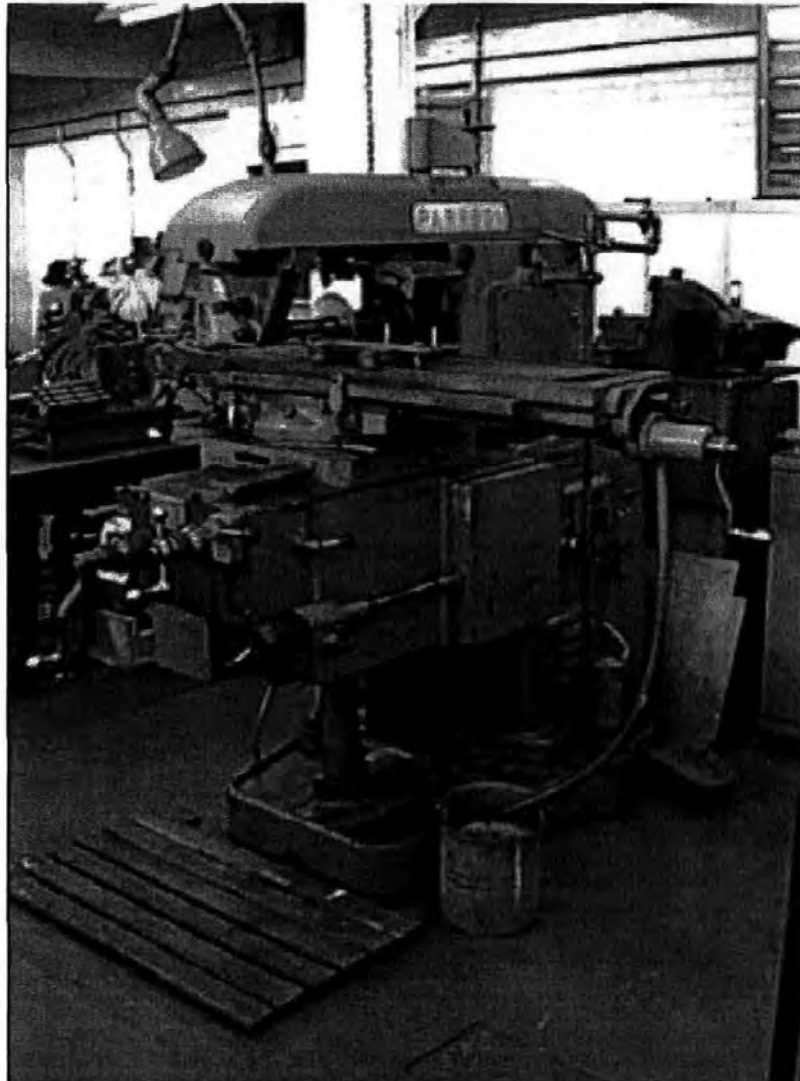


Figure B7-2: Universal milling machining used to cut plates

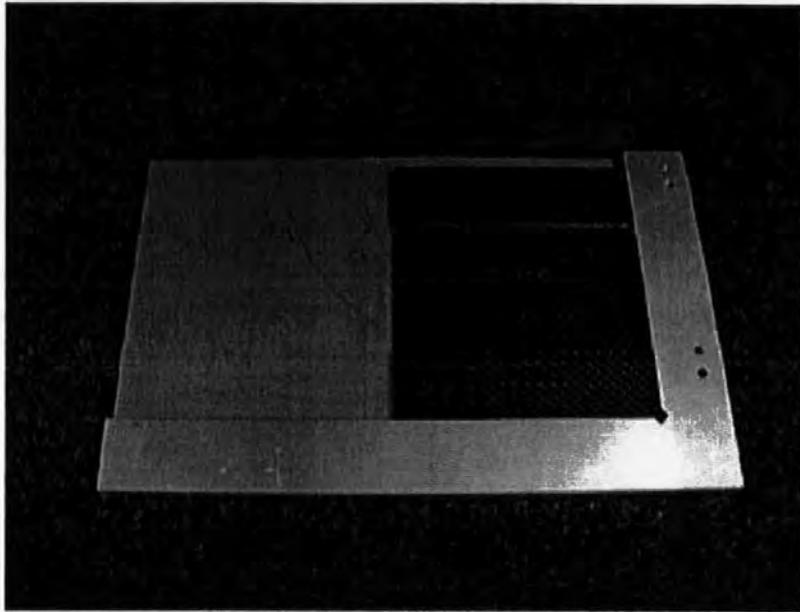


Figure B7-3: End tabs and pre-preg film adhesive positioned on trimmed plate

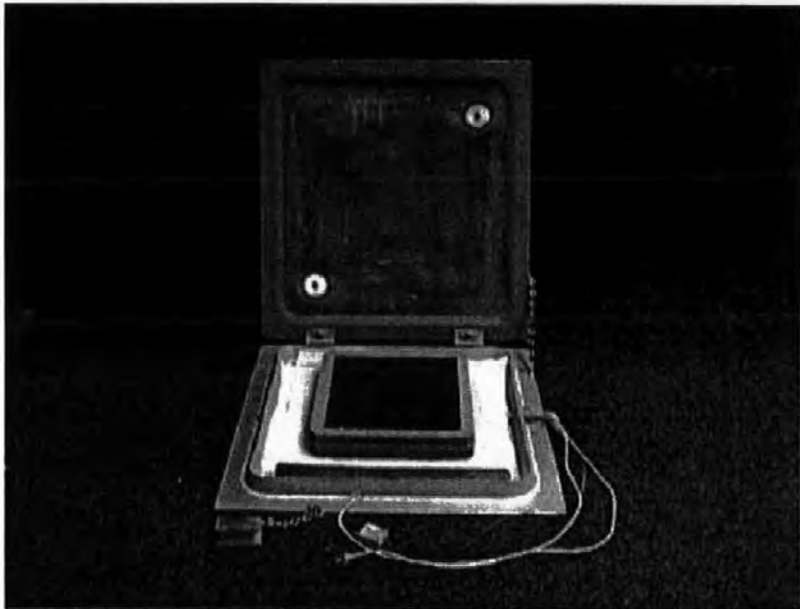


Figure B7-4: Stack of trimmed plates with end tabs applied prior to vacuum consolidation

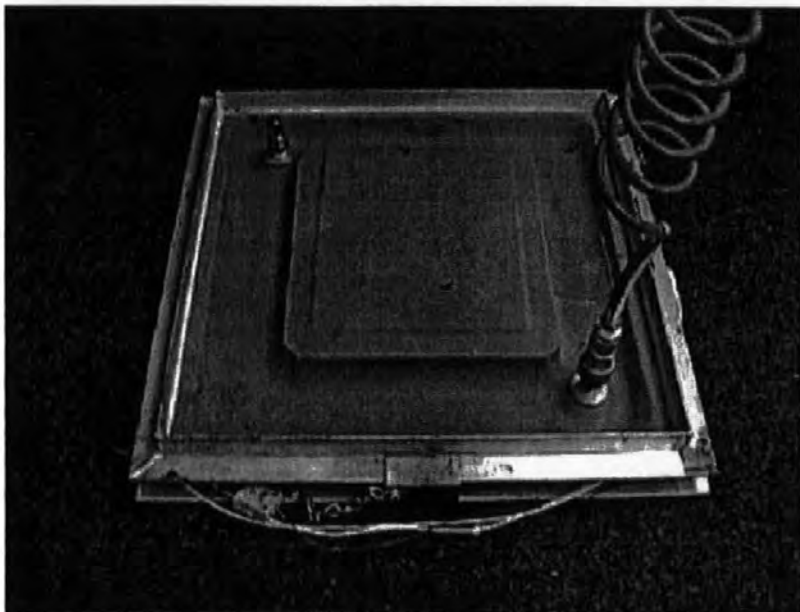


Figure B7-5: Vacuum consolidation of trimmed plates and end tabs

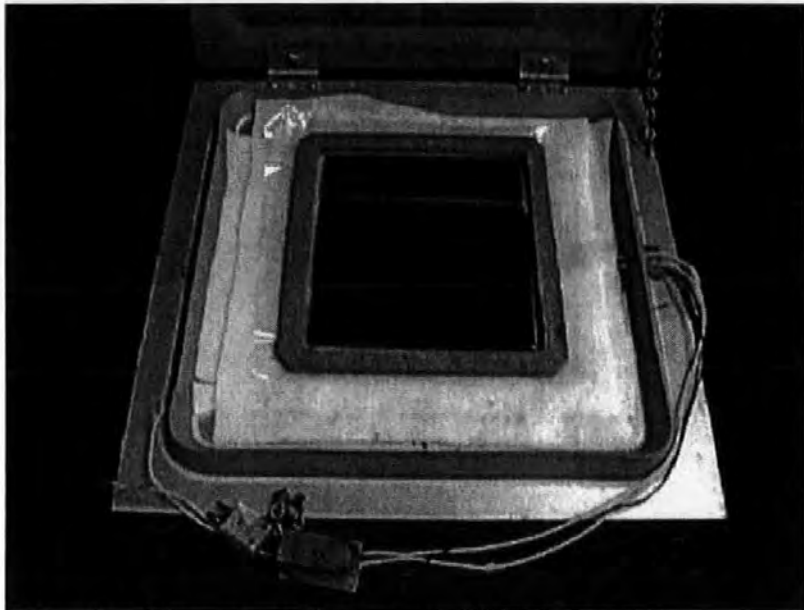


Figure B7-6: End tabs adhered to oven cured / vacuum consolidated plates

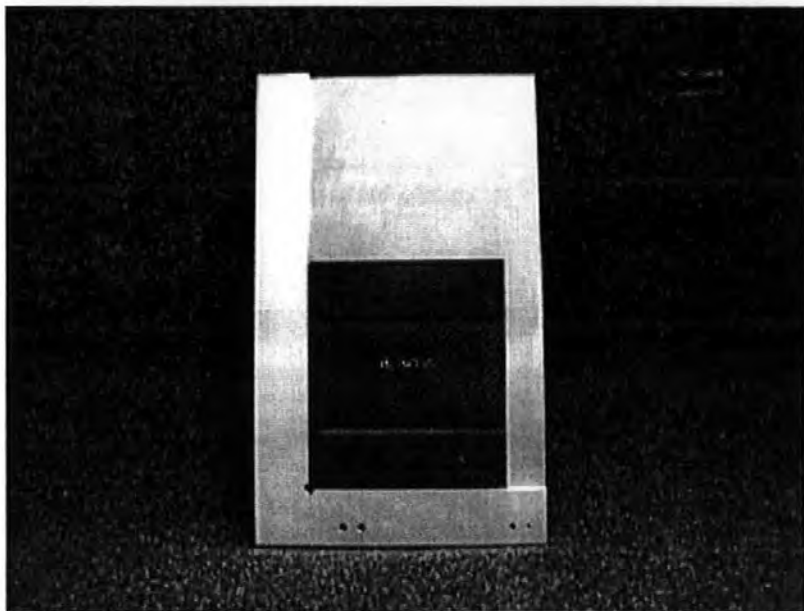


Figure B7-7: Check for trueness of adhered end tabs on plate

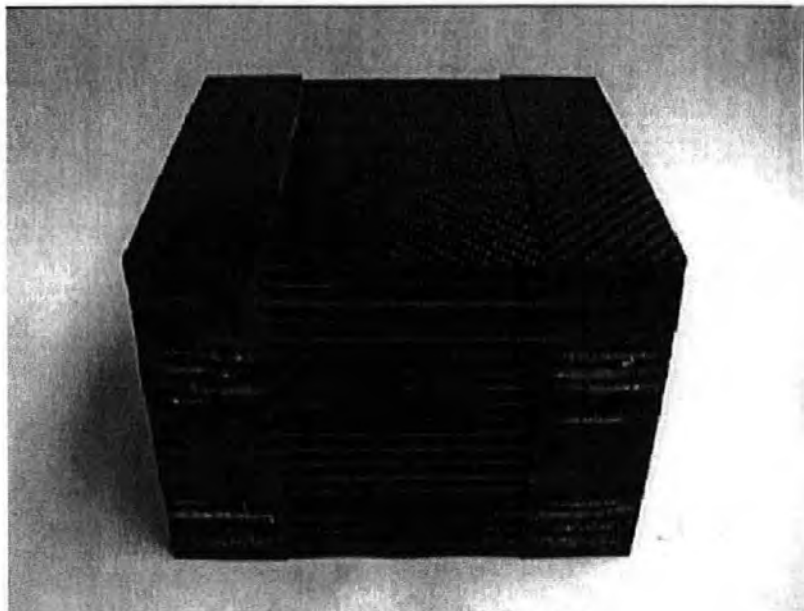


Figure B7-8: Stack of mechanical test plates for new concept Carr fabrics

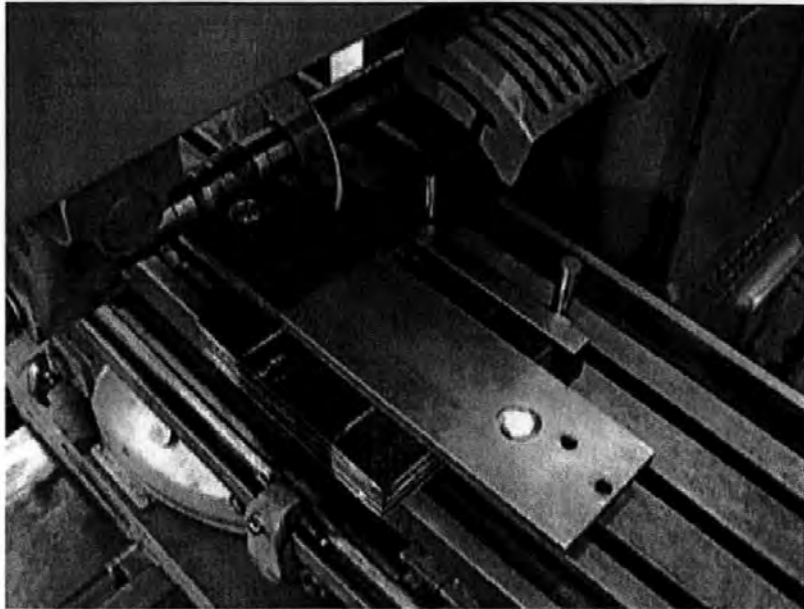


Figure B7-9: Cutting of tension / compression mechanical test coupons with Universal milling machine

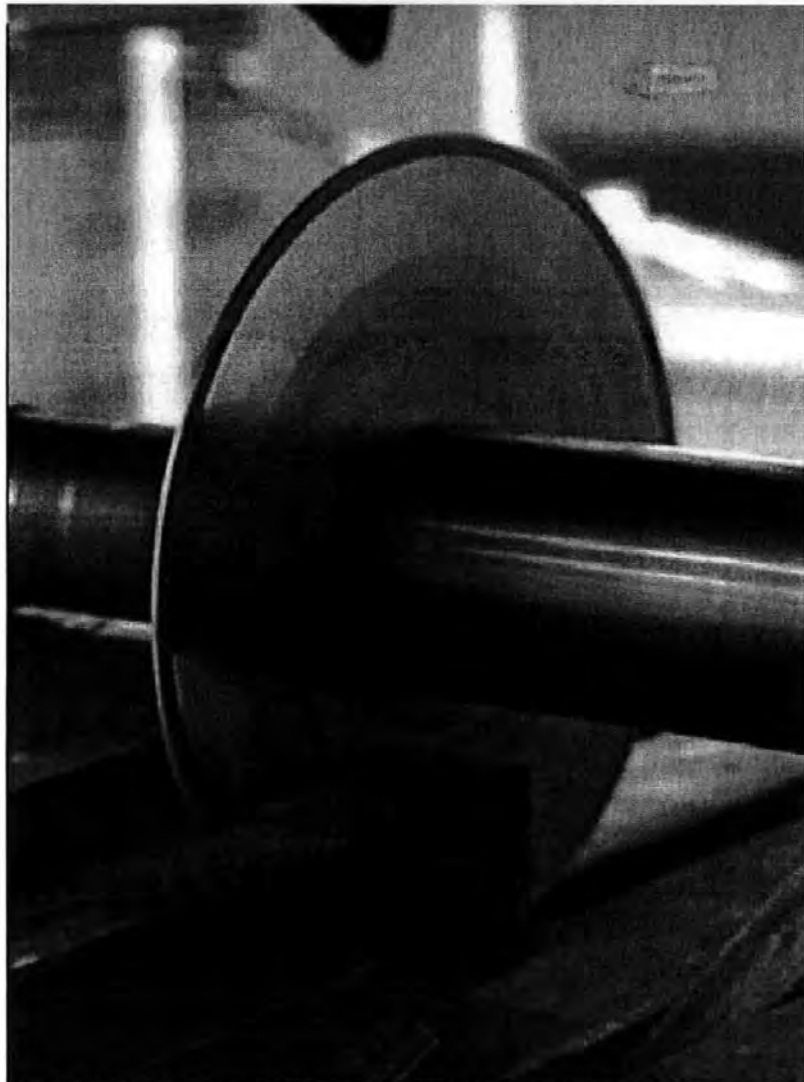


Figure B7-10: Cutting of tension / compression mechanical test coupons with Universal milling machine

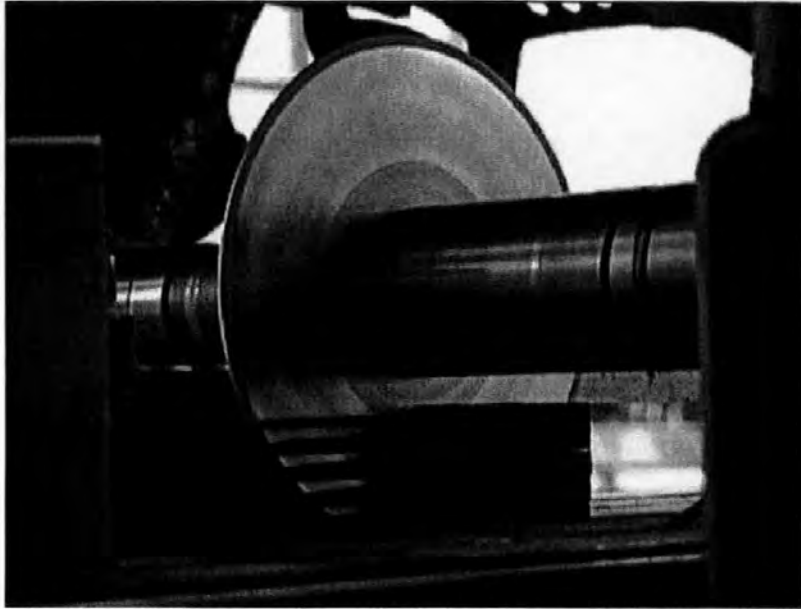


Figure B7-11: Cutting of tension / compression mechanical test coupons with Universal milling machine

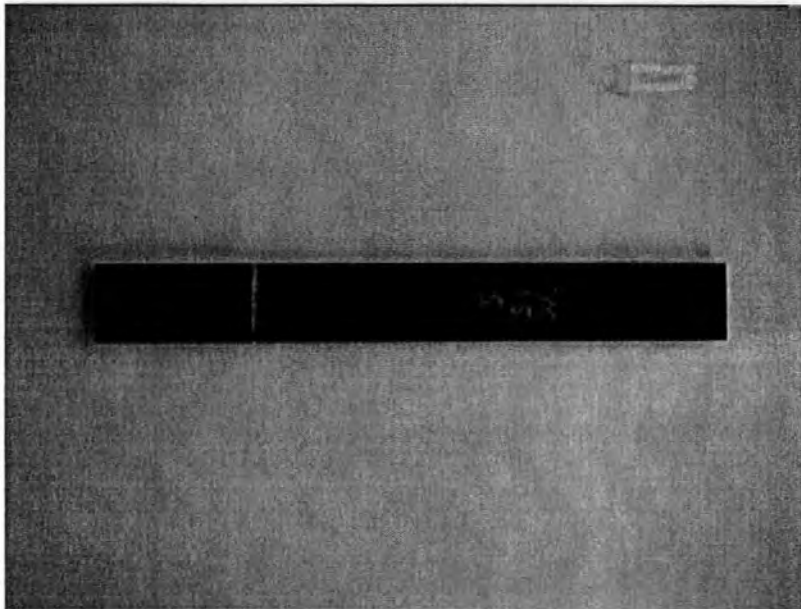


Figure B7-12: Front view of compression test coupon

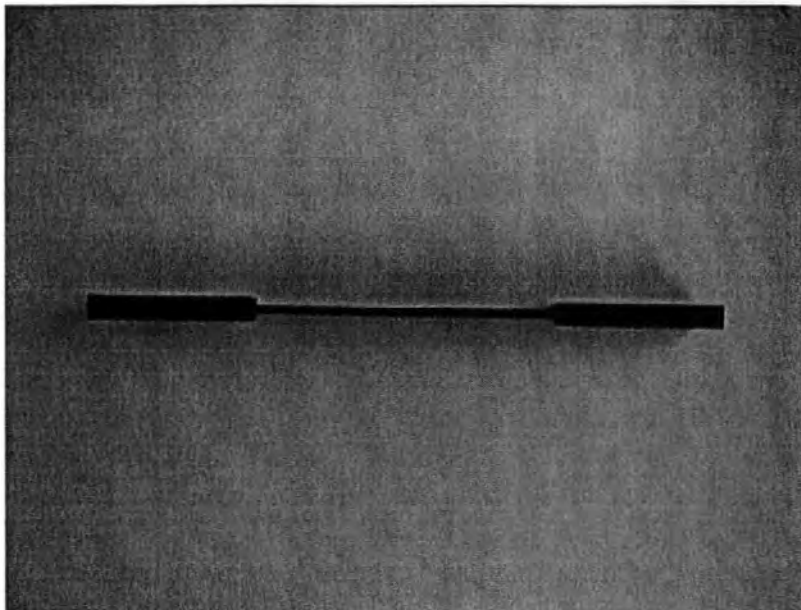


Figure B7-13: Side view of compression test coupon

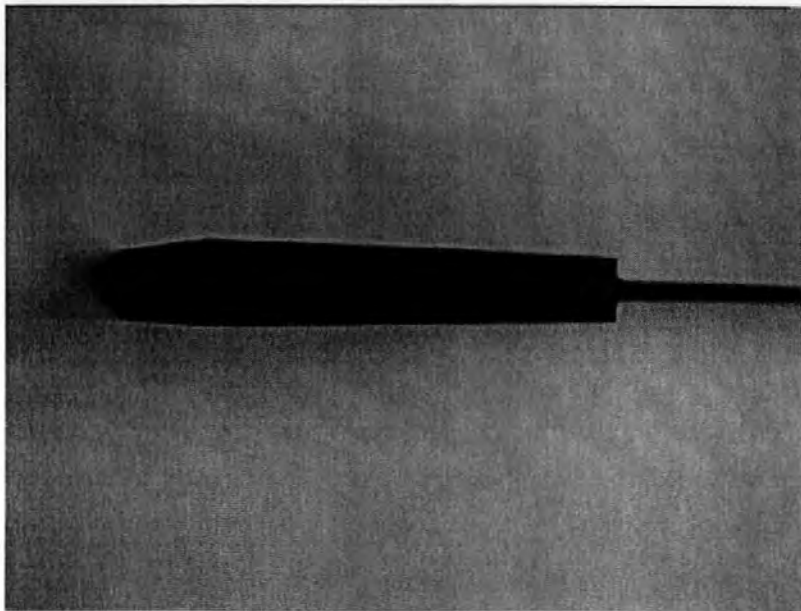


Figure B7-14: Close of the end of a compression test coupon

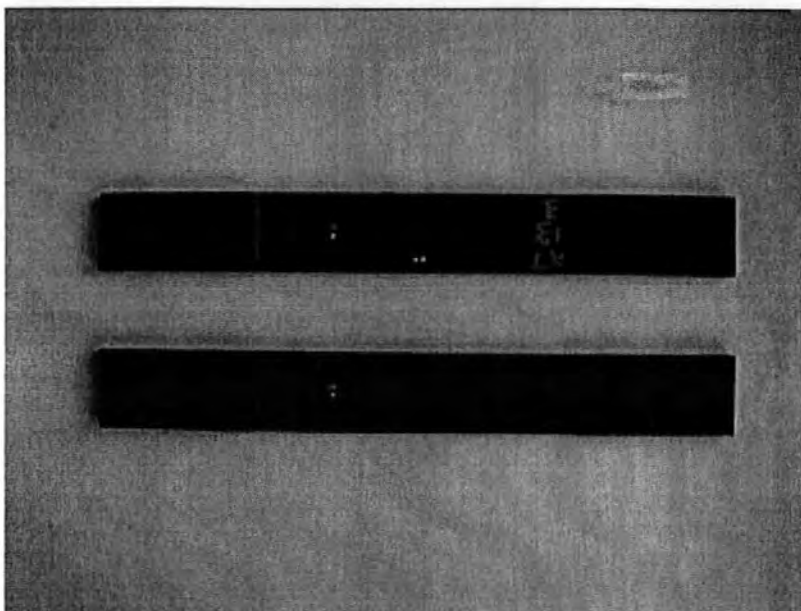


Figure B7-15: Tensile test coupons with strain gauges applied

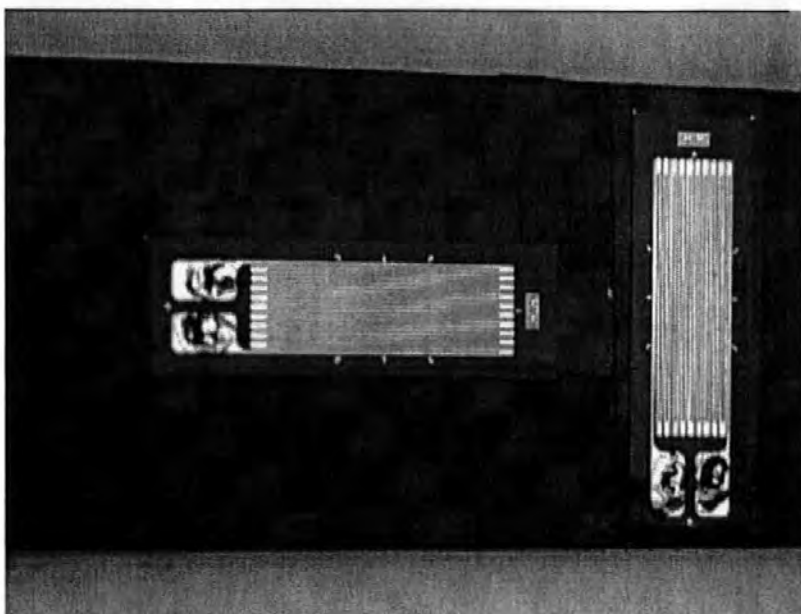


Figure B7-16: Close up of strain gauges on tensile test coupon

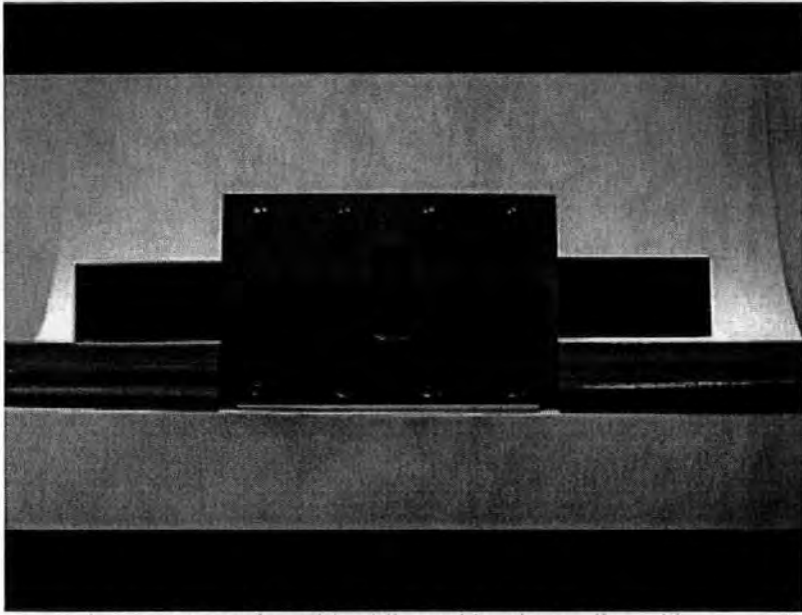


Figure B7-17: Compression test coupon in anti-buckling guide prior to align with spacers (front face shown)

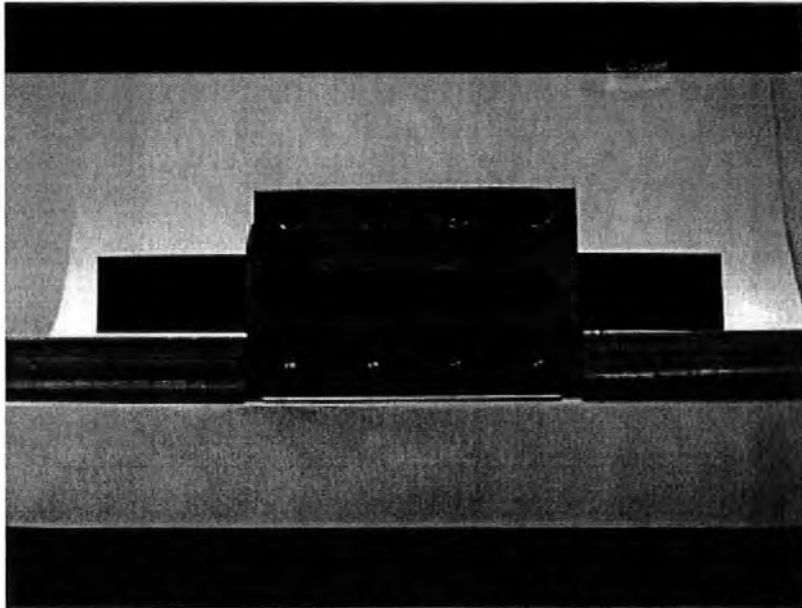


Figure B7-18: Compression test coupon in anti-buckling guide prior to align with spacers (rear face shown)

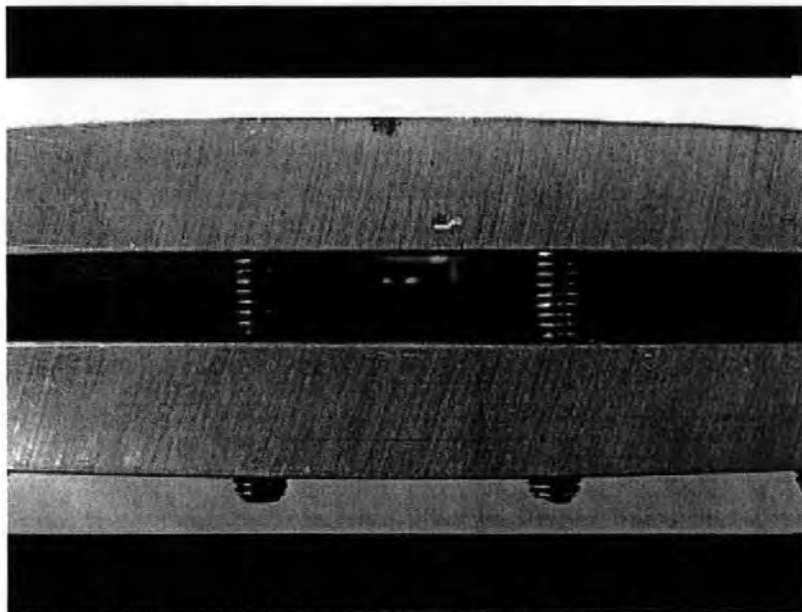


Figure B7-19: Side view of compression test coupon in anti-buckling guides



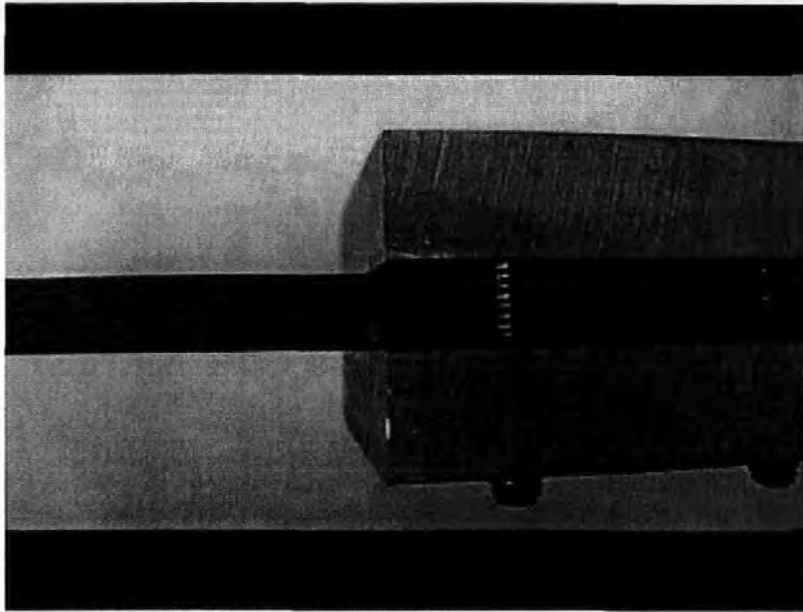


Figure B7-20: Close up of the end of the anti-buckling guide

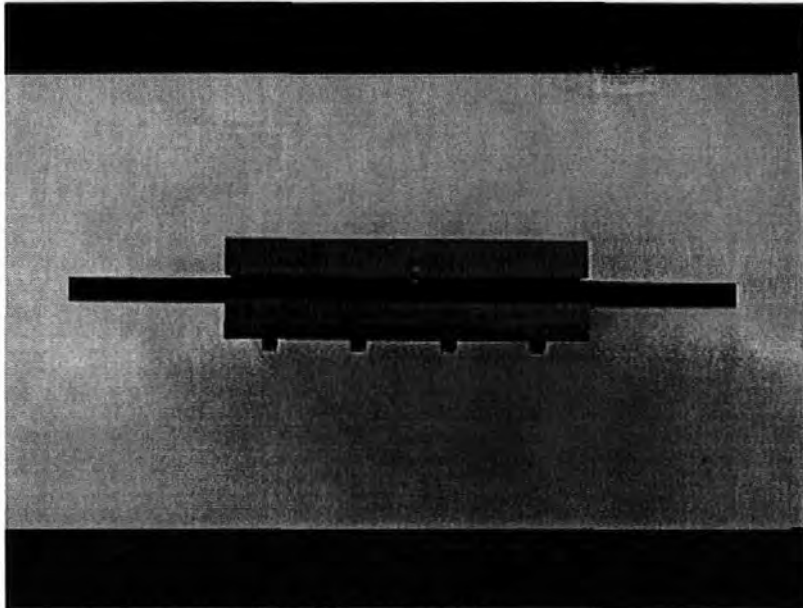


Figure B7-21: Compression test coupon in anti-buckling guide



Figure B7-22: Equipment used to test, control and record tension and compression testing

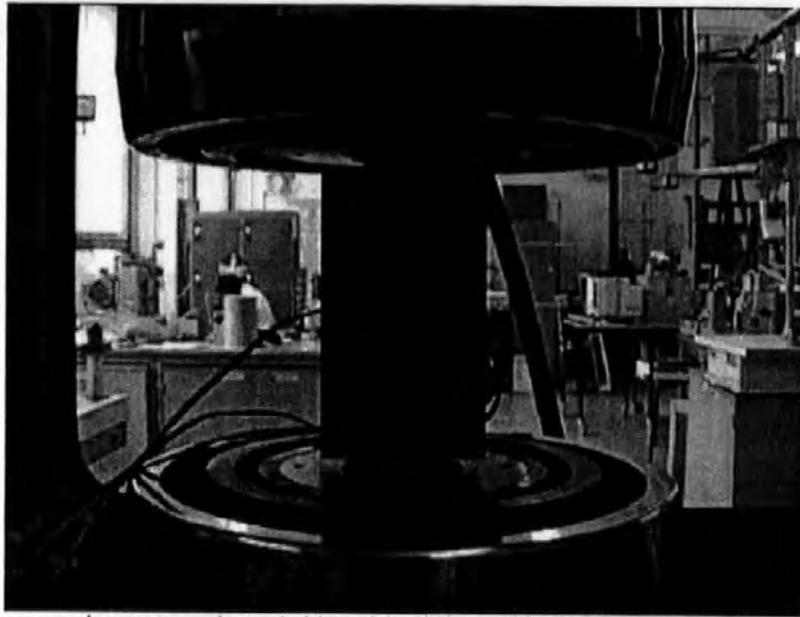


Figure B7-23: Compression test specimen (with anti-buckling guide fitted) during testing

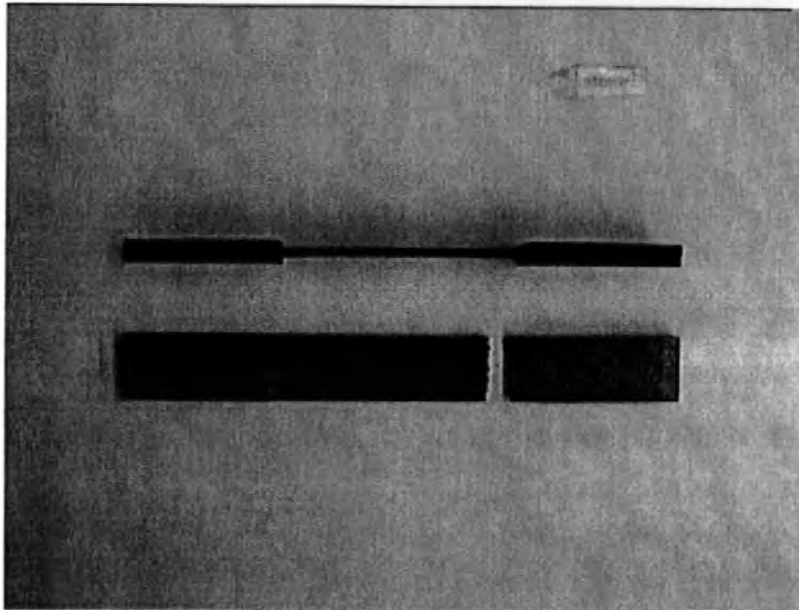


Figure B7-24: Failed tensile test coupon (intact coupon shown to indicate failure location)

## Appendix C: Text and data-files on CD-ROM

The text, Figures and Tables  
from this thesis  
are included on a CD-ROM  
inside the back cover  
of the bound thesis.